Iron-Sulfur Cluster-Containing Enzymes Involved in Isoprenoid Biosynthesis and Electron Bifurcation

by

Selamawit Menghisteab Ghebreamlak

A dissertation submitted to the Graduate Faculty of
Auburn University
in partial fulfillment of the
requirements for the Degree of
Doctor of Philosophy

Auburn, Alabama
May 8, 2016

Keyword: Isoprenoid biosynthesis, electron bifurcation, iron sulfur cluster, iron-sulfur flavoprotein IspH, Hdr

Approved by

Eduardus C. Duin, Chair, Associate Professor of Chemistry and Biochemistry
Holly R. Ellis, Professor of Chemistry and Biochemistry
Douglas C. Goodwin, Associate Professor of Chemistry and Biochemistry
Bradley L. Merner, Assistant Professor of Chemistry and Biochemistry
Forrest Smith, Associate Professor of Drug Discovery and Development

Abstract

Iron-sulfur-cluster-containing proteins are present in all living organisms. They are involved in a wide array of biological processes such as electron transfer, substrate binding and activation, regulation of enzyme activity and gene expression, sensing of reactive species, radical generation and sulfur donation. The work in this dissertation is focused on the spectroscopic characterization of two proteins that contain [4Fe-4S] clusters in their active site, (*E*)-4-hydroxy-3-methylbut-2-enyl diphosphate reductase (IspH) and subunit A of heterodisulfide reductase (HdrA).

(*E*)-4-hydroxy-3-methylbut-2-enyl diphosphate (HMBPP) reductase is the terminal enzyme in the biosynthesis of isoprenoids via the 1-deoxy-D-xylulose-5-phosphate (DOXP) pathway. IspH catalyzes the conversion of (*E*)-4-hydroxy-3-methylbut-2-enyl diphosphate (HMBPP) into two five carbon products, isopentenyl diphosphate (IPP) and dimethylallyl diphosphate (DMAPP). The DOXP pathway is responsible for the biosynthesis of isoprenoids in many pathogenic eubacteria, plastid containing eukaryotes, and parasitic protozoans. Humans use a different pathway, making the DOXP route a promising target for the development of herbicides and antimicrobials. To develop potential inhibitors for the DOXP pathway the catalytic mechanism of IspH has been investigated. Colorimetric assays, site-directed mutagenesis, and spectroscopic methods (EPR, ENDOR and Mössbauer) have been employed in this work to study the role of the [4Fe-4S] cluster and several conserved amino acid residues in the active site of the enzyme.

EPR-monitored rapid-freeze-quench experiments with wild type IspH under turnover conditions in the presence of a reductant and substrate showed the formation of two paramagnetic species. The first signal denoted FeS-I, was further characterized with ^{57}Fe-ENDOR and Mössbauer spectroscopies. The electronic and magnetic properties of this intermediate are similar to a HiPIP-like $[4Fe\text{-}4S]^{3+}$ species that was detected in ferredoxin:thioredoxin reductase, indicating the direct binding of the substrate to a cluster that has a formal 3+ oxidation state. This species is also similar to an EPR active intermediate that was trapped in IspG, another DOXP pathway enzyme, and heterodisulfide reductase. The second species, FeS-II, represents a cluster with product bound because a similar signal was observed when dithionite-reduced enzyme was incubated with IPP or DMAPP.

In EPR-monitored rapid-freeze-quench experiments with mutant IspH (H124F, E126Q and T167C) similar and additional paramagnetic intermediates were observed. When reduced H124F and T167C IspH were incubated with HMBPP, two EPR active intermediates are detected that are similar to the species in the WT enzyme. This is in line with the fact that both of these mutants were active, albeit with lower catalytic activity. The E126Q mutant on the other hand, has no activity and a paramagnetic species (designated FeS-III) that is different from the EPR active species in the WT enzyme can be detected. When dithionite-reduced E126Q IspH was incubated with IPP or DMAPP, an identical signal was observed.

The FeS-III species detected in the E126Q mutant is considered a reaction intermediate by several groups and several hypothetical mechanisms are based on the electronic and magnetic properties of this species. Our freeze-quench data, however, suggests that this species appears

much later in the reaction than the FeS-I species, which makes the catalytic relevance of this species questionable. The kinetic and spectroscopic analyses are in line with an important role in catalysis for some of the mutated amino acids. H124 and T167 are proposed to participate in the correct orientation of the substrate, while the E126 residue is involved in the dehydration of the HMBPP. Although the kinetic data obtained here does not argue against the current reaction mechanism, there is the real concern that some aspects are based on the properties of the FeS-III species detected in the E126Q mutant and not on the properties of the true reaction intermediate, FeS-I. This species needs to be further investigated, particularly using ENDOR studies of IspH incubated with ^{13}C-labeled HMBPP.

Heterodisulfide reductase, also referred as Hdr, is an iron-sulfur flavoprotein that catalyzes the reversible cleavage of CoM-S-S-CoB. Heterodisulfide reductase is involved in the flavin-based electron bifurcation mode of energy conservation in methanogenic archaea. Since the Hdr enzyme contains up to 7 iron-sulfur clusters, it was investigated if it was possible to just study the A subunit. This subunit harbors FAD, which is the supposed site of the bifurcation. HdrA, from *M. marburgensis* was overexpressed in *M. maripaludis* and was successfully purified. The enzyme contained substoichiometric amounts of [4Fe-4S] clusters and in vitro cluster reconstitution successfully increased the cluster content. FAD was absent and attempts to reconstitute it were not successful. EPR-based redox titration of HdrA failed to show a particular paramagnetic species that was detected in the redox titration of Hdr and the whole Hydrogenase/Hdr complex. This cluster is proposed to be the direct electron acceptor for the

high-potential electron from the FAD. The absence of the EPR signature indicates that the HdrA subunit cannot be used in these studies.

Acknowledgement

I dedicate this work to all the educators in my home country, Eritrea. Without them I could not have been where I am today and become the person that I am today.

First and foremost, I would like to express my sincere gratitude to my advisor Dr. Duin, for his continuous support of my PhD studies. Thank you for giving me the opportunity to be part of your group and for your guidance, patience, immense knowledge and encouragement throughout my graduate career. I could not have imagined having a better advisor and mentor.

Besides my advisor, I would like to thank the rest of my thesis committee Drs. Douglas Goodwin, Holly Ellis, Bradley Merner and Forrest Smith for their valuable comments and instructive suggestions to my research and dissertation.

Special thanks goes to our collaborators: Drs. Brian Hoffmann, Nicolas Lees and Joshua Tesler for the ENDOR measurements; Dr Sebastian Stoian for the Mössbauer measurements; Dr Leigh for providing *M. marburgensis* HdrA enzyme and Drs. Dr. Michael Groll and Ingrid Span for providing *E. coli* wild type and mutant plasmids.

I would like to extend my gratitude to previous members of Dr. Duin's group Xiao, Divya, Ovee and Suman. I am also thankful to the current students Carly, Robel, Bryan and Rachel. Thank you for your support, companionship and the enjoyable environment. I would like to express my sincere gratitude and appreciation to everyone who have enriched my life during my time in Auburn.

My endless gratitude goes out to my family, especially my mom, my sisters and Amare Araia, who with their continuous love and support have made me the person I am.

Last, but not least, I want to thank my husband Yohannes for his patience, understanding and loving support throughout writing this thesis and my life in general.

Table of Contents

List of Tables

List of Figures

List of Abbreviations

A. aeolicus	*Aquifex aeolicus*
CoB	Coenzyme B
CoM	Coenzyme M
CDP-ME	4-Diphosphocytidyl-2-*C*-methyl-D-erythritol
CDP-MEP	4-Diphosphocytidyl-2-*C*-methyl-D-erythritol-2-phosphate
CW	Continuous wave
DOXP	1-Deoxy-D-xylulose-5-phosphate
DMAPP	Dimethylallyl diphosphate
DXS	1-Deoxy-D-xylulose-5-phosphate synthase
E. coli	*Escherichia coli*
ENDOR	Electron nuclear double resonance spectroscopy
EPR	Electron paramagnetic resonance spectroscopy
Ferredoxin	Fd
FTR	Ferredoxin:thioredoxin reductase
Fe-S	Iron-sulfur cluster
Hdr	Heterodisulfide reductase
HDS	Heterodisulfide
HiPIPs	High-potential iron-sulfur proteins
HMG-CoA	Hydroxymethylglutaryl-CoA

HMBPP	1-Hydroxy-2-methyl-2-(*E*)-butenyl-4-diphosphate
HYSCORE	Hyperfine sublevel correlation
IPP	Isopentenyl pyrophosphate
IspC	1-Deoxy-D-xylulose 5-phosphate reductoisomerase
IspD	2-*C*-Methyl-D-erythritol-4-phosphate cytidyltransferase
IspE	4-Diphosphocytidyl-2-*C*-methyl-D-erythritol kinase
IspF	2-*C*-Methyl-D-erythritol-2,4-cyclodiphosphate synthase
IspG	1-Hydroxy-2-methyl-2-*(E)*-butenyl-4-diphosphate synthase
IspH	(*E*)-4-Hydroxy-3-methyl-2-butenyl diphosphate reductase
IUB	International Union of Biochemistry
M. marburgensis	*Methanothemobacter marburgensis*
M. maripaludis	*Methanococcus maripaludis*
MEcPP	2-*C*-Methyl-D-erythritol 2,4-cyclodiphosphate
MEP	2-*C*-Methyl-D-erythritol 4-phosphate
MVA	Mevalonate
P. falciparum	*Plasmodium falciparum*
SDS-PAGE	Sodium dodecyl sulfate-polyacrylamide gel electrophoresis
RFQ	Rapid-freeze-quench
WT	Wild type

CHAPTER 1 : Introduction

1.1 Isoprenoids

Isoprenoids are one of the oldest and largest groups of naturally occurring biomolecules. These natural products are structurally and functionally diverse. The building blocks of isoprenoids are two simple five carbon isoprenes, isopentenyl diphosphate (IPP) and dimethylallyl diphosphate (DMAPP). Initial condensation of the isoprene units followed by complex and diverse chemistry affords over 25,000 isoprenoid compounds. Some examples are given in **Fig 1.1**. These compounds are involved in many aspect of every living organism's biological processes. To name a few: aerobic respiration (ubiquinone), membrane stability (sterols), visual and photosynthetic pigments (chlorophylls), reproductive hormones (steroid hormones), defensive agents (monoterpenes), and as photo-protective agents (carotenoids) (1–4).

Up to two decades ago, the mevalonate (MVA) pathway was believed to be the sole pathway for the biosynthesis of IPP and DMAPP in all living organisms. A second non-mevalonate pathway, called 1-deoxy-D-xylulose-5-phosphate (DOXP) pathway, was discovered due to the inconsistencies observed in the mevalonate research (2, 5, 6). Very recently a third alternate mevalonate pathway has been discovered for the biosynthesis of IPP (7).

The mevalonate pathway is the biosynthetic method for the formation of IPP in animals, plants, fungi, the majority of archaea and a few eubacteria. In this pathway acetyl-CoA is the source of the C-backbone **(Fig 1.2)**. A 3-hydroxy-3-methylglutaryl-CoA molecule formed by the condensation of three acetyl-CoA is converted to mevalonate. The IPP is a product of two phosphorylation steps followed by decarboxylation of the mevalonate. The isomerization of IPP affords DMAPP (5, 8).

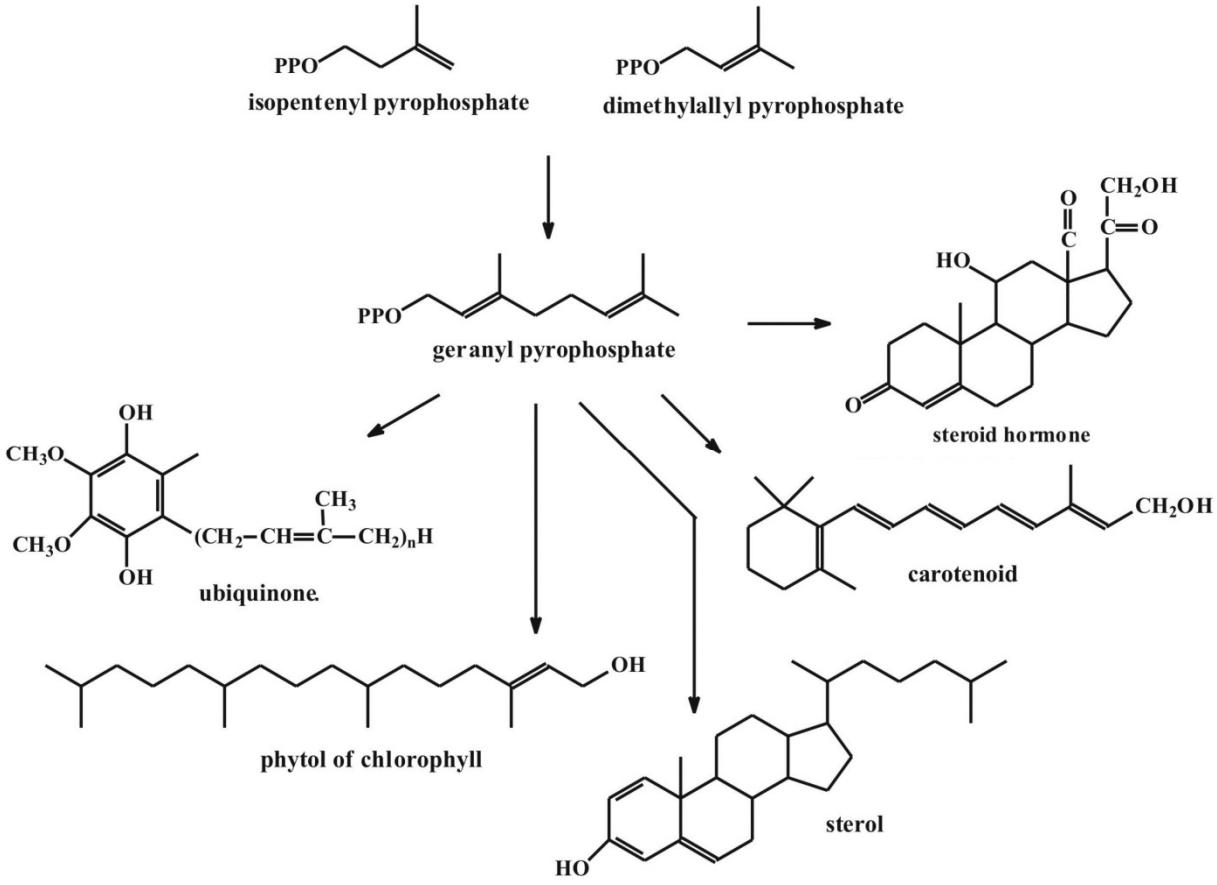

Figure 1.1: Example of isoprenoids found in nature.

Table 1.1: Distribution of isoprenoid biosynthesis pathways in the three domains of life and some of the kingdoms.

	Mevalonate		DOXP
	Classical	Alternate	
Bacteria	✓	✗	✓
Archaea	✓	✓	✗
Fungi	✓	✗	✗
Algae	✓	✗	✓
Plant	✓	✗	✓
Protozoa	✓	✗	✓
Animals	✓	✗	✗

Combination of phylogenetic analysis and biochemical characterization has been instrumental in the discovery and identification of two alternate mevalonate pathways for the biosynthesis of IPP in some archaea **(Fig 1.2)**. In both biosynthetic pathways, as in the classical mevalonate pathway, the primary precursor is acetyl-CoA. Some of the mevalonate pathway enzymes are absent (7, 9–11).

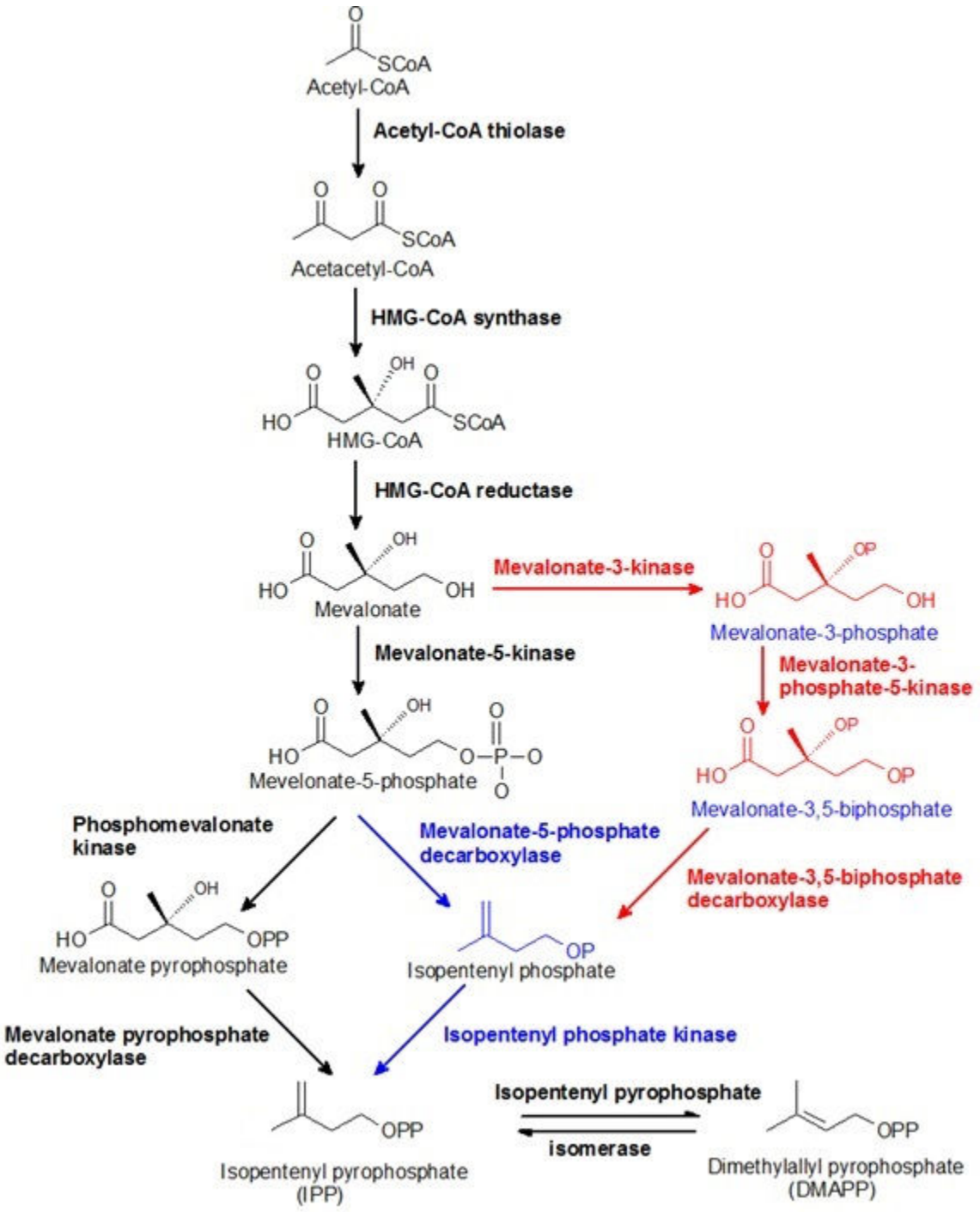

Figure 1.2: Classical (black) and alternate (blue and red) mevalonate pathways. Adapted from (9).

1.2 DOXP pathway

The DOXP pathway, a mevalonate independent biosynthetic pathway, is the choice of IPP and DMAPP synthesis for many eubacteria, plastid containing eukaryotes and parasitic protozoans. In this pathway, also referred as 2-*C*-methyl-D-erythritol-4-phosphate (MEP) or non-mevalonate pathway, pyruvate and glyceraldehyde-3-phosphate condensation is the beginning of the biosynthesis **(Fig 1.3)** (2, 4, 6).

Isotope labeling studies in bacteria and plant species were important in the discovery and affirmation of the DOXP pathway in the 1990's. The results were inconsistent with the long held dogma of the universality of the mevalonate pathway. In bacteria ^{13}C-labeled glucose, acetate, erythrose and pyruvate were used as single source of carbon. Incorporation of the isotope on to the final product, polyterpenoid, as well as the labeling pattern, showed discrepancy with the expected labeling patterns based on the mevalonate pathway (6, 12, 13).

Evidence for the presence of the DOXP pathway came from labeling studies in plant systems. In plants there is compartmentation of the two pathways, mevalonate pathway operates in the cytoplasm whereas the DOXP pathways is present in the chloroplast. A ^{14}C labeled mevalonate was converted into triterpenes and sterols, but not incorporated into the monoterpenes and carotenoids. Another instance was when isotopically labeled 1-deoxy-D-xylulose was used and it was observed that the molecule was efficiently incorporated into carotenoid and phytol. Additionally, the labeling pattern showed a process which is in the frame of the DOXP pathway (12–14). Furthermore, inhibition studies in plants with mevalonin, an HMG-CoA reductase inhibitor, didn't have any effect on the synthesis of carotenoids and the chlorophylls. In contrast, sterol biosynthesis was inhibited (13, 15).

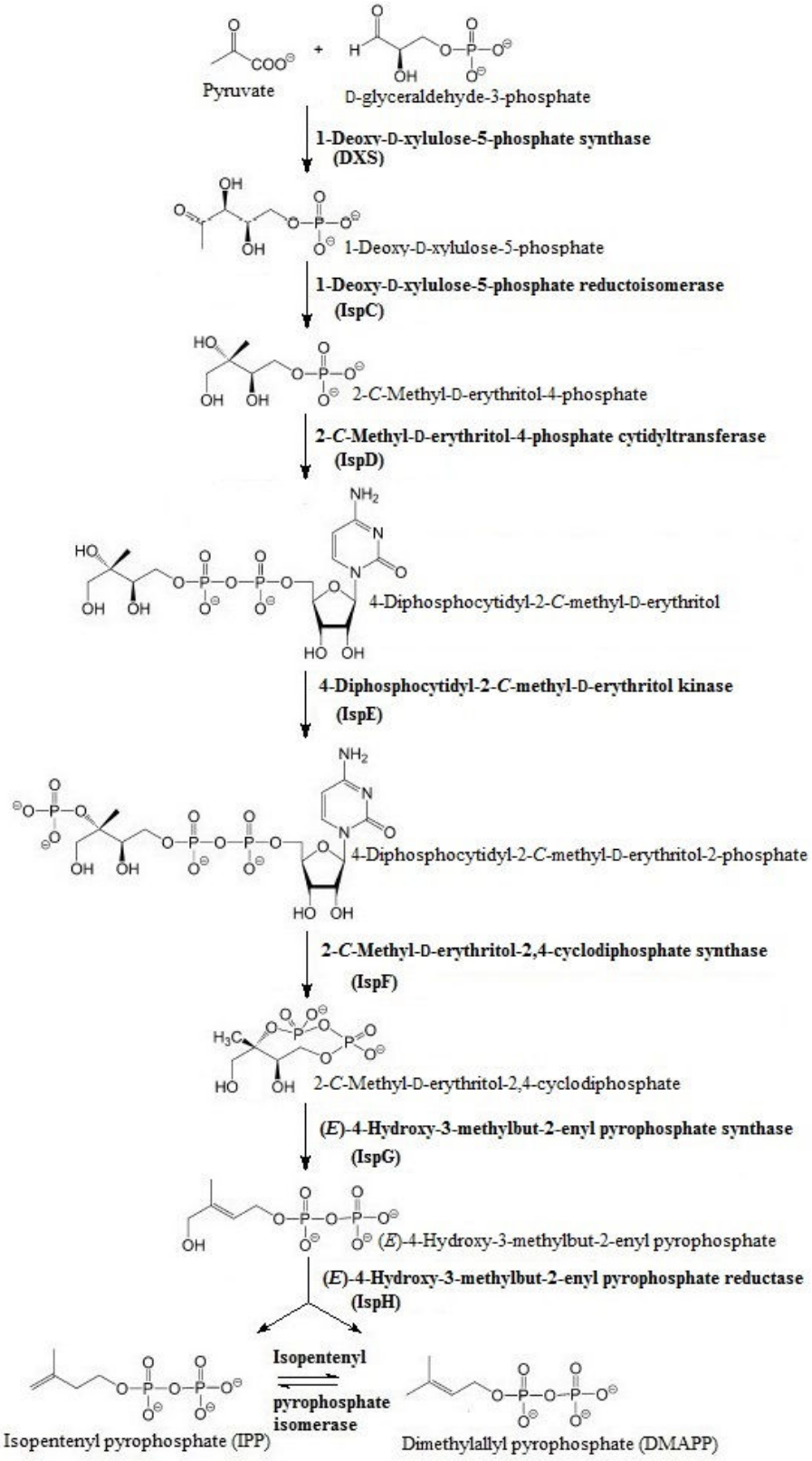

Figure 1.3: DOXP pathway.

1.2.1 Enzymes of the DOXP pathway

In the biosynthesis of the universal precursors, IPP and DMAPP, via the DOXP pathway seven enzymes that are nonhomologous to the mevalonate pathway are involved. All the enzymes are structurally and functionally varied. The reaction mechanism of the first five enzymes have been well established.

a. 1-Deoxy-D-xylulose-5-phosphate synthase (DXS, EC: 4.1.3.37)

The first intermediate in the DOXP pathway is 1-deoxy-D-xylulose-5-phosphate, formed by the transketolase-like decarboxylation of pyruvate and D-glyceraldehyde-3-phosphate **(Fig 1.4A)**. The reaction is catalyzed by thiamine and divalent cation (Mn^{+2}, Mg^{+2}) dependent 1-deoxy-D-xylulose-5-phosphate synthase. DOXP, besides being an intermediate in IPP and DMAPP biosynthesis, is also involved in thiamine (vitamin B1) and pyridoxol (vitamin B6) biosynthesis (16–18).

b. 1-Deoxy-D-xylulose 5-phosphate reductoisomerase (IspC, E.C: 1.1.1.267)

IspC is the first committed enzyme of the pathway and is involved in the intramolecular rearrangement and reduction of DOXP to afford 2-*C*-methyl-D-erythritol-4-phosphate (MEP) **(Fig 1.4B)**. Divalent cations, such as Mn^{2+}, Co^{2+} and Mg^{2+}, and NADPH are paramount for the reaction to proceed. IspC has been a target of an antimalarial drug, fosmidomycin (17, 19, 20).

c. 2-C-Methyl-D-erythritol-4-phosphate cytidyltransferase (IspD, E.C: 2.7.7.60)

A CTP-dependent reaction converts MEP into 4-diphosphocytidyl-2-*C*-methyl-D-erythritol (CDP-ME) **(Fig 1.4C)**. Divalent ions Mg^{2+}, Co^{2+} and Mn^{2+} are used as cofactors in catalysis (17, 21, 22).

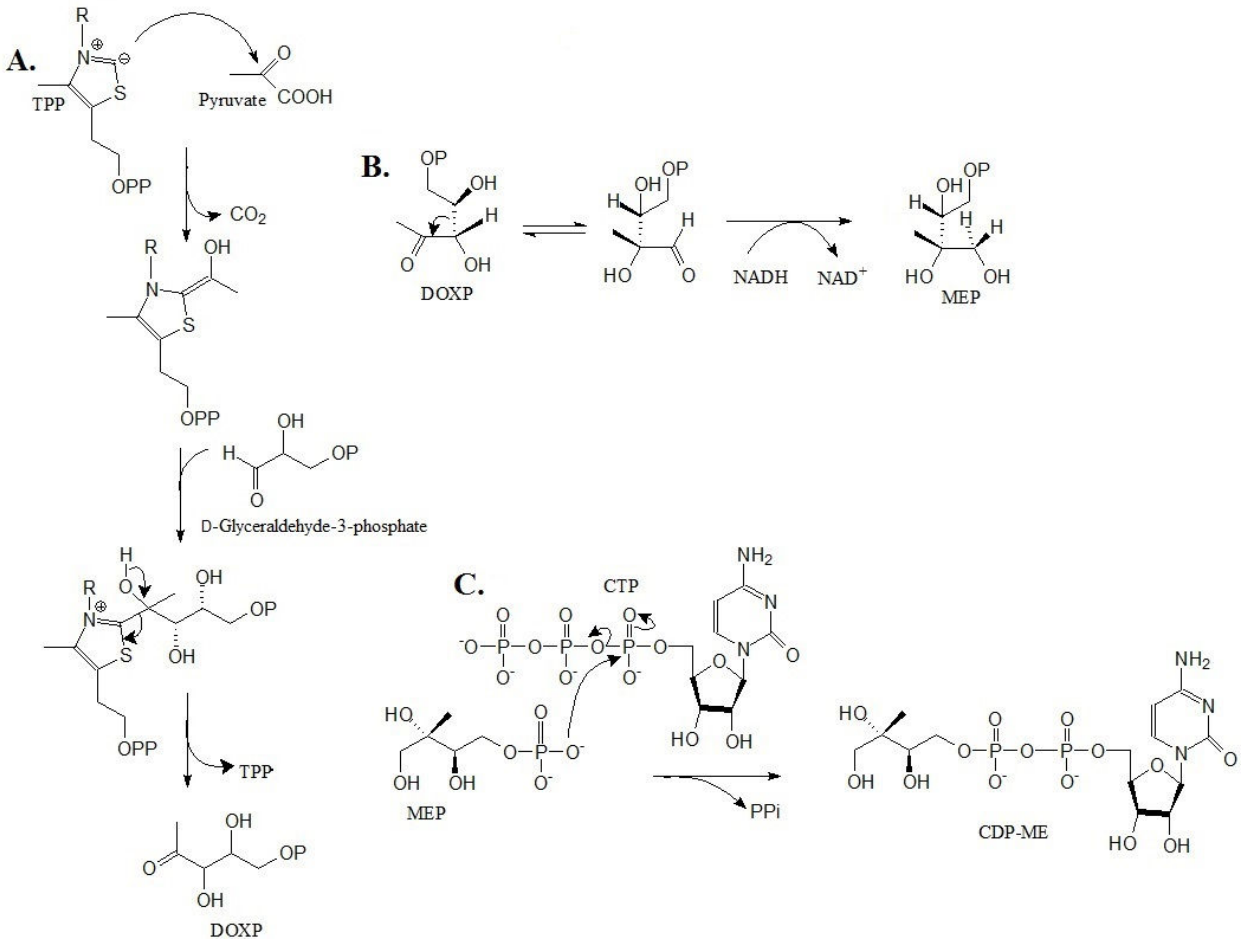

Figure 1.4: Reactions catalysed by DXS (A), IspC (B) and IspD (C).
Adapted from (17).

d. 4-Diphosphocytidyl-2-C-methyl-D-erythritol kinase (IspE, EC: 2.7.1.148)

4-Diphosphocytidyl-2-*C*-methyl-D-erythritol-2-phosphate (CDP-MEP) is synthesized by the phosphorylation of CDP-ME at C-2 **(Fig 1.5 A).** The reaction is catalyzed by the action of IspE, an ATP and Mg^{2+} dependent enzyme (23–25).

e. 2-C-Methyl-D-erythritol-2,4-cyclodiphosphate synthase (IspF, E.C. 4.6.1.12)

IspF is the fifth enzyme of the DOXP pathway and partakes in the conversion of CDP-MEP to a cyclic intermediate, 2-*C*-methyl-D-erythritol-2,4-cyclodiphosphate (MEcPP). There is an intermolecular transphophorylation accompanied by the release of CMP **(Fig 1.5 B)**. Divalent ions, Zn^{2+}, Mg^{2+}, Mn^{2+} are involved in the catalysis (26, 27).

f. E-4-Hydroxy-3-methylbut-2-nyl pyrophosphate synthase (IspG, E: 1.17.7.1)

IspG is an Fe-S cluster containing enzyme and catalyzes the reductive dehydration of MEcPP to (*E*)-4-hydroxy-3-methylbut-2-enyl pyrophosphate (HMBPP). This enzyme will be discussed in detail in **section 1.3.2.3** (17, 28, 29).

g. (E)-4-Hydroxy-3-methylbut-2-enyl pyrophosphate reductase (IspH, E: 1.17.1.2)

The last enzyme in the DOXP pathway is IspH. Like IspG, this enzyme has an Fe-S cluster as its cofactor and is involved in the reductive dehydration of HMBPP to IPP and DMAPP (30, 31). The elucidation of the mechanism of this enzyme is the main topic of this dissertation.

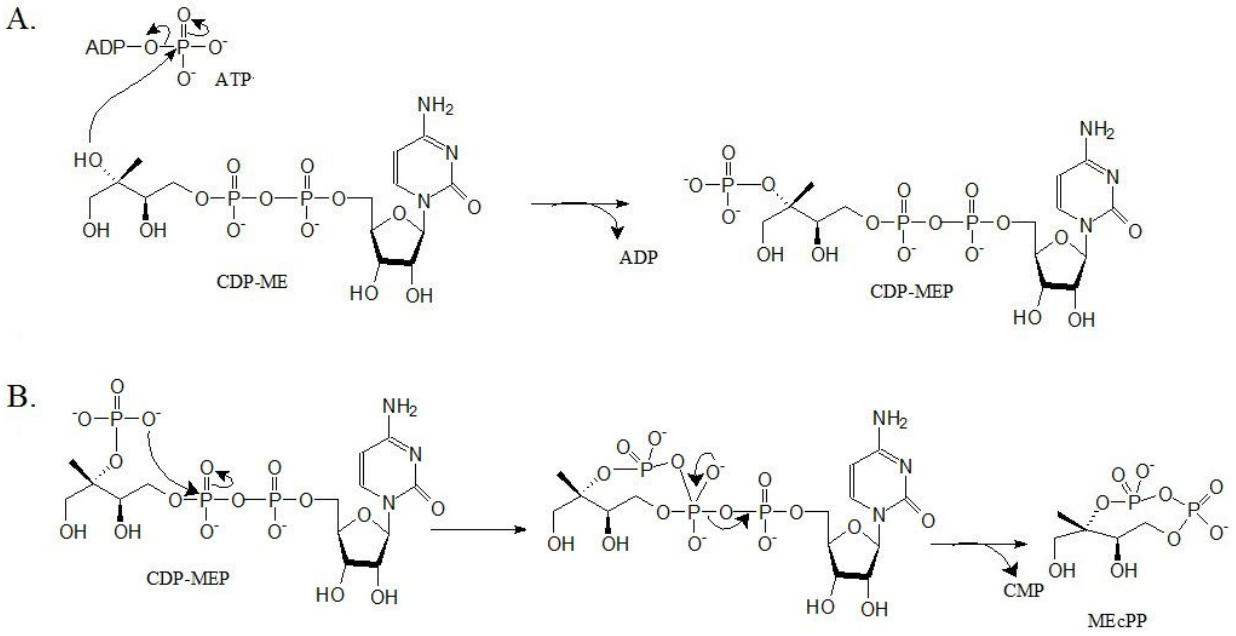

Figure 1.5: Reactions catalysed by IspE (A) and IspF (B).
Adapted from (25, 27).

1.2.2 DOXP pathway as therapy target and in biotechnology

As the DOXP pathway is essential in plant plastids, pathogenic eubacteria and pathogenic protozoa, but absent in humans, the route can be targeted by herbicides and antimicrobials. The list of pathogenic bacteria that use the DOXP pathway and the diseases they cause is presented in **Table 1.2**.

There is a continuing search for novel herbicides and antimicrobials. Compounds have been identified as potential inhibitors of the DOXP enzymes through ligand-based design, structure-based design, mechanism-based design and from high-throughput screening. A number of hits have been reported **(Table 1.3)**. Ketoclomazone (commercially available herbicide), fluoropyruvate and 2-methyl-3-(4-fluorophenyl)-5-(4-methoxy-phenyl)-4*H*-pyrazolo[1,5-*a*]pyrimidin-7-one have been reported to inhibit DXS activity (32–34). Research has also shown the feedback inhibition of DXS by IPP and DMAPP (35).

Fosmidomycin, a natural antibiotic isolated from *Streptomyces lavendualae,* is a potent herbicidal and antimicrobial targeting the second enzyme of the pathway, IspC. Fosmidomycin has been structurally modified to increase its hydrophobicity and its antimicrobial efficacy (36–39). A search for compounds that target the IspD is also underway. L-Erythritol-4-phosphate, azolopyrimidine derivatives and pseudilin derivatives have shown inhibitory effect against the enzyme (40–42). Non-phosphate cytidine derivatives have been reported as inhibitors of the kinase IspE (43).

The activity of the fifth enzyme of the DOXP pathway, IspF, was decreased by the action of fluorescent derivatives of cytidine diphosphate (CDP), imidazole derivatives and benzimidazole-based compounds (44, 45). It was shown that maculosin, a metabolite from *Bacillus subtilis*, has antimicrobial activity against *E. coli* and targets IspG (46). The activity of

both IspG and IspH was decreased by alkyne diphosphates. IspH is also inhibited by pyridine diphosphates and HMBPP analogs (47).

However, the only antimicrobial that has reached phase II clinical study is fosmidomycin and has been investigated for almost two decades. Fosmidomycin has been used and evaluated as a chemotherapeutic agent for acute uncomplicated *Plasmodium falciparum,* the etiologic agent of malaria, in Mozambique, Gabon and Thailand. Even though fosmidomycin is effective, it has a short half-life in plasma as well as poor oral availability thus high doses of the compound have to be used to achieve the desired effect. Fosmidomycin is more efficient when used in combination with clindamycin, but this makes the treatment cost ineffective (19, 39, 48, 49).

Besides being a therapeutic target the DOXP pathway is responsible in the biosynthesis of a plethora of isoprenoid metabolites that are used as pharmaceuticals, pigments, fragrance, flavors and agrochemicals **(Table 1.4)** (50–53). The pathway can be manipulated so as to overproduce these natural products. The potent antitumor drug paclitaxel (trade name Taxol) can be isolated from the *Taxus brevifolia* pacific yew tree. There is, however, a limited supply of these slow growing trees. Production was improved by applying combinatorial biosynthetic strategies in *E. coli* (54). In addition, advances in customized metabolic engineering and synthetic biology has been used to increase β-carotene, ubiquinone and lycopene production in *E. coli* (55–57).

Table 1.2: Major Human bacterial pathogens that use DOXP and the diseases they cause. Adapted from (58).

Microorganism	Disease
Gram-negative cocci	
Neisseria meningitidis	Meningitis, Waterhouse–Friderichsen syndrome
N. gonorrhea	Gonorrhoea
Gram-positive non-spore-forming rods	
Corynebacterium diphtheriae	Diphtheria
Listeria monocytogenes	Listeriosis
Actinomyces israelii	Keratoactinomycosis
Nocardia sp.	Bronchopneumonia
Gram-positive spore-forming rods	
Bacillus anthracis	Anthrax
Clostridium histolyticum	Gas gangrene
C. difficile	Colitits
C. botulinum	Botulism
C. tetani	Tetanus
Gram-negative rods	
E. coli	Enterocolitis, urinary tract infection
Salmonella typhi	Typhus
S. paratyphi	Bacteraemia
Shigella sonnei	Typhus
Yersinia enterocolitica	Enterocolitis, diarrhoeal
Y. pseudotuberculosis	Gastroenteritis
Y. pestis	Plague
Klebsiella pneumoniae	Pneumonia
K. ozaenae	Ozena, atrophic rhinitis
K. rhinoscleromatis	Rhinoscleroma
Serrratia marcescens	Wound infections, sepsis
Proteus sp.	Wound infections, sepsis
Pseudomonas sp.	Wound infections, sepsis
Brucella abortus	Morbus Bang
B. melitensis	Malta fever
Francisella tularensis	Tularaemia
Haemophilus influenzae	Pneumonia, meningitis
H. ducreyi	Ulcus molle
Pasteurella sp.	Wound infections, sepsis
Bordetella pertussis	Pertussis

Table 1.2: Continued

Microorganism	Disease
Gram-negative/spiral-shaped bacteria	
Vibrio cholerae	Cholera
H. pylori	Gastritis Type B
Campylobacter jejuni	Enterocolitis
Spirochaetal bacteria	
Treponema pallidum	Syphilis
T. vincenti	Necrotizing gingivitis
Chlamydia psittaci	Psittacosis
C. trachomatis	Chlamydia
C. pneumoniae	Pneumonia
C. lymphogranulomatosis	Lymphogranulomatosis
Wall-less bacteria	
Mycoplasma penetrans	Urogenital infections

Table 1.3: DOXP pathway enzymes and their inhibitor.

Enzyme	Example of inhibitors
DXS	Ketoclomazone, 5-(4-methoxy-phenyl)-4*H*-pyrazolo[1,5-*a*]pyrimidin-7-one, fluoropyruvate, IPP and DMAPP
IspC	Fosmidomycin, FR900098
IspD	L-erythritol-4-phosphate, azolopyrimidine and pseudilin derivatives
IspE	Cytidine derivatives
IspF	Fluorescent derivatives of CDP, imidazole and benzimidazole derivatives
IspG	Maculosin, alkyne diphosphate
IspH	HMBPP analogs, alkyne diphosphate, pyridine diphosphates

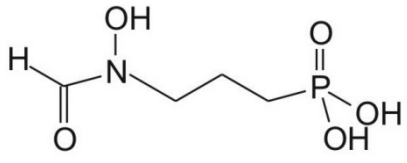

Fosmidomycin

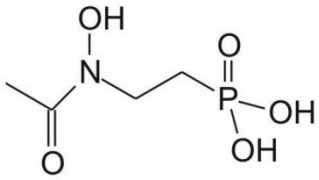

FR900098

Table 1.4: Examples of plant metabolites and their application/(s).

Plant metabolite	Source	Application
Paclitaxel	*Taxus brevifolia*	Antitumor drug
β-carotene, lycopene	*Dunaliella sp*	Pharmaceuticals, color, food industry, provitamin A
Vinblastine and Vincristine	*Catharanthus roseus*	Antitumor drugs
Pyrethroids	*Chrysanthemum cinerariaefolium*	Insecticide
Sclareol	*Salvia sclarea*	Fragrance industry
Steviol	*Stevia rebaudiana*	As sweetener in food industry
Diterpene resin acid	*Pinus spp*	Industrial coatings and inks

1.3 Iron-sulfur proteins (Fe-S proteins)

IspH is an iron-sulfur protein. In the following sections the properties of this class of proteins and their cofactors will be discussed, as well as some of the biophysical techniques used to study them. Iron-sulfur proteins are metalloenzymes that contain one or more iron-sulfur clusters as their cofactors. Even though iron-sulfur proteins are one of the oldest catalysts and play a central role in the biological processes of all life forms, ranging from electron transfer to DNA repair, they were not discovered until the 1960s. The cluster is a low-molecular weight inorganic molecule comprising one to eight Fe atoms bridged by inorganic sulfide (S^{2-}). Besides the acid-labile bridging sulfides, the Fe is coordinated to cysteine thiols, a link to the polypeptide chain of proteins, resulting in tetrahedral coordination of the Fe sites. In some occasions the Fe site is coordinated to non-cysteine ligands such as; other amino acid side chains (aspartate, histidine, glutamate, serine), main chain peptide groups, cofactors, and/or relatively simple inorganic molecules or species like water (in the form of either H_2O or OH^-), carbon monoxide (CO), cyanide (CN^-) or substrate molecules, as well as some more complex molecules. The non-cysteine ligand can impart specific properties to the Fe-S cluster that can be crucial for its designated function (59).

The International Union of Biochemistry (IUB) classifies the Fe-S proteins into two categories: simple and complex iron-sulfur proteins. Simple Fe-S proteins contain one or more iron-sulfur clusters. Whereas, the complex Fe-S proteins have other active redox centers such as flavin, molybdenum or heme, besides the cluster (60).

1.3.1 Types of Iron-sulfur cluster and their properties

In metalloenzymes, there are a variety of Fe-S clusters and the basic cluster types are; mono nuclear [Fe], rhombic [2Fe-2S], cuboidal [3Fe-4S] and cubane [4Fe-4S] **(Fig 1.6)**. The versatility of the Fe-S cluster function is attributed to its remarkable chemistry. Different properties of the cluster such as electron transfer, coordination chemistry and the ability to undergo cluster interconversion are exploited.

1.3.1.1 Cluster conversion/interconversion, sulfur and ligand exchange

Conditions such as the presence of O_2, reducing agents and iron chelators can cause conversion/interconversion among the different structures of Fe-S clusters **(Fig 1.7)**. It has been reported that mutation of one of the Cys ligands in *Clostridium pasteurianum* rubredoxin to Ala resulted in the conversion of the mononuclear $Fe(S\text{-}Cys)_4$ to a [2Fe-2S] cluster. In fumarate nitrate reduction (FNR) protein from *E. coli* interconversion between a [4Fe-4S] cluster and a [2Fe-2S] cluster has been observed. It has also been reported that oxidation of a [4Fe-4S] cluster in aconitase resulted in the formation of an inactive [3Fe-4S] cluster, which can be reversed by adding Fe in a reducing environment (61–63).

Flexibility of the Fe-S cluster was demonstrated by labeling studies with sulfide which showed the tendency of the sulfide in the cluster to exchange with free sulfide in solution (64). Moreover, it has been reported that a ligand exchange takes place when a cuboidal [3Fe-4S] cluster was converted to linear a [3Fe-4S] cluster (65).

A. Single non-heme iron

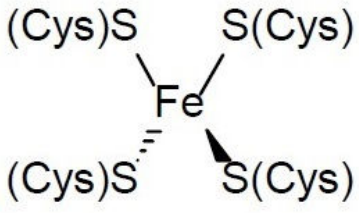

B. [2Fe-2S]

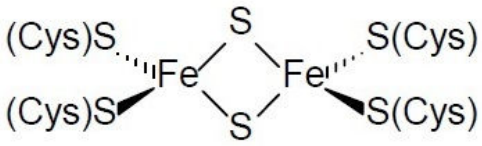

C. [3Fe-4S]

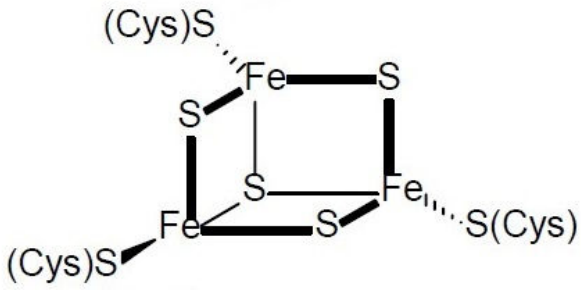

D. [4Fe-4S]

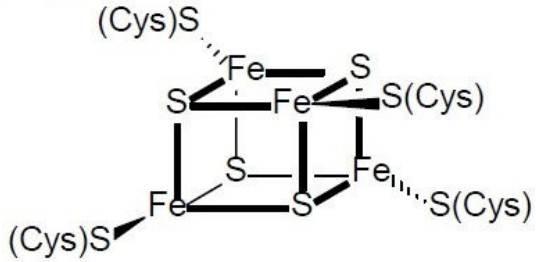

Figure 1.6: Structures of the common Fe-S clusters in living organisms.
Adapted from (66).

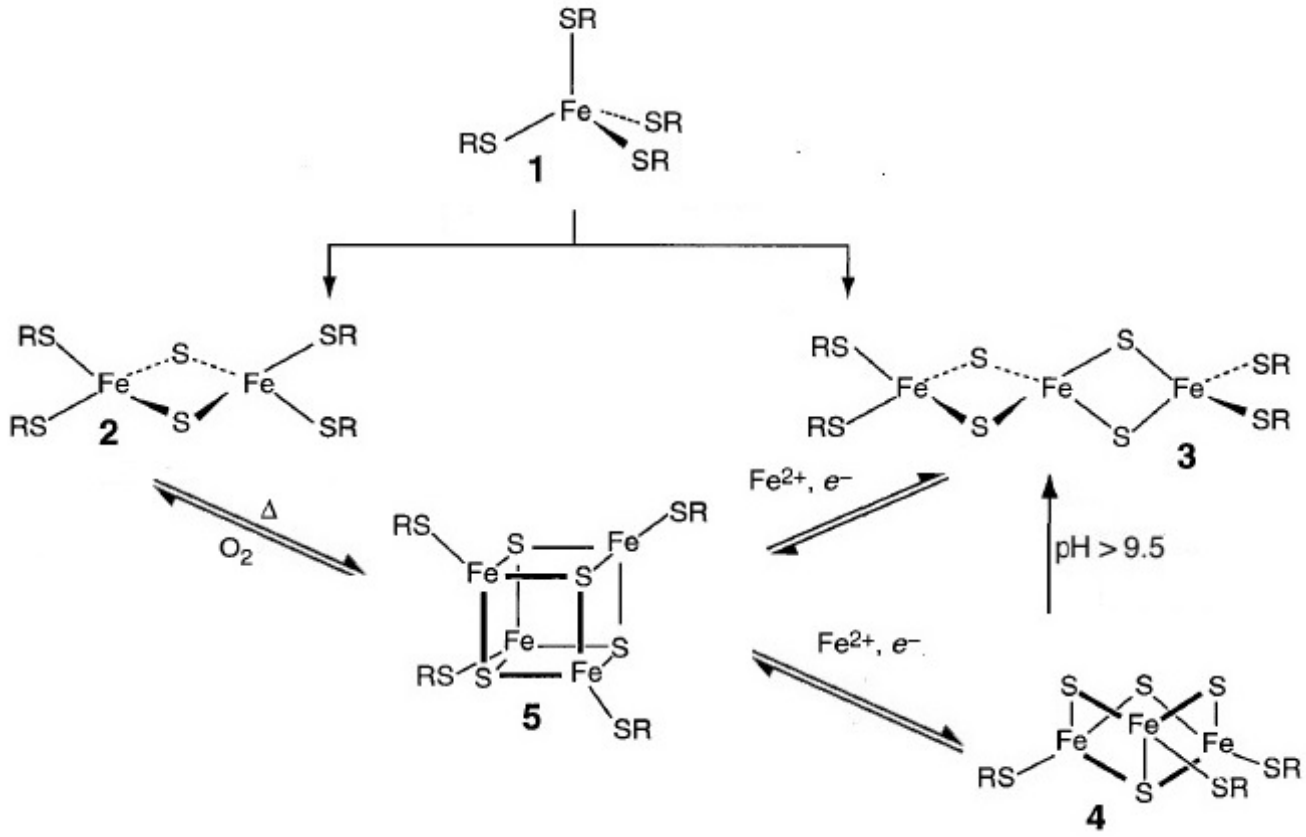

Figure 1.7: Possible Fe-S cluster conversions and interconversions.
(1) mononuclear [Fe], (2) binuclear [2Fe-2S], (3) linear [3Fe-4S], (4) cuboidal [3Fe-4S] and (5) cubane [4Fe-4S]. Adapted from (67).

1.3.1.2 Oxidation states and Redox properties

The common Fe-S clusters can exist in different oxidation states and the number of potential oxidation states can be determined. A cluster with *n* irons can exhibit a maximum of *n*+1 oxidation states. Summing the oxidation states of the cluster components ($Fe^{2+/3+}$ and the bridging S^{2-}) and neglecting ligand-based oxidation events, the charge of the cluster could be calculated. As shown in **Fig 1.8** the typical cluster oxidation states encountered in protein bound clusters are +1 and +2 for the [2Fe-2S] clusters, 0 and +1 for the [3Fe-4S] clusters, +1 and +2 for ferredoxin-type [4Fe-4S] clusters, and +2 and +3 for high-potential iron-sulfur proteins (HiPIP) [4Fe-4S] clusters. Each of the cluster redox couples has a characteristic reduction potential, which is critical for their function as electron transfer cofactors. The redox potential of the Fe-S cluster is further modified by the protein environment and its role is changed as such. For example, when two of the terminal Cys ligands for a [2Fe-2S] cluster are replaced with His residues, clusters called Rieske clusters are formed. Rieske clusters have the same core oxidation state as the typical [2Fe-2S] cluster, but their overall charge is changed resulting in more positive and functionally specific redox potentials. Fe-S proteins have a wide range of redox potentials, from -0.650V to +0.45V **(Fig 1.9)** (68–70).

1.3.1.3 Electron delocalization, spin states and magnetism

Electronic structure and magnetic properties of the iron site affects the reactivity as well as the function of an Fe-S protein in living organisms. Spectroscopic techniques, such as Electron Paramagnetic Resonance (EPR), Electron Nuclear Double Resonance (ENDOR), Magnetic Circular Dichroism (MCD) and Mössbauer as well as computational approaches have been, and still are, instrumental in supplying valuable information about the electronic and

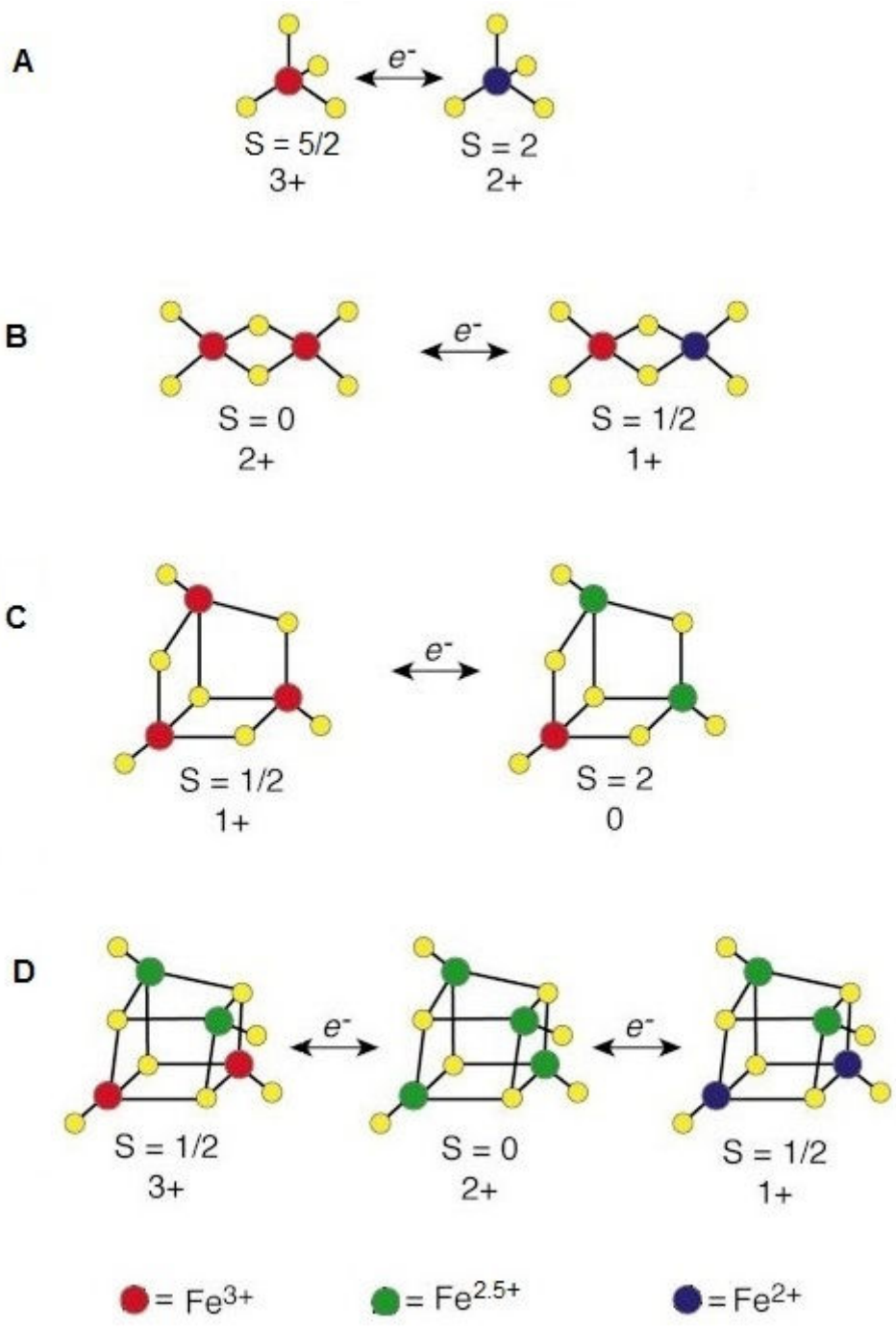

Figure 1.8: Spin state and core oxidation state for the common iron-sulfur clusters. Adapted from (71)**.**

magnetic properties of molecules.

The individual iron ions in Fe-S clusters are high-spin with either +2 or +3 oxidation states. The d^5 ferric ion (Fe^{3+}) has a high spin S = 5/2 state, whereas the d^6 ferrous ion (Fe^{2+}) has a high spin S = 2 state. The total spin of the cluster can be calculated from the spin state of the individual iron ions. In its oxidized state the binuclear cluster $[2Fe\text{-}2S]^{2+}$ contains only two valence-localized Fe^{3+} and antiferromagnetic coupling of the pair affords a spin state S = 0. The reduced $[2Fe\text{-}2S]^{1+}$ cluster contains valence-localized Fe^{3+} and valence-localized Fe^{2+}, resulting in a cluster with an electronic spin of S = 1/2 due to antiferromagnetic coupling of the ions. The antiferromagnetic coupling of three Fe^{3+} in the $[3Fe\text{-}4S]^{1+}$ state of cuboidal clusters result in a ground state spin of S = 1/2 . The $[3Fe\text{-}4S]^{0}$ reduced state has S = 2 as a consequence of the delocalized $Fe^{2.5+}/Fe^{2.5+}$ pair (ferromagnetic coupling of a Fe^{2+} and a Fe^{3+}), giving rise to S = 9/2, which is coupled antiparallel to the S = 5/2 spin of the third Fe^{3+}. The total spin for the [4Fe-4S] cluster in its most oxidized $[4Fe\text{-}4S]^{3+}$ state is S = 1/2. In this state the Fe^{3+}/Fe^{3+} pair is ferromagnetically coupled to yield spin S = 5. One Fe^{3+} is ferromagnetically coupled with a Fe^{2+} to afford a $Fe^{2.5+}/Fe^{2.5+}$ delocalized pair with S = 9/2, which is further coupled antiferromagnetically to the S = 5. The $[4Fe\text{-}4S]^{2+}$ state is a combination of 2 Fe^{3+} and 2 Fe^{2+} and a spin state S = 0 is generated by the antiferromagnetic coupling of two valence-delocalized $Fe^{2.5+}/Fe^{2.5+}$ pairs. Whereas the reduced $[4Fe\text{-}4S]^{1+}$ state either S = 1/2 or 3/2 is obtained. The spin S = 1/2 is observed when the Fe^{2+}/Fe^{2+} pair is ferromagnetically coupled to yield spin S = 4, which is coupled antiparallel with the mixed-valence pair with S = 9/2. The ultra-reduced $[4Fe\text{-}4S]^{0}$ state with all Fe^{2+} has S = 4 and has been identified in few enzymes. There is antiferromagnetic coupling of two valence localized Fe^{2+} resulting in a spin of S = 0 and the

ferromagnetic coupling of the other two Fe^{2+} (S = 4), followed by the antiferromagnetic coupling of the pair to afford the total cluster spin (71–73).

Fe-S clusters containing iron centers with unpaired electrons and half integer (and its multiple) ground state spin impart a paramagnetic property to the cluster and are weakly attracted to an externally applied magnetic field. Whereas iron centers with a whole integer spin state are diamagnetic species that are weakly repelled by an externally applied magnetic field.

1.3.2 Iron-sulfur proteins in living organisms

Fe-S clusters are one of the most common prosthetic groups in living organisms. The first identified and published function of these non-heme iron proteins was simple electron transfer. Besides the redox function that includes proton-coupled electron transfer and oxidation or reduction of substrates, Fe-S clusters facilitate multiple nonredox functions such as substrate binding and activation, regulation of enzyme activity and gene expression, sensing of reactive species, radical generation and sulfur donation. **Table 1.5** lists some of the biological functions of Fe-S proteins/clusters that have been identified up to date. These functions are attributed to the unique structural and reactivity properties of iron sulfur clusters (59, 71).

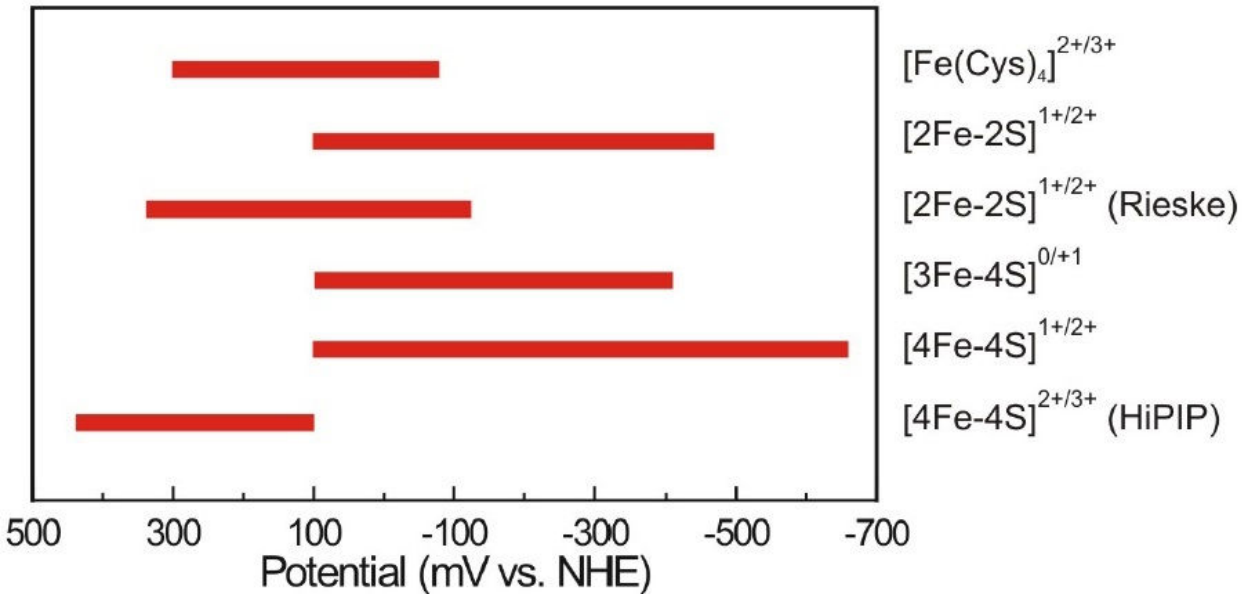

Figure 1.9: Midpoint potential range of different iron-sulfur clusters.
Adapted from (66)**.**

Table 1.5: Function of Fe-S cluster containing proteins.
Adapted from (59)

Function	Cluster type	Examples
Electron transfer	[2Fe-2S], [3Fe-4S], [4Fe-4S]	Ferredoxin, redox enzymes
Coupled proton and electron transfer	[2Fe-2S]	Rieske protein
	[8Fe-7S]	Nitrogenase
Substrate binding and activation	[4Fe-4S]	(De) hydratases
	[4Fe-4S]	Radical SAM enzymes
	[4Fe-4S]-siroheme	Sulfite reductase
Fe or cluster storage	[2Fe-2S]	Ferredoxin
	[4Fe-4S]	Polyferredoxin
Structural	[4Fe-4S]	Endonuclease III
	[4Fe-4S]	Mut Y
Regulation of enzyme activity	[4Fe-4S]	Glutamine PRPP amidotransferase
	[2Fe-2S]	Ferrochelatase
Regulation gene expression	[4Fe-4S]/ [2Fe-2S]	FNR
	[4Fe-4S]	IRP
	[2Fe-2S]	IscR
Disulfide reduction	[4Fe-4S]	Ferredoxin:thioredoxin reductase
	[4Fe-4S]	Heterodisulfide reductase
Sulfur donation	[2Fe-2S]	Biotin synthase

Both enzymes, IspH and HDR, in my research projects contain a [4Fe-4S] cluster in their active site that is believed to be directly involved in substrate binding and electron transfer. In the next sections I will discuss Fe-S proteins that have an active-site cluster involved in electron transfer and/or substrate binding.

1.3.2.1 Aconitase

Aconitase is a hydrolyase that catalyzes the reversible isomerization of citrate and isocitrate via a *cis*-aconitate intermediate in the citric acid cycle. An as-isolated aconitase contains an inactive $[3Fe\text{-}4S]^{2+}$ cluster that is held in place by three cysteine residues from the protein. The cuboidal cluster is converted in to an active enzyme $[4Fe\text{-}4S]^{2+}$ cluster by the addition of Fe^{2+} (63, 74, 75). This fourth iron site is referred to as the unique or apical iron and is coordinated to a hydroxyl ligand besides the three bridging sulfides. During catalysis the citrate is bound to the unique iron site through its carboxyl and hydroxyl oxygen atoms and protonation of the hydroxyl bound to the iron site by an acid, His 101, occurs. This results in a hexa-coordinated unique iron. Changes in Mössbauer and EPR data for an $^{57}Fe^{2+}$ activated aconitase were observed when citrate was added. Further, cluster coordination to water, citrate and isocitrate were demonstrated with the help of labeling studies (76, 77). The reaction proceeds by the formation of the *cis*-aconitate intermediate, when a Ser 642 abstracts a proton from C2 of the citrate. The *cis*-aconitate is flipped by 180° about the C2-C3 double bond. Reversal of the acid-base catalysis yields isocitrate **(Fig 1.10)** (77, 78).

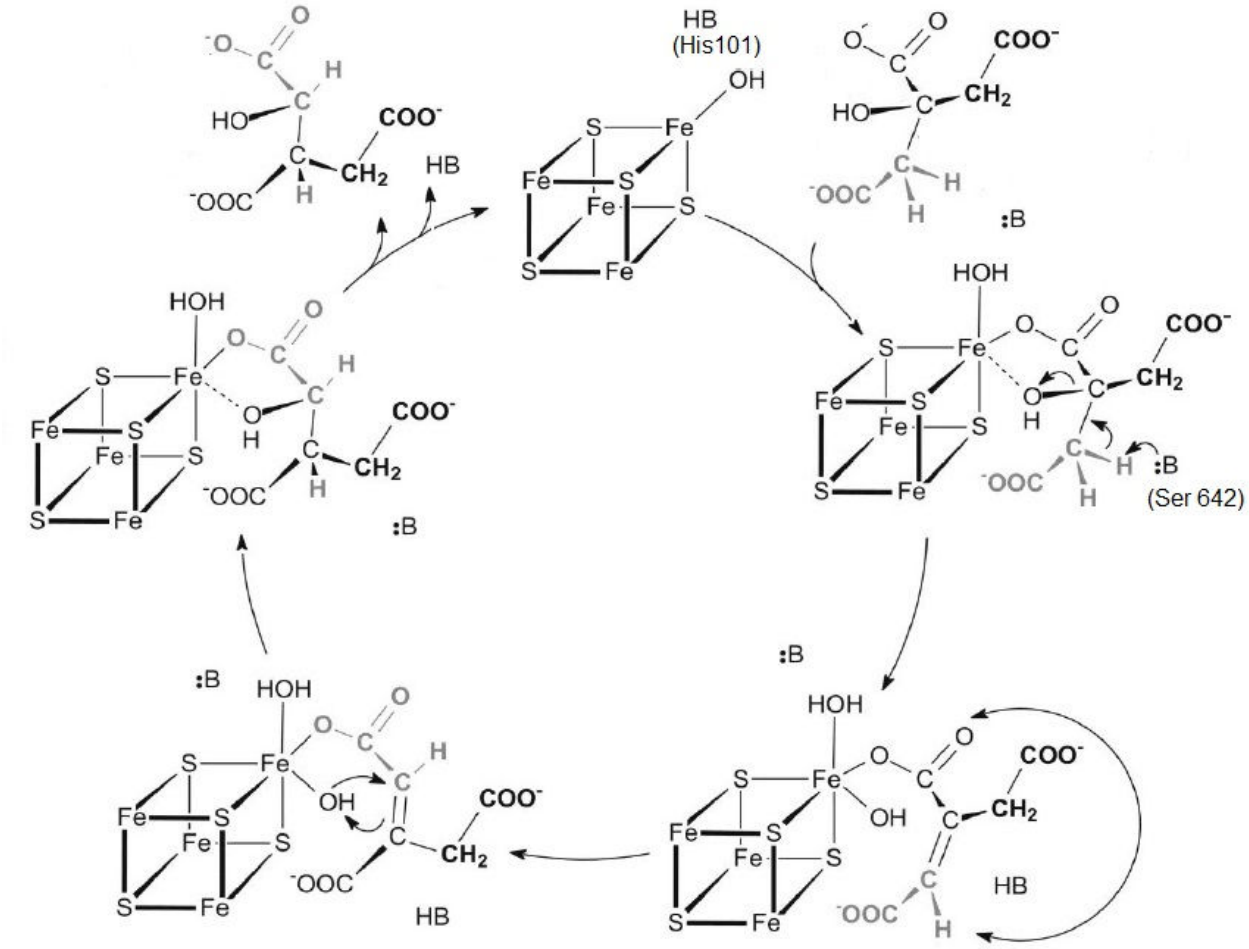

Figure 1.10: Proposed reaction mechanism for aconitase.

1.3.2.2 Ferredoxin:thioredoxin reductase (FTR)

Ferredoxin:thioredoxin reductase is a [4Fe-4S] protein in chloroplast and catalyzes the sequential two electron reduction of thioredoxin disulfide by ferredoxin. In as-isolated FTR the cluster is in a $[4Fe\text{-}4S]^{2+}$ state and near the cluster there is a redox-active disulfide (79–81).

The mechanism of action of FTR involves initial electron transfer from ferredoxin via the cluster and breaking of the disulfide bond forming a thiyl radical and a thiolate **(Fig 1.11).** A stable thiyl radical or a $[4Fe\text{-}4S]^{+}$ cluster have not been observed in EPR and it has been proposed that two internal electron transfers from the cluster to the thiyl radical, results in an EPR active $[4Fe\text{-}4S]^{3+}$ cluster. The unique iron of the $[4Fe\text{-}4S]^{3+}$ cluster is ligated to three bridging S^{2-}, a Cys ligand and the cysteinyl radical. The nucleophilic cysteine attacks the thioredoxin disulfide bond, forming a new heterodisulfide thioredoxin intermediate. The second electron transfer from another ferredoxin cleaves the heterodisulfide bond, fully reducing the thioredoxin, reducing the cluster to its original $[4Fe\text{-}4S]^{2+}$ state, and regenerating the disulfide bond in the active site of FTR (79–81). EPR, Mössbauer, ENDOR and redox titration studies of the one-electron-reduced intermediate supports the presence of a $[4Fe\text{-}4S]^{3+}$ cluster with modified HiPIP-like properties. This difference is attributed to the association of the $[4Fe\text{-}4S]^{3+}$ cluster to the active-site cysteinyl residue (82, 83).

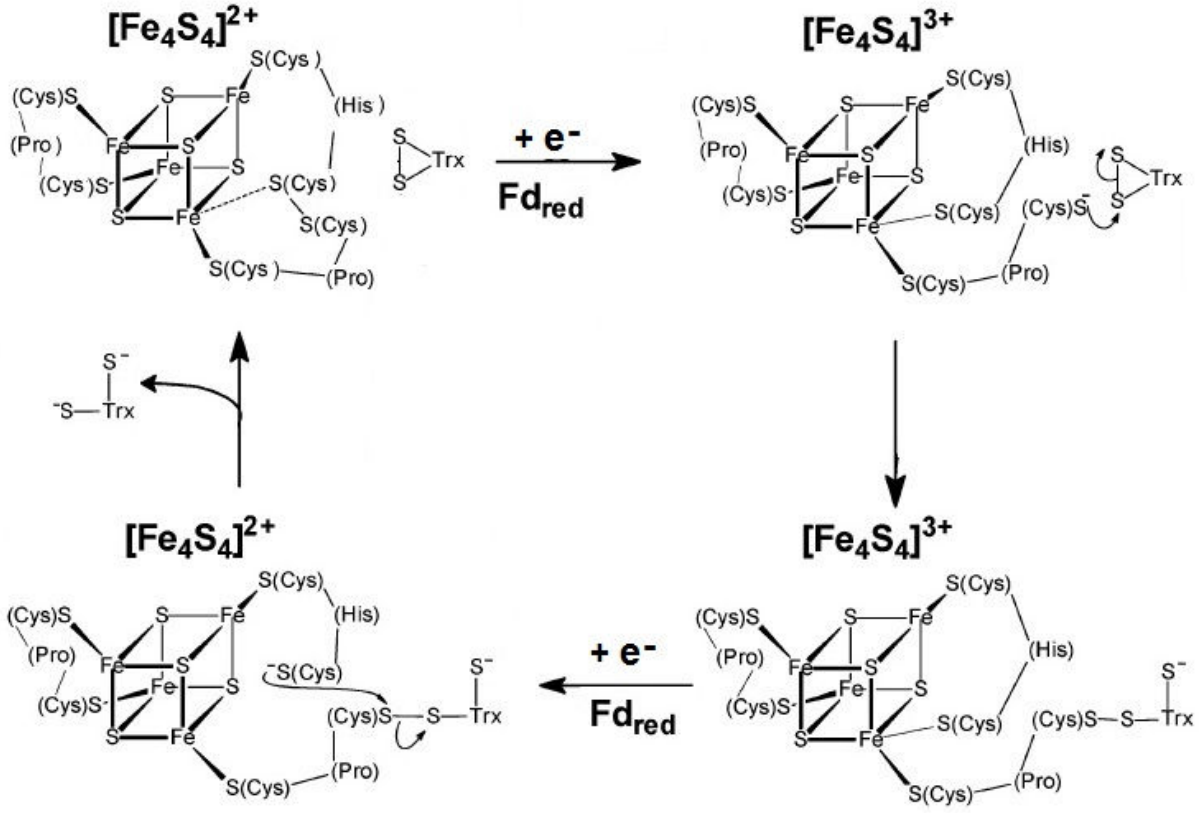

Figure 1.11: Proposed reaction mechanism for FTR.
Adapted from (80)**.**

1.3.2.3 (E)-4-Hydroxy-3-methylbut-2-enyl pyrophosphate synthase (IspG)

IspG, also referred to as GcpE, is a [4Fe-4S] enzyme that catalyzes the reductive dehydration of 2-*C*-methyl-D-erythritol-2,4-cyclodiphosphate (MEcPP) to (*E*)-4-Hydroxy-3-methylbut-2-enyl pyrophosphate (HMBPP) in the DOXP pathway **(Fig 1.3)**. The cluster is involved in a sequential two electron transfer and substrate binding (28, 29, 84). As of now, the in vivo electron source has not been established. The cluster has three of its iron sites bound to three bridging S^{2-} and a Cys ligand. X-ray crystallography and Mössbauer spectroscopy investigations have indicated the presence of a fourth apical iron. In as-isolated IspG the apical iron is coordinated to a non-cysteine ligand, a Glu residue in the active site, whereas during catalysis it is bound to the substrate (85, 86). The reaction mechanism of IspG involves initial deprotonation of the C3 hydroxyl group and subsequent binding of MEcPP to the apical iron of the $[4Fe\text{-}4S]^{2+}$ cluster through the C3 oxygen. This is followed by the opening of the cyclodiphosphate ring and formation of a carbocation at C2. The first electron transfer is followed by two internal electron transfers to the substrate resulting in the formation of a ferraoxetane intermediate. At this point the cluster is in a HiPIP-like $[4Fe\text{-}4S]^{3+}$ state and is bound to the C2 of MEcPP. Transfer of the second external electron and protonation of the leaving hydroxyl group affords a water molecule and HMBPP **(Fig 1.12)**. Spectroscopic studies such as EPR, hyperfine sublevel correlation (HYSCORE) and ENDOR were instrumental in identifying the cluster-bound ferraoxetane intermediate (47, 87, 88).

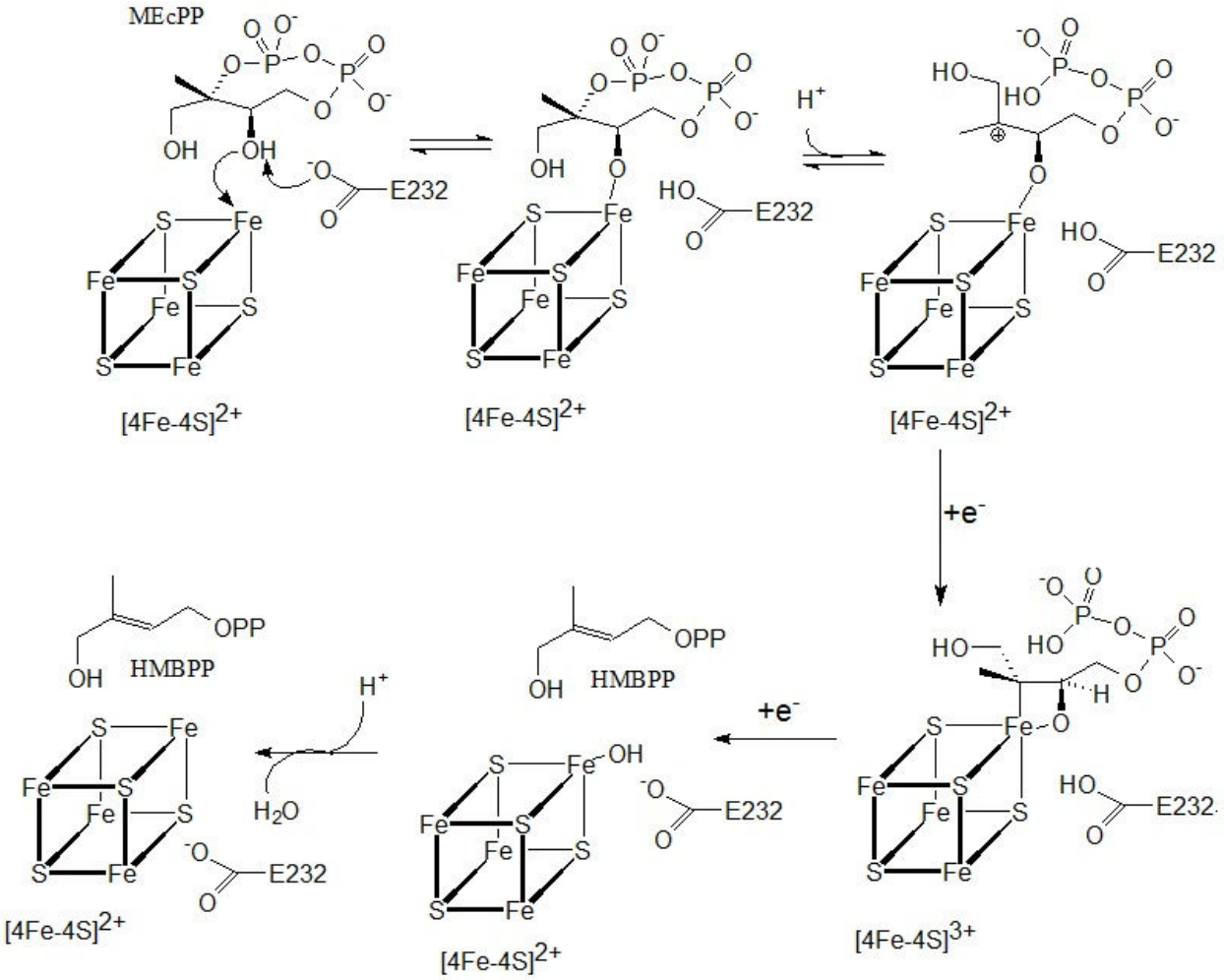

Figure 1.12: Proposed reaction mechanism for IspG.
Adapted from (47).

1.4 Spectroscopic Techniques for the characterization of Fe-S cluster centers

Many physical and chemical methods contribute to the current understanding and progress in Fe-S protein research, but no single method will provide the solution for many open questions regarding an Fe-S enzyme in a biological system. To probe the Fe-S clusters in metalloproteins a combination of spectroscopic methods that targets certain properties of the Fe can be employed. In these research projects electron paramagnetic resonance (EPR), electron nuclear double resonance (ENDOR) and Mössbauer were applied. The last two techniques were done in collaboration with the group of Brian Hoffmann at the Northwestern University and Sebastian Stoian of the MagLab in Tallahassee, FL.

1.4.1 Electron Paramagnetic Resonance (EPR)

Electron paramagnetic resonance (EPR) spectroscopy, also called electron spin resonance (ESR) spectroscopy was introducted by Zavoisky in 1944. EPR is a spectroscopic technique that measures the absorption of microwave radiation between energy levels of an unpaired electron placed in a strong magnetic field. It characterizes the properties and probes the environment of a paramagnetic center. EPR spectroscopy is widely used in the investigation of biological systems that encompass paramagnetic species like metal ions, substrate radicals, triplet states and redox-active centers in proteins. The transition metal ions are usually open–shell systems, i.e., they contain partially filled *d* or *f* shells, and they have one (S = 1/2) or more (S > 1/2) unpaired electrons in at least one of their common oxidation states. The paramagnetic centers can be identified and quantified without interference from diamagnetic species in the protein. Thus, EPR spectroscopy can be a means to study the structure and function of active sites of enzymes containing EPR active cofactors (89, 90).

1.4.1.1 Paramagnetic property of the common Fe-S clusters

As discussed in **section 1.3.1** the Fe-S clusters in Fe-S proteins have characteristic and varied electronic and magnetic properties which can impart a paramagnetic character on the cluster center. Certain oxidation states of a cluster have a paramagnetic species giving a distinct EPR spectrum with specific peaks and patterns **(Fig 1.13)**. Therefore, EPR spectroscopy can be used to identify and quantify paramagnetic species from which structural and functional characterization of the Fe-S protein can be deduced (91).

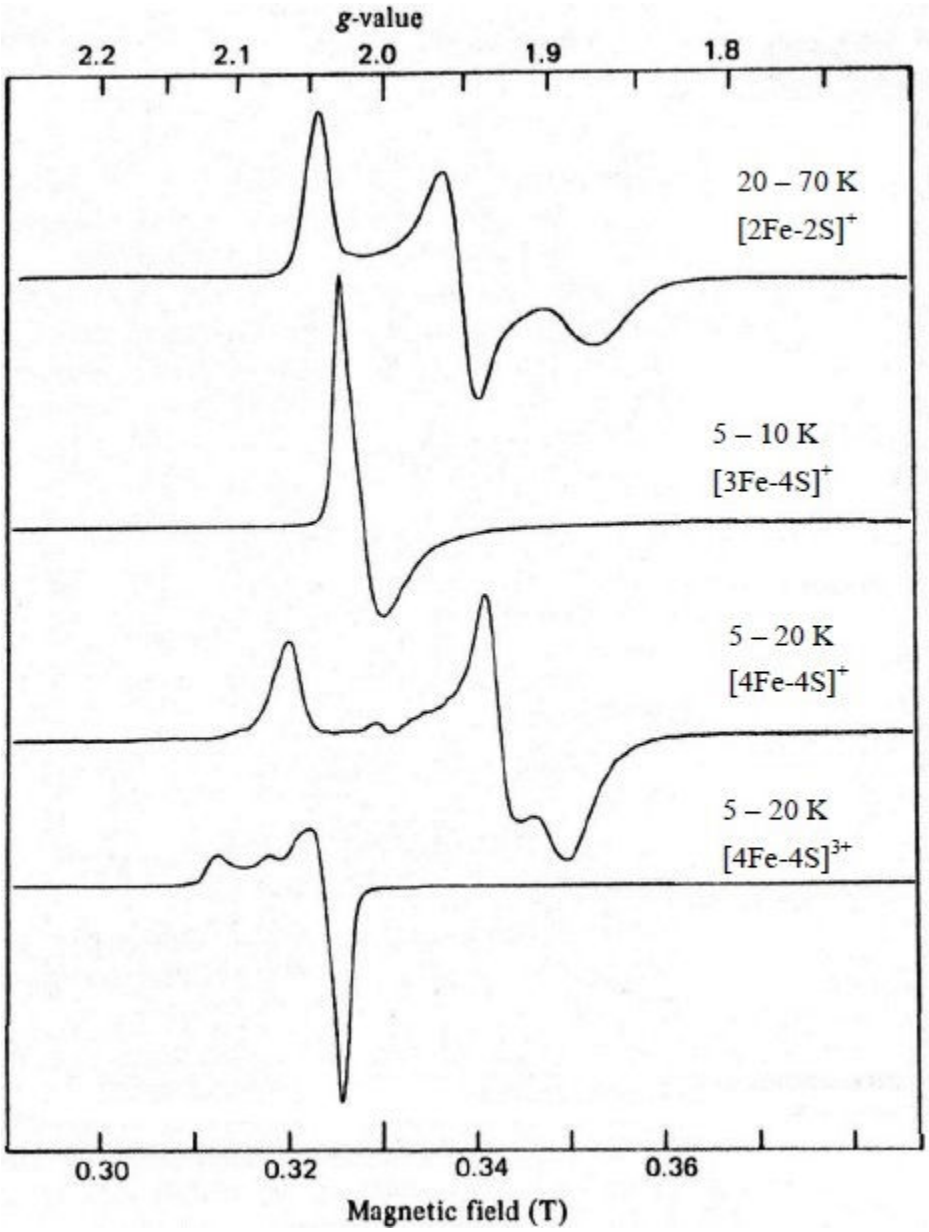

Figure 1.13: EPR spectra of iron-sulfur clusters.
Adapted from (91).

1.4.1.2 Basic principle

Spectroscopy is the measurement and interpretation of the energy differences between the atomic or molecular states. Knowledge of the energy differences (ΔE) is used to infer the identity, structure and dynamics of a sample. According to Planck's law, electromagnetic radiation will be absorbed if:

$$\Delta E = h\nu, \quad (1)$$

Where h is Planck's constant and ν is the frequency of the radiation.

Unlike the conventional spectroscopy, in EPR electronic constraints prevent the varying of the frequency (ν) of the radiation, instead the magnetic field is swept. The most commonly used frequency is in the range of 9-10 GHz (X-band) and the first derivative of the true absorption is recorded.

The interaction of the magnetic moment (μ) of an isolated electron with an externally applied magnetic field (B_0) results in the splitting of the energy level of the electron and this phenomenon is called the Zeeman effect **(Fig 1.14)**. The magnetic field produces two energy levels, highest and lowest energy state depending on alignment of B_0 along or against the magnetic moment. The projection of the electron spin, m_s, on the direction of the magnetic field is used to identify the two states, the parallel state as $m_s = -1/2$ and the antiparallel is $m_s = +1/2$. The electronic Zeeman energy of the states can be calculated as:

$$E = -\mu B_0 \quad (2)$$

Where $\mu = g_e \beta m_s$, β is a conversion constant called the Bohr magneton and g_e is the spectroscopic g factor of the free electron.

$$E_{½} = ½\, g_e \beta B_0 \quad (3)$$

$$E_{-½} = -½\, g_e \beta B_0 \quad (4)$$

Absorption of energy will occur when the condition in (5) is satisfied

$$\Delta E = g_e \beta B_0 = h\nu \quad (5)$$

The total angular momentum of an electron in a molecule has both the intrinsic spin angular momentum ($\bar{S}$) and orbital angular momentum ($\bar{L}$). These two magnetic moments interact, and the energy of this spin-orbit interaction depends on their relative orientations.

Electron in space

$$\bar{\mu} \propto g_e \bar{S} \quad (6)$$

Electron in a molecule

$$\bar{\mu} \propto g_e \bar{S} + \bar{L} \quad (7)$$

The spin-orbit coupling term is proportional to $\bar{S}$ and both terms on the right can be combined changing the value of g_e to g,

$$\bar{\mu} \propto g \bar{S} \quad (8)$$

$$\Delta E = h\nu = (g_e + \delta g)_0 = g \beta B_0 \quad (9)$$

The value of g can be calculated from ν (in MHz) and B_0 (in Gauss) using,

$$g = h\nu / \beta B_0 \quad (10)$$

$$g = 0.7145\nu / B_0 \quad (11)$$

Where $h = 6.626 \cdot 10^{-34}$ J·s; $\beta = 9.274 \cdot 10^{-28}$ J·G^{-1}

The quantity '$g_e + \delta g$ ', the g-factor, contains the chemical information on the nature of the bond between the electron and the molecule, the electronic structure of the molecule and can be taken as a fingerprint of the molecule.

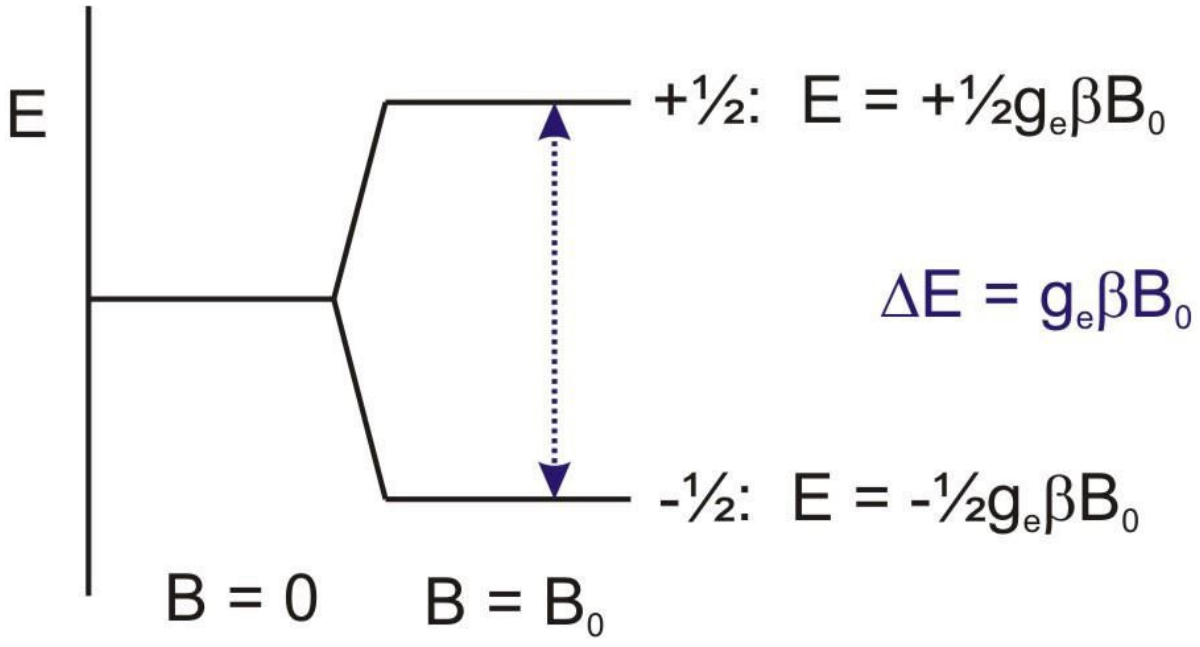

Figure 1.14: The Zeeman effect.

1.4.1.3 Line shape

Orbitals in a molecule are oriented and the magnitude of mixing of spin angular momentum to orbital angular momentum is direction dependent or anisotropic. A paramagnetic molecule has a principal axis system and the g-factors measured along these axes are called the principal g-factors, labeled as g_x, g_y and g_z. **Fig 1.15** represents the absorption and first-derivative spectra for three different classes of anisotropy. When $g_x = g_y = g_z$, it is designated as isotropic; when $g_x = g_y \neq g_z$, it is axial, and when $g_x \neq g_y \neq g_z$, it is rhombic. In biomolecular EPR spectroscopy the parameters are analyzed in frozen solution samples so as to fix the molecules in all possible orientations, resulting in resolution of the g-values.

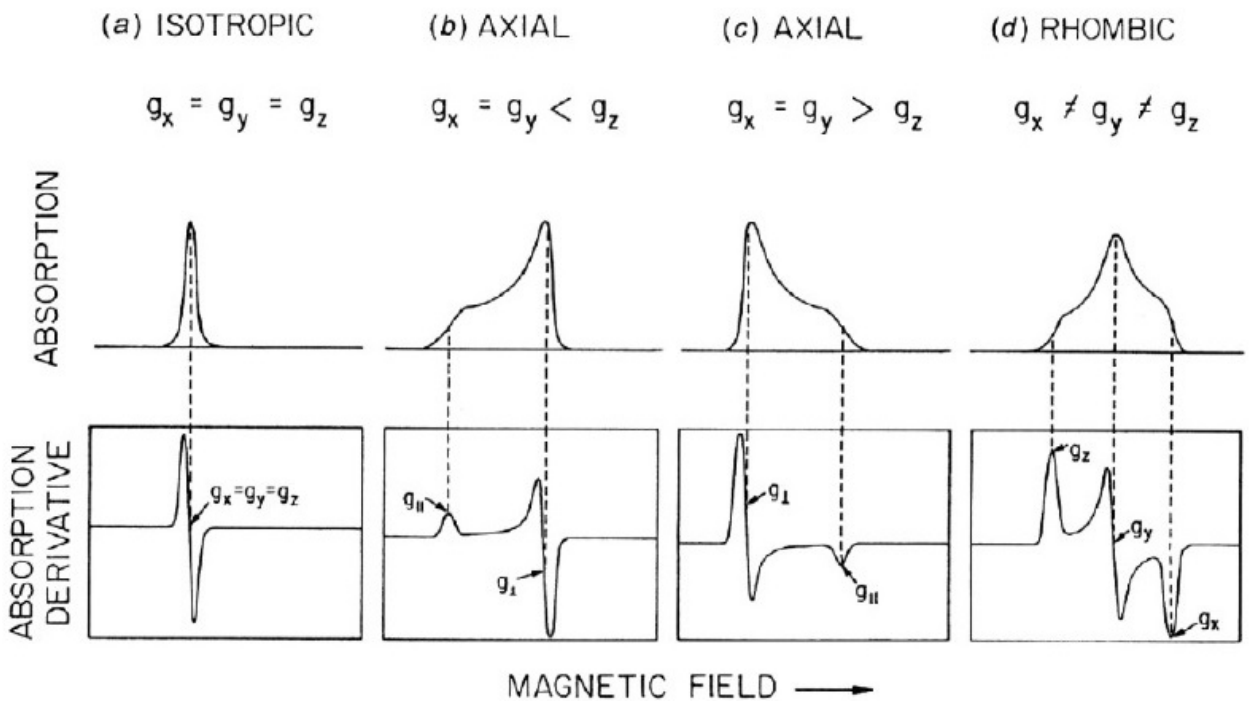

Figure 1.15: Schematic representation of the different types of g-anisotropy and the resulting EPR spectra.
Adapted from (92)**.**

1.4.1.4 Magnetic interactions

In EPR spectroscopy besides the Zeeman interaction there are other types of interaction that do occur. The first two types are caused by the interaction of the unpaired electron with a magnetic nucleus and are named nuclear hyperfine interaction. It is termed hyperfine when the nuclear magnetic moment arises from the parent nucleus, whereas in superhyperfine interaction the magnetic moment is from a neighboring nucleus. The third type is the interaction between two unpaired electrons on different atoms normally within a molecule and it is termed spin-spin interaction.

The hyperfine interaction adds an energy term to the Zeeman expression and the energy becomes:

$$\Delta E = h\nu = g\beta B_0 + hAm_I \quad (12)$$

Where A is the hyperfine coupling constant and m_I is the magnetic quantum number for the nucleus.

The m_I has $2I + 1$ possibilities and hence hyperfine interaction splits the Zeeman transition into $2I + 1$ lines of equal intensity. The local field of the nucleus either adds or subtracts from the applied B_0 field. As a result the energy levels are split **(Fig. 1.16)** and the EPR spectra will be different than when only Zeeman interaction is accounted for. Some of the nuclei which are of interest and often appear in biomolecules are listed in **Table 1.6**.

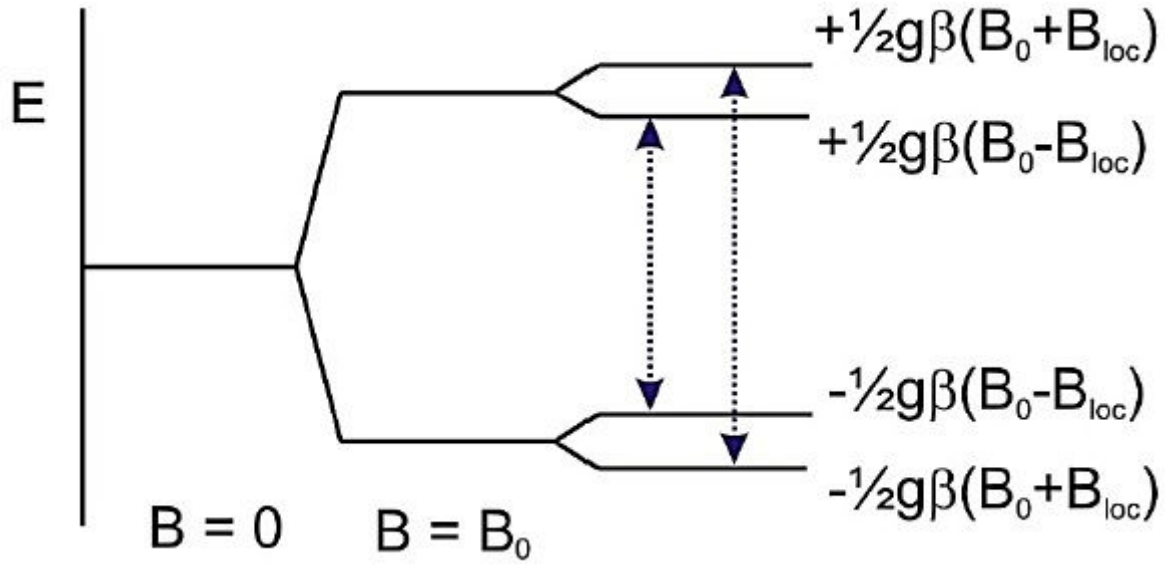

Figure 1.16: Nuclear hyperfine interaction.

Table 1.6: List of the nuclei that are important in biology, their isotopes and the corresponding nuclear spins.

Ligand	Isotope	Nuclear spin
H	1, 2	1/2,1
C	13	1/2
N	14, 15	1, 1/2
O	17	5/2
F	19	1/2
P	31	1/2
S	33	3/2
Cl	35, 37	3/2
As	75	3/2
Se	77	1/2
Br	79, 81	3/2
I	127	5/2
V	50, 51	6, 7/2
Mn	55	5/2
Fe	57	1/2
Co	59	7/2
Ni	61	3/2
Cu	63, 65	3/2
Mo	95, 97	5/2
W	183	1/2

1.4.2 Electron Nuclear Double Resonance (ENDOR)

EPR spectroscopy is a valuable method in the identification and characterization, to some extent, of paramagnetic centers. When a paramagnetic center is in the vicinity of nuclei, there will be electron-nuclear interactions that are manifested as hyperfine interactions. Since the EPR linewidth is broad (for a single-crystal Gaussian linewidth range is 200-500 MHz; ca 7-18 mT) these interactions are generally not well resolved. In addition, if the hyperfine couplings are small in magnitude but large in number there will be overlap of spectra resulting in poor resolution. There are many nuclei **(Table 1.6)** that could be ligands or are present in compounds coordinated to paramagnetic centers, such as Fe-S clusters, in the active site of an enzyme of interest. Knowledge of the interactions would be important in understanding the properties and function of the cluster in a protein. ENDOR spectroscopy is used to detect these interactions and gain insight in to the interactions (93).

The ENDOR spectrometer consists of a standard EPR spectrometer with an NMR radio frequency source and a radio frequency coil within the microwave cavity. In ENDOR spectroscopy the sample is analyzed with both EPR and NMR simultaneously, enhancing spectral resolution of small hyperfine couplings. Hyperfine interaction can be measured directly and is governed by spin Hamiltonian. For a system with effective electron spin S = 1/2 and a single nucleus with I = 1/2 the Hamiltonian is expressed as:

$$H = g_e\beta_e BS - g_n\beta_n BI + SAI \quad (13)$$

Where β_e and β_n are electronic and nuclear magnetons; g_e and g_n are the electronic and nuclear g factors; A is the nuclear hyperfine coupling constant.

The first term in the equation represents the electron Zeeman interaction (with a magnitude of ~10 GHz), the second term is the nuclear Zeeman interaction (1-15 MHz) and the

last term is the electron-nuclear hyperfine interaction (0-10 MHz). EPR transitions involve a change in electronic spin level $\Delta M_S = \pm 1$, $\Delta M_I = 0$, while ENDOR transitions are: $\Delta M_S = 0$, $\Delta M_I = \pm 1$.The interactions, their energy levels and allowed transitions in EPR and ENDOR are illustrated in **Fig 1.17**.

The energies of the interactions are expressed as:

$$E(m_S m_I) = g_e \beta_e B m_S - g_n \beta_n B m_I + h A m_S m_I \quad (14)$$

ENDOR spectra are measured at static magnetic fields, corresponding to a single EPR resonance. A nucleus at this fixed magnetic field will resonate at a Larmor frequency, ν_N, which changes with magnetic field, B. An unpaired electron spin creates an internal field that perturbs the magnetically active nuclear spins as well as the internal magnetic field felt by that nuclear spin. ENDOR measures the interaction induced chamge in the internal field of the nuclei and is reported as hyperfine coupling interaction tensor, A. Transitions in ENDOR may be Larmor centered, ν_N , and split by the hyperfine coupling or the transition may be centered at half of the hyperfine coupling (A/2) and split by $2\nu_N$. A nucleus with spin I can have 4*I possible number of ENDOR lines. For example for ^{57}Fe with I = 1/2, two ENDOR line are expected. In addition to the ability of ENDOR to resolve weaker hyperfine interactions, the nuclear Zeeman (Larmor) frequency can be used to identify the interacting nuclei. The hyperfine coupling constant, A, could provide information regarding the electron-nuclear spin distance, bonding, geometry and structure of the sample under analysis (93, 94).

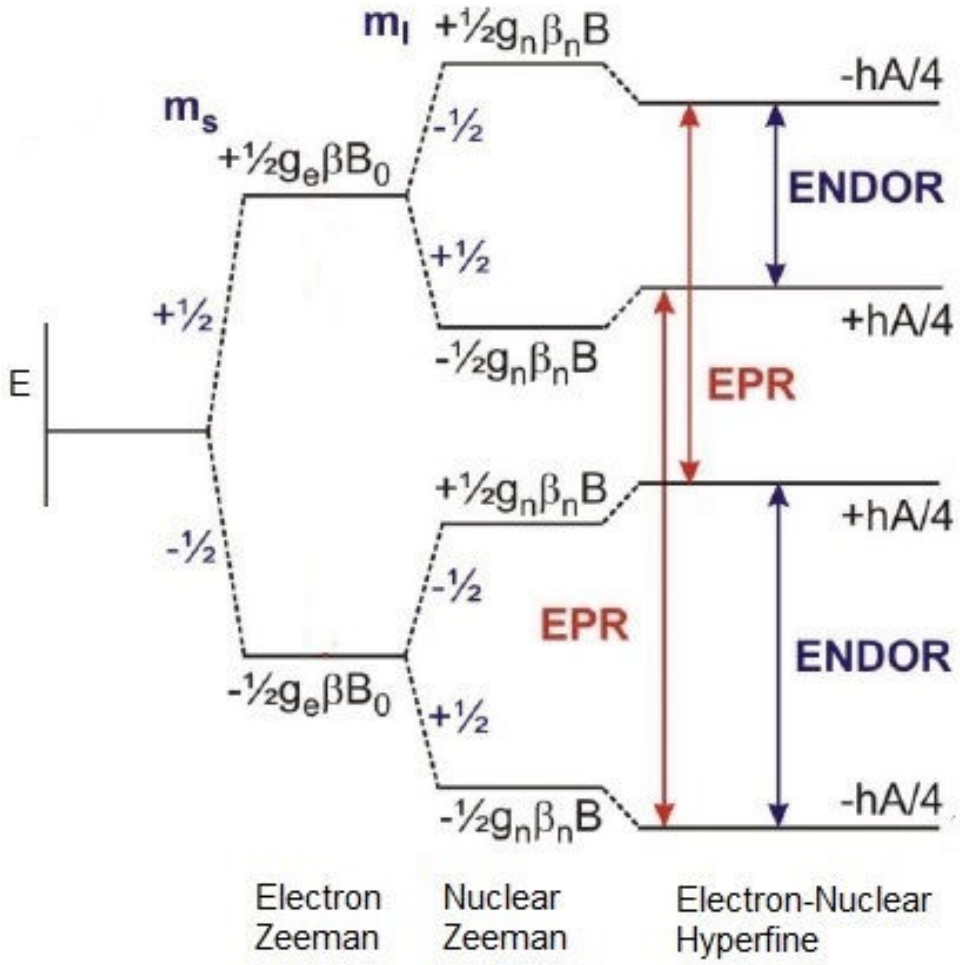

Figure 1.17: Energy level diagram for a system with S = ½ and I = ½.
Adapted from (94)**.**

1.4.3 Mössbauer (MB)

Mössbauer is a γ-ray resonance spectroscopy where radiation emitted by an excited state of a nucleus is absorbed by another nucleus of the same type of atom. In Mössbauer, γ-radiation emission and absorption should take place without imparting recoil energy. This recoil free phenomenon is called Mössbauer effect and is observed by placing the mössbauer active nucleus in a solid or frozen solution matrix. The Mössbauer effect is detected in isotopes with very low lying excited states and has been observed in isotopes of 44 elements such as ^{57}Fe, ^{191}Ir, ^{197}Au, ^{119}Sn, ^{121}Sb, ^{125}Te, ^{129}I. Of all the Mössbauer active atoms, the nucleus ^{57}Fe has been studied extensively using Mössbauer spectroscopy (95, 96).

During Mössbauer analysis γ-rays transmitted through the sample are measured by a detector. Hyperfine interactions shift the transition energy, disturbing emitted and absorbed γ-ray resonance. To compensate for the energy change and conserve resonance the γ-ray is modulated by moving the source relative to the observer with a range of velocity. At a velocity where there is resonance between the γ-radiation and the absorbing nuclei, a fraction of the radiation will be absorbed resulting in a drop in transmittance observed as a dip in the spectrum. All parameters of Mössbauer are reported in units of mm s^{-1}.

The resonance of the nuclear ground and excited states are shifted due to the electrical monopole interaction of the nuclear charge distribution and the electrons at the nucleus. This interaction gives rise to isomer shift (δ), a quantity that is directly obtained from the center of the Mössbauer spectrum **(Fig 1.18-A)**. The isomer shift measures the s-electron density around the nucleus. The s-electron density can be affected by the screening effect of d-electrons. This shielding effect is dependent on the occupancy of the d-orbital and hence can be used to determine the oxidation state of a metal center. For example, Fe^{2+} with a d^6 electron

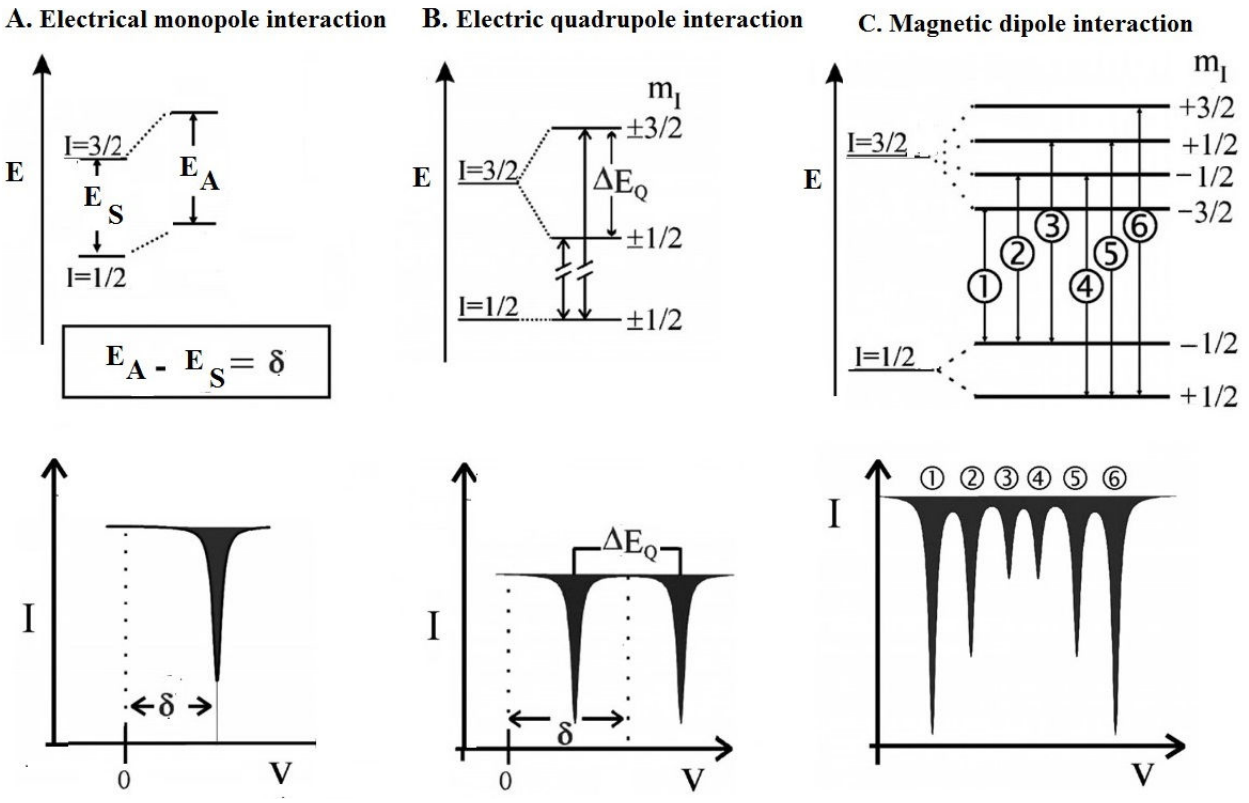

Figure 1.18: Interactions in Mössbauer spectroscopy and the resulting theoretical Mössbauer spectra

E_S and E_A are the energy changes in the source and absorber respectively. Adapted from (96).

configuration has a larger positive isomer shift than Fe^{3+} (d^5). This is because of the greater screening effect on the s-electrons by the d-electrons in Fe^{2+}. The isomer shift values are also altered by spin state and coordination environment of the metal center **(Table 1.7).**

A second interaction, called electric quadrupole interaction, is observed when the nucleus is placed in an electronic environment resulting in quadrupole splitting. Quadrupole splitting (ΔE_Q) is due to the interaction of the nuclear quadrupole moment and the electric field gradient from the electron surrounding the Mössbauer active nucleus. For ^{57}Fe the Mössbauer spectra will change from a singlet to a doublet **(Fig 1.18-B)**.

The third nuclear interaction observed is the magnetic or hyperfine splitting. This phenomena, also known as the Zeeman effect, results from the interaction of the magnetic moment of the nuclear ground and excited states with a magnetic field. The magnetic field will split the nuclear levels into $2I + 1$ substates. In case of ^{57}Fe the magnetic dipole interaction leads to a spectrum with sextet splitting **(Fig 1.18-C)**.

Mössbauer spectroscopy yields characteristic spectra for the different types of Fe-S clusters and it is a reflection of the formal charges (and therefore spin states) of each iron ion and the way they are spin coupled to each other in the cluster. On top of that Mössbauer is eminently suitable to study the magnetic property of EPR inactive Fe-S cluster species. Fe-S clusters with one to four iron sites have typical Mössbauer parameters **(Table 1.8)** and by deducing these parameters from the spectra one can pin point the valence state, spin state, oxidation state and coordination environment of the iron site in Fe-S proteins (97). Therefore a combination of EPR and Mössbauer spectroscopy data can be important in conclusive structural, functional and mechanistic studies of an Fe-S protein.

Table 1.7: ΔE_Q and δ values for biologically important compounds.
Adapted from (95).

Oxidation state	Spin state	Ligand set	ΔE_Q (mm/s)	δ (mm/s)
Fe^{4+}	2	Fe-(O, N)	0.5-1.0	0.0-0.1
	1	Hemes	1.0-2.0	0.0-0.1
		Fe-(O, N)	0.5-4.3	-0.20-0.10
Fe^{3+}	5/2	Hemes	0.5-1.5	0.35-0.45
		Fe-S	< 1.0	0.20-0.35
		Fe-(O, N)	0.5-1.5	0.40-0.60
	3/2	Hemes	3.0-3.6	0.30-0.40
	1/2	Hemes	1.5-2.5	0.15-0.25
		Fe-(O, N)	2.0-3.0	0.10-0.25
Fe^{2+}	2	Hemes	1.5-3.0	0.85-1.0
		Fe-S	2.0-3.0	0.60-0.70
		Fe-(O, N)	2.0-3.2	1.1-1.3
	0	Hemes	< 1.5	0.3-0.45

Table 1.8: Typical Mössbauer parameters of most common Fe-S clusters.
Adapted from (97).

Cluster type	Formal valences[a]	Spin	δ (mm/s) (4.2K)	$\|\Delta E_Q\|$ (mm/s)
$[Fe]^{3+}$	Fe^{3+}	5/2	0.32	0.5
$[Fe]^{2+}$	Fe^{2+}	2	0.70	3.25
$[2Fe\text{-}2S]^{2+}$	$2Fe^{3+}$	0	0.27	0.6
$[2Fe\text{-}2S]^{1+}$	Fe^{3+}, Fe^{2+}	1/2	0.35, 0.65	0.6, 2.7
$[3Fe\text{-}4S]^{1+}$	3 Fe^{3+}	1/2	0.27	0.63
$[3Fe\text{-}4S]^{0}$	$\{Fe^{2+}/Fe^{3+}\}$, Fe^{3+}	2	0.46, 0.32	1.47,0.52
$[4Fe\text{-}4S]^{1+}$	$\{Fe^{2+}/Fe^{3+}\}$, 2 Fe^{2+}	1/2	0.5, 0.58	1.32, 1.89
$[4Fe\text{-}4S]^{2+}$	2 $\{Fe^{2+}/Fe^{3+}\}$	0	0.42	1.12
$[4Fe\text{-}4S]^{3+}$	$\{Fe^{2+}/Fe^{3+}\}$, $2Fe^{3+}$	1/2	0.4, 0.29	1.03, 0.88

[a]Mixed-valence pairs are indicated by brackets {–}

Fig 1.19 shows examples of Mössbauer spectra for some Fe-S clusters in proteins. Spectra for a $[2Fe\text{-}2S]^{2+}$ cluster show one quadrupole doublet with $\delta = 0.27$ mm/s for the two Fe^{3+} sites. The $[2Fe\text{-}2S]^{+}$ cluster spectrum exhibits two distinct quadrupole doublets, an inner doublet with $\delta = 0.30$ mm/s for valence-localized Fe^{3+} site and an outer doublet with $\delta = 0.72$ mm/s for the valence-localized Fe^{2+} site. Mössbauer characteristic spectra for the $[3Fe\text{-}4S]^{+}$ cluster has one quadrupole doublet with $\delta = 0.27$ mm/s that is representative of three equivalent Fe^{3+}sites. Reduction of the cluster to a $[3Fe\text{-}4S]^{0}$ cluster results in a minor doublet with $\delta = 0.32$ mm/s for an Fe^{3+} site and a major doublet with $\delta = 0.46$ mm/s for the delocalized $Fe^{2.5+}/Fe^{2.5+}$ pair. The super-oxidized $[4Fe\text{-}4S]^{3+}$ cluster has an inner major doublet with $\delta = 0.29$ mm/s for the two Fe^{3+} sites and a minor doublet with $\delta = 0.4$ mm/s for the $Fe^{2.5+}/Fe^{2.5+}$ pair. Spectra for the $[4Fe\text{-}4S]^{2+}$ cluster has a single quadrupole doublet with $\delta = 0.45$ mm/s for two equivalent $Fe^{2.5+}/Fe^{2.5+}$ pairs. The $[4Fe\text{-}4S]^{1+}$ cluster has an inner doublet with $\delta = 0.49$ mm/s representative of the $Fe^{2.5+}/Fe^{2.5+}$ pair and a second doublet with $\delta = 0.62$ mm/s for the Fe^{2+}/Fe^{2+} pair (67, 98).

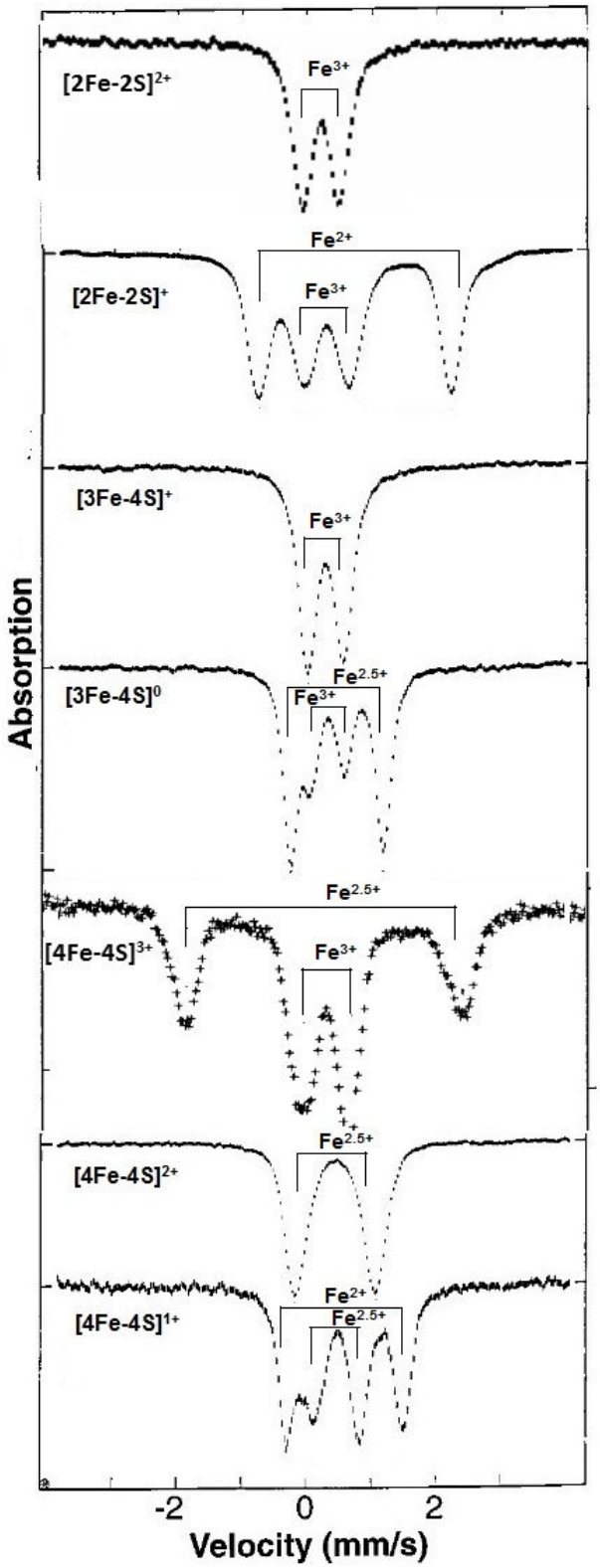

Figure 1.19: Mössbauer spectra for Fe-S clusters in their different oxidation states. Quadrupole doublets are indicated by brackets. Adapted from (67, 98, 99)**.**

CHAPTER 2 : (*E*)-4-Hydroxy-3-methylbut-2-enyl diphosphate Reductase - IspH

2.1 Literature review

IspH, also known as LytB, is the ultimate enzyme in the DOXP pathway and catalyzes the 2 H^+/ 2 e^- reductive dehydration of (*E*)-4-hydroxy-3-methylbut-2-enyl pyrophosphate (HMBPP) to isopentenyl pyrophosphate (IPP) and dimethylallyl pyrophosphate (DMAPP) **(Fig 1. 3)** (30, 31, 100, 101).

The natural electron source has not been established. The NAD(P)H/flavodoxin reductase/flavodoxin system or ferredoxin have been proposed as candidates. In vitro, donors such as photoactivated deazaflavin, NADPH/ferredoxin reductase/ferredoxin, NAD(P)H/flavodoxin reductase/flavodoxin, and dithionite alone or with methyl viologen have been used to determine the activity (47, 102)**.** The enzyme activity is significantly affected by the source of the enzyme (*E. coli*, *A. aeolicus*, or *P. falciparum*), enzyme type (as-isolated or reconstituted), electron donor as well as the conditions used. IspH from *A. aeolicus* with reduced methyl viologen as the electron donor has a specific activity of 6.6 µmol $min^{-1}mg^{-1}$ at 60°C and 1.95 µmol $min^{-1}mg^{-1}$ at room temperature (100, 103). *E. coli* IspH in combination with the NADH-flavodoxin reductase-flavodoxin reducing system has a specific activity of 0.7 µmol min^{-1} mg^{-1} and a specific activity of 3.4 µmol min^{-1} mg^{-1} was observed with photoactivated deazaflavin (104). Like the activity of IspH, the ratio of IPP to DMAPP formed is dependent on the origin of the enzyme, enzyme type and electron source. In the literature the reported IPP:DMAPP ratio are in the range of 4:1 and 6.3:1 (100, 104).

Very recently another unexpected function was discovered for IspH, its ability to catalyze the hydration of acetylenes to aldehyde and ketone. This function was stumbled upon during X-ray crystallography studies to determine the interaction of acetylene inhibitors with

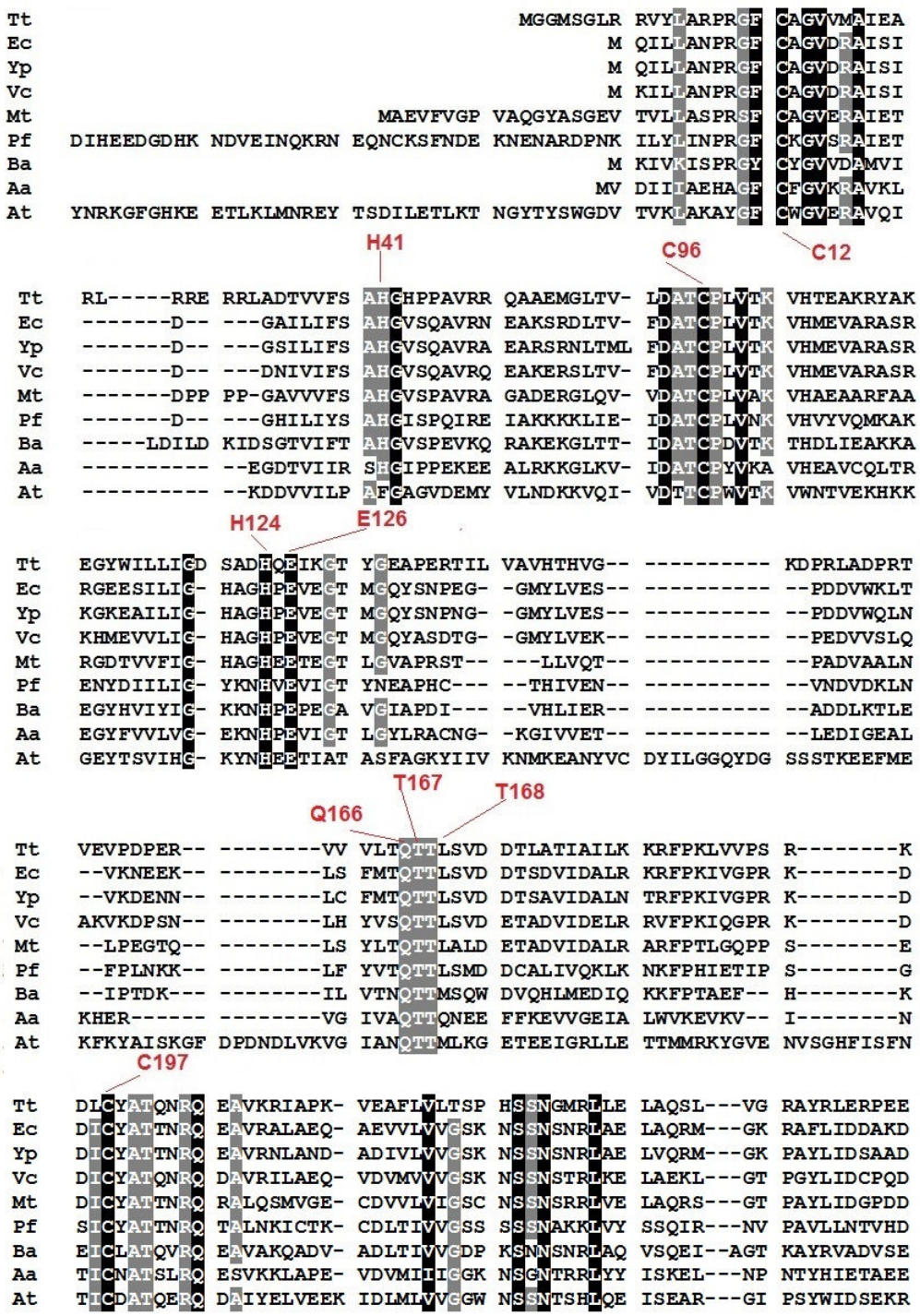

Figure 2.1: Amino acid sequence alignment for a selected set of IspH proteins.
Numbers refer residues in the *E. coli* sequence. Tt, *Thermus thermophilus*; EC, *Escherichia coli* ; Yp, *Yersinia pestis*; Vc, *Vibrio cholerae*; Mt, *Mycobacterium tuberculosis*; Pf, *Plasmodium falciparum*; Ba, *Bacillus anthracis*; Aa, *Aquifex aeolicus*; At, *Arabidopsis thaliana*. Black background, 100% conserved. Gray background 80% conserved.

oxidized IspH (105).

2.1.1 Active site of IspH and the Fe-S cluster

The amino acid sequence alignment of IspH (using Blosum62-12-2) from 75 organisms shows the presence of three conserved Cys residues. Other highly conserved residues are E126, H124, H41, T167, S225 and N227 in *E. coli* numbering. In IspH from *E. coli* mutation of any of the cysteine residues significantly decreased the enzyme activity. The Cys residues tether the cluster to the protein environment. It is important to point out that the place of the Cys residues in the sequence presented in **Fig 2.1** (only 9 organisms shown) has no homology with any of the typical consensus sequence for [4Fe-4S] clusters (e.g: Cys-X-X-Cys-X-X-Cys-X_n-Cys-Pro) (104).

The crystal structure of as-isolated IspH from both *E. coli* and *A. aeolicus* has been solved. In both organisms, the enzyme has a "trefoil" fold with three α/β domains (D1, D2 and D3) surrounding a hydrophobic central cavity (ca.10° A x 20° A) with a [3Fe- 4S] cluster bound to three Cys residues, C12, C96 and C197 (C13, C96, and C193 in *A. aeolicus*) **(Figs 2.2)**. The cavity is located at the front side of the enzyme and the cluster is found at the bottom of this crevice. It is proposed that the substrate enters and product exits the active site through the opening of the cavity. The overall structure of the IspH in *E. coli* and *A. aeolicus* is very similar. In both enzymes the conserved E126 is in close proximity of the cluster. The central cavity is also lined by a series of polar residues, including the highly conserved H41, H124, S225, and N227 (H42, H124, S221, and N223 in *A. Aeolicus*). When crystal structures of the two enzymes were superimposed, the *A. aeolicus* domain D3 was tilted by about 20° with respect to domains D1 and D2 causing widening of the central cavity of the enzyme **(Fig 2.3)**. It was observed that the dihedral angles of R9-G10-F11 from *E. coli* and A10-G11-F12 from *A. aeolicus* and C197

(*E. coli*) and C193 (*A. aeolicus*) were different. It is proposed that these amino acids could be involved in the opening (*A. aeolicus* conformation) and closing (*E. coli* conformation) of the active site cavity (106, 107).

There has been a debate about the type of the Fe-S cluster in the active site. Even though the crystal structure of the as-isolated IspH from *E. coli* and *A. aeolicus* has a [3Fe-4S] cluster, EPR studies have indicated otherwise. Duin and coworkers showed that the as-isolated dithionite-reduced IspH from *A. aeolicus*, *P. falciparum* and *E. coli* showed characteristic [4Fe-4S]$^{+}$ EPR spectra confirming the presence of an oxygen sensitive [4Fe-4S] cluster **(Fig 2.5A)**. In addition there was a direct linear correlation between cluster content and reactivity (103).

Mössbauer spectroscopy based characterization of IspH from *E. coli* also supported the presence of a [4Fe-4S]$^{2+}$ cluster. The isomer shift and quadrupole splitting suggested the presence of a $Fe^{2.5+}/Fe^{2.5+}$ delocalized pair and another mixed valence-localized Fe^{2+}/Fe^{3+} pair. The parameters for the $Fe^{2.5+}$ pair (δ = 0.42 mm/s and ΔE_Q = 1.21 mm/s) and the Fe^{3+} site (δ = 0.37 mm/s and ΔE_Q = 0.89 mm/s) are characteristic for tetrahedrally sulfur-coordinated Fe centers. Whereas the Fe^{2+} site (δ = 0.89 mm/s and ΔE_Q = 1.97 mm/s) exhibits parameters that are indicative of an Fe center bound to non-sulfur ligands, 3 N/O. The identity of the ligand has not been determined. Addition of HMBPP to the as-purified enzyme significantly decreases the isomer shift of the valence-trapped Fe^{2+} to δ = 0.64 mm/s, indicating a direct coordination of HMBPP to the cluster (108, 109).

Cocrystallization of the as-isolated *E. coli* IspH with HMBPP supports the presence of a [4Fe-4S] cluster. The crystal structure has a closed conformation with HMBPP coordinated to the unique Fe of the [4Fe-4S] cluster through the oxygen of the hydroxyl group, forming an alkoxide complex **(Fig 2.4)**. The substrate is oriented in such a way that the three allylic carbons

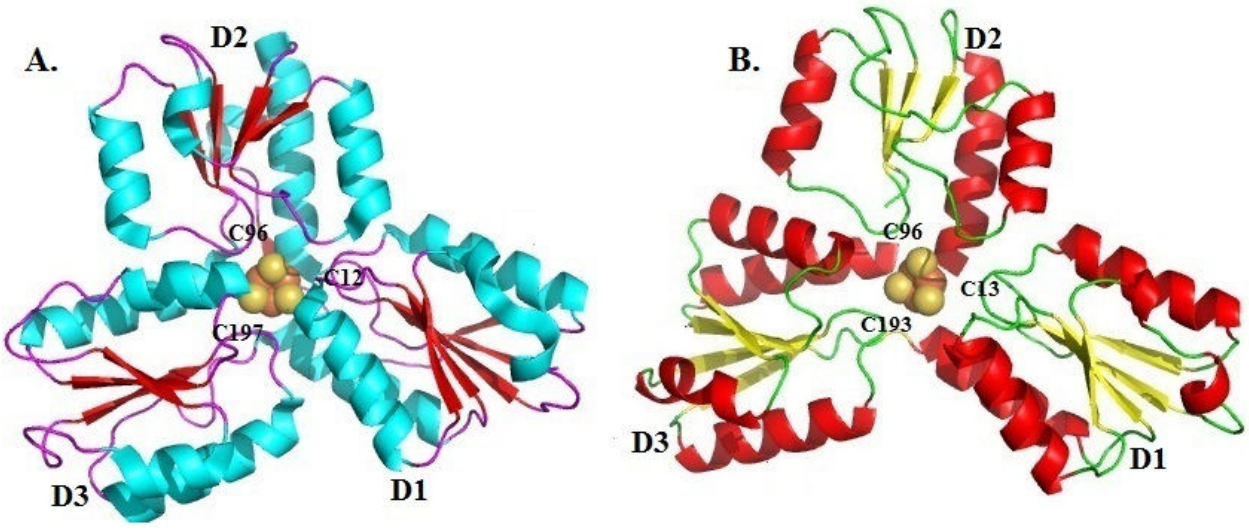

Figure 2.2: Structure of IspH from (A) *E. coli* (PDB: 3F7T) and (B) *A. aeolicus* (PDB: 3DNF).

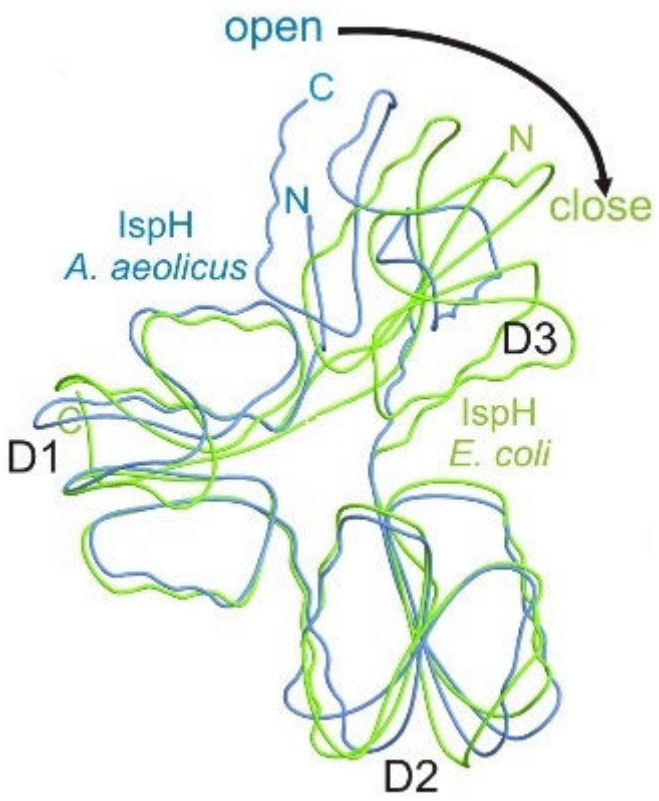

Figure 2.3: Superposition of the crystal structure of IspH from *E. coli* (green) and *A. aeolicus* (blue).
Adapted from (106).

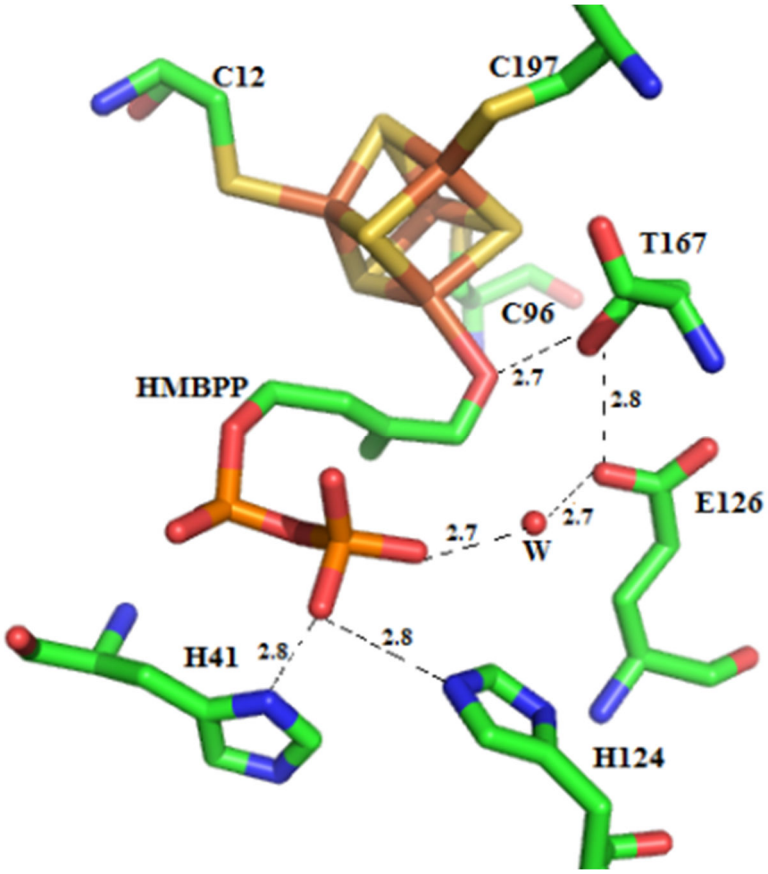

Figure 2.4: Detail of the structure of the active site of IspH from *E. coli* cocrystallized with HMBPP (PDB: 3KE8).

are sandwiched between the pyrophosphate moiety and the apical iron center. In the active site a network of hydrogen-bonds are formed among the substrate, the amino acids lining the cavity (including the conserved E126, H124, H41 and T167) and a water molecule forming a cyclic conformation. The water molecule has been proposed as the initial proton donor for dehydration (110, 111).

For the conversion of HMBPP to IPP and DMAPP a total of two electrons are sequentially transferred. By limiting the availability of electrons, one can stall and trap an intermediate in the reaction mechanism. For IspH a one-electron-reduced form of the enzyme was induced by incubating the as purified enzyme with an excess of dithionite and subsequently removing the excess dithionite to yield an EPR active $[4Fe\text{-}4S]^{+}$ form **(Fig 2.5A)**. A second paramagnetic intermediate was observed when HMBPP was added to the one-electron-reduced IspH **(Fig 2.5B)**.

The induced paramagnetic species has a slightly rhombic signal, which for convenience will be called FeS-I, with g-values 2.173, 2.013, and 1.997. This species is similar to a signal detected in FTR, Hdr and IspG (80, 87, 103, 112). The EPR spectra, with the average g value greater than g_e (with the exception of Hdr), of these enzymes are similar with those observed for high-potential iron-sulfur proteins (HiPIPs) with a $[4Fe\text{-}4S]^{3+}$ cluster. Unlike the signals for HiPIPs which are observed under highly oxidizing conditions the IspH, FTR, Hdr and IspG signals were trapped under reducing condition. Also the signal for HiPIPs can only be detected at temperatures below 20 K. Whereas the IspH, FTR, Hdr and IspG signals are saturated below 20 K and can be detected up to 150 K. The HiPIP-like spectra in FTR, Hdr and IspG have been proposed to represent an intermediate where the cluster is a $[4Fe\text{-}4S]^{3+}$ based species and directly binding substrate. Based on the similarities of both the shape and temperature behavior of the

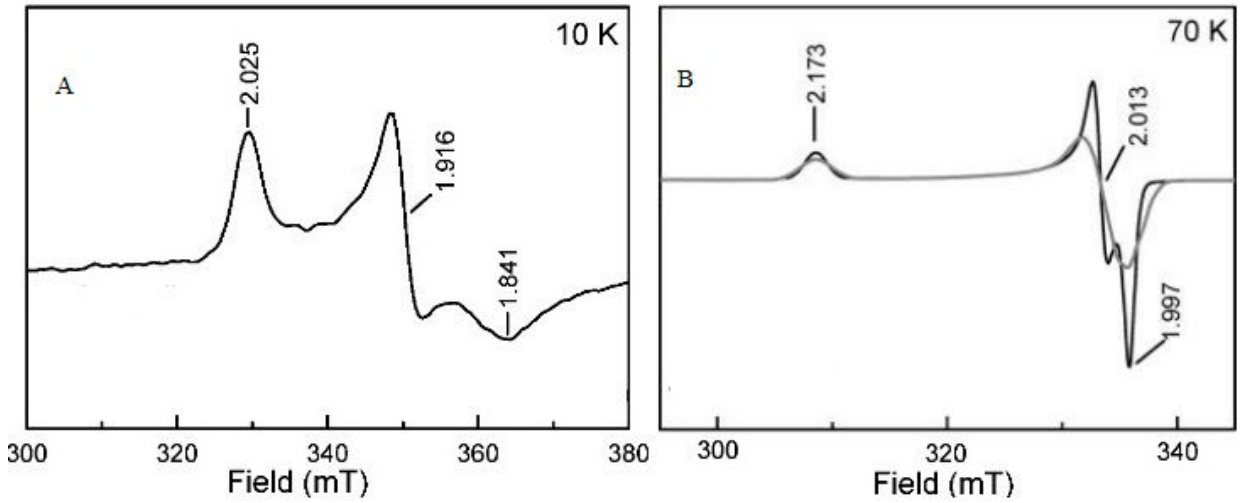

Figure 2.5: EPR signals detected in the one-electron-reduced experiment with *A. aeolicus* IspH.
(A) $[4Fe\text{-}4S]^{+}$ reduced signal for natural Fe-containing enzyme. (B) FeS-I species with natural Fe-containing enzyme (black) and ^{57}Fe-labeled enzyme (gray). Adapted from (103).

IspH signal with those EPR signals detected in FTR, Hdr and IspG, it was proposed that the intermediate in the one-electron-reduced experiment is a $[4Fe\text{-}4S]^{3+}$ species. For both IspG and IspH, however, there is only indirect evidence for this assignment.

EPR analysis of one-electron-reduced ^{57}Fe-enriched IspH incubated with HMBPP resulted in the broadening of the FeS-I EPR signal **(Fig 2.5B)**, confirming that the signal is Fe-S cluster-based. Furthermore the HiPIP-like intermediate was analyzed with ENDOR spectroscopy. ^{31}P-ENDOR revealed the presence of a weak ^{31}P hyperfine splitting **(Fig 2.6A)** with a coupling constant of about 0.17 MHz. This data suggests that the phosphate at the C1 of HMBPP is near the cluster center, but the small coupling constant indicates the phosphate is not directly bound to the cluster and the Fe-P distance was estimated to be 6.6 Å. Pulsed ^{2}H-ENDOR studies of the one-electron-reduced IspH incubated with [4-^{2}H]-HMBPP showed the presence of a ^{2}H-coupling with the Fe-S cluster, with a maximal coupling of 5.4 MHz **(Fig 2.6B).** The distance between the metal center and the deuterium at C4 in FeS-I intermediate was estimated to be 3.4 Å. It was suggested that the C4 hydroxyl of HMBPP was ligated to the unique iron of the Fe-S cluster (103). But HYSCORE labeling studies of WT IspH incubated with [4-^{17}O]-HMBPP, didn't show any ^{17}O hyperfine interaction, indicating the absence of Fe-O bond. The lack of direct Fe-O coordination was also observed in the HYSCORE studies of a paramagnetic species trapped in E126Q mutant IspH upon reduction and subsequent reaction with HMBPP, this species will be referred to as FeS-III in this work. When the FeS-III species was generated with [4-^{17}O]-HMBPP a weak ^{17}O hyperfine interaction was observed (ca 1 MHz) (113). Unlike IspG, where the C3-hydroxyl of MEcPP initially ligates the cluster and remains coordinated throughout the reaction mechanism, in IspH there is an initial binding of the oxidized cluster to the substrate hydroxyl followed by the rotation of the hydroxyl group away from the

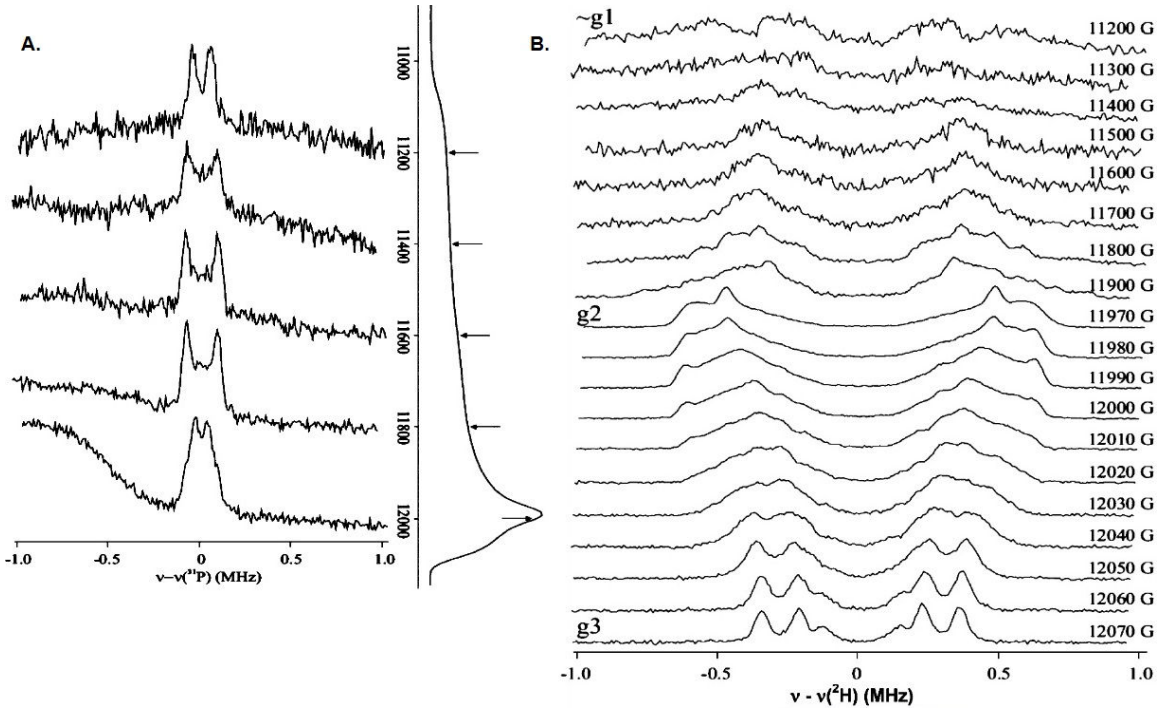

Figure 2.6: (A) CW EPR (35 GHz) and pulsed ^{31}P-ENDOR spectra of ^{57}Fe-labeled FeS-I species. (B) Pulsed ^{2}H-ENDOR spectra of the FeS-I species when induced with [4-^{2}H] HMBPP.
Adapted from (103).

apical Fe of the cluster upon reduction.

2.1.2 Conserved amino acid residues in IspH active site

The crystal structures of both *A. aeolicus* and *E. coli*, and the bioinformatics data, indicate that there are a number of conserved residues in the active site that can be critical for catalysis. As of now the exact role of each amino acid has not been solidified. Site-directed mutagenesis coupled with specific activity and spectroscopic studies have been instrumental in proposing the contribution of each amino acid (99, 107).

Replacing E126 by A, D and Q afforded mutants with very low activity (99, 107). Mutation of T167 to N and V yielded an insoluble protein. T167C and T167S variants showed 32% and 99% activity respectively (106, 111). Cocrystallization of E126D, E126Q and T167C with HMBPP showed a closed conformation orientation and a [3Fe-4S] cluster in the active site. The alkoxide complex for wild type crystallized with HMBPP was not observed instead the hydroxylmethyl of the substrate rotates away from the cluster and a new hydrogen bond network has been observed. The superimposition of the crystal structure of the mutants and the WT shows no obvious changes in the local structure (111). EPR spectroscopy analysis of a paramagnetic species formed (FeS-III) by incubating HMBPP with one-electron-reduced mutants from *A. aeolicus*, E126A and E126Q, was different than the WT IspH with g values 2.120, 2.002, and 1.965 **(Fig 2.7)** (103). ^{13}C-ENDOR spectroscopy studies of E126A IspH incubated with [U-^{13}C]-HMBPP showed a hyperfine coupling constant of 1.7 MHz for C-2 and 0.8 MHz for C-3 of HMBPP, corroborating the rotation of the hydroxyl observed in the crystal structure (114). Thr167 has been proposed to be involved in the formation and stabilization of the alkoxide complex intermediate and as well as dehydration. The Glu126 has been proposed to be involved in the protonation of hydroxyl group and/or protonation at C2 or C4 of the substrate.

In the *E. coli* crystal structure (3KE8) the HMBPP diphosphate group is hydrogen bonded to seven residues: H41, H74, H124, S225, S226, N227 and S269. It has been observed that these amino acids structurally rearrange when the enzyme active site is opening and closing, except for the H124. It would be expected that mutation of only one amino acids might not have a significant effect on the active site environment and hence activity. But H124N, S225C, and N227Q variants were found to be inactive. Also replacing H41, H74, and H124 by Ala afforded an insoluble protein, while H41N and H74N mutants were found to be active (106).

Unlike IspH from *E. coli*, mutating H42 and H124 to alanine yielded a soluble protein in *A. aeolicus.* EPR data was collected for *A. aeolicus* variants H42A, H42F, H124A and H124F that were prepared by incubating HMBPP with one-electron-reduced mutants **(Fig 2.7)**. During activity assays H42F variant had partial activity and the FeS-I paramagnetic species was detected. Whereas the H42A variant lost most of it activity and the one-electron-reduced signal, $[4Fe\text{-}4S]^{+}$, was observed but not the FeS-I species. It was suggested that the presence of the ring in the Phe might have caused less disturbance in the active site conformation. It was proposed the H42 might play a role in the transition of the open to the closed conformation and its mutation might have caused a conformational change in the active site.

Both H124F and H124A showed insignificant activity. When HMBPP was added to the one-electron-reduced signal, in both variants the $[4Fe\text{-}4S]^{+}$ spectra disappeared. But the FeS-I was detected only in the H124F, albeit the spin concentration was low. In the H124A mutant a radical like signal was observed. The fact that the H124 doesn't rearrange when IspH active site is closed or open makes it important for substrate docking. It was proposed that the binding of the substrate was affected and the transfer of the first electron results in a substrate based radical species that is not stabilized by the cluster.

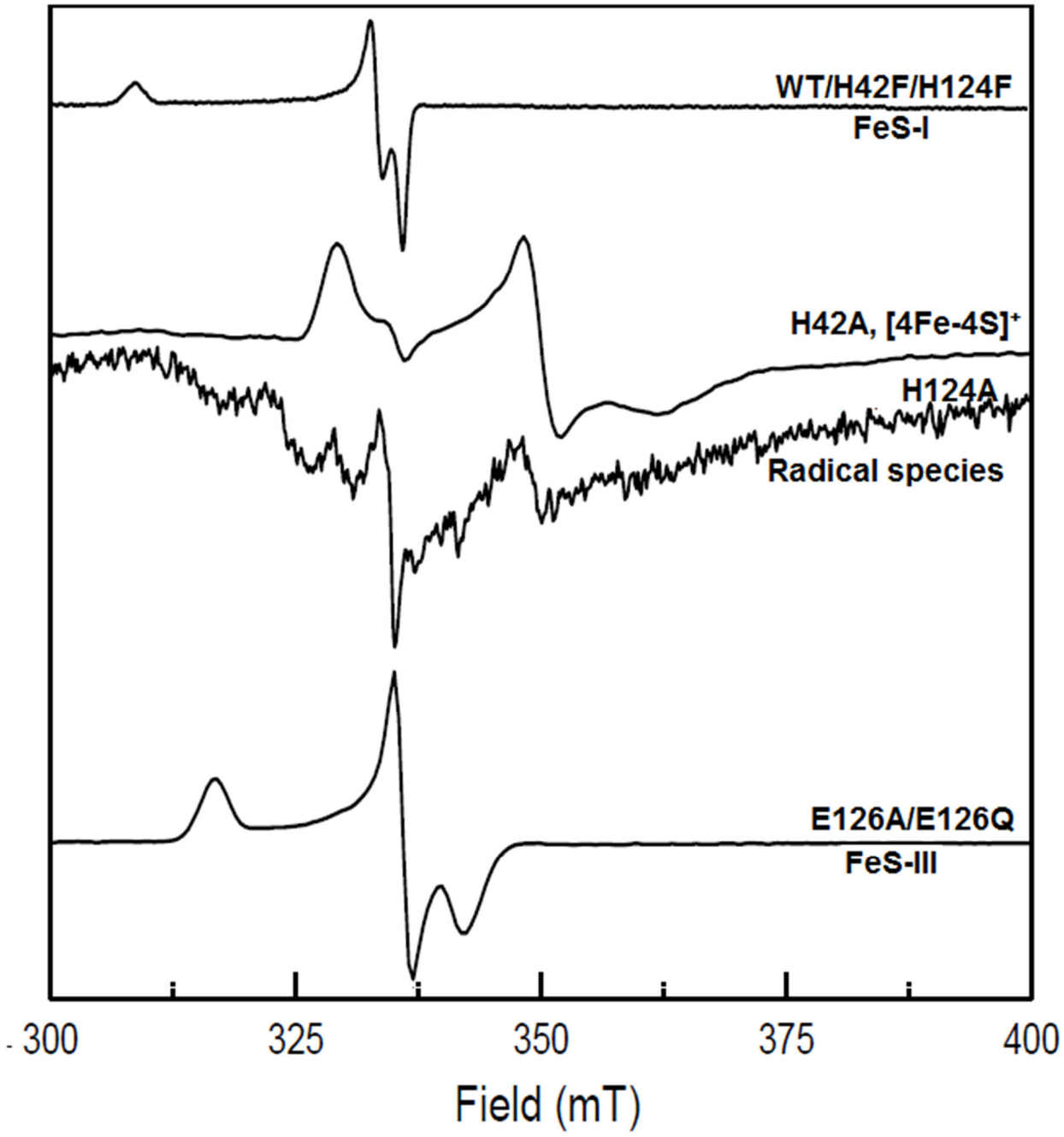

Figure 2.7: Overview of the EPR active species detected in one-electron reduced WT and mutant enzymes incubated with HMBPP.
All samples were measured at 50K except for H42A, which was measured at 10K.

2.1.3 Proposed reaction mechanisms for IspH

For the sequential two electron reduction and dehydration of HMBPP to IPP and DMAPP a number of mechanisms have been proposed for IspH. One mechanism is based on the formation of an allyl radical **(Fig 2.8)**. Initially the HMBPP forms an alkoxide complex with the apical iron of the $[4Fe\text{-}4S]^{2+}$ cluster, that is stabilized by T167. The first electron transfer reduces the cluster followed by rotation of the hydroxylmethyl of the substrate away from the apical iron and formation of an allyl radical. The hydroxyl group is protonated by E126 and water is released. A second electron transfer creates an anionic allyl intermediate followed by the protonation at C2 or C4 to yield IPP or DMAPP respectively (111). The proton donor for the last step has been proposed to be the diphosphate group of HMBPP. The proposed allylic radical intermediate, which is expected to be EPR active, was not observed when HMBPP was incubated with one-electron-reduced IspH, instead a HiPIP-like Fe-S cluster-based signal was observed. As already mentioned EPR analysis of one-electron-reduced ^{57}Fe-labeled IspH incubated with HMBPP resulted in the broadening of the HiPIP-like paramagnetic intermediate, confirming that the signal is Fe-S cluster-based and not a radical species. In addition, the ^{13}C-ENDOR study of E126A IspH incubated with [U-^{13}C]-HMBPP doesn't show a large hyperfine coupling expected for a radical substrate (103, 116).

A second reaction mechanism that has been proposed is a Birch reduction-like mechanism **(Fig 2.9)** (117, 118). HMBPP is directly bound to the apical iron, which is proposed to be the key step in catalysis, and the first electron transfer reduces the $[4Fe\text{-}4S]^{2+}$ cluster. Subsequent electron transfer from the cluster to the substrate triggers dehydration of HMBPP and formation of an allyl radical intermediate. In this mechanism T167 (*E. coli* numbering) has been proposed as the ultimate proton donor for the dehydration. Upon the

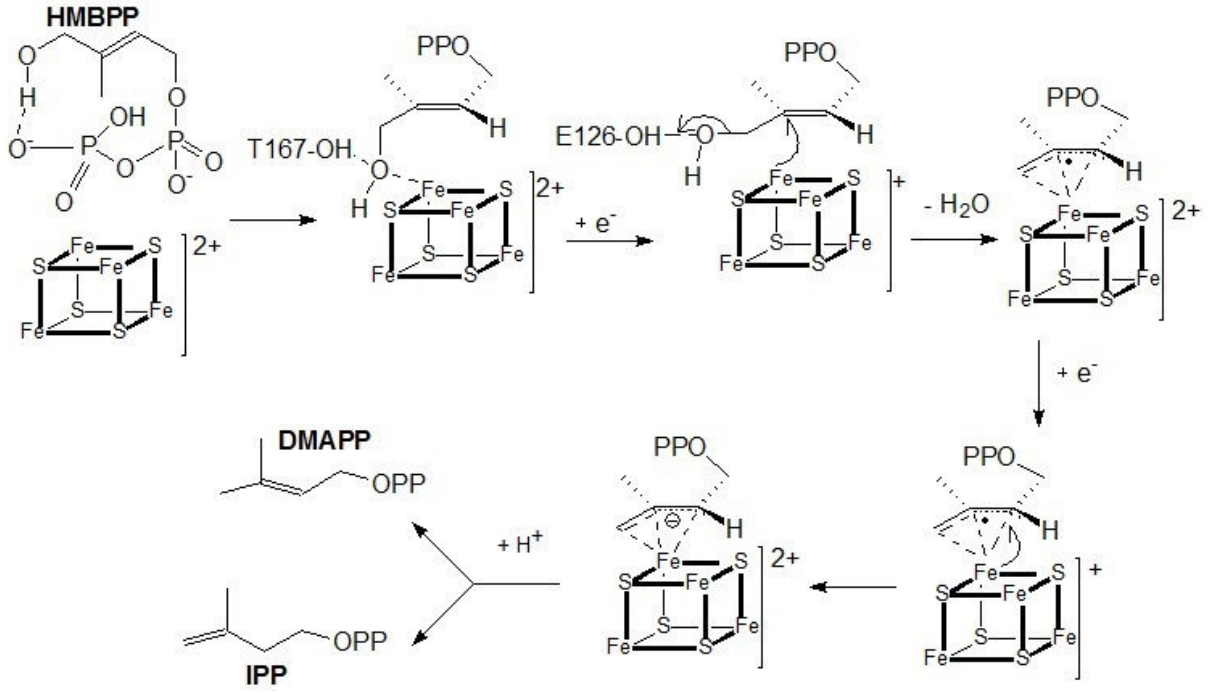

Figure 2.8: Proposed IspH Mechanism-I.
Adapted from (111).

an second electron transfer an allylic anion is formed and protonation at either C2 or C4 position produces IPP or DMAPP respectively. The terminal phosphate group of HMBPP has been proposed in mediating the final protonation step. As with the first proposed mode of action if there is an allyl radical, EPR analysis should show an isotropic radical signal if such a species is stable enough to be detected, but this was not the case.

The third mode of catalysis is a bioorganometallic mechanism, where there is an interaction between the cluster and the π-system of HMBPP. As shown in **Fig 2.10** initially an alkoxide intermediate is formed between the HMBPP hydroxyl group and the apical iron of the $[4Fe\text{-}4S]^{2+}$ cluster. Transfer of the first electron reduces the cluster followed by the rotation of HMBPP hydroxylmethyl group away from the apical iron. A π-interaction between the cluster and the alkene group stabilizes the intermediate. E126 is the proposed proton donor for the dehydration of the substrate. This is followed by an internal two electron transfer to HMBPP affording an η^3-allyl anion intermediate that is stabilized by the HiPIP-like $[4Fe\text{-}4S]^{3+}$ cluster. Second electron transfer to the η^3-allyl anion intermediate followed by protonation at C2 and C4 yields IPP and DMAPP respectively. In the presence of an excess reductant the products can rebind to the cluster. This was supported by the fact that a paramagnetic species was trapped when dithionite-reduced WT IspH was incubated with IPP, which we are calling FeS-II (113, 116). The basis for this mechanism is the spectroscopic and the crystallographic studies of the inactive E126Q mutant IspH. It has been proposed that the paramagnetic species observed in the E126Q mutant, FeS-III intermediate, to represent the π-complex in this mechanism. But the kinetic competence of this intermediate has not been established and it could be a dead end product from a side reaction. Also the oxidation state of this intermediate has not been established. The HiPIP-like intermediate with $[4Fe\text{-}4S]^{3+}$ cluster, has been proposed to be similar

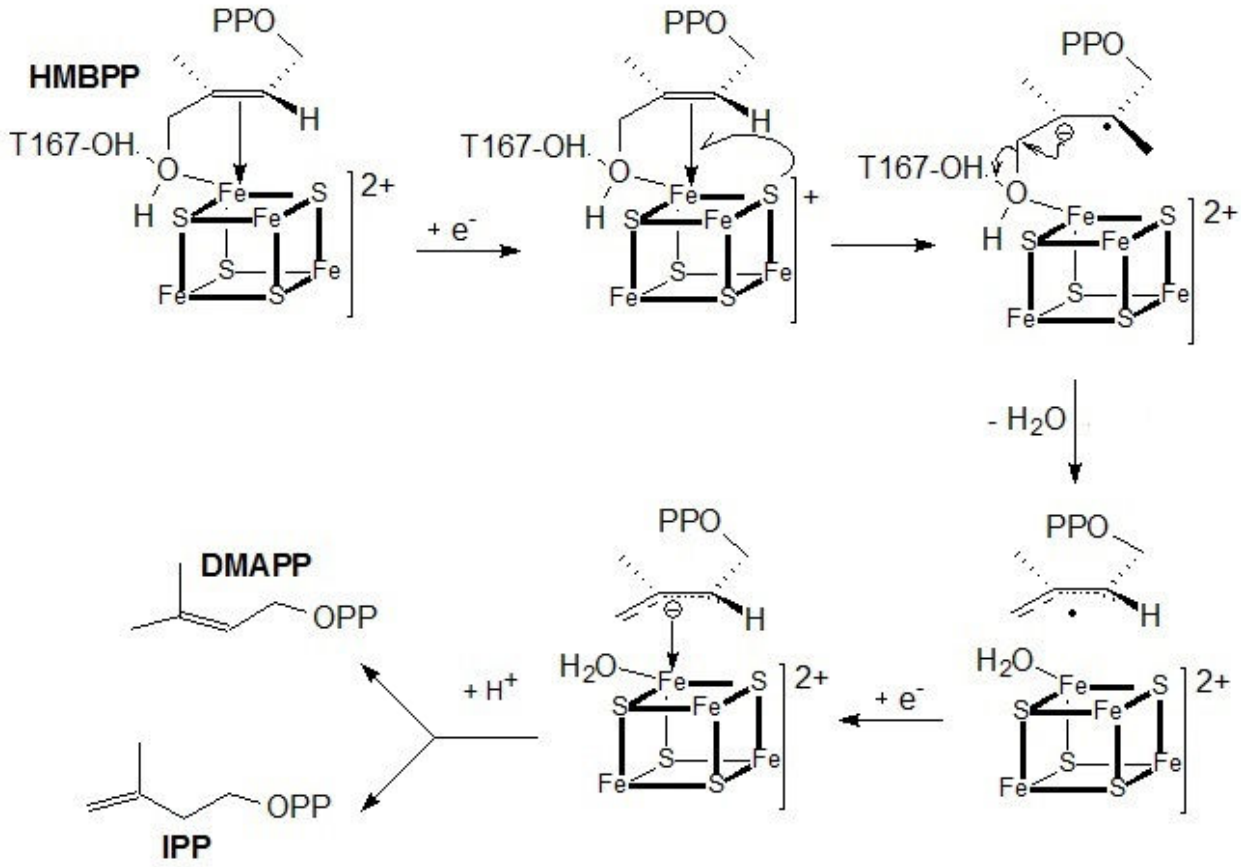

Figure 2.9: Proposed IspH Mechanism-II.
Adapted from (117).

to the intermediate that was observed in the one-electron-reduced (FeS-I) experiment. The assignment of this intermediate was based on the similarity of its g-value and temperature behavior to an intermediate detected in the well-studied FTR. Both the FeS-I and FeS-III intermediates have g-values that are representative of the HiPIP clusters, but the kinetic competence as well as the oxidation state of the FeS-III species hasn't been determined experimentally. The presence of the proposed intermediates, FeS-I, FeS-II and FeS-III, in the overall reaction path has not been analyzed. Hence rapid-freeze-quench experiments should be used to analyze the catalytic action of IspH under turnover and pre-steady-state conditions.

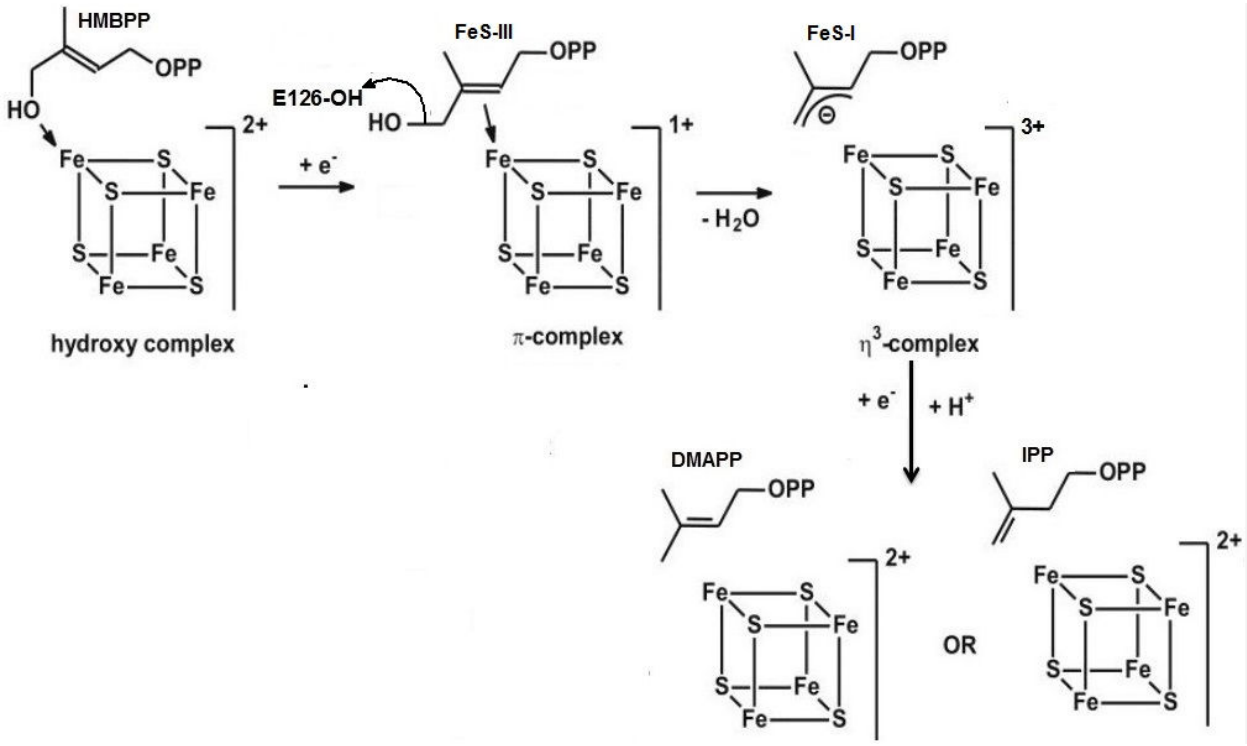

Figure 2.10: Proposed IspH Mechanism-III.
Adapted from (47).

2.1.4 Inhibition of IspH

Worldwide millions of people suffer and die due to infectious diseases each year. In 2014 globally, mainly in low income countries, close to 2 million people died due to tuberculosis and malaria (112, 113). It is paramount to develop antimicrobials to combat these infectious diseases. Antimicrobials can target cellular structures, biosynthesis of macromolecular compounds and biochemical processes. There has been an increase in antimicrobial drug resistance and the efficacy of many available therapies has been compromised (121). In 2014 approximately 480,000 people developed multidrug resistant TB (MDR-TB) and there were about 190,000 deaths from MDR-TB (120). This crisis calls for the rapid development of novel anti-infective agents and identification of novel targets for anti-infective drugs. Since the DOXP pathway is found in a wide group of pathogenic bacteria and apicomplexan parasites but absent in all mammals **(Table 1.2)**, the enzymes in this pathway are possible targets for anti-infective drugs.

There have been ongoing research in the development and characterization of inhibitors and drug leads that target IspH **(Fig 2.11)**. HMBPP analogs have been synthesized by substituting the terminal hydroxyl with a thiol group (IC_{50} = 0.21 μM) and an amino group (IC_{50} = 0.15 μM). Mössbauer studies of the as-isolated IspH in the presence of either (*E*)-4-mercapto-3-methylbut-2-enyl diphosphate or (*E*)-4-amino-3-methylbut-2-enyl diphosphate showed an isomer shift similar to that of IspH incubated with HMBPP. This indicates that the analogs coordination mode is similar to that of the substrate, the apical iron of the cluster binds the thiol and amino moiety of the analogs. This was supported by the crystal structure of the as-isolated IspH cocrystallized with either the thiol or the amino analog. It is not clear if inhibition occurs due to binding to the reduced or oxidized cluster (109, 122). By taking advantage of the metallacycle mode of catalysis (mechanism III), novel alkyne diphosphate inhibitors were

identified as inhibitors. ENDOR based labeling studies of [U-$^{13}C_3$] propargyl diphosphate incubated with IspH showed a hyperfine coupling constant of 6 MHz. Based on this finding it has been proposed that the inhibitor binds the apical iron of the reduced cluster in a sideways-on mode through its C≡C π-orbital. The most potent inhibitor was but-3-ynyl diphosphate with an IC_{50} of 0.45 μM (123). Screening of compound libraries also lead to the discovery of pyridine diphosphates as inhibitors of IspH. It has been proposed that the nitrogen atom of the aromatic ring interacts with the apical iron of the reduced cluster in side-on η^2 coordination and the most potent inhibitor that was reported was (pyridine-3-yl) ethyl diphosphate with an IC_{50} of 9.1 μM. The binding mode was supported by the large ^{14}N hyperfine coupling constant in HYSCORE spectra observed when IspH was incubated with (pyridine-3-yl) methyl diphosphate (123, 124). As of now the exact inhibition mechanism of the inhibitors is not well understood.

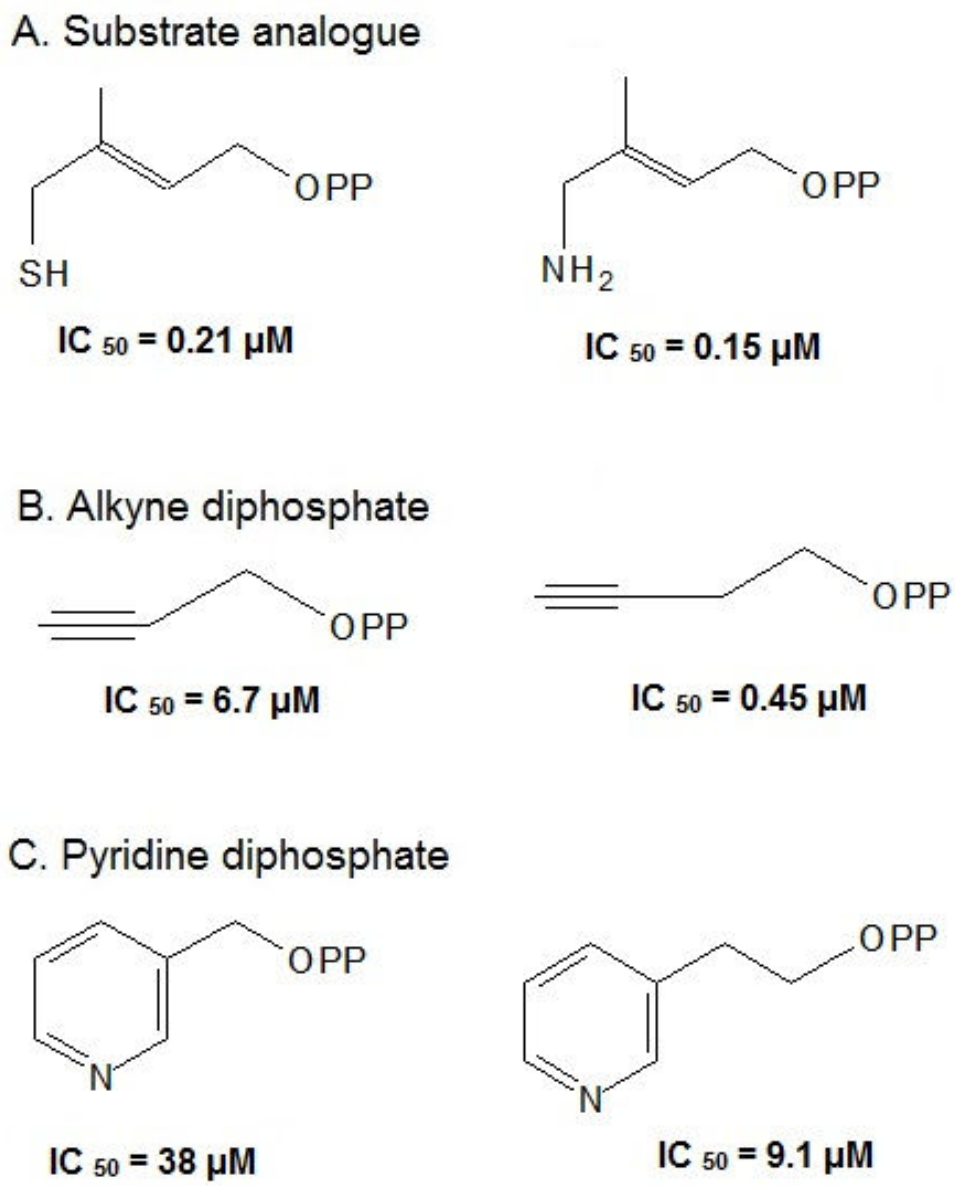

Figure 2.11: IspH inhibitors.

2.1.5 Statement of research

In this research project several questions related to the function of IspH in the conversion of HMBPP to IPP and DMAPP will be addressed.

I. The kinetic competence of the FeS-I intermediate, observed when the one-electron-reduced IspH was incubated with HMBPP, will be investigated. EPR-based rapid-freeze-quench will be used to study the formation of intermediates pre-steady-state and under turnover conditions.

II. It has been proposed that the FeS-I intermediate is an oxidized HiPIP-like species with a $[4Fe\text{-}4S]^{3+}$ cluster. ENDOR and Mössbauer spectroscopy will be used to establish the redox state and other properties of this intermediate.

III. In the crystal structure of the IspH protein from *A. aeolicus* and *E. coli*, there are conserved amino acids that have been proposed to be involved in hydrogen bonding and a role for several amino acid residues in catalysis has been implied. H124 might be involved in diphosphate binding and correct orientation of HMBPP. T167 (*E. coli* numbering) has been proposed as the proton source for the dehydration step. E126 could be involved in the dehydration step as well as a protonation of C2 or C4. Site-directed mutagenesis, photometric assays and EPR-based rapid-freeze-quench under single and multiple turnover conditions will be used to investigate the role of these residues.

IV. FeS-III intermediate, the EPR active species trapped when one-electron-reduced IspH *E. coli* E126Q variant was incubated with HMBPP, has been proposed to be an intermediate in the reaction mechanism of IspH **(Fig 2.10)**. Kinetic competency of this intermediate, under turnover conditions, will be established using EPR-based-kinetics studies.

V. ENDOR and Mössbauer spectroscopy will be used to probe the redox state of FeS-III intermediate in the E126Q mutant.

2.2 Materials and Methods

2.2.1 Chemicals

E. coli strain XL-1 blue was purchased from Agilent technology (Santa Clara, CA). IPP, DMAPP and HMBPP were from Echelon biosciences (Salt Lake City, UT). Sodium dithionite was from Alfa Aesar (Haverhill, MA). All gases and gas mixtures were from Airgas (Radnor Township, PA). All other chemicals were from AMRESCO (Solon, OH), Acros (New Jersey, USA) or Sigma-Aldrich (St. Louis, MO). His-trap Ni^{2+} affinity and PD-10 columns were from GE Healthcare (Uppsala, Sweden). Centricon and amicon ultrafiltration units were from Millipore (Billerica, MA). Elemental ^{57}Fe (97-98%) was purchased from WEB Research (Edina, MN) or from Cambridge Isotope Laboratories, Inc. Tewksbury, MA. $^{57}FeCl_3$ was prepared by dissolving ^{57}Fe (solid) in 37% HCl at room temperature. After all iron was dissolved, 5 M NaOH was added to bring the $^{57}FeCl_3$ solution to a pH of 4-5. The stock solution was stored at 4ºC until use.

Purification steps, sample handling and experiments were done in an anaerobic glove box (Coy Laboratory Products, Inc., Grass Lake, MI) filled with a mixture of 95% N_2 and 5% H_2 or a Vacuum Atmospheres Co. (Hawthorne, CA) dry box filled with argon. Anaerobic buffers and solutions were used in all procedures. The buffers were filtered over a 0.45 μm membrane (Fisher Scientific Pittsburg, PA), boiled and purged under constant flow of nitrogen gas. Subsequently the buffers were stirred under vacuum for 2-3 hrs. The closed-off bottles were repressurized with argon and directly used or stored. All buffers and solutions were equilibrated and stirred overnight inside the glove box before use.

2.2.2 (E)-4-Hydroxy-3-methylbut-2-enyl diphosphate (HMBPP) Synthesis

HMBPP, the substrate for IspH, was synthesized as described in the literature (125, 126).

2.2.2.1 (E)-4-Chloro-2-methylbut-2-en-1-ol

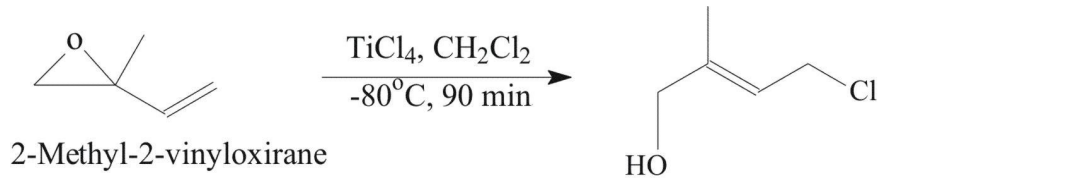

2-Methyl-2-vinyloxirane

(E)-4-Chloro-2-methylbut-2-en-1-ol

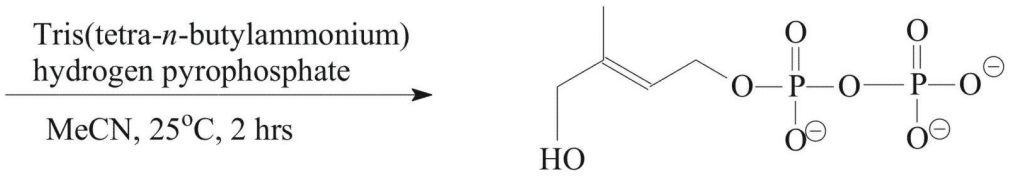

(E)-4-Hydroxy-3-methylbut-2-enyl diphosphate

$TiCl_4$ (285 mg, 1.50 mmol, 165 µL) was dissolved in 3 mL of dry CH_2Cl_2 under argon and the solution was cooled to -80 to -90°C followed by drop-wise addition, with stirring, of 84.0 mg of 2-methyl-2-vinyloxirane in 0.40 mL of dry CH_2Cl_2. The mixture was stirred for 90 min and the reaction was quenched with 5 mL 1 N HCl. When the mixture was warmed to room temperature the phases separated. The aqueous layer was extracted 4 times with 20 mL of diethyl ether and the combined organic phase was dried over $MgSO_4$. The organic extract was purified with flash chromatography (diethyl ether/ hexane 1:1 v/v). Collected fractions were run on TLC (ethyl acetate/hexane 1:4 v/v) and stained with $KMnO_4$. Fractions that contain the desired product were collected and the solvent was removed to afford, (*E*)-4-chloro-2-methylbut-2-en-1-ol. Purity of the product was confirmed with NMR spectroscopy.

^{1}H NMR (CD_3CN, 400 MHz): 5.62 (*tq*, *J* = 8.2; 1.58, 1H), 4.16 (*d*, *J* = 8.2, 2H), 3.89 (*s*, 2H), 1.64 (*d*, *J* = 1.60, 3H).

2.2.2.2 Tris (tetra-n-butylammonium) hydrogen pyrophosphate

Disodium dihydrogen pyrophosphate (3.13 g, 14.0 mmol) was dissolved in 25 mL of deionized water containing 1 mL of concentrated NH_4OH. The clear solution was passed over a cation exchange resin Dowex 50WX8 (2 × 30 cm, H^+ form) and developed with deionized water. The first 150 mL fraction was collected and titrated with tetrabutylammonium hydroxide to pH 7.3. The fractions were lyophilized resulting in a flocculent white tris(tetra-n-butylammonium) hydrogen pyrophosphate.

2.2.2.3 (E)-4-Hydroxy-3-methylbut-2-enyl diphosphate

Tris(tetra-*n*-butylammonium) hydrogen pyrophosphate (227 mg, 0.250 mmol) in 400 µL of MeCN was added slowly to 25.0 mg of (*E*)-4-chloro-2-methylbut-2-en-1-ol (0.210 mmol) in 250 µL of MeCN affording an orange-red solution. The solution was stirred for 2 hrs at room temperature and the solvent was removed under reduced pressure. The orange-colored oily residue was dissolved in 3 mL of H_2O and passed over a column of DOWEX 50WX8 (1×4 cm, NH_4^+ form) that has been prequilibrated with 20 mL of 25 mM NH_4HCO_3. The diphosphate was eluted with 20 mL of 25 mM NH_4HCO_3, flash frozen and lyophilized to yield tan colored (*E*)-1-hydroxy-2-methylbut-2-enyl-4-diphosphate (HMBPP).

^{1}H NMR (D_2O, 400 MHz): 5.52 (*tq*, *J* = 6.9, 1H), 4.39 (*t*, *J* = 7.2, 2H), 3.88 (*s*, 2H), 1.57 (*s*, 3H).

2.2.3 Cloning and transformation

The pASK-IBA33+ plasmid containing the *Aa*I*spHwt* gene, from *A. aeolicus,* and encoding ampicillin resistance was generously provided by Dr. Hassam Jomaa (Justus-Leibig University, Giessen, Germany). The genes were expressed under anhydrotetracycline induction. The IspH H124F and E126Q mutants from *A. aeolicus* were encoded with an ampicillin resistance pASK-

IBA33+ expression vector. The gene was expressed under anhydrotetracycline induction. These plasmids were gift of Dr. Eric Oldfield (University of Illinois, Urbana-Champaign, IL).

E. coli wild type and mutants (T167C and E126Q) were a generous gift of Dr. Michael Groll (Center of Integrated Protein Science, Munich, Germany). The *ispH* gene was cloned into an ampicillin resistance pQE30 plasmid.

In the lab of Dr E. Duin the respective plasmids were transformed into *E. coli* XL-1 blue cells by heat shock of the cells at 42°C for 45 seconds. The transformed cells were inoculated in SOC medium and grown at 37°C for 2 hrs. The cells were inoculated on LB agar plates containing ampicillin (100 mg/L) and incubated at 37°C overnight. Colonies were selected for continuing growth. These cultures were used to prepare glycerol stocks that were stored at -80°C.

2.2.4 Expression and purification

A cell culture, 5 ml, was started on an SOC medium (20 g tryptone, 5 g yeast extract, 0.5 g NaCl, 10 ml 1 M MgSO4, 10 ml 1 M $MgCl_2$, 20% glucose, 100 mg ampicillin per liter). Cells were grown for 6 hrs at 37°C with constant shaking (250 rpm). The 5 ml culture was used to inoculated 50 ml SOC medium which was supplemented with 50 µl 1 M $FeCl_3$ (for a ^{57}Fe-isotope-enriched protein, $^{57}FeCl_3$ was used) and allowed to grow overnight while shaking (250 rpm) at 37 °C. The overnight culture was transferred to a 1L diluted SOC medium containing 500 µl 1M $FeCl_3$.

In the case of IspH from *A. aeolicus* the cell culture (WT and mutants) was grown to an of OD_{600} 0.4-0.6 before inducing with 0.1 mg/L (final concentration) of anhydrotetracycline. *E. coli* cultures (WT and mutants) were not chemically induced. The cultures, from both organisms, were incubated until the OD_{600} reached 3-4.5 and were harvested by centrifugation at 5,000 rpm for 20 minutes. Cell pellets were stored at -80 °C.

The cell pellet was resuspended in 100 ml 30 mM Tris-HCl, 100 mM NaCl, pH 8.0 (buffer A), and lysed by sonication, 3 times for 3 min each at 60% power with a 0.5 sec on/0.5 sec off pulse on ice, followed by centrifugation at 126,603 x g for 20 min at 4°C (Beckman XL-70 Ultracentrifuge, TYPE 45 Ti Rotor, Beckman Coulter, Inc.). The supernatant from *A. aeolicus* was subjected to a heat treatment by incubation at 65°C in a water-bath for 30 mins followed by a centrifugation step at 126,603 x g for 30 mins. The cell extract after the first (*E. coli*) and second (*A. aeolicus*) centrifugation step was filtered with a 0.2 µM filter (Millipore) and loaded to a pre-washed His-trap Ni^{2+} affinity column, The protein was eluted with an imidazole gradient (0 to 100% 500 mM imidazole) in 30 mM Tris-HCl, 100 mM NaCl , pH 8.0 (buffer A). Pure IspH fractions, ascertained by SDS-PAGE, were pooled and immediately used or stored at 4°C.

2.2.5 Protein concentration

The protein concentration was determined with Bradford assay with bovine serum albumin as a standard or by measuring the absorbance at 280nm using ε = 26,930 $M^{-1}cm^{-1}$ (*A. aeolicus*) or ε = 19,940 $M^{-1}cm^{-1}$ (*E. coli*) (127).

2.2.6 Iron determination

Ferrozine-based colorimetry was used for determination of the iron content of the protein (128). All containers and pipette tips used were boiled in 1 M HCl and washed with ultra-pure water. Iron standards (0, 10, 20, 30, 40, 50 µM) were prepared by dissolving ferrous ethylenediammonium sulfate in 10 mM HCl. The iron releasing reagent was prepared by mixing equal volumes of 1.2 M HCl and 4.5 % potassium permanganate. The iron chelating and reducing reagent contained 6.5 M ferrozine, 13.1 mM neocuprine, 2 M ascorbic acid, and 5 M ammonium acetate in a 25 ml solution. To 1 ml iron standard samples and the protein samples

0.5 ml of the iron releasing reagent was added, followed by incubation at 60°C in a water-bath for 2 hrs. To each sample 100 µl of the iron chelating and reducing reagent was added and incubated for at least another 30 mins. The absorbance at 562 nm was used to obtain the value for the samples and to generate a standard curve, from which the iron concentration in the protein samples was determined.

2.2.7 Circular dichroism (CD)

Proper folding of the E126Q and T167C mutant IspH from *E. coli* was checked with CD spectroscopy (Jasco J-810 spectropolarimeter Easton, MD). Spectra for wild type and mutant IspH (10 µM of enzyme in 5 mM potassium phosphate buffer, pH 8.0) were obtained by transferring 200 µl of enzyme into a 0.5 mm path length cuvette which was capped inside the glove box. All CD data were collected from 300 to 190 nm. Spectra were corrected by subtracting the CD spectra of the buffer obtained under similar conditions. Each spectrum is the average of 8 accumulations. CD spectroscopy investigation of the H124F and E126Q mutants from *A. aeolicus* were performed by Weiya Xu. The enzymes were overexpressed from glycerol stock that was stored at -80°C.

2.2.8 Steady-state kinetic analysis

A photometric assay was used to investigate the steady-states kinetics of IspH. To a solution of IspH (in 30 mM Tris-HCl, 100mM NaCl, pH 8.0), sodium dithionite, the redox dye methyl viologen and varied concentrations of HMBPP were added. The change in absorbance at 603 nm due to reduced methyl viologen as a function of time was monitored. The study was achieved under anaerobic conditions with a temperature controlled cuvette holder (q pod) inside a glovebox that was connected through fiber optics to an Agilent 8453 UV-visible

Spectrophotometer (Palo Alto, CA). For IspH from *A. aeolicus* (wild type and mutants) measurements were done at both 25°C and 65°C. For *E. coli* (wild type and mutants) all measurements were performed at 25°C. The data were fit to the Michaelis-Menten equation using Origin software to obtain the steady-state kinetic parameters which were calculated as the average of three separate experiments.

2.2.9 Rapid-freeze-quench (RFQ)

The rapid-freeze-quench method was used to trap intermediates in the enzymatic reaction. A setup shown schematically in **Fig. 2.12** (Kin-Tek Laboratories, Inc, La Marque, TX) was used to rapidly mix and freeze samples. Sodium dithionite reduced IspH (wild type and variants) was loaded in one syringe and in the second syringe HMBPP was loaded. Enzyme and substrate were set to ratios of either 1:1 or 1:10 (single turnover and multiple turnover respectively) and incubated at 25°C. The reaction mixture, a final volume of 300 µl, was aged and quenched at a pre-determined time period in cold isopentane. The 'snow' was subsequently packed to an EPR tube. For control the as-isolated enzyme was also prepared. Dithionite reduce enzyme was mixed with buffer A to get the reduced sample. Samples for longer incubation time were mixed by hand and quenched with cold ethanol. Each method had at least 2 to 3 overlapping time points. Each sample was analyzed by EPR spectroscopy.

2.2.10 Redox titration

Redox titration of IspH from *E. coli*, in the absence of HMBPP, was performed using sodium dithionite as the reductant and potassium ferricyanide as the oxidant in the presence of dye-mediators. 2-hydroxy-1,4-naphthoquinone (E°′= -145 mV), phenosafranin (E°′= -252 mV) , anthraquinone-2-sulfonate (E°′= -255 mV), safranin O (E°′= -289 mV), neutral red (E°′= - 325

mV), benzyl viologen (E°′= -350 mV) and methyl viologen (E°′= -453 mV) were used as mediators at a final concentration of 50 μM. The potential was measured, at 25°C under stirring, with a Ag/AgCl reference electrode that was connected to a redox titration cell. The measured redox potentials were corrected to obtain their value relative to the standard electrode potential (SHE) by subtracting -200 mV. IspH was placed in the titration cell and the dye mediators were added. The protein-dye mediator mixture was fully reduced by adding dithionite, to a potential of -740 mV vs Ag/AgCl (-540 mV vs SHE). The sample was titrated in the oxidizing direction with potassium ferricyanide and rereduced with sodium dithionite. When the mixture has equilibrated at the desired potential, every 10-25 mV a 300 μl aliquot was transferred in to a calibrated EPR tube and immediately frozen in liquid nitrogen. EPR spectra were recorded and a titration curve was prepared by fitting the data to the Nernest equation (**Equation 15**), which was rewritten to express the detectable amount of reduced species, using Origin software to obtain the mid-point potential of IspH.

$$y = h/ (1+ \exp ((n/25.693)*(x-E)) \quad (15)$$

Where: h is height of the curve
n is the amount of electrons involved
E the mid-point potential
x are potential readings (in mV) obtained during titration

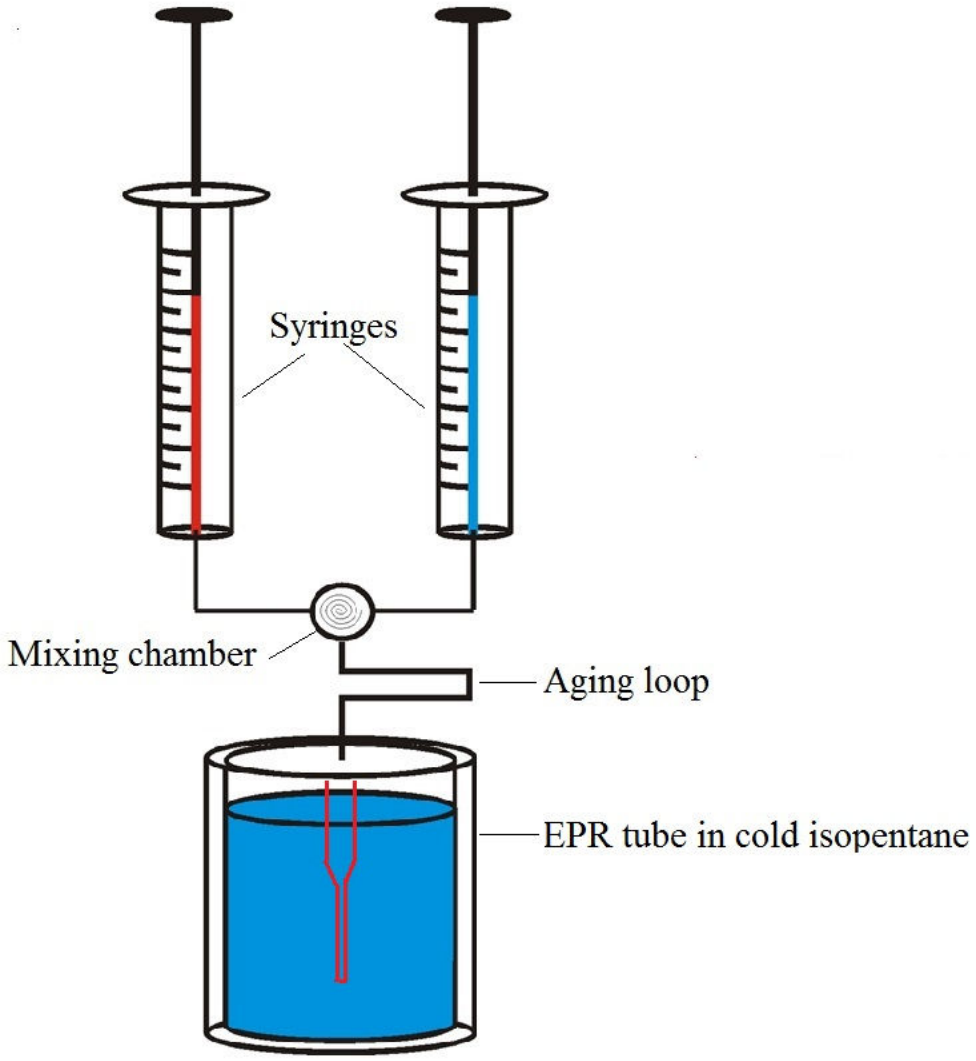

Figure 2.12: Schematic set up for the rapid-freeze-quench experiment.

2.2.11 ENDOR sample preparation and data collection

To determine the electronic properties of the intermediates FeS-I and FeS-III, ^{57}Fe enriched wild type and mutant IspH respectively was analyzed with ENDOR. Some of these samples were prepared by Weiya Xu. To trap the FeS-I intermediate ^{57}Fe-labeled as-isolated WT IspH (*P. falciparum*) was incubated with excess sodium dithionite. The excess dithionite was removed using a PD-10 column to obtain the one-electron-reduced form of the enzyme. An intermediate signal was induced by incubating the one-electron-reduced IspH with HMBPP for 25 s in an ENDOR tube. To determine the electronic properties of the intermediate FeS-III, ENDOR samples were prepared by incubating dithionite-reduced ^{57}Fe-labeled E126Q mutant IspH (*E. coli* and *A. aeolicus*) with HMBPP for one minute at room temperature. The reactions were quenched using cold ethanol. The ENDOR samples were prepared are summarized in **Table 2.1**. Pulsed Davies ENDOR data were collected by Nicholas Lees and Joshua Tesler in the group of Brian Hoffman at Northwestern University, Evanston, IL. Samples were stored in liquid nitrogen and transported in a nitrogen dry-shipper (Taylor-Wharton, Minnetonka, MN).

2.2.12 Mössbauer sample preparation and data collection

To determine the oxidation state of the different [4Fe-4S] species for WT IspH, ^{57}Fe-enriched IspH (*E. coli*) was analyzed with Mössbauer. Oxidized samples were prepared by mixing as-isolated IspH with only buffer or HMBPP. Reduced sample was obtained by mixing the enzyme with sodium dithionite. A sample containing the FeS-II species was prepared by incubating dithionite-reduced IspH with IPP. All samples were transferred in to a Mössbauer cell and an EPR tube that were frozen simultaneously (30 sec) in liquid nitrogen and cold ethanol respectively. To probe the electronic properties of the intermediate FeS-III, samples were

prepared by incubating dithionite-reduced ^{57}Fe-labeled E126Q mutant IspH (*A. aeolicus*) with HMBPP for one minute at room temperature and the reaction was quenched by placing the Mössbauer cell in liquid nitrogen.To prepare a one-electron-reduced sample, ^{57}Fe-labeled wild type enzyme (*E. coli*) was incubated with an excess of sodium dithionite. The excess dithionite was removed from the sample by passage through a desalting PD-10 column to obtain the one-electron-reduced form of the enzyme. An intermediate signal (FeS-I) was induced by adding HMBPP. The sample was transferred into a Mössbauer cell and frozen in liquid nitrogen at about 30 sec after mixing. An overview of the samples prepared is presented in **Table 2.2**. Mössbauer data were collected by Dr Sebastian Stoian in the National High Magnetic Field Laboratory (MagLab), Florida State University, Tallahassee, FL. Samples were stored in liquid nitrogen and transported in a nitrogen dry-shipper (Taylor-Wharton, Minnetonka, MN).

2.2.13 EPR data collection

CW EPR spectra were collected at X-band frequency with a Bruker EMX spectrometer (Bruker Biospin Corporation, Billerica, MA) fitted with the ER-4119-HS high sensitivity perpendicular-mode cavity. An Oxford Instruments ESR 900 helium flow cryostat in combination with an ITC 503S temperature controller was used for measurements in the 4.5-300 K range. A liquid nitrogen finger Dewar was fitted to the cavity for 77 K measurements. Instrument conditions were: microwave frequency of 9.386 GHz; field modulation frequency of 100 kHz and modulation amplitude of 0.6 mT. Sample specific settings are given in the legends to the figures.

Quantitation of the spin concentration of EPR-active species within a sample was determined by comparison of the double integral of the EPR intensity with that of a 10 mM copper perchlorate standard (10 mM $CuSO_4$, 2 M $NaClO_4$, 10 mM HCl). The spin concentration

was corrected for the amount of [4Fe-4S] cluster present in the sample. When multiple paramagnetic species were present in the samples, a spectrum that has only one of the species was subtracted from the overlapping spectrum to get the second spectrum and vice versa. If this was not possible the individual signals were simulated. The double integration value of individual species was obtained and spin concentration determined same as for the single species spectrum. The software packages developed by either S. P. J. Albracht or Fred Hagen were used for spectral simulation and double integration of the signals (129, 130).

Table 2.1: Overview of ENDOR samples prepared.

IspH samples	Source	Cluster type	Cluster concentration (mM)	Spin concentration (mM)
One-electron-reduced with HMBPP	*P. falciparum*	$[4Fe\text{-}4S]^{3+}$	1.7	0.2
E126Q + dithionite + HMBPP	*E. coli*	$[4Fe\text{-}4S]^{+}$	0.66	0.19
E126Q + dithionite + HMBPP	*A. aeolicus*	$[4Fe\text{-}4S]^{+}$	0.766	0.493

Table 2.2: Overview of Mössbauer samples prepared.

IspH samples	Source	Cluster type	Cluster concentration (mM)	Spin concentration (mM)
WT (as-such)	*E. coli*	$[4Fe\text{-}4S]^{2+}$	1.04	n.a
As-such + HMBPP	*E. coli*	$[4Fe\text{-}4S]^{2+}$	0.98	n.a
As-such + dithionite (reduced)	*E. coli*	$[4Fe\text{-}4S]^{+}$	2.6	0.42
Reduced + IPP	*E. coli*	$[4Fe\text{-}4S]^{+}$	0.94	0.67
One-electron-reduced with HMBPP	*E. coli*	$[4Fe\text{-}4S]^{3+}$	0.6	0.8
E126Q + dithionite + HMBPP	*A. aeolicus*	$[4Fe\text{-}4S]^{+}$	0.766	0.493

n.a = not available

2.3 Results

2.3.1 (E)-4-Hydroxy-3-methylbut-2-enyl diphosphate (HMBPP) Synthesis

The final step in the HMBPP synthesis is the DOWEX 50WX8 column step (see **section 2.2.2**). Fractions that contain HMBPP, as analyzed with TLC, were lyophilized and analyzed by ^{1}H NMR **(Fig 2.13)**. The percentage purity of HMBPP was determined with 1,4,-dioxane as an internal standard. From the NMR spectrum it can be concluded that the sample is close to pure. The weight percentage of the HMBPP in the powdered sample is only 24%. We assume the 76% is all salt.

2.3.2 Expression and purification

Wild type and mutant IspH from *E. coli* and *A. aeolicus* were overexpressed in *E. coli* X-L1 blue cells and purified from the cell extract using a Ni-affinity column (see **sections 2.2.3** and **2.2.4**). The purity of the protein was determined by SDS-PAGE **(Fig 2.14)**. The SDS-PAGE for the wild type and mutant proteins showed prominent bands at around 36 kDa for *E. coli* IspH **(Fig 2.14-A)** and 32 kDa for IspH from *A. aeolicus* **(Fig 2.14-B)**.

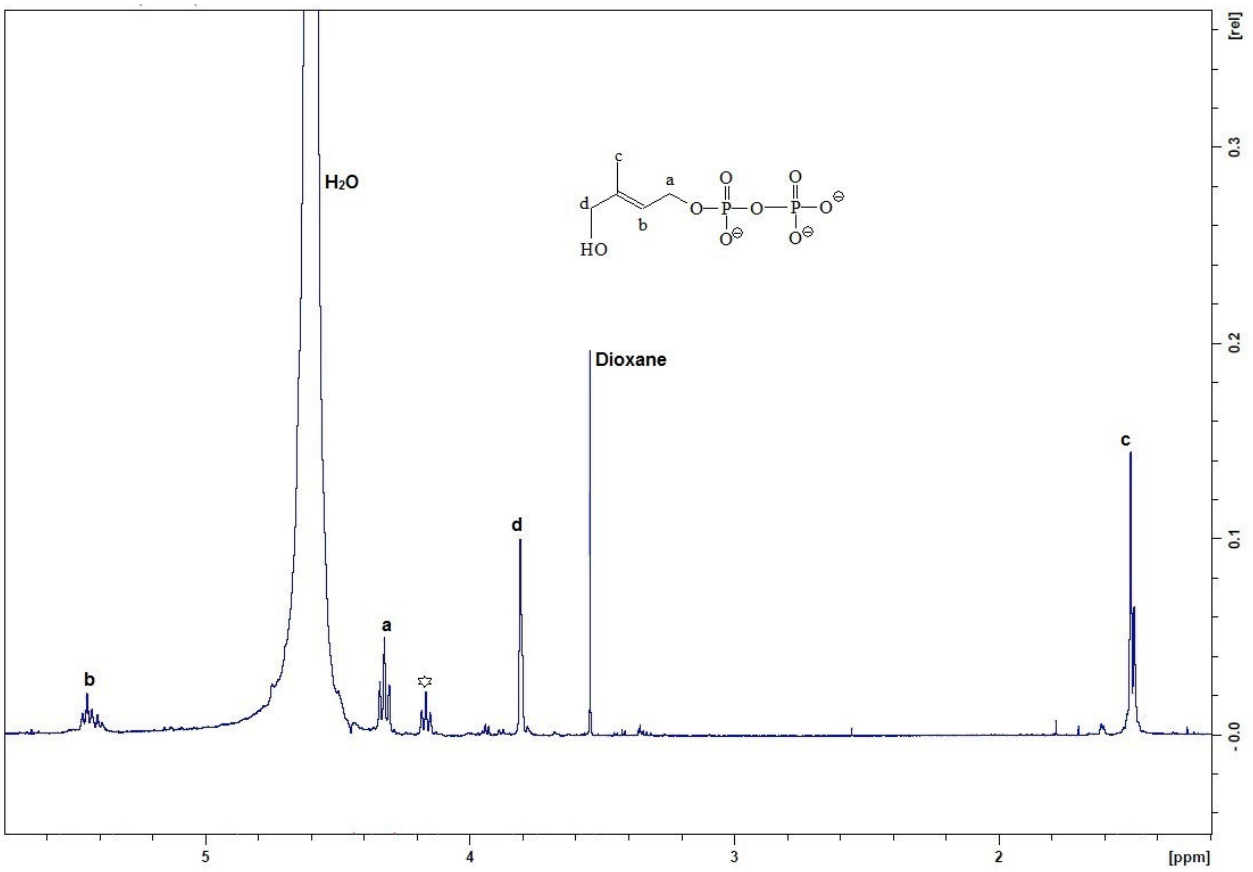

Figure 2.13: ^{1}H NMR spectrum of HMBPP (D_2O, 400 MHz).

* unassigned impurity.

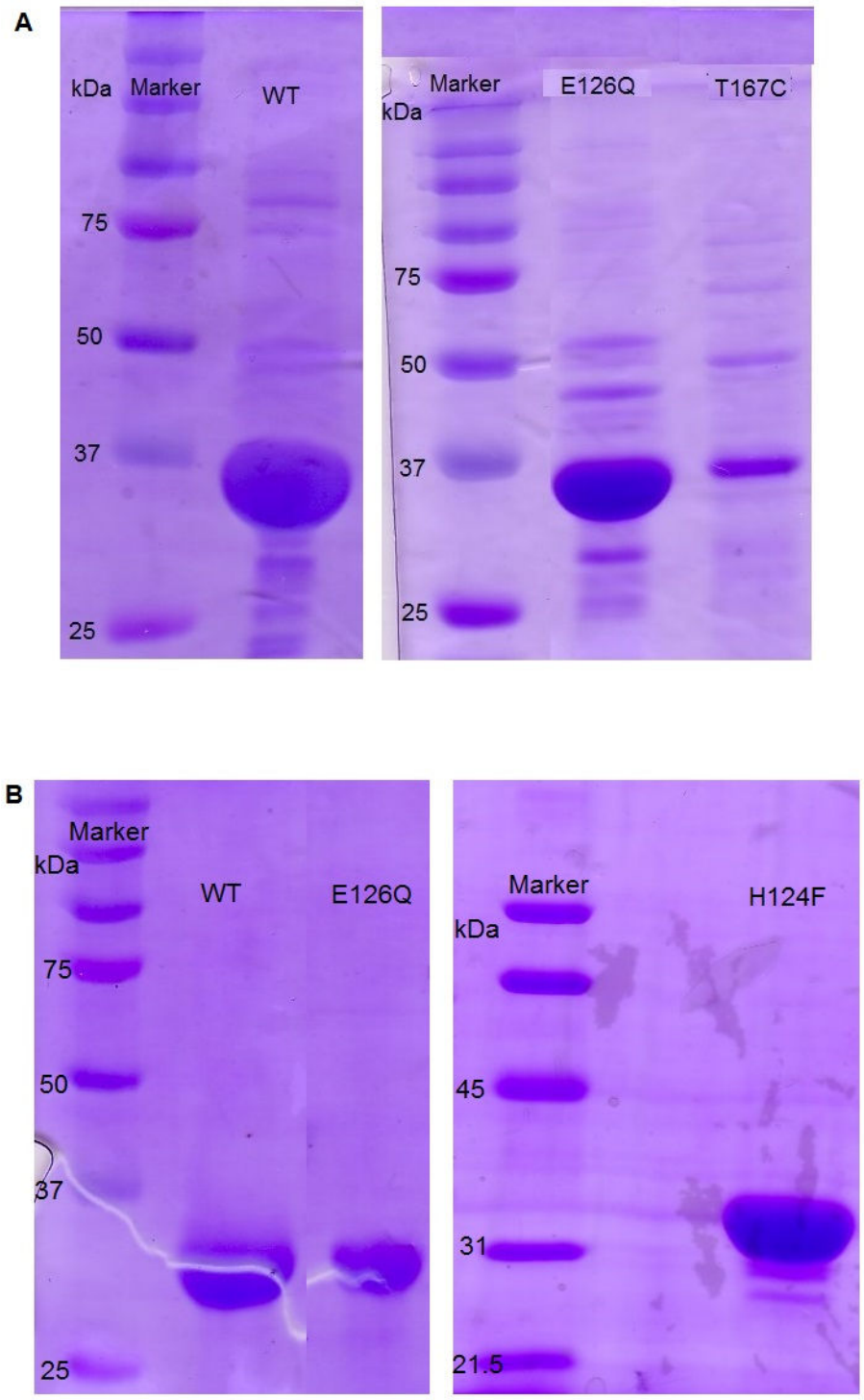

Figure 2.14: SDS-PAGE analysis of purified IspH.
(A) IspH wild type and mutants from *E. coli*. (B) IspH wild type and mutants from *A. aeolicus.*

2.3.3 Wild type and mutant IspH from E.coli

2.3.3.1 Circular dichroism (CD)

To check the proper folding of the mutants, circular dichroism spectra were measured for WT and, E126Q and T167C mutant IspH **(Fig. 2.15)**. The data showed that all the protein samples have a very similar overall spectral shape, indicating that there are no significant structural differences.

2.3.3.2 Steady-state kinetic analysis

Activity assays of WT, E126Q and T167C IspH were performed in 30 mM Tris-HCl, 100 mM NaCl, pH 8, in the presence of reduced methyl viologen at 25°C. The Michaelis-Menten equation was used to determine the steady-state kinetic constants which were corrected for cluster content. **Table 2.1** shows the overall comparison of the kinetic parameters for wild-type and mutant IspH at 25°C. The data shows that the T167C mutant still has 30 % of the WT activity, while the E126Q mutant was completely inactive.

2.3.3.3 Rapid-freeze-quench studies

The rapid-freeze-quench (RFQ) technique in combination with EPR spectroscopy was used to trap and acquire kinetic information on paramagnetic species formed during the reaction of IspH (wild type and mutant) with HMBPP in the presence of dithionite as reductant. Enzyme (cluster) and substrate concentrations were set to a 1:1 (single turnover) or a 1:10 (multiple turnover) ratio. The reaction mixture was incubated for a desired time interval at room temperature, followed by rapid mixing, incubation, and freezing to stop the reaction. In the following sections the results of the RFQ for the WT and mutant enzyme will be presented and

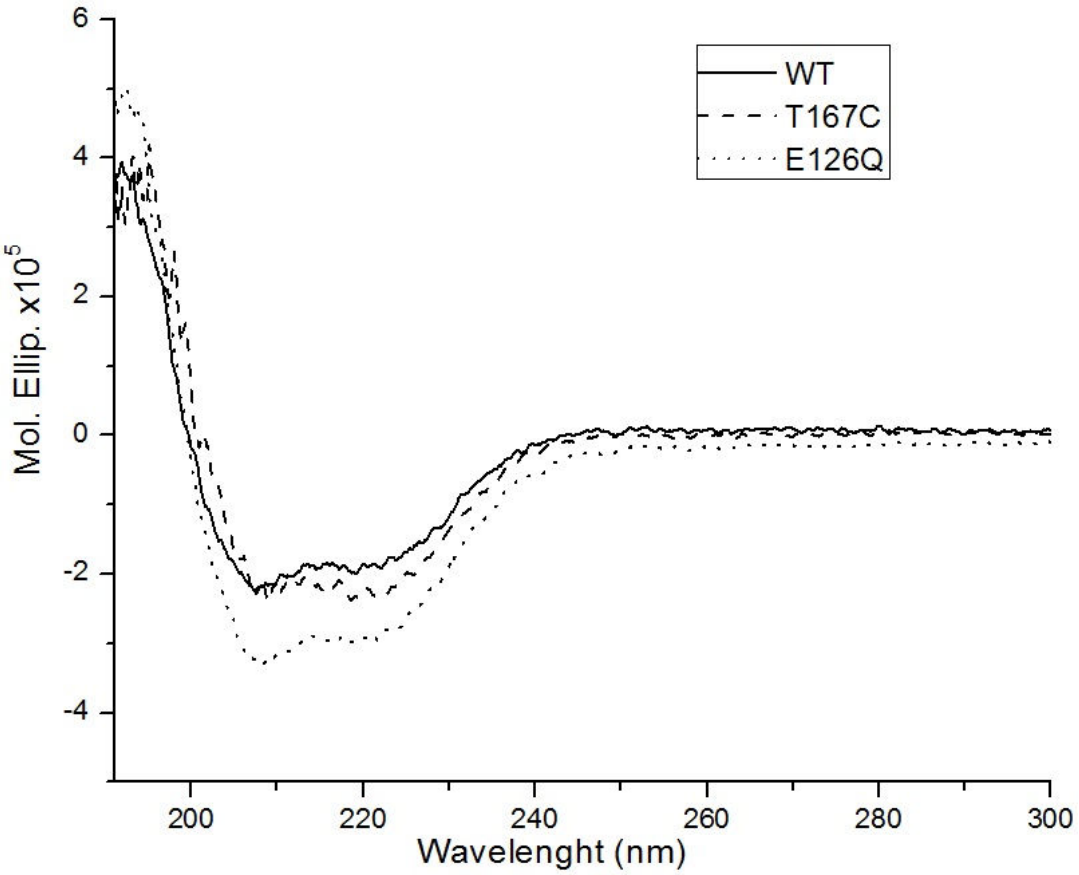

Figure 2.15: Circular dichroism spectra for wild type and mutated IspH from *E. coli*.
Solid line: wild typ. Dashed line: E126Q. Dotted line: T167C.

Table 2.3: Cluster content, k_{cat}, Km and k_{cat}/Km for IspH from *E. coli*.
Reaction mixture contained 37.5 µM dithionite, 60 µM methyl viologen, 2 µM enzyme and 10-400 µm HMBPP in a total volume of 1 ml.

Enzyme (IspH)	Cluster content (%)	k_{cat} (s^{-1})	Km (µM)	k_{cat}/Km ($\mu M^{-1} s^{-1}$)
E. coli WT	54	1.29 ± 0.07	65.9 ± 10.1	0.02 ± 0.003
T167C	28	0.39 ± 0.04	161.4 ± 53.7	0.002 ± 0.0008
E126Q	36	n.d	n.d	n.d

n.d = not detected

discussed. RFQ experiments were performed in doublet or triplicate and the data presented are representative for the enzyme behavior in all studies.

I. Wild type IspH from E. coli

Measurement of the sample prepared in both the single turnover and the multiple turnover experiments for wild type *E. coli* in the presence of HMBPP revealed the formation of two EPR active species at 70 K **(Fig 2.16** and **Fig 2.17)**. In addition to the species detected at 70 K, the EPR signal due to the reduced cluster, with g values 2.035 and 1.84, can be detected at 7 K **(Fig 2.19** and **Fig 2.20)**. Under both experimental conditions there was the immediate oxidation of the reduced cluster **(Fig 2.19** and **Fig 2.20)** and the concomitant development of a low spin (S = 1/2) near-axial signal with g values of 2.176, 2.008 and 2.00. The intensity of this signal peaked and then slowly decreased. In the single turnover experiment the signal was detectable up to 8 s, in the multiple turn over experiment up to 5 s. This spectrum is similar to that of the FeS-I species, the HMBPP bound intermediate with a HiPIP-like $[4Fe\text{-}4S]^{3+}$ cluster that was trapped in the one-electron-reduced experiment for wild type IspH **(Fig 2.5)**. At 1 sec, in single turnover condition, an additional spectrum with g values of 2.08, 2.006 and 1.991 was detected. After 8 s only this second species remained. For the multiple turnover condition the second EPR active species started forming after 5 s. We are denoting this species as FeS-II. A paramagnetic species similar to FeS-II was trapped when dithionite-reduced IspH was incubated with either IPP or DMAPP **(Fig 2.18)**. Therefore it is assigned to a product-cluster species. The development of the FeS-II species observed in the single turnover RFQ is in line with the catalytic turnover determined in the methyl viologen dependent kinetic assay, in which one turnover takes about 1 s **(Table 2.3)**. Note that concomitantly with the FeS-II species also the $[4Fe\text{-}4S]^{+}$ species returns **(Fig 2.19** and **Fig 2.20)**.

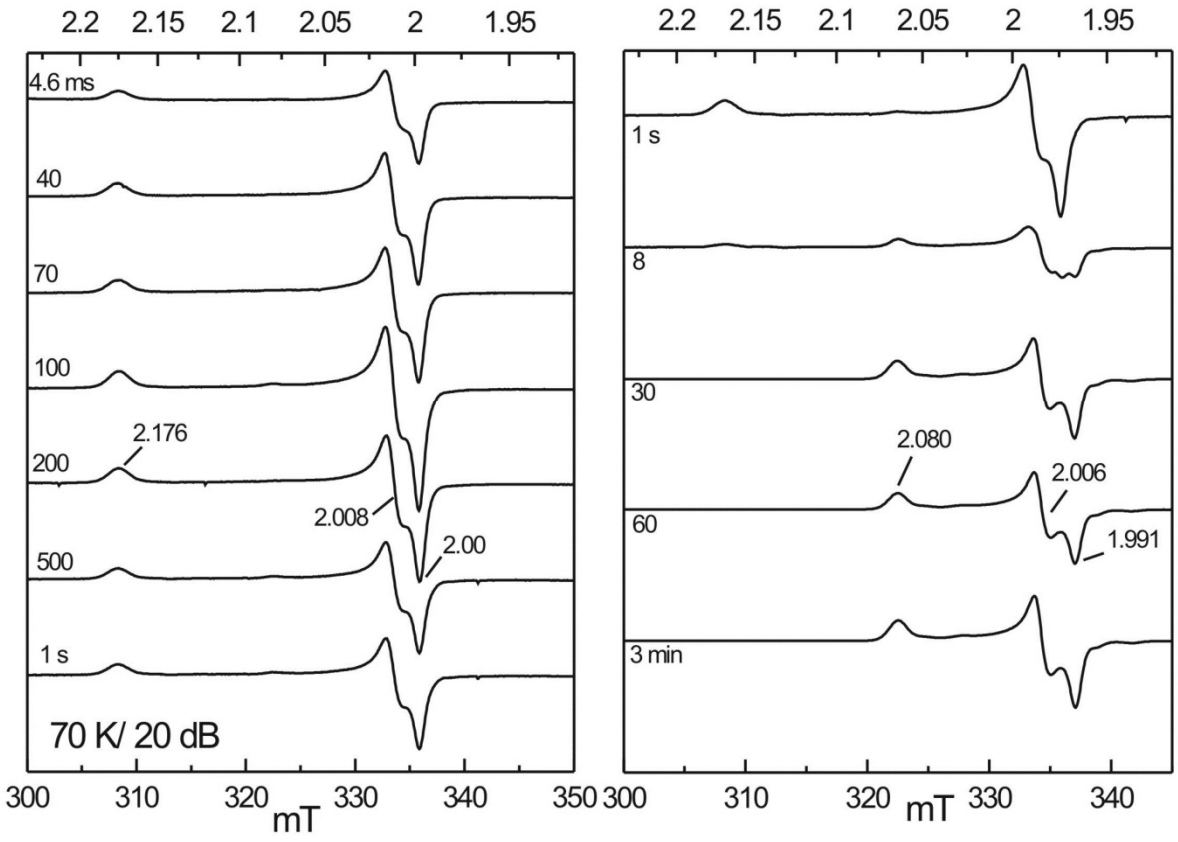

Figure 2.16: Single turnover rapid-freeze-quench EPR spectra of wild type IspH from *E. coli* at 70 K.

Dithionite-reduced IspH was incubated with HMBPP at a 1:1 ratio at different time intervals. Final concentrations: 165 μM IspH cluster, 33 mM dithionite and 165 μM HMBPP.

Both panels are plotted on different scales. The actual intensities are plotted in **Fig 2.26**.

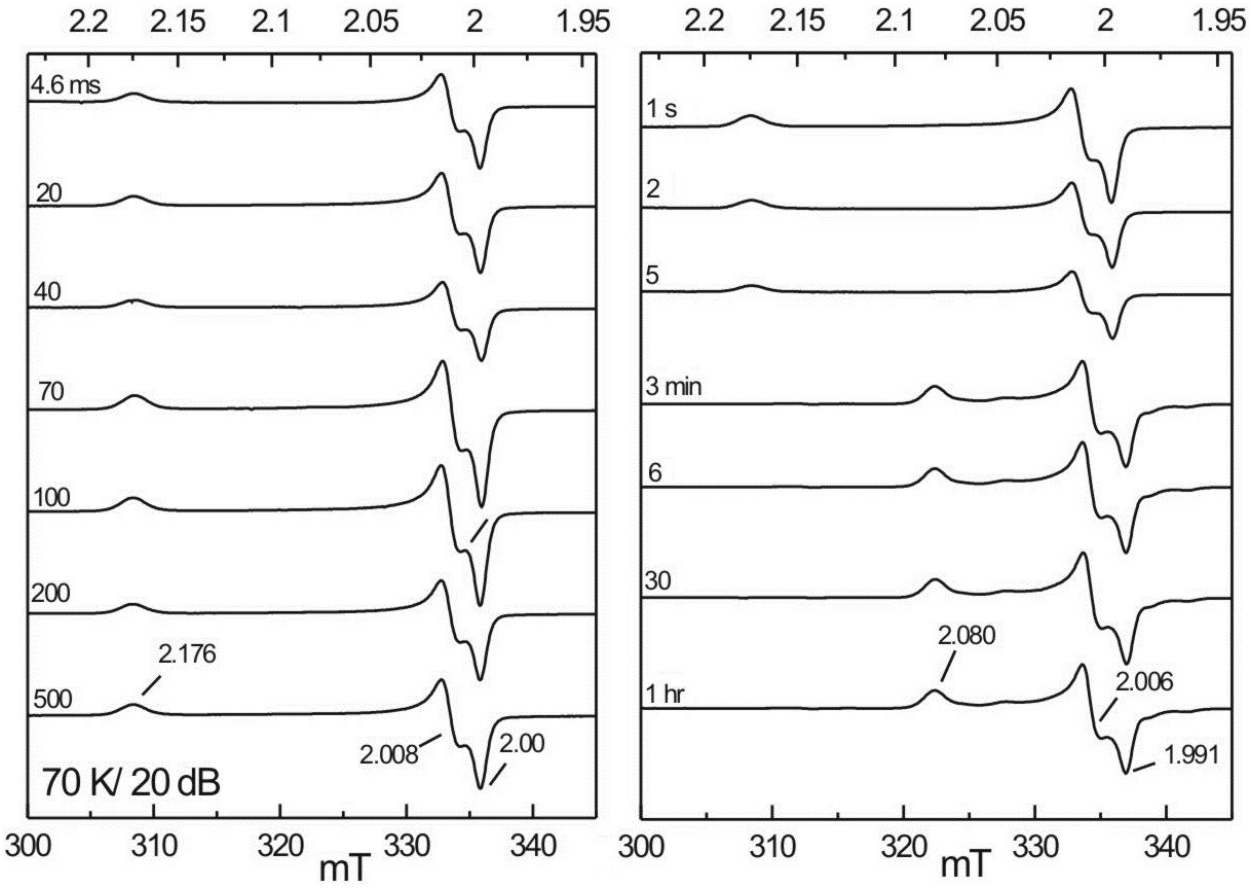

Figure 2.17: Multiple turnover rapid-freeze-quench EPR spectra of wild type IspH from *E. coli* at 70 K.

Dithionite-reduced IspH was incubated with HMBPP at a 1:10 ratio. Final concentrations: 165 μM cluster, 33 mM dithionite and 1.65 mM HMBPP.

Both panels are plotted on different scales. The actual intensities are plotted in **Fig 2.26**.

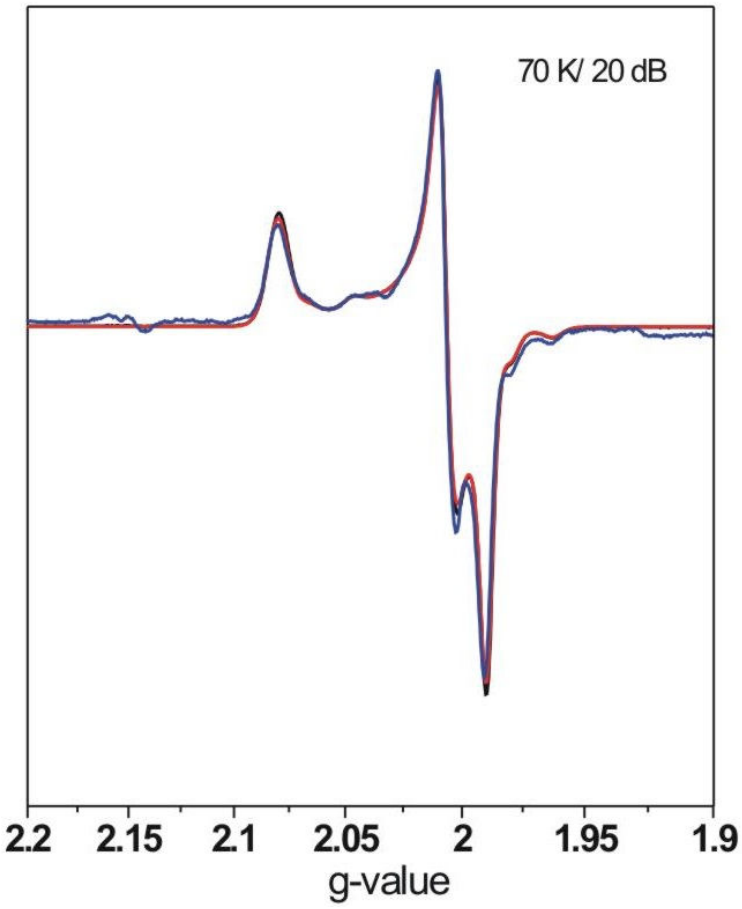

Figure 2.18: EPR spectra dithionite-reduced wild type IspH from *E. coli* with HMBPP (black), IPP (red) and DMAPP (blue).

The black spectrum was obtained by incubating WT IspH with HMBPP and dithionite for 3 min. Final concentrations: 165 μM cluster, 33 mM dithionite and 1.65 mM HMBPP.

To obtain the products signal, reduced IspH was incubated with IPP or DMAPP for 30 s. Final concentrations: 319 mM cluster, 33 mM dithionite, IPP 4.49 mM and DMAPP 4.49 mM.

The intensity of the spectra obtained with IPP and DMAPP is much lower than that of the IspH plus HMBPP. In this figure the spectra have been normalized for comparison of the signal shape.

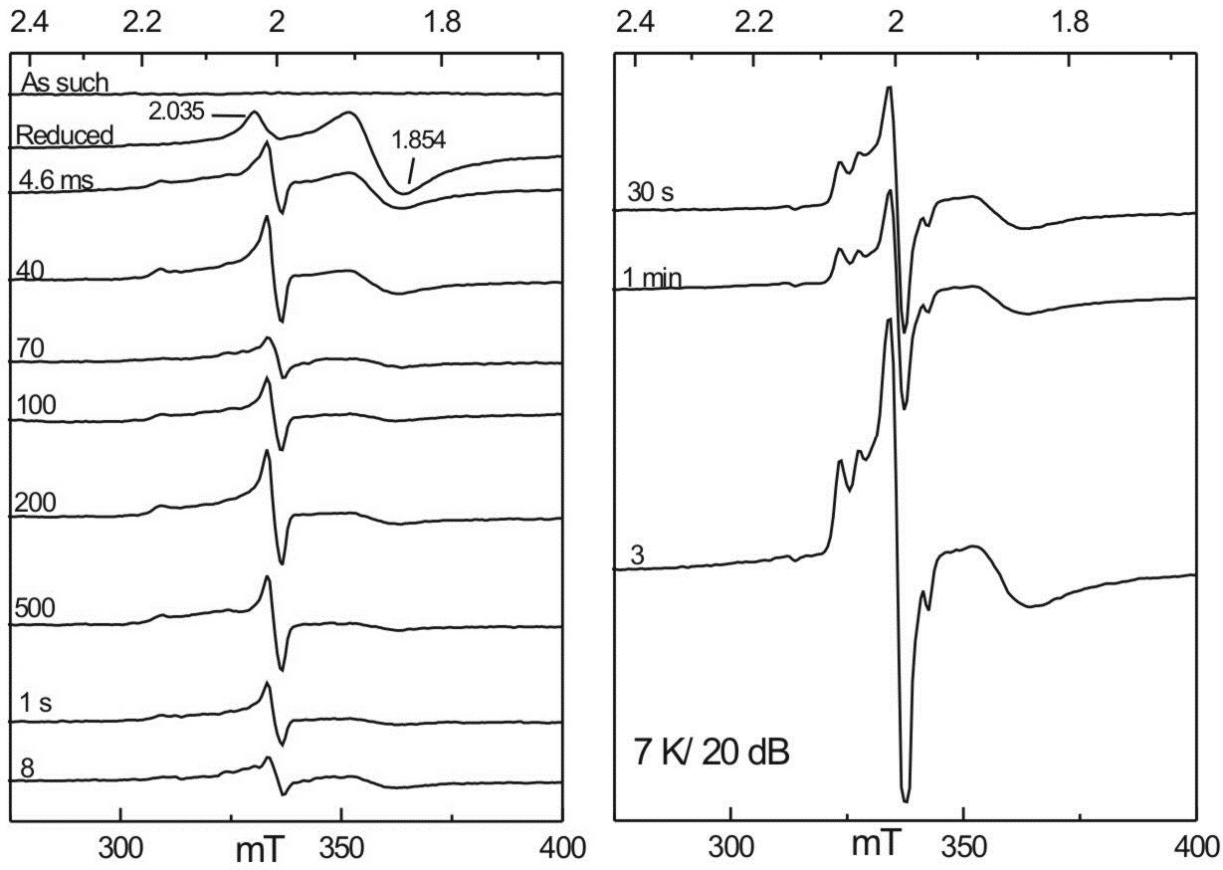

Figure 2.19: Single turnover rapid-freeze-quench EPR experiment spectra for WT IspH from *E. coli* at 7 K.

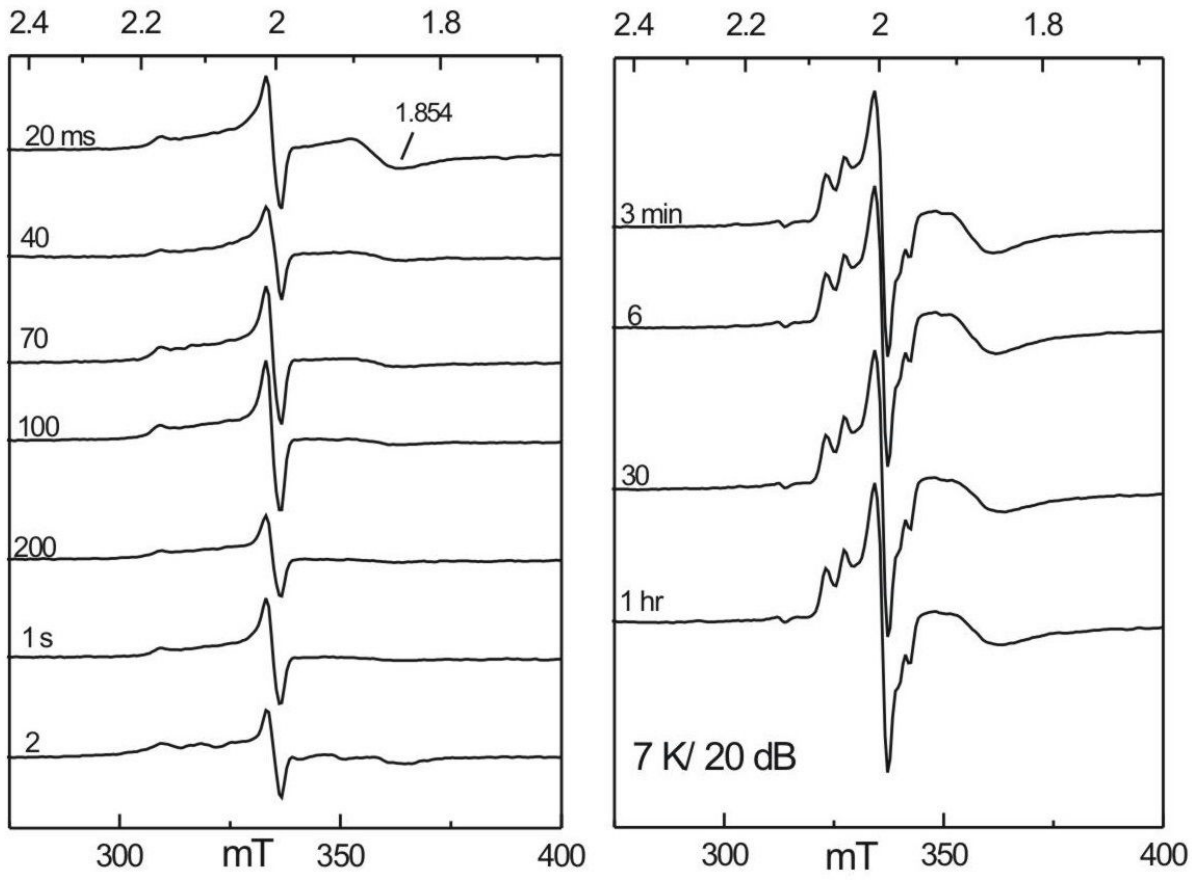

Figure 2.20: Multiple turnover rapid-freeze-quench EPR spectra for WT IspH from *E. coli* at 7 K.

II. E126Q variant from E. coli

In the rapid-freeze-quench study of E126Q IspH under single turnover and multiple turnover conditions a paramagnetic species with g values of 2.134, 2.005 and 1.971 was observed at 70K **(Fig 2.21** and **Fig 2.22)**. The signal appears at the beginning of the series and its intensity increases with time. This species is similar to the EPR active FeS-III, the species that was trapped when one-electron-reduced E126Q and E126A mutants were incubated with HMBPP **(Fig 2.7)**. A similar signal was induced when a dithionite-reduced E126Q IspH from *A. aeolicus* was incubated with IPP or DMAPP **(Fig 2.36).** This signal was present in the as-isolated as well as the dithionite-reduced E126Q IspH **(Fig 2.21** and **Fig 2.22)**. **Figs 2.23** and **2.24** show the spectra obtained for both series at 7 K. A slow disappearance of the $[4Fe\text{-}4S]^{+}$ cluster is detected.

III. T167C variant from E. coli

In the multiple turnover rapid-freeze-quench experiment of T167C two EPR active species that are similar to the species in the wild type were detected at 70 K **(Fig 2.25)**. This is the first time that the effect of a mutation of the T167 in the active site of the IspH has been spectroscopically investigated. The slightly rhombic FeS-I intermediate with g values 2.172, 2.01 and 1.996 appeared at the beginning of the series and decreased in intensity at 2 s. In samples collected after 8 min only the FeS-II species with g values 2.080, 2.006 and 1.991 was detected. Based on the colorimetric kinetic assay of T167C, one turnover takes about 3 s **(Table 2.3)**. Hence in the multiple turnover (1:13) RFQ it would be expected for the FeS-II species to start developing at around 34 s, unfortunately EPR samples were not collected around that incubation time. As in the WT and E126Q IspH the reduced cluster was detected at 7 K **(Fig 2.25)**. Slow

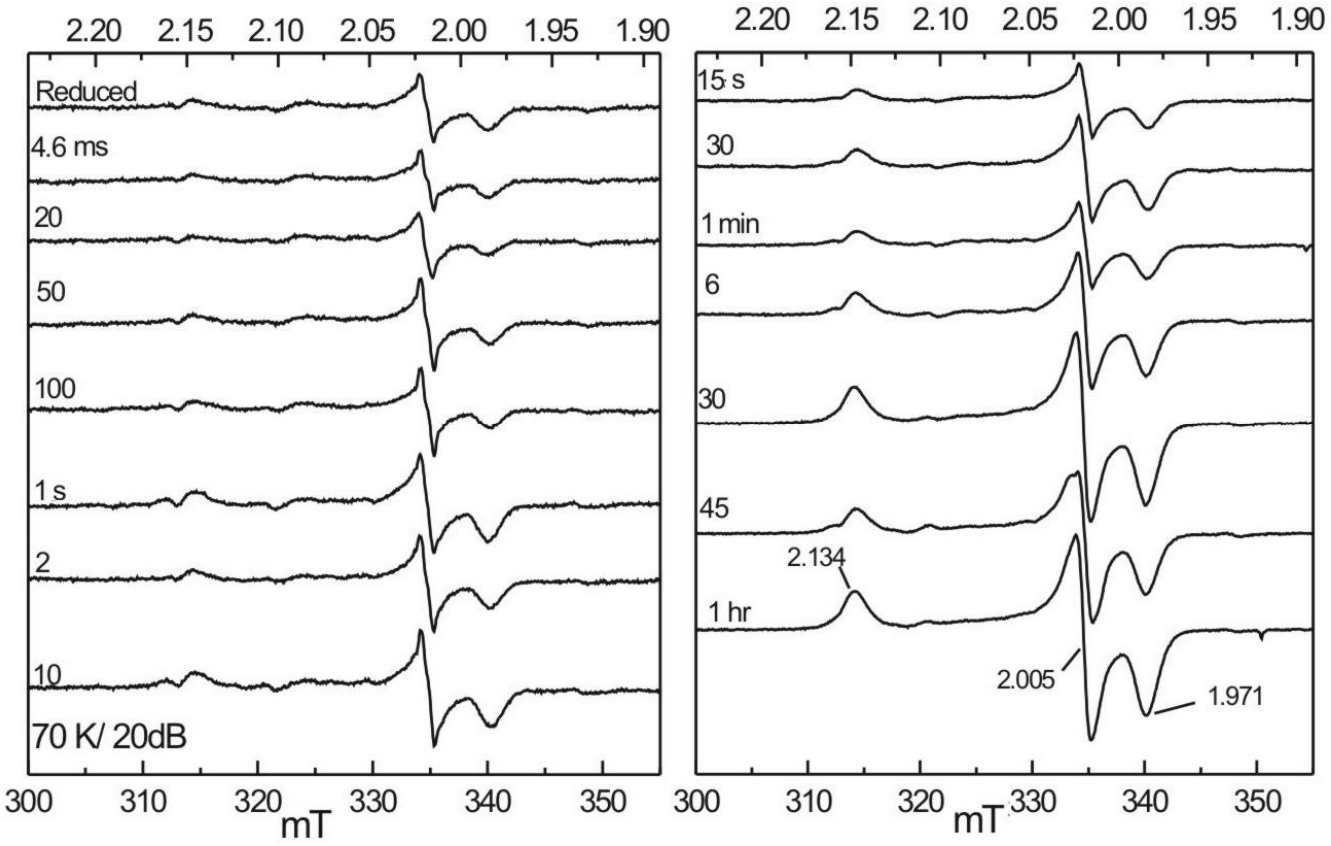

Figure 2.21: Single turnover rapid-freeze-quench EPR spectra of E126Q IspH from *E. coli* at 70 K.

Dithionite-reduced IspH was incubated with HMBPP at a 1:1 ratio. Cluster concentration 70.9 μM, dithionite 33 mM, HMBPP 70.9 μM.

Both panels are plotted on different scales. The actual intensities are plotted in **Fig 2.26**.

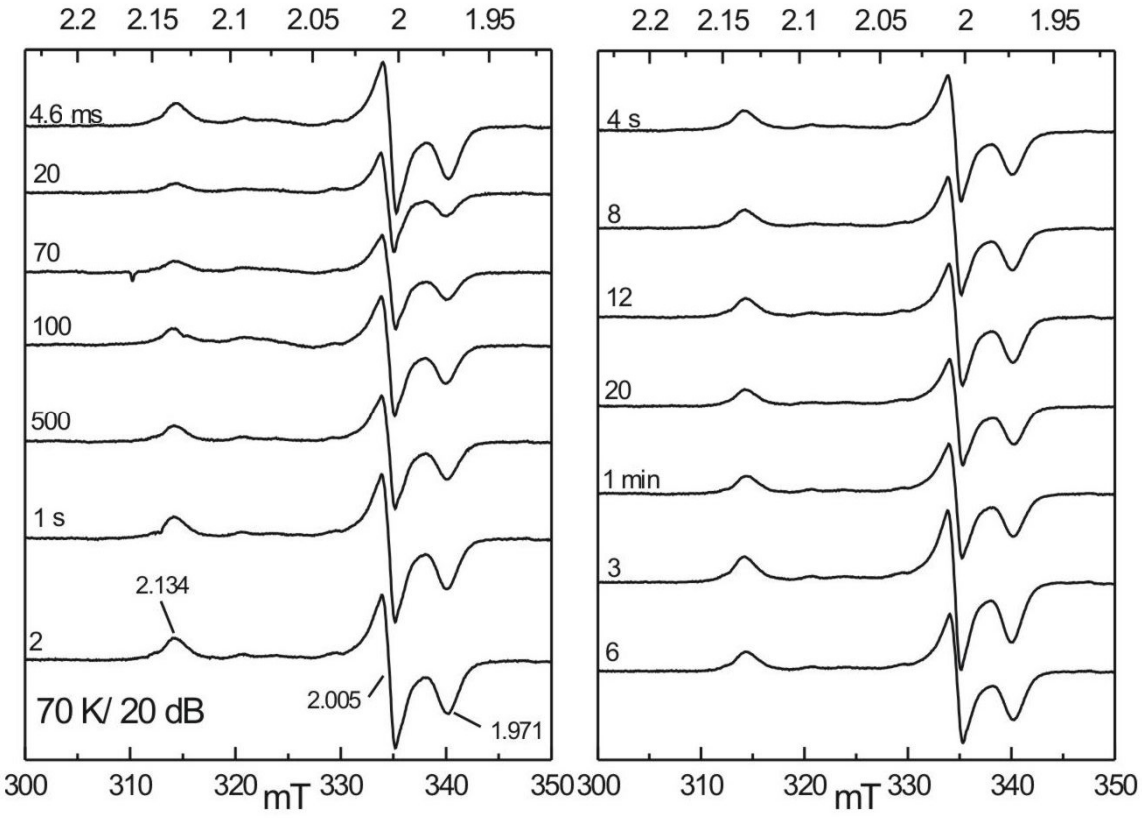

Figure 2.22: Multiple turnover rapid-freeze-quench EPR spectra of E126Q variant from *E. coli* at 70 K.

Dithionite-reduced IspH was incubated with HMBPP at a 1:10 ratio. Cluster concentration 102.28 μM, dithionite 33 mM, HMBPP 1.5 mM.

Both panels are plotted on different scales. The actual intensities are plotted in **Fig 2.26**.

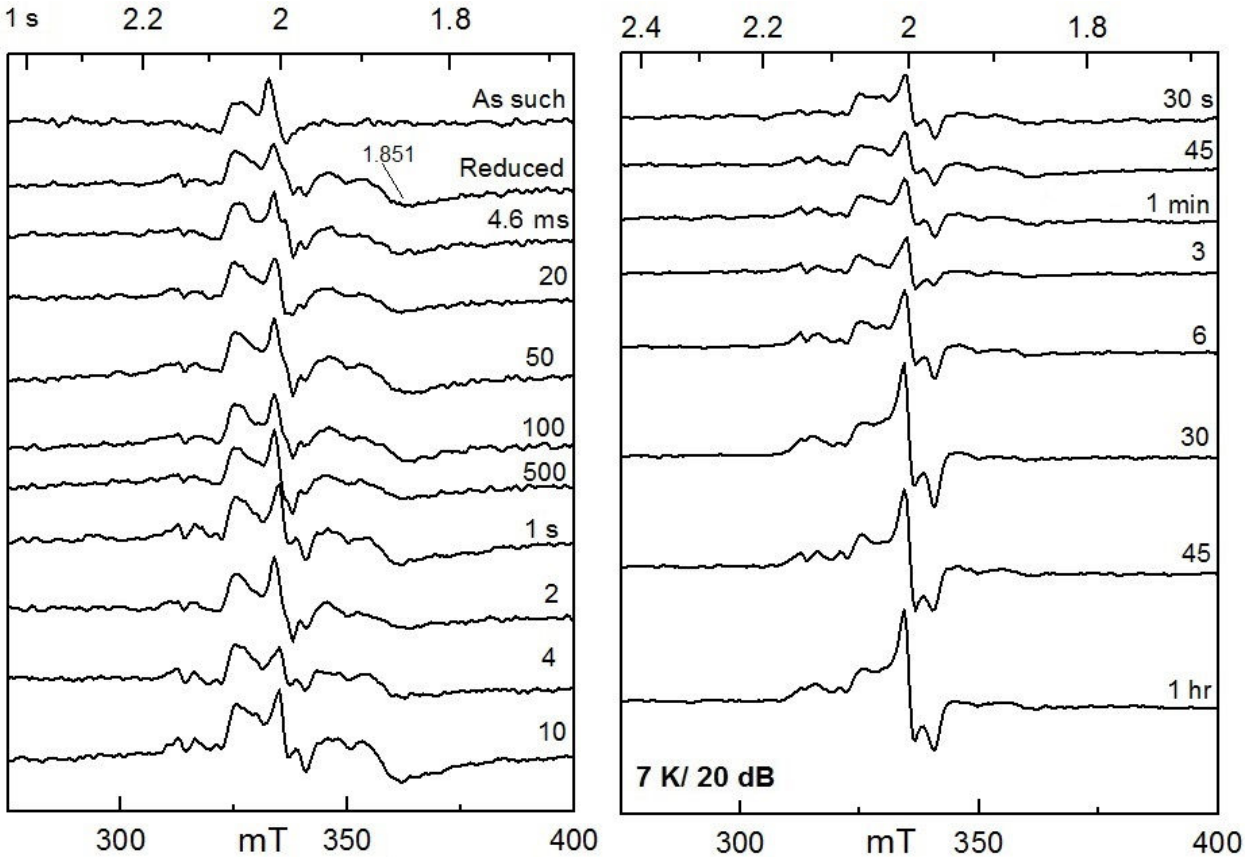

Figure 2.23: Single turnover rapid-freeze-quench EPR spectra for E126Q IspH from *E. coli* at 7 K.

Both panels are plotted on different scales. The actual intensities are plotted in **Fig 2.26**.

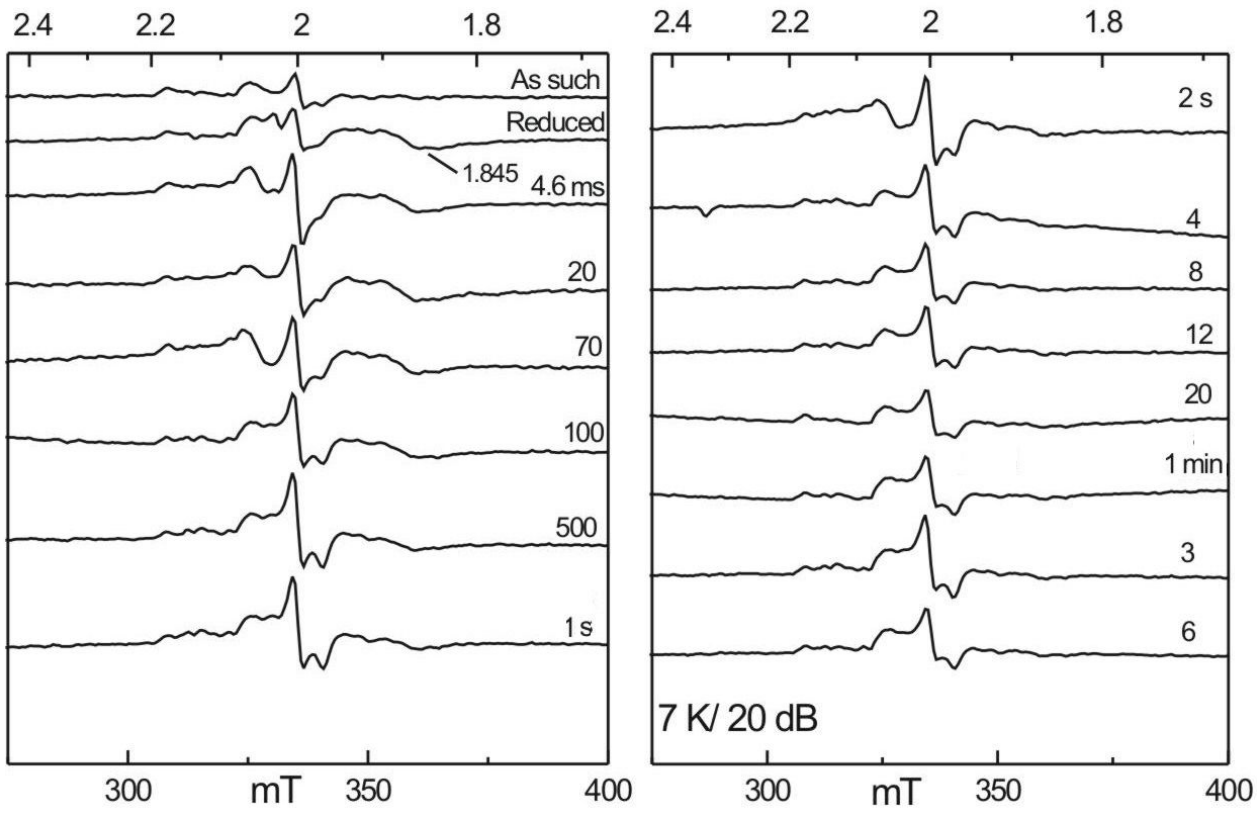

Figure 2.24: Multiple turnover rapid-freeze-quench EPR spectra for E126Q IspH from *E. coli* at 7 K.

Both panels are plotted on different scales. The actual intensities are plotted in **Fig 2.26**.

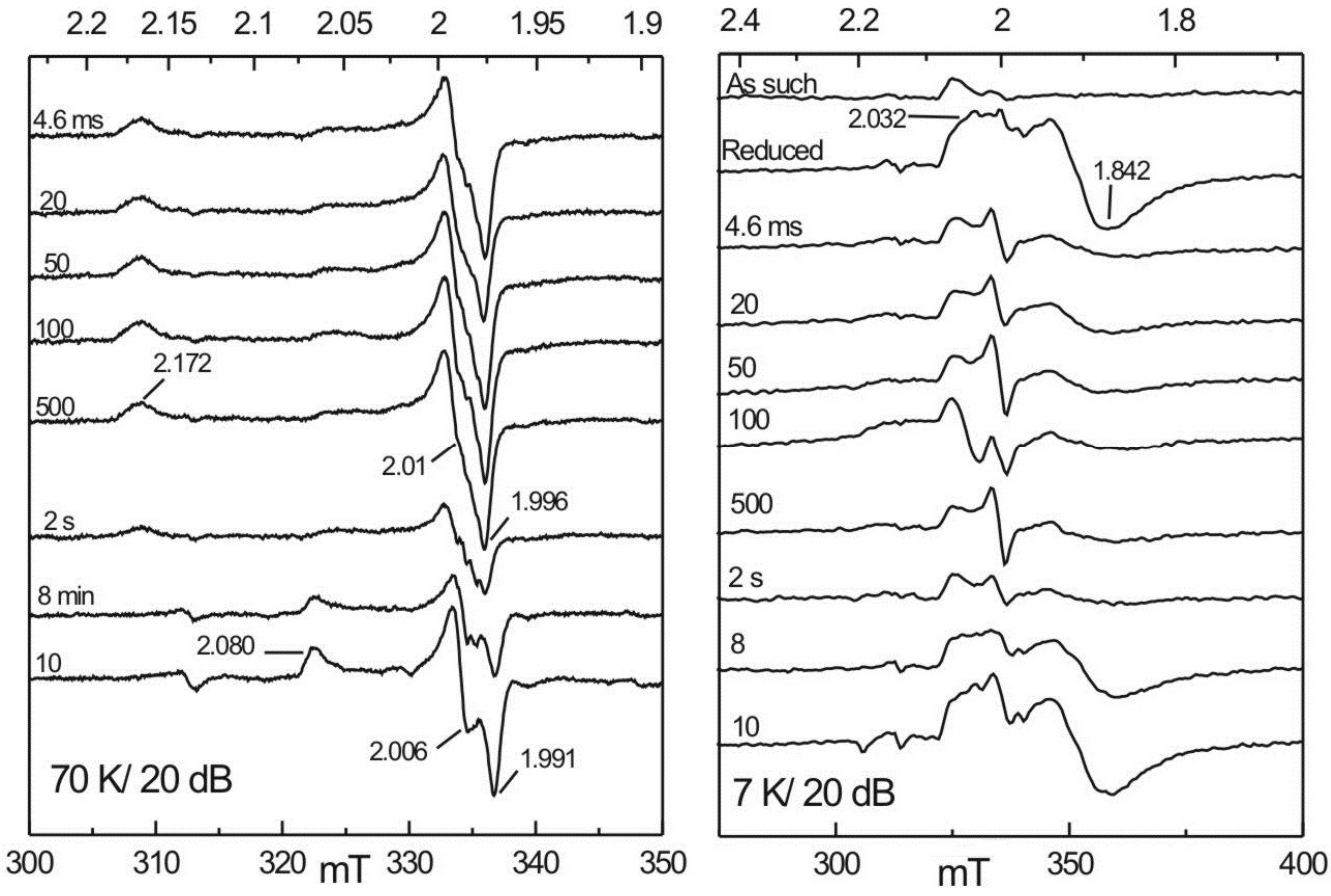

Figure 2.25: Multiple turnover rapid-freeze-quench EPR spectra of T167C mutant from *E. coli* at 7 and 70 K.
Final concentrations: Cluster 75 μM, dithionite 33 mM, and HMBPP 1 mM.

disappearance and reappearance of the $[4Fe\text{-}4S]^+$ cluster was detected in the time range measured.

IV. Overview of EPR active species in E. coli

For comparison the spin intensities of the different signals were determined either through direct double integration of the signals or through simulation of the different components when more than one species was present followed by double-integration of the separate components. These data are collected in **Figure 2.26**. Note that in the E126Q mutant, the FeS-III species is already present in the as-isolated enzyme **(Fig 2.21** and **Fig 2.22)**. We assume that this signal accumulates in the recombinant enzyme when it is expressed in *E. coli*. Since we are interested in the development of the FeS-III species in our experiment we determined the amount present before the experiment and corrected the signal intensity in all samples with this amount. The spin intensities were corrected for packing. About 35% of EPR signal is lost due to the incomplete packing of the enzyme "snow" in the EPR tubes.

The plots confirm the trend that in WT enzyme the $[4Fe\text{-}4S]^+$ signal is lost quickly. At the same time the FeS-I species develops **(Fig 2.26-A and B)**. Most likely we are detecting the fast binding of the substrate to the cluster and the concomitant change in redox state from 1+ to 3+. At the end of the reaction the $[4Fe\text{-}4S]^+$ cluster signal comes back and, most likely, a product-$[4Fe\text{-}4S]^+$ species **(Fig 2.26A and B)**. The ratio of the 2 is probably determined by the dissociation constants of the enzyme for the products. For the E126Q mutant a different behavior is observed. It appears as if the $[4Fe\text{-}4S]^+$ signal is slowly converted into the FeS-III species in the multi-turnover experiment **(Fig 2.26D)**. In the single-turn-over experiment there does not appear to be a connection between the 2 events **(Fig 2.26C)**.

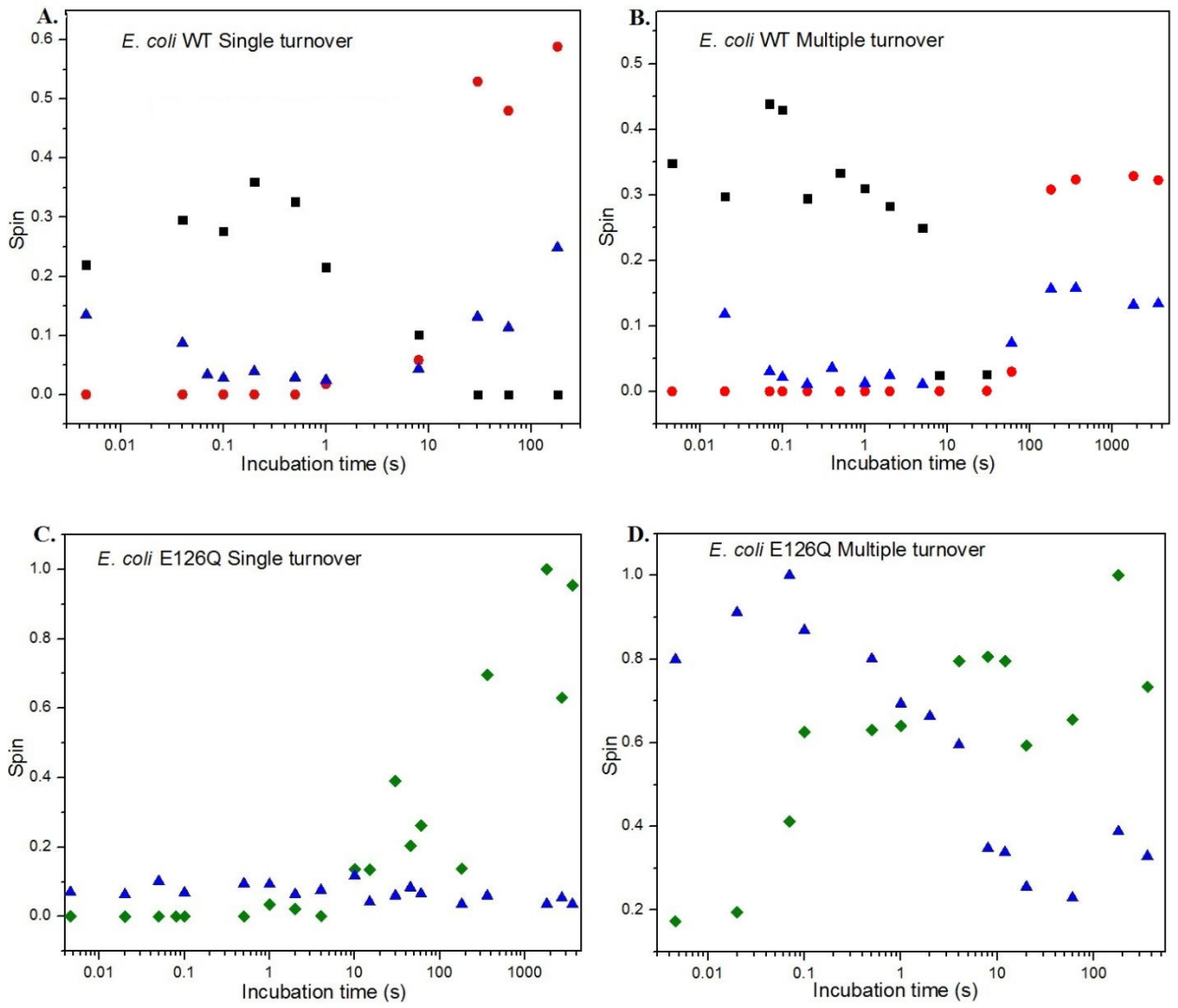

Figure 2.26: Overview of the intensity of paramagnetic species in freeze-quench studies of WT and E126Q IspH from *E. coli*.

Black squares are WT intermediate signal, FeS-I. The red circles are WT product signal (FeS-II), blue triangle reduced $[4Fe\text{-}4S]^{+}$ cluster and the green diamond for the E126Q species, FeS-III. The signal intensity of the FeS-III species in the E126Q mutant experiments were corrected for the amount present in the dithionite-reduced enzyme.

2.3.4 Wild type and mutant IspH from A. aeolicus

2.3.4.1 Steady-state kinetic analysis

As with the IspH from *E. coli* the kinetic parameters for wild type, H124F and E126Q IspH were obtained colorimetrically in the presence of methyl viologen in 30 mM Tris-HCl, 100 mM NaCl, pH 8. **Table 2.2** and **2.3** shows the overall comparison of the kinetic parameters for wild-type and variants at 25°C and 65°C respectively. The data shows that the H124F mutant still has activity, albeit very low, 6.6 % and 4.9 % at 25°C and 65°C respectively, while the E126Q mutant was completely inactive.

2.3.4.2 Rapid-freeze-quench studies

Rapid-freeze-quench (RFQ) in combination with EPR spectroscopy was performed to acquire kinetic information on the intermediates formed when dithionite-reduced IspH (wild type and mutant) was incubated, at varied time intervals, with HMBPP at room temperature. In the reaction mixture, the enzyme (cluster) and substrate concentrations were set to either 1:1 or 1:10 ratios. In the following sections the results of the RFQ for the wild type and mutant enzyme will be presented and discussed. RFQ data are representative of doublet and triplicate runs. When applicable the spin intensities were corrected for packing.

I. Wild type A. aeolicus

Measurements of samples prepared in both the single turnover and the multiple turnover experiments for wild type *A. aeolicus* in the presence of HMBPP revealed the formation of two paramagnetic species **(Fig 2.27** and **Fig 2.28)**. Under both reaction conditions a high spin (S = 3/2) species with two visible g values of 4.668 and 3.384, developed at the beginning of the

Table 2.4: Cluster content k_{cat}, Km and k_{cat} /Km for IspH from *A. aeolicus* at 25°C.
Reaction mixture contains 37.5 µM dithionite, 60 µM methyl viologen, 2 µM enzyme and 16-400 µm HMBPP in a total volume of 1 ml.

Enzyme (IspH)	Cluster content (%)	k_{cat} (s^{-1})	Km (µM)	k_{cat} /Km ($\mu M^{-1}s^{-1}$)
A. aeolicus WT	53	1.36 ± 0.13	50.5 ± 13.4	0.03 ± 0.008
H124F	45	0.09 ± 0.022	186 ± 146.9	0.0005 ± 0.0004
E126Q	43	n.d	n.d	n.d

Table 2.5: Cluster content k_{cat}, Km and k_{cat} /Km for IspH from *A. aeolicus* at 65°C.
Reaction mixture contains 37.5 µM dithionite, 60 µM methyl viologen, 2 µM enzyme and 16-400 µm HMBPP in a total volume of 1 ml.

Enzyme (IspH)	Cluster content (%)	k_{cat} (s^{-1})	Km (µM)	k_{cat} /Km ($\mu M^{-1}s^{-1}$)
A. aeolicus WT	53	5.31 ± 0.48	46.05 ± 12.69	0.12 ± 0.033
H124F	45	0.26 ± 0.01	15.64 ± 1.67	0.017 ± 0.001
E126Q	43	n.d	n.d	n.d

series and disappeared after 1 s (single turnover) and 5 s (multiple turnover). This spectra was detected at 7 K and probably represents the FeS-I species, an intermediate in which the substrate is bound to a HiPIP-like $[4Fe\text{-}4S]^{3+}$ cluster. When one-electron-reduced IspH from *A. aeolicus* and HMBPP are mixed by hand the FeS-I species has spin state S = 1/2. The generation of the spin state S = 3/2 must be an artifact of the procedure used, in which the reaction mixture was sprayed into a cold isopentane to quench the reaction. The second EPR active species, detected at 70 K, has g values of 2.073, 2.006 and 1.991 that are similar to the FeS-II species detected in the rapid-freeze-quench data for WT enzyme from *E. coli* with HMBPP as well as the spectra observed when reduced *E. coli* IspH was mixed with IPP or DMAPP **(Fig 2.16 - Fig 2.18).** This species started to develop from around 80 ms and increases in intensity at longer incubation time. The FeS-II develops faster in the RFQ based assay when compared to the methyl viologen dependent kinetic assay at 25°C, in which the catalytic turnover was approximately 0.74 s/ cycle **(Table 2.4)**. Besides the FeS-I and FeS-II species detected at 7 K and 70 K respectively, the reduced cluster was also detected at 7 K **(Fig 2.29** and **Fig 2.30)**. As with the *E. coli* enzyme a quick disappearance, followed by a slow reappearance is observed.

II. H124F variant from A.aeolicus

As with the WT enzyme, multiple turnover RFQ data for the dithionite-reduced H124F variant incubated with HMBPP resulted in the formation of two paramagnetic species **(Fig 2.31)**. The first signal has the same electronic properties, g values of 4.668 and 3.384, as the FeS-I species detected at 7 K in the wild type *A. aeolicus*. The intensity of this signal decreased gradually and it disappeared after 6 min. Another feature with g values of 2.079, 2.004 and 1.989 started forming after 3 min and can be detected at 70K. A spectrum with similar g values was detected at 70 K when dithionite-reduced H124F was incubated with IPP **(Fig 2.32)**. This

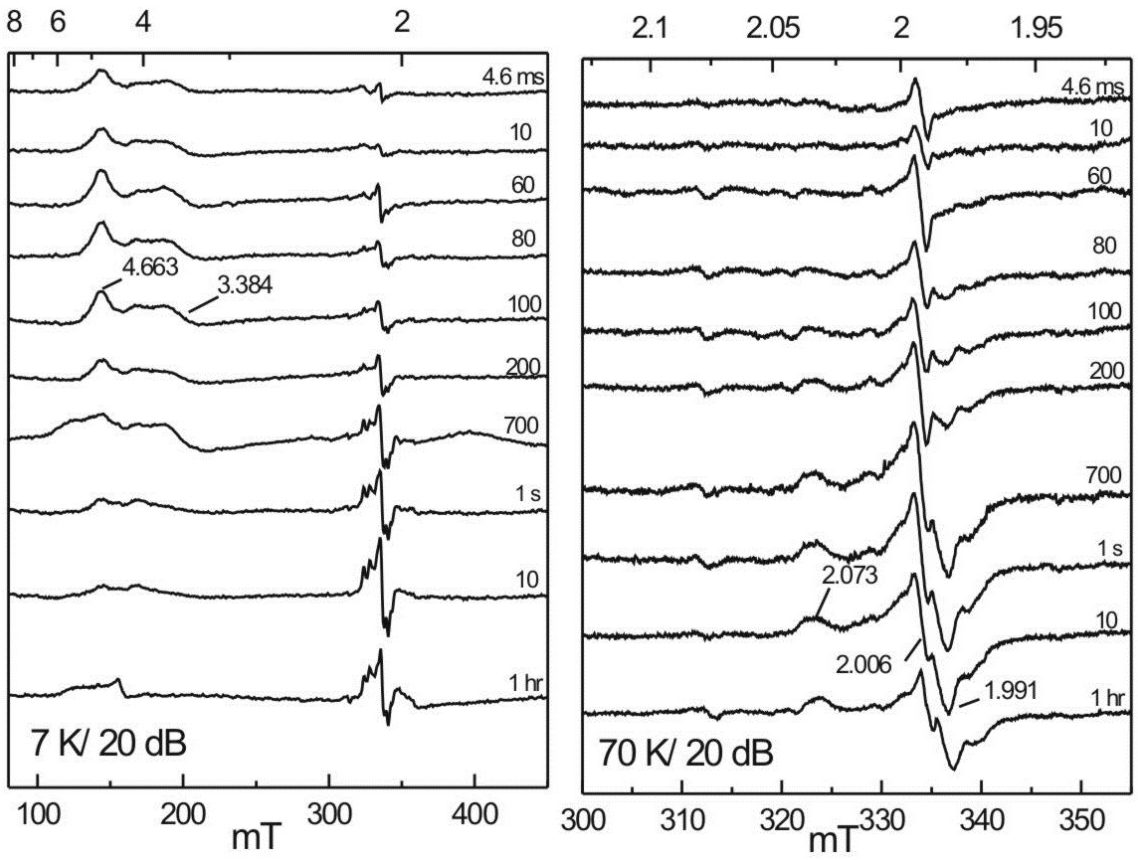

Figure 2.27: Single turnover rapid-freeze-quench EPR experiment for wild type IspH from *A. aeolicus* at 7 and 70 K.
Cluster concentration 124 μM, dithionite 33 mM, HMBPP 124 μM.

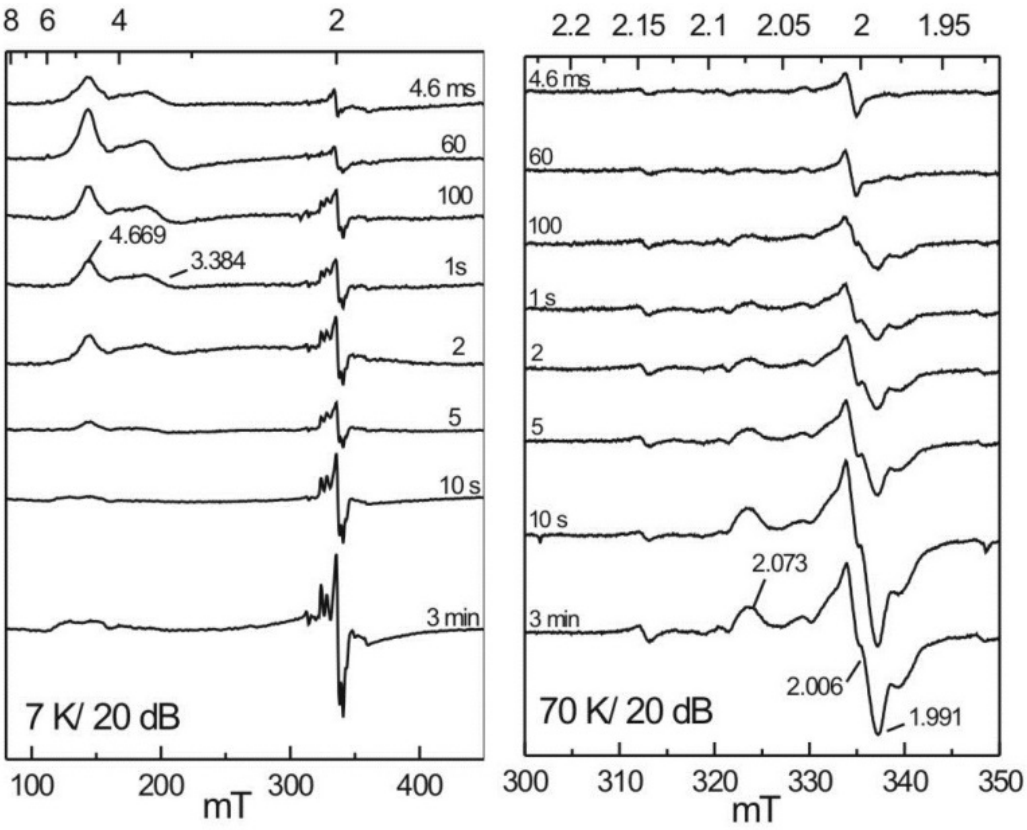

Figure 2.28: Multiple turnover rapid-freeze-quench EPR experiment for wild type IspH from *A. aeolicus* at 7 and 70 K.
Cluster concentration 135.5 μM, dithionite 33 mM, HMBPP 1.5 mM.

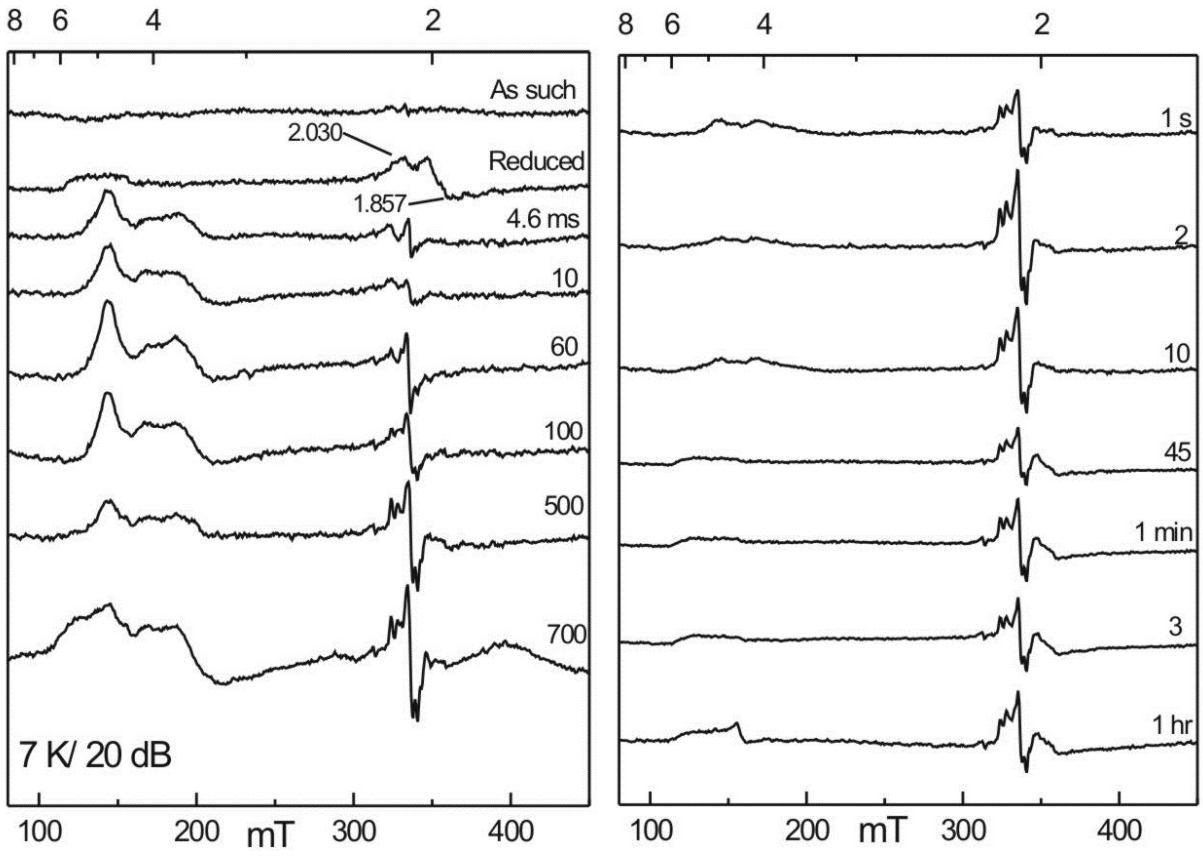

Figure 2.29: Single turnover rapid-freeze-quench EPR experiment for wild type IspH from *A. aeolicus* at 7 K.

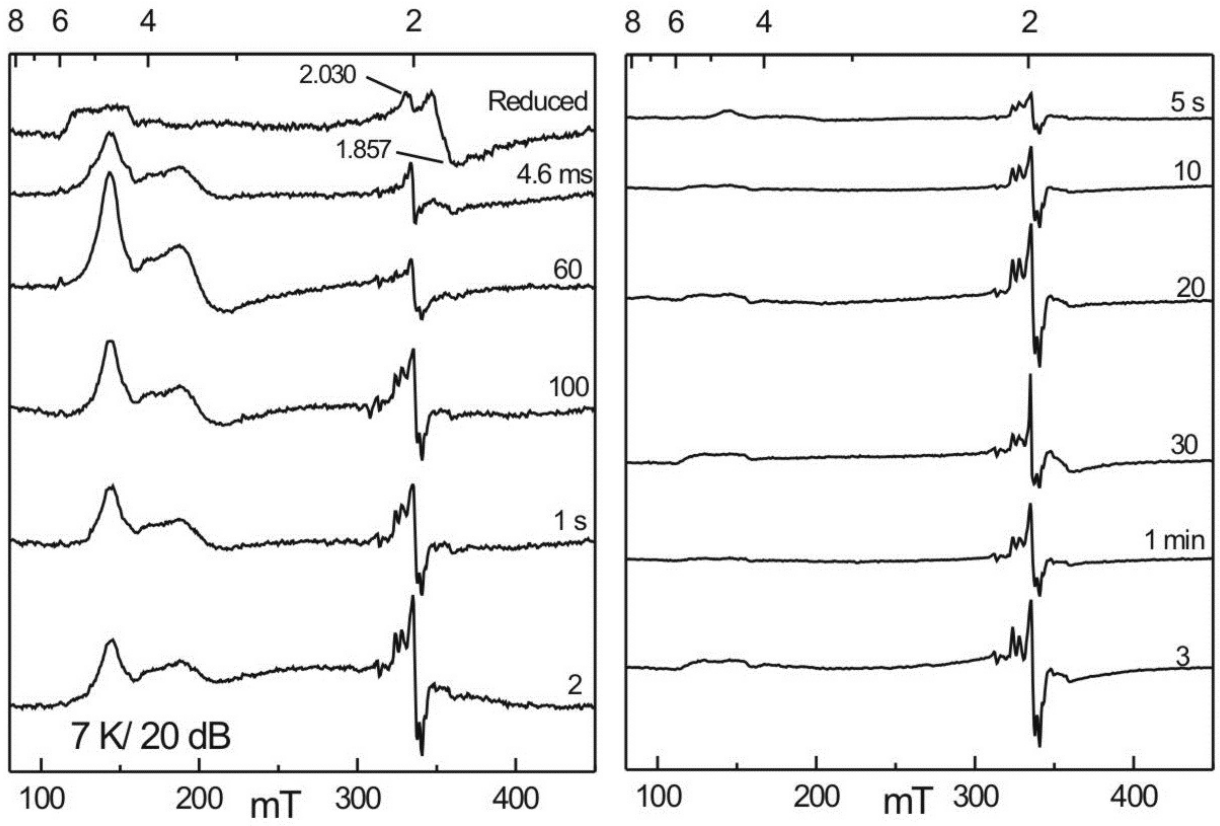

Figure 2.30: Multiple turnover rapid-freeze-quench EPR experiment for wild type IspH from *A. aeolicus* at 7 K.

intermediate is the FeS-II species that was observed in wild type IspH from both *E. coli* and *A. aeolicus*. The appearance of this signal can be explained as the product rebinding (or staying attached) to the reduced $[4Fe\text{-}4S]^{1+}$ cluster. There is a discrepancy between the parameters obtained with the colorimetric assay and the freeze-quench experiment. The methyl viologen based activity assay had a turnover number of about 11s while the freeze-quench data showed the development of the FeS-II species after 3 min. The reason for this could be that a significant amount of IPP and DMAPP has to be produced before rebinding can be detected. From previous work we also know that the reaction in the presence of reduced methyl viologen can be significantly faster than the reaction in the presence of dithionite only. At 7 K the reduced $[4Fe\text{-}4S]^{1+}$ cluster signal was detected (**Fig 2.33)**. The cluster is more difficult to detect due to the overlap with the other signals present but a similar trend of the initial disappearance followed by the slow reappearance of the signal can be detected under the reaction conditions.

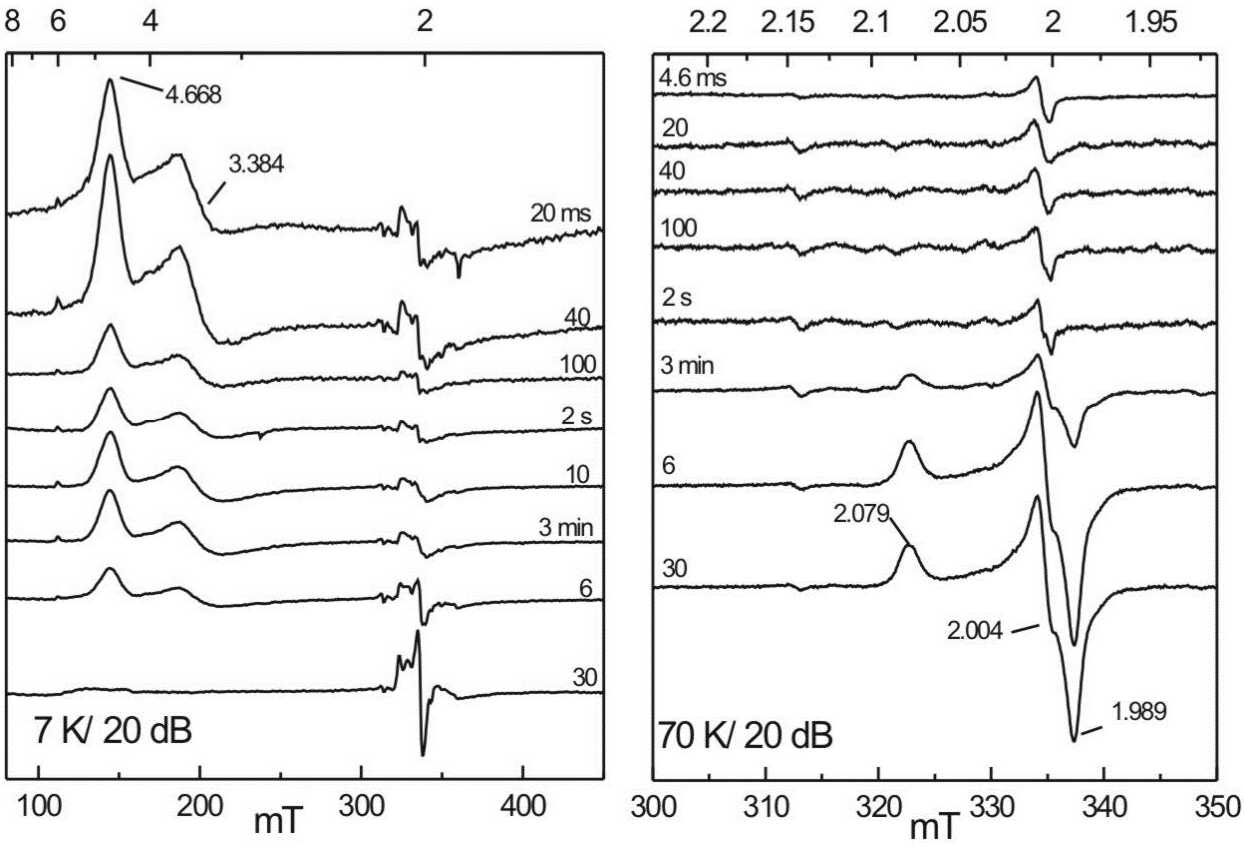

Figure 2.31: EPR spectra for multiple turnover rapid-freeze-quench experiment of H124F mutant from *A. aeolicus* at 7 and 70 K.

Cluster concentration 123 μM, dithionite 33 mM, HMBPP 1.5 mM.

Both panels are plotted on different scales. The actual intensities are plotted in **Fig 2.38**.

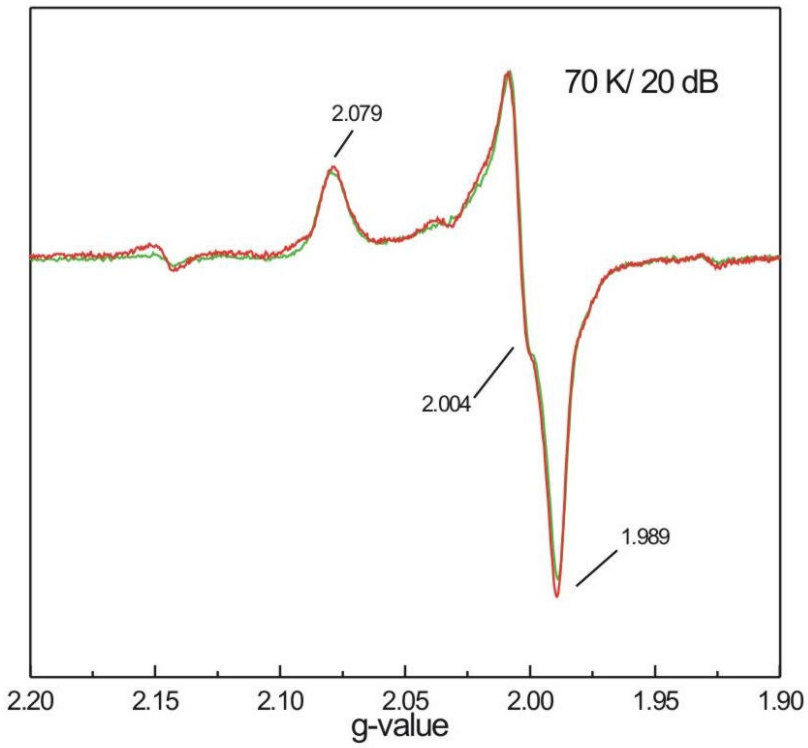

Figure 2.32: EPR data for reduced H124F IspH incubated with HMBPP (green) and IPP (red).
A sample containing 240.8 µM IspH (cluster concentration) and 33 mM dithionite was incubated for 30 s with 3.4 mM of IPP in a final volume of 277 µl. Multiple turnover spectra for reduced H124F in the presence of HMBPP incubated for 30 min was used for comparison.

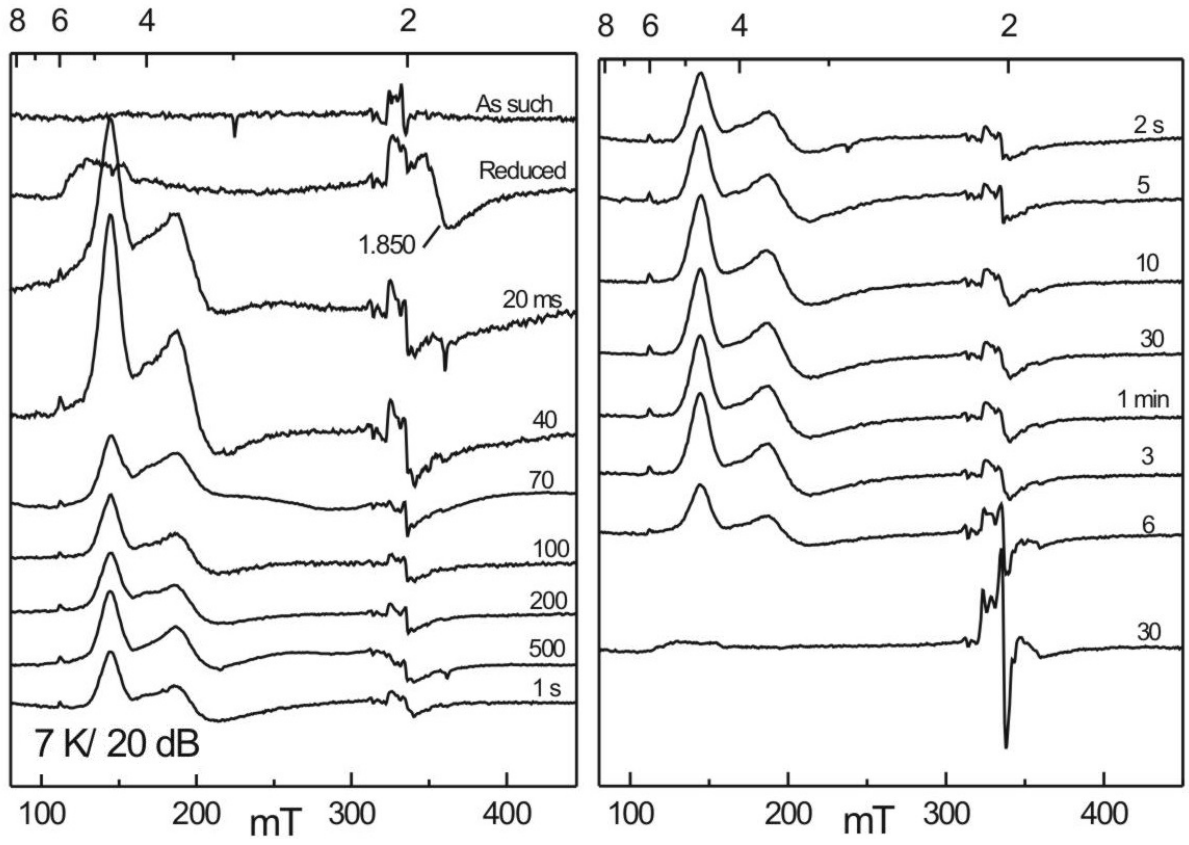

Figure 2.33: EPR spectra for multiple turnover rapid-freeze-quench experiment of H124F mutant from *A. aeolicus* at 7 K.

III. E126Q variant from A. aeolicus

A stable EPR signal that is similar to the E126Q mutant from *E. coli* was observed for the mutant from *A. aeolicus* in both single turnover and multiple turnover conditions. The paramagnetic species, whose intensity increases with time, was detected at 70 K and has g values 2.117, 2.003 and 1.964 **(Fig 2.34** and **Fig 2.35)**. This signal is similar to the EPR active FeS-III, the species that was trapped when one-electron-reduced E126Q and E126A were incubated with HMBPP **(Fig 2.7)**. A similar signal was trapped when the dithionite-reduced E126Q was incubated with IPP or DMAPP **(Fig 2.36)**. Unlike the E126Q mutant from *E. coli* the FeS-III species was not observed in the as-isolated and the dithionite-reduced E126Q **(Fig 2.36)**. The reduced $[4Fe\text{-}4S]^{+}$ cluster signal was detected at 7 K and a set of spectra are shown in **Fig 2.37**. As with the *E. coli* E126Q mutant IspH a slow disappearance of the cluster is detected, slow in comparison to the WT IspH and the other mutants.

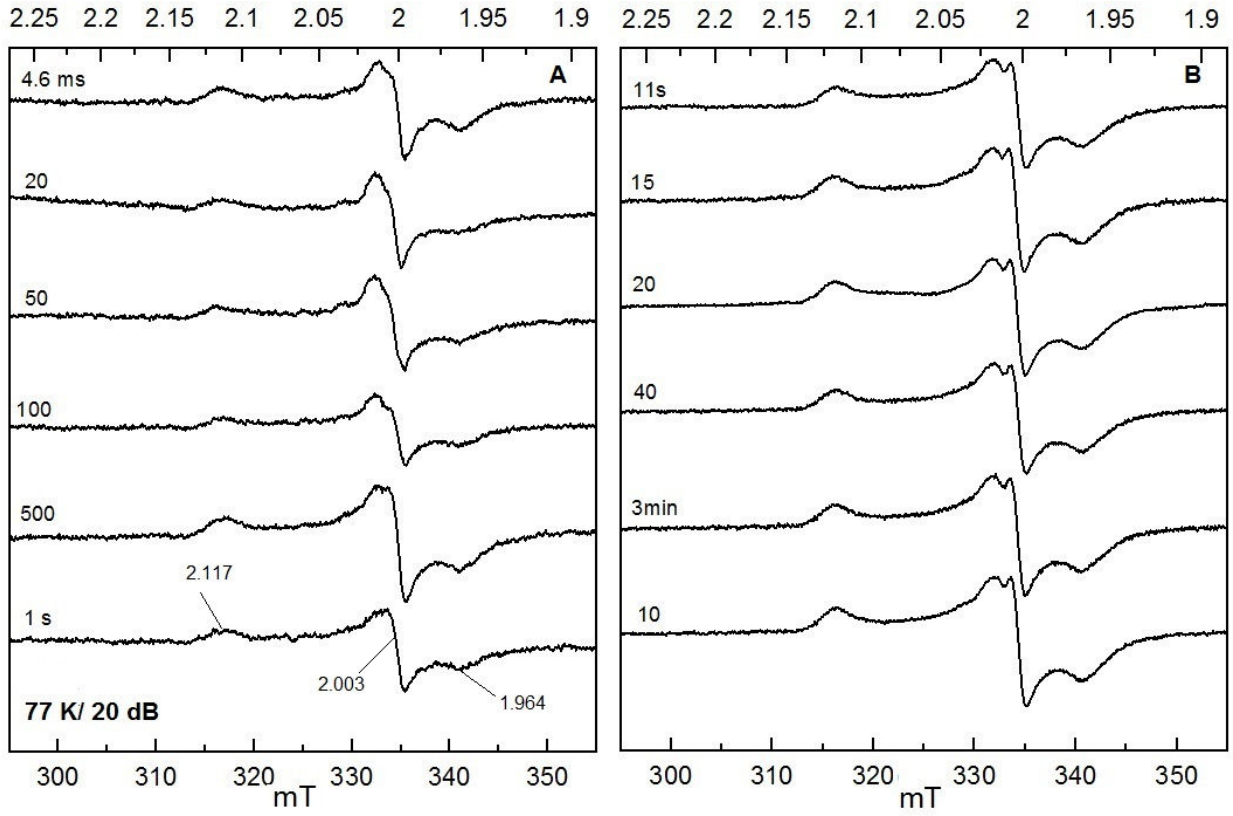

Figure 2.34: Single turnover rapid-freeze-quench EPR data for E126Q variant from *A. aeolicus* at 77 K.

Cluster concentration 150 μM, dithionite 33 mM and HMBPP 150 μM.

Panel A and B are plotted on different scales. The actual intensities are plotted in **Fig 2.38**.

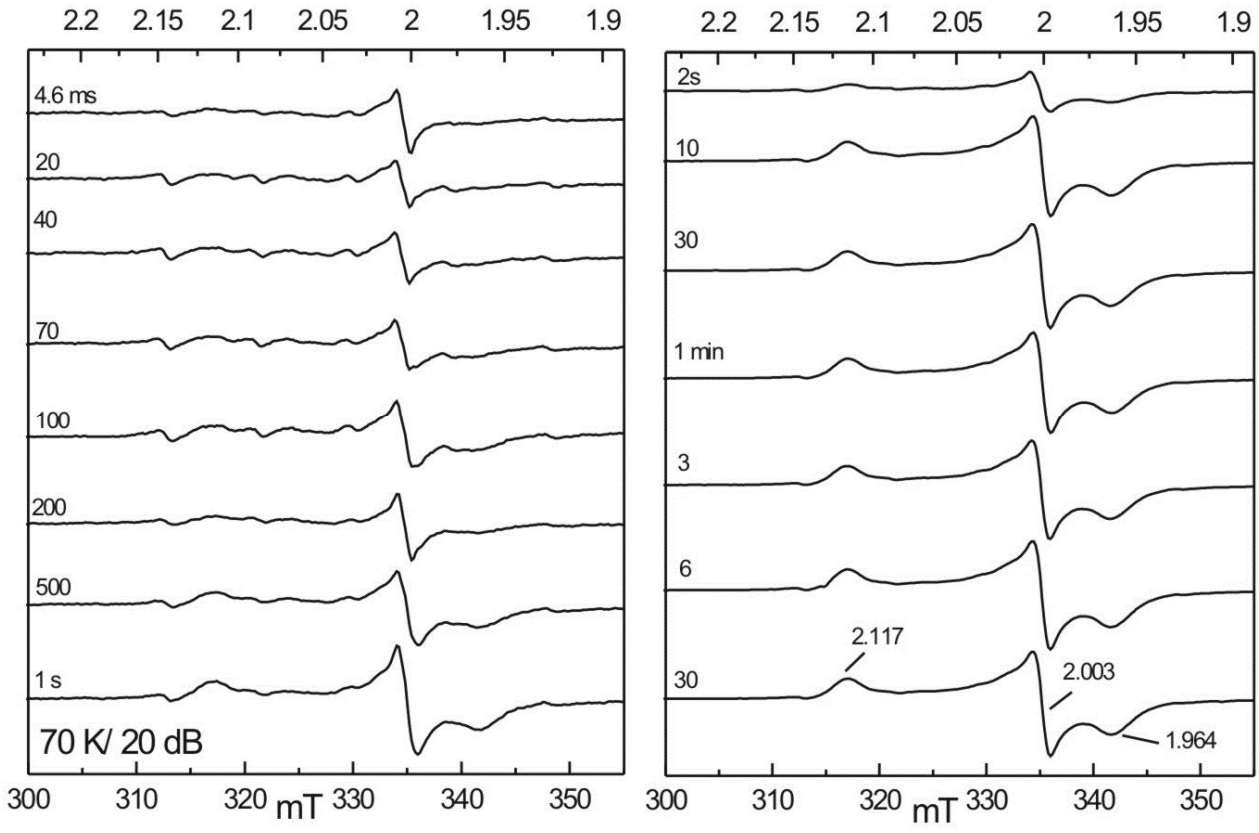

Figure 2.35: Multiple turnover rapid-freeze-quench EPR experiment for E126Q IspH variant from *A. aeolicus* at 70 K.
Final concentrations: Cluster 164.8 µM, dithionite 33 mM and HMBPP 1.65 mM.
Both panels are plotted on different scales. The actual intensities are plotted in **Fig 2.38**.

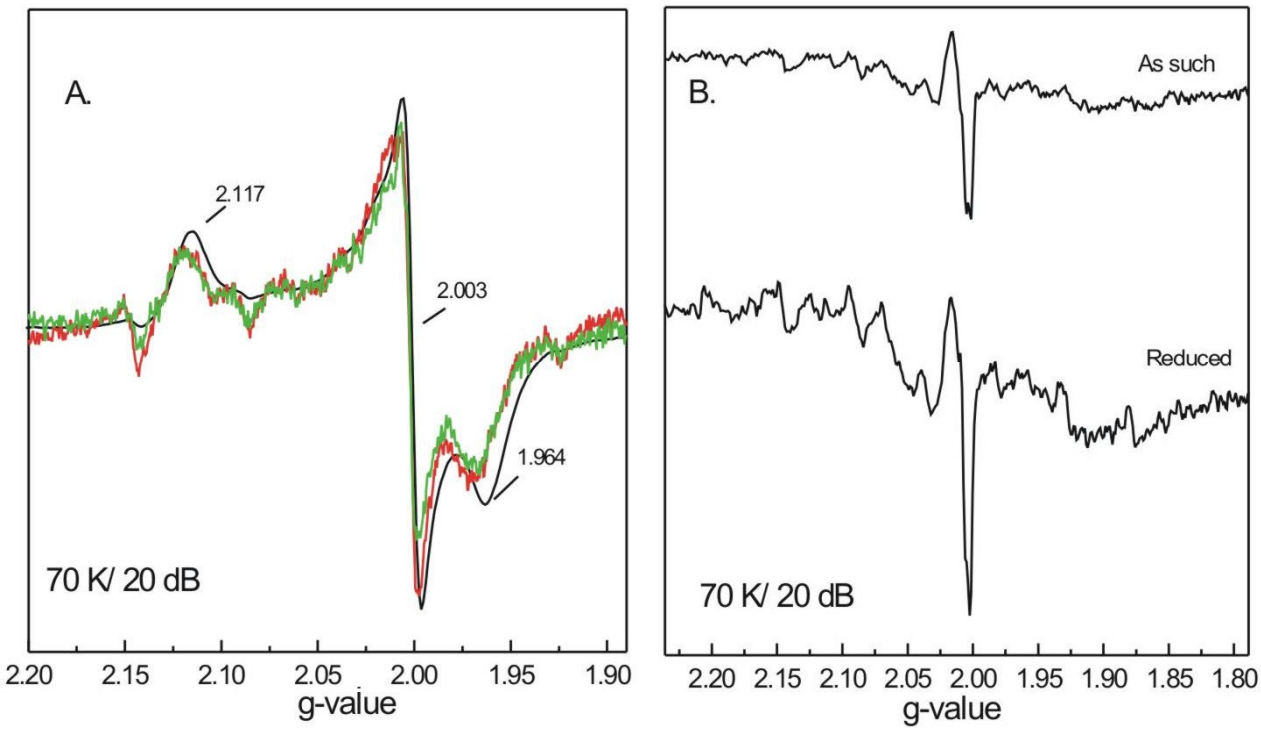

Figure 2.36: (A) Reduced E126Q IspH from *A. aeolicus* incubated with HMBPP (black), IPP (red) and DMAPP (green). (B) as-such and dithionite-reduced E126Q.
A sample containing 103 µM IspH (cluster concentration) and 33 mM dithionite was incubated for 30 s with 3 mM of IPP or DMAPP in a final volume of 300 µl. Multiple turnover spectra for reduced E126Q in the presence of HMBPP incubated for 6 min was used for comparison.

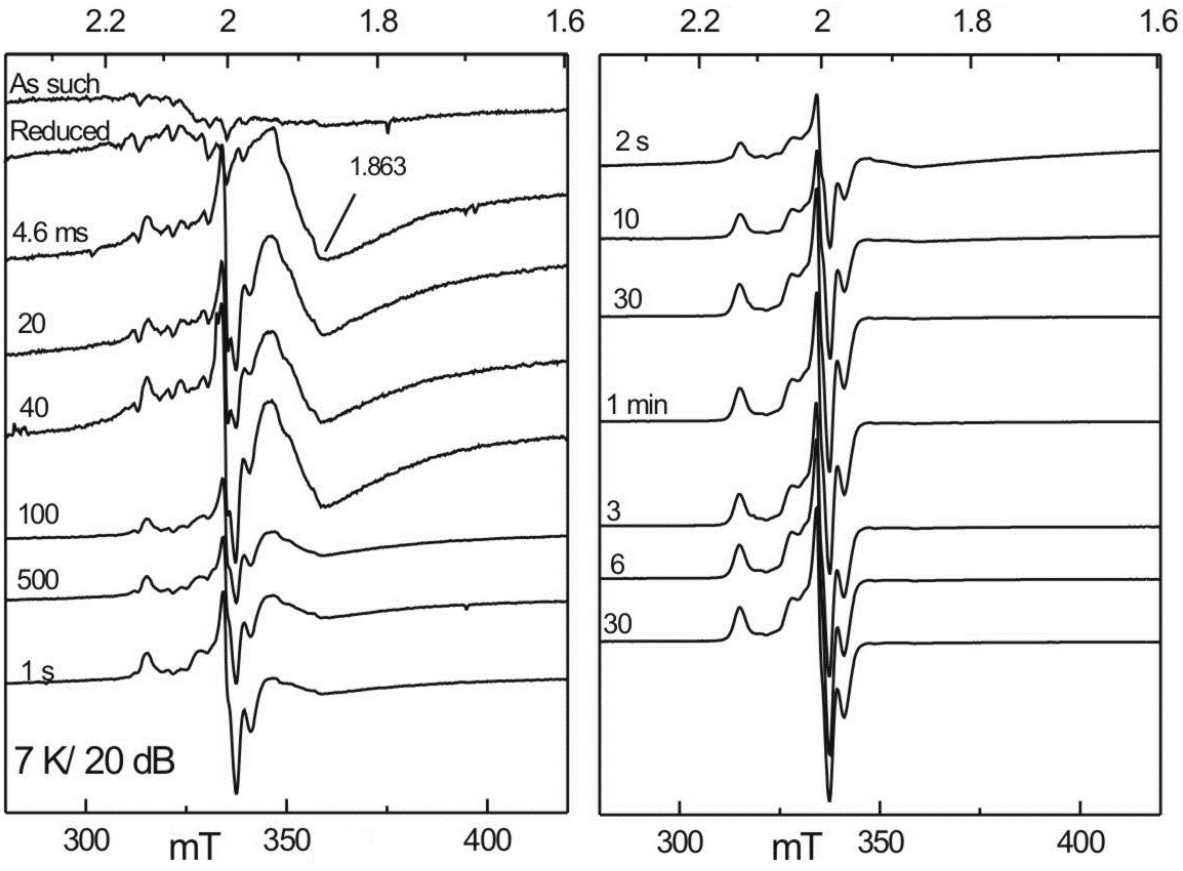

Figure 2.37: Multiple turnover rapid-freeze-quench EPR experiment for E126Q IspH from *A. aeolicus* at 7 K.

IV. Overview of EPR active species in A. aeolicus

For easy comparison all the signal intensities were estimated and plots of signal intensity vs. time can be found in **Figure 2.38**. In the WT enzyme the intensity of the $[4Fe\text{-}4S]^{+}$ signal is close to 0 at 4.6 ms, and most of the FeS-I species is already present. Since it is impossible to get the signal intensity for the FeS-I species we set the intensity to the same amount as was found for the *E. coli* enzyme. This is done to at least get an idea of the trends of the signal development and disappearance. These trends are the same as found for WT enzyme, the plots confirm the trend that in WT enzyme the $[4Fe\text{-}4S]^{+}$ signal is lost quickly. At the same time the FeS-I species develops. Most likely we are detecting the fast binding of the substrate to the cluster and the concomitant change in redox state from 1+ to 3+. At the end of the reaction the $[4Fe\text{-}4S]^{+}$ cluster signal comes back and a product-$[4Fe\text{-}4S]^{+}$ species is detected. The ratio of the 2 is probably determined by the dissociation constants of the enzyme for the products. For the E126Q mutant a different behavior is observed. It appears as if the $[4Fe\text{-}4S]^{+}$ signal is slowly converted into the FeS-III species in the multi-turnover experiment **(Fig 2.38D)**. We do not have the $[4Fe\text{-}4S]^{+}$ data for the single-turn-over experiment **(Fig 2.38C)**.

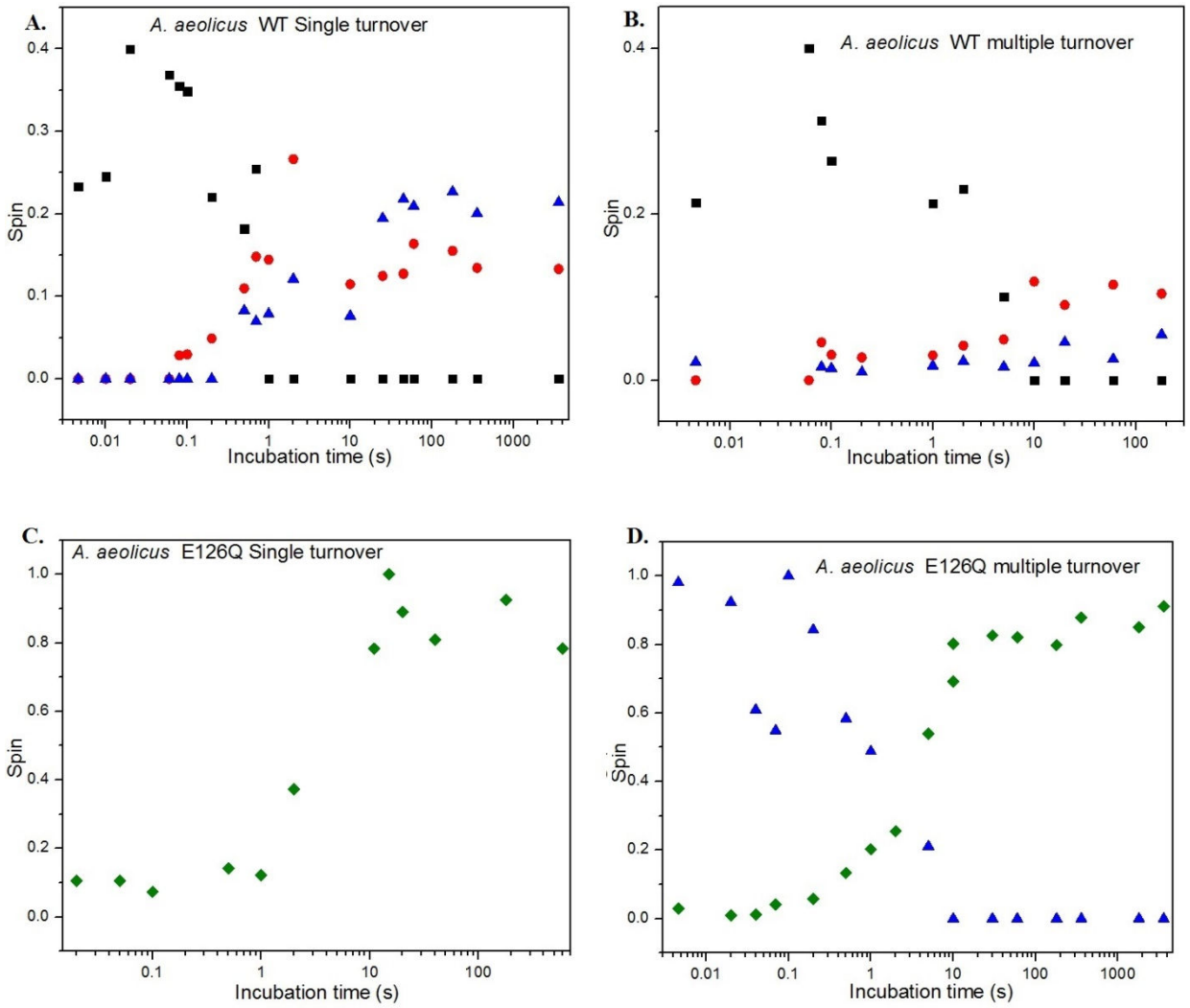

Figure 2.38: Overview of spin intensity of paramagnetic species in freeze-quench studies with WT and E126Q IspH from *A. aeolicus*.
Black squares are WT intermediate signal, FeS-I. The red circles are WT product signal (FeS-II), blue triangles are reduced $[4Fe\text{-}4S]^{+}$ cluster and the green diamonds for E126Q species, FeS-III.

2.3.5 Redox titration

In the redox titration of wild type IspH from *E. coil*, as expected, the EPR signal for a $[4Fe\text{-}4S]^{+}$ cluster with g values of 2.039 and 1.893 was detected throughout the measured redox potential range **(Fig 2.39)**. The EPR signal is sharp and most intense at -540 mV. A decrease in intensity as well as signal broadening was observed with an increase in potential. The estimated midpoint potential of the cluster center was -541.95 mV **(Fig 40)**. Besides the $[4Fe\text{-}4S]^{+}$ EPR signal the sample showed a radical signal around g = 2. This feature is due to the presence of benzyl viologen and methyl viologen, dye mediators, which show a radical signal in the lower potential range. The oxidation-reduction of the process was fully reversible (not shown).

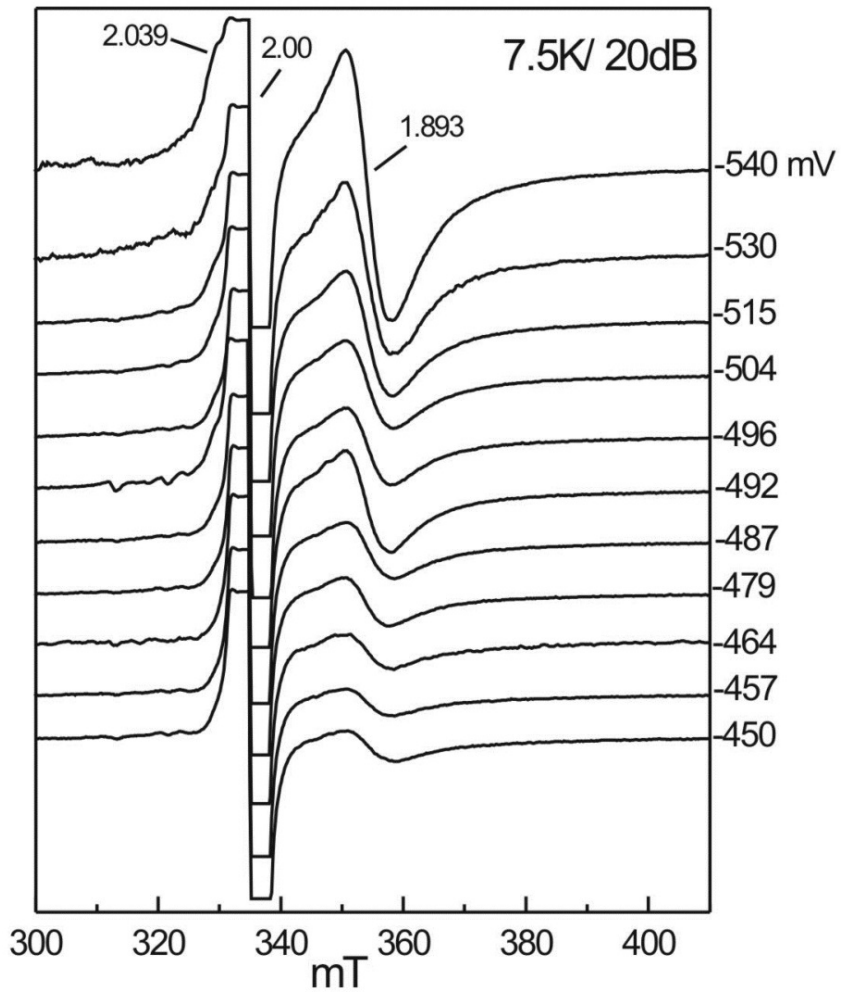

Figure 2.39: Spectra of the EPR-monitored redox titration of IspH from *E. coli*.

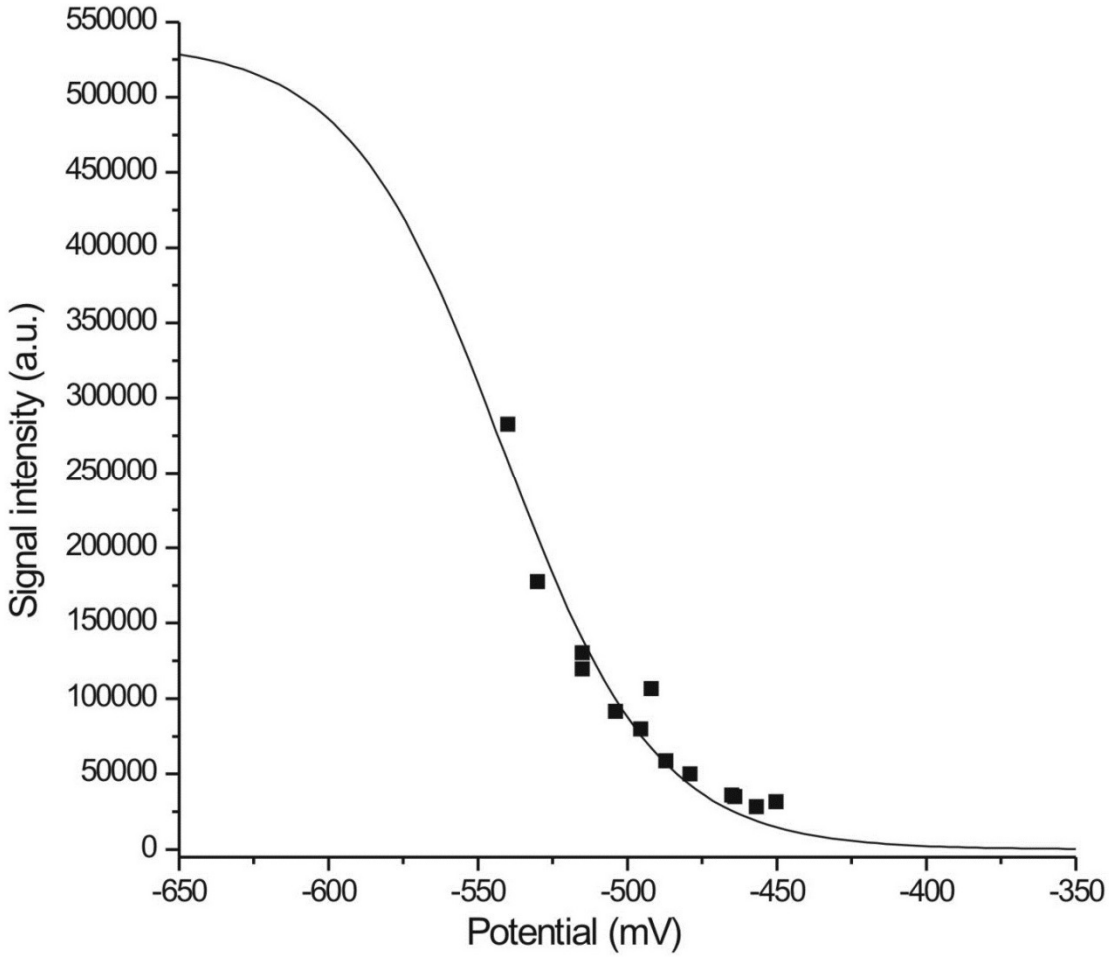

Figure 2.40: EPR-monitored redox titration curve for IspH from *E. coli*.
Data points correspond to the amplitude of the trough centered at g = 1.893. The solid line is a Nernst plot, n = 1 with E_m = -541.95 mV. Height (h) in equation (15) was left open during the fitting process.

2.3.6 ENDOR

To determine the identity and property of the [4Fe-4S] cluster-based intermediate trapped when one-electron-reduced IspH from *E. coli, A. aeolicus* and *P. falciparum* was incubated with HMBPP, ^{57}Fe-ENDOR was employed. ^{57}Fe-pulsed Davies ENDOR spectra of ^{57}Fe-labeled IspH (*P. falciparum*) were recorded at the canonical orientations of the g tensors in the EPR line **(Fig 2.41)**. The intermediate, FeS-I, ENDOR signal taken at a field corresponding to g_1 showed eight resolved peaks which correspond to the $\nu_+/\ \nu_-$ pairs of the four ^{57}Fe ions of the cluster. The peaks were assigned to four doublets centered at A/2 with a Larmar splitting of 2ν = 3.15 MHz, which are labelled as $Fe_{1\text{-}4}$ in **Fig 2.42.** The hyperfine coupling constants for each Fe in the cluster are listed in **Table 2.6**. The values and signs of the hyperfine coupling constants are consistent with the hyperfine coupling constants for a $[4Fe\text{-}4S]^{3+}$ or a $[4Fe\text{-}4S]^{1+}$ cluster where the $Fe^{2.5+}/Fe^{2.5+}$ pair are negative and have large hyperfine coupling constants (Fe_3 and Fe_4). While the hyperfine coupling constants for the Fe^{3+}/Fe^{3+} pair are positive and smaller (Fe_1 and Fe_2). ENDOR samples for reduced E126Q incubated with HMBPP have not been analyzed yet.

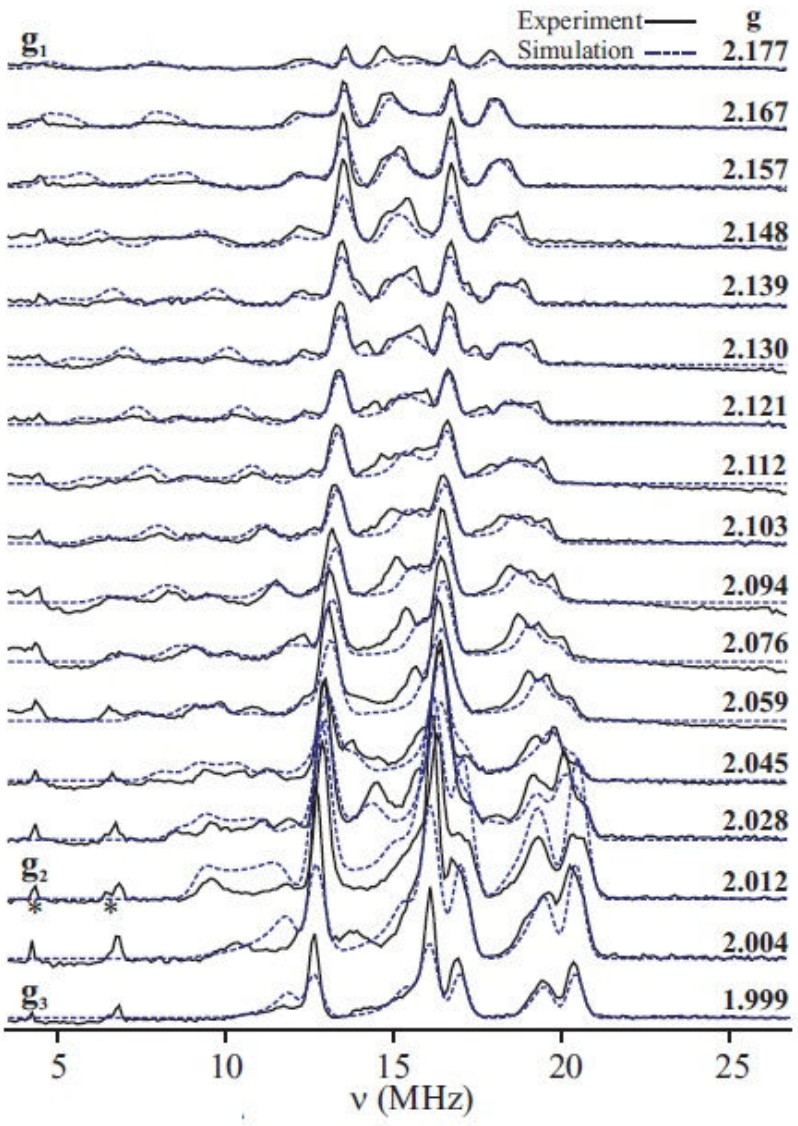

Figure 2.41: 35 GHz pulsed Davies ENDOR spectra of FeS-I at 2 K.
A sample containing 1.7 mM one-electron-reduced IspH and 33mM HMBPP was incubated for 25 s at RT before freezing. Data collected at the indicated g values (black), and simulations (blue, dashed). Conditions: microwave frequency 34.834 - 34.884 GHz, microwave pulse length 80 ns, τ = 800 ns, RF pulse length 20 μs, repetition rate 100 ms, 80 - 200 transients/point. Sample was prepared by Weiya Xu and data collected by Nicholas Lees.

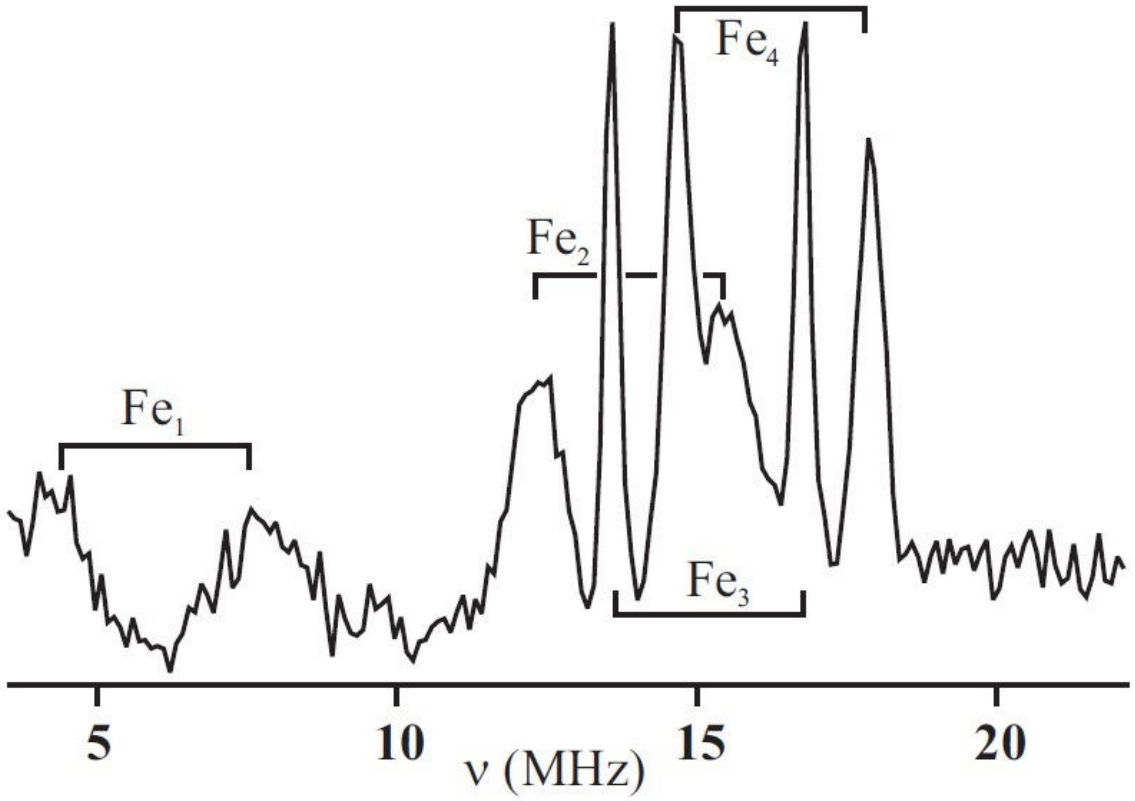

Figure 2.42: Pulsed Davies ENDOR spectra of FeS-I at g_1 and the individual Fe ions.

Table 2.6: ^{57}Fe Hyperfine coupling tensor for FeS-I intermediate.

Fe site	A_x (MHz)	A_y (MHz)	A_z (MHz)	A_{iso} (MHz)[a]
Fe_1 (Fe^{3+})	+ 12.0	+ 22.0	+ 27.5	+ 20.5
Fe_2 (Fe^{3+})	+ 30.3	+ 29.5	+ 28.5	+ 29.4
Fe_3 ($Fe^{2.5+}$)	- 27.0	- 35.0	- 36.0	- 32.7
Fe_4 ($Fe^{2.5+}$)	- 32.5	- 38.0	- 35.9	- 35.9

[a] Isotropic coupling were obtained as $A_{iso} = (A_x + A_y + A_z)/3$.

2.3.7 Mössbauer

To investigate the ground state electronic property of individual Fe sites within the cluster, ^{57}Fe-labeled IspH samples were prepared at different conditions and were assessed with Mössbauer spectroscopy. All the experimental data were simulated to deduce the components in the spectra. Zero-field Mössbauer spectra of an as-such IspH from *E. coli* indicated three distinct spectral components that have a relative area of 2:1:1 **(Fig 2.43 A-1)**. The major quadruple doublet, component in red, has an isomer shift δ = 0.45 mm/s and quadrupole splitting ΔE_Q = 1.23 mm/s which is characteristic for a tetrahedrally sulfur-coordinated valence-delocalized Fe^{2+}/Fe^{3+} ($Fe^{2.5+}$) pair. The isomer shift δ = 0.37 mm/s and the quadrupole splitting ΔE_Q = 0.94 mm/s for the blue labeled component are typical for a tetrahedrally sulfur-coordinated Fe and is representative of a high spin Fe^{3+} site. The quadruple doublet in green has δ = 0.90 mm/s and ΔE_Q = 1.93 mm/s which is characteristic for a high-spin Fe^{2+} ion that is bound to non-sulfur ligands, 3 N/O. The strong-field Mössbauer spectrum of the as-isolated IspH displayed a magnetic splitting that is only due to the applied magnetic field indicating that the cluster is diamagnetic **(Fig 2.43 A-2)**. Both the zero-field and high-field data indicate that the cluster is a diamagnetic (S = 0) $[4Fe\text{-}4S]^{2+}$ species. This observation is consistent with the absence of an EPR active species in the as-isolate IspH **(Fig 2.45 trace A**).

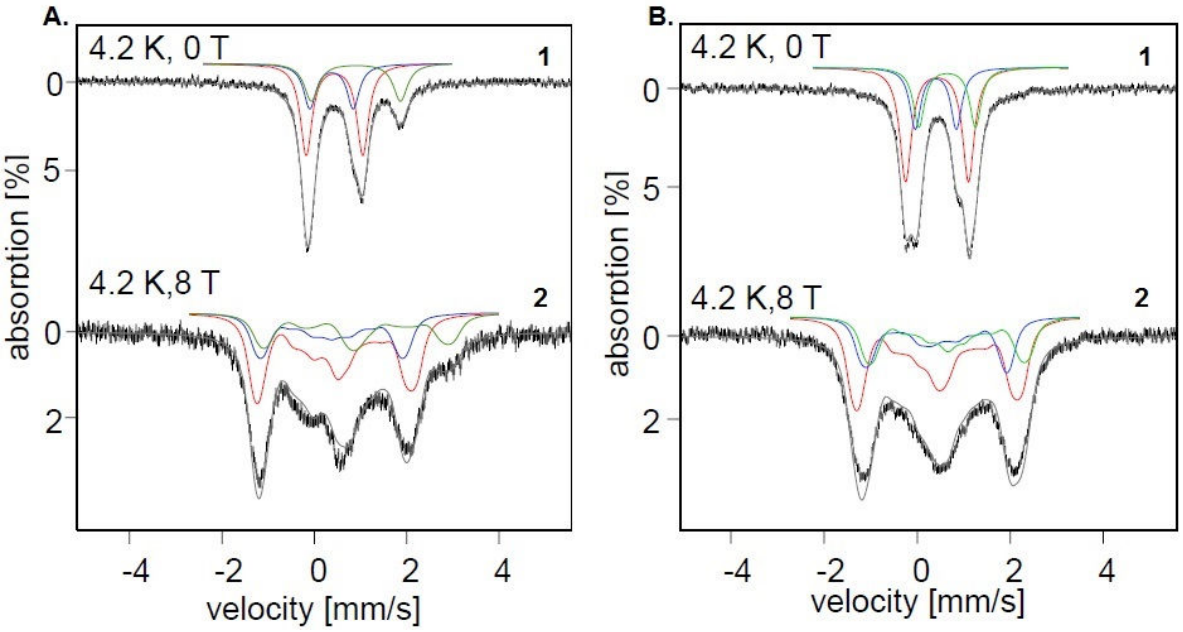

Figure 2.43: Variable-field Mössbauer spectra recorded at 4.2 K IspH from *E. coli*. (A) As-isolated (B) As-isolated incubated with HMBPP.

The hatched and solid gray traces are the experimental data and simulation respectively. Spectra in red, blue and green represent individual components $Fe^{2.5+}$ pair, Fe^{3+} and Fe^{2+} respectively. Enzyme (cluster) 1.04mM (A) and 0.98 mM (B) and HMBPP 8.1 mM. Data collected by Sebastian Stoian.

Incubation of the as-such IspH with HMBPP resulted in a Mössbauer spectrum that exhibited three distinct quadrupole doublets in zero-field **(Fig 2.43 B-1)**. The quantities for the $Fe^{2.5+}/Fe^{2.5+}$ pair (red spectra - δ = 0.45 mm/s and ΔE_Q = 1.35) and the valence-localized Fe^{3+} (blue spectra - δ = 0.38 mm/s and ΔE_Q = -0.88 mm/s) are similar to the values observed for the as-such enzyme. The third component of the spectrum (green spectra) has a quadrupole splitting similar to that of the as-such enzyme, ΔE_Q = 1.22 mm/s, whereas the isomer shift δ = 0.64 mm/s is lower. The change in the isomer shift is characteristic of a valence-trapped Fe^{2+} coordinated to a non-sulfur ligand, most likely the hydroxyl oxygen of HMBPP. The strong-field Mössbauer spectrum displayed magnetic splitting that is due to the applied magnetic field indicating that the cluster is diamagnetic **(Fig 2.43 B-2)**. Both the zero-field and high-field data indicate that the cluster is a diamagnetic (S = 0) $[4Fe\text{-}4S]^{2+}$ species.

Mössbauer spectroscopy analysis of dithionite-reduced ^{57}Fe enriched IspH showed two quadrupole doublets with an intensity ratio of 1:1 **(Fig 2.44)**. A valence-delocalized Fe^{2+}/Fe^{3+} pair (inner doublet) and a valence-localized Fe^{2+}/Fe^{2+} pair were detected. In the EPR sample that was made by reducing IspH with dithionite, in parallel to the Mössbauer sample, the $[4Fe\text{-}4S]^{+}$ signal was detected **(Fig 2.45 trace B**).

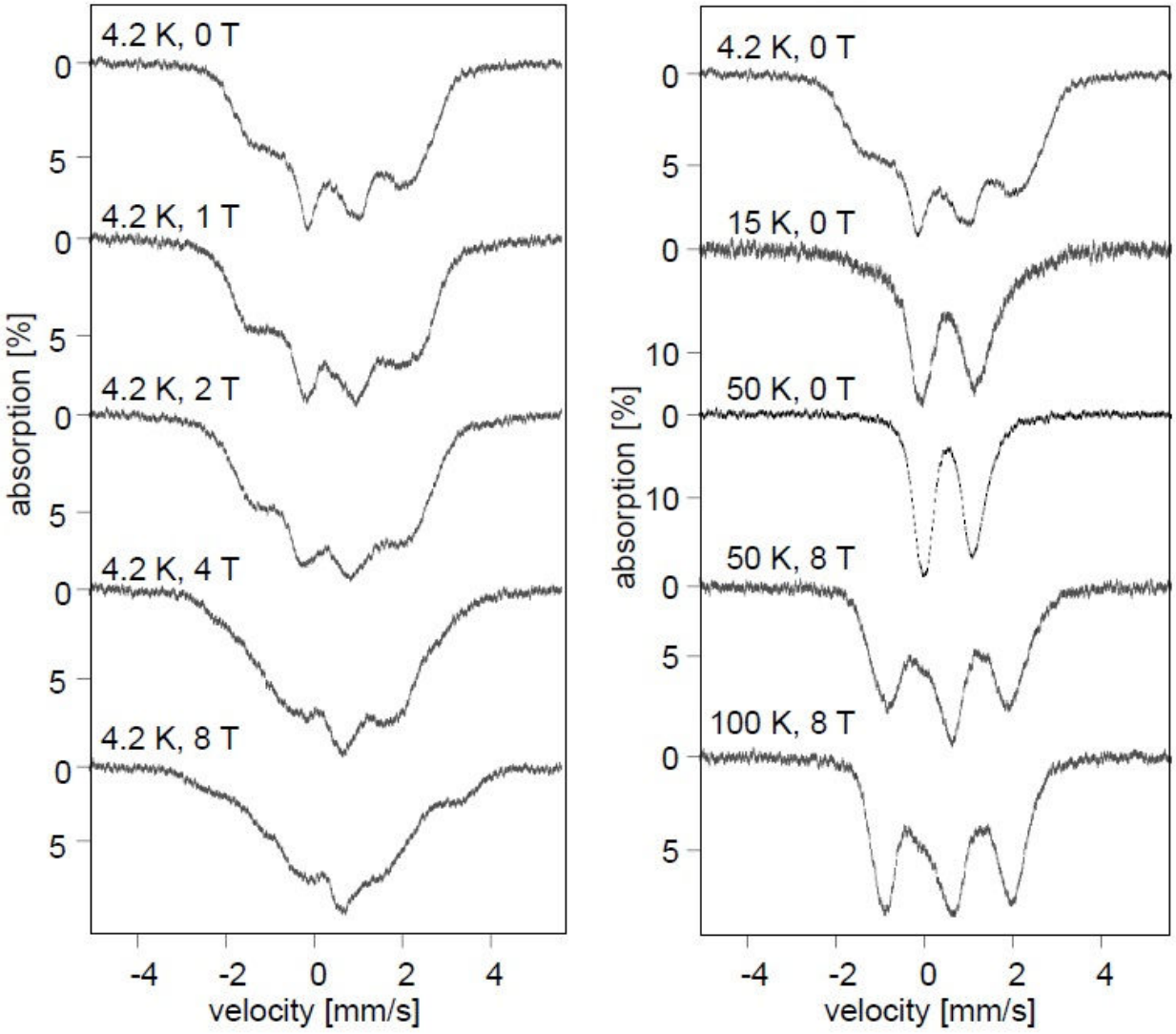

Figure 2.44: Field and temperature-dependent Mössbauer spectra recorded for the dithionite-reduced ^{57}Fe enriched IspH from *E. coli*.
Sample was prepared by incubating 2.6 mM enzyme (cluster) with 50 mM dithionite. Data collected by Sebastian Stoian.

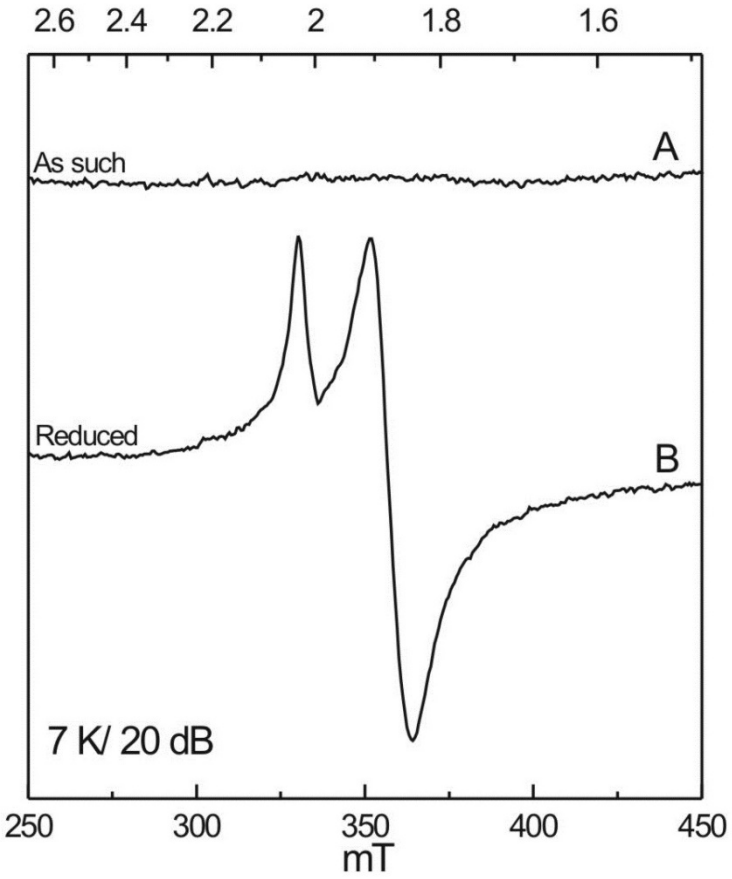

Figure 2.45: EPR spectra of (A) as-such and (B) dithionite-reduced IspH from *E. coli*. IspH (cluster) 110 μM and 22 mM dithionite.

To probe the HMBPP induced FeS-I intermediate, one-electron-reduced, ^{57}Fe-labeled, wild type enzyme (*E. coli*), was incubated with HMBPP for 30 s and the reaction was stopped by freezing the sample in liquid nitrogen. Field-dependent Mössbauer spectroscopy analysis at 4.2 K, showed that the sample contained two distinct spectra **(Fig 2.46)**. One component that is labeled in red accounts for 44% of the spectral area. This spectrum is similar to the one observed when the as-such IspH was incubated with HMBPP in which the cluster is a $[4Fe\text{-}4S]^{2+}$ with spin state S = 0. The second component, labeled in blue, accounts for 50% of the spectra. To determine the identity of the second spectra the zero-field Mössbauer spectra of the as-isolated enzyme in the presence of HMBPP (**Fig 2.47 trace B)** was subtracted from that of the one-electron-reduced IspH in the presence of HMBPP **(Fig 2.47 trace A**). The resulting spectra in **Fig 2.47 trace C** showed two spectral components with an intensity ratio of 1:1. The component shown in red was assigned to a valence-localized Fe^{3+}/Fe^{3+} ion pair with isomer shift δ = 0.36 mm/s and quadrupole splitting ΔE_Q = 0.75 mm/s. The blue component has an isomer shift δ = 0.45 mm/s and a quadrupole splitting ΔE_Q = 1.35 mm/s that is characteristic for a valence-delocalized, mixed valent Fe^{2+}/Fe^{3+} pairs. Field-dependent spectra of **trace C** displayed magnetic splitting due to both the internal and the applied magnetic field **(Fig 2.48)**. The magnetic hyperfine coupling constant, A, for the valence-delocalized $Fe^{2.5+}/Fe^{2.5+}$ pairs was calculated as A_x = -24 T, A_y = -24 T, A_z = -20 T. Whereas for the valence-trapped Fe^{3+}/Fe^{3+} pair the values were A_x = 24 T, A_y = 22 T, A_z = 20 T. The opposite signs of the hyperfine coupling constants indicate antiparallel alignment of the spins for the valence-delocalized and valence-localized pairs. Both the zero-field and the high-field data indicate a paramagnetic intermediate with a $[4Fe\text{-}4S]^{3+}$ cluster and spin state S = 1/2.

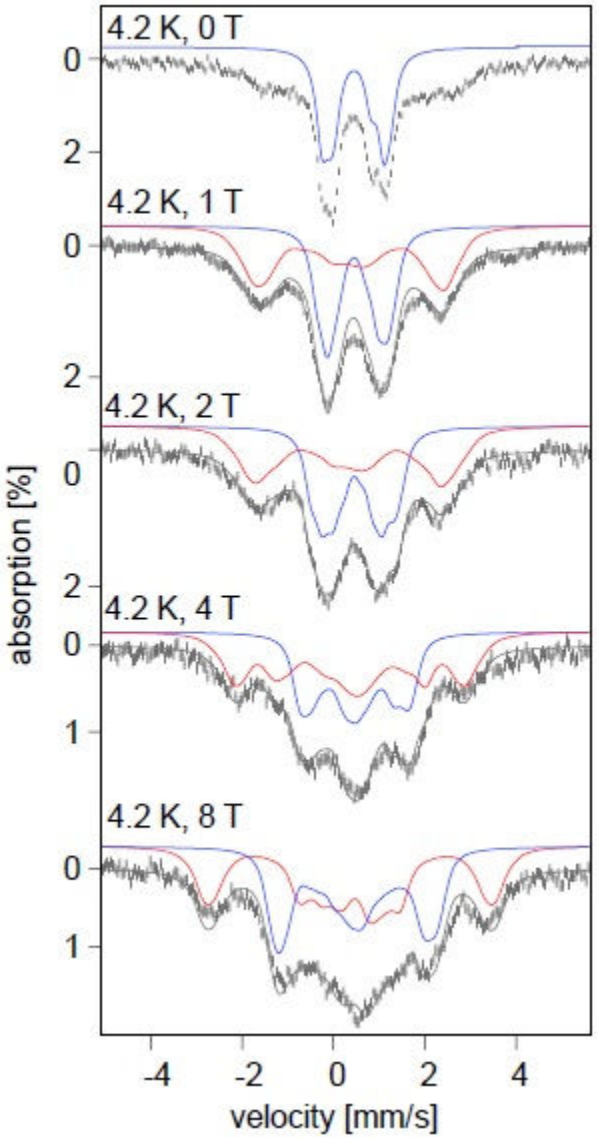

Figure 2.46: Field-dependent Mössbauer spectra of a one-electron reduced ^{57}Fe enriched *E. coli* IspH in the presence of HMBPP.
The hatched and solid gray lines are the experimental data and simulation respectively. Spectra in blue and red represent a substrate-bound $[4Fe\text{-}4S]^{2+}$ cluster and substrate-bound $[4Fe\text{-}4S]^{3+}$ intermediate respectively. Enzyme (cluster) 0.6 mM, dithionite 33 mM and HMBPP 8.1 mM. Data collected by Sebastian Stoian.

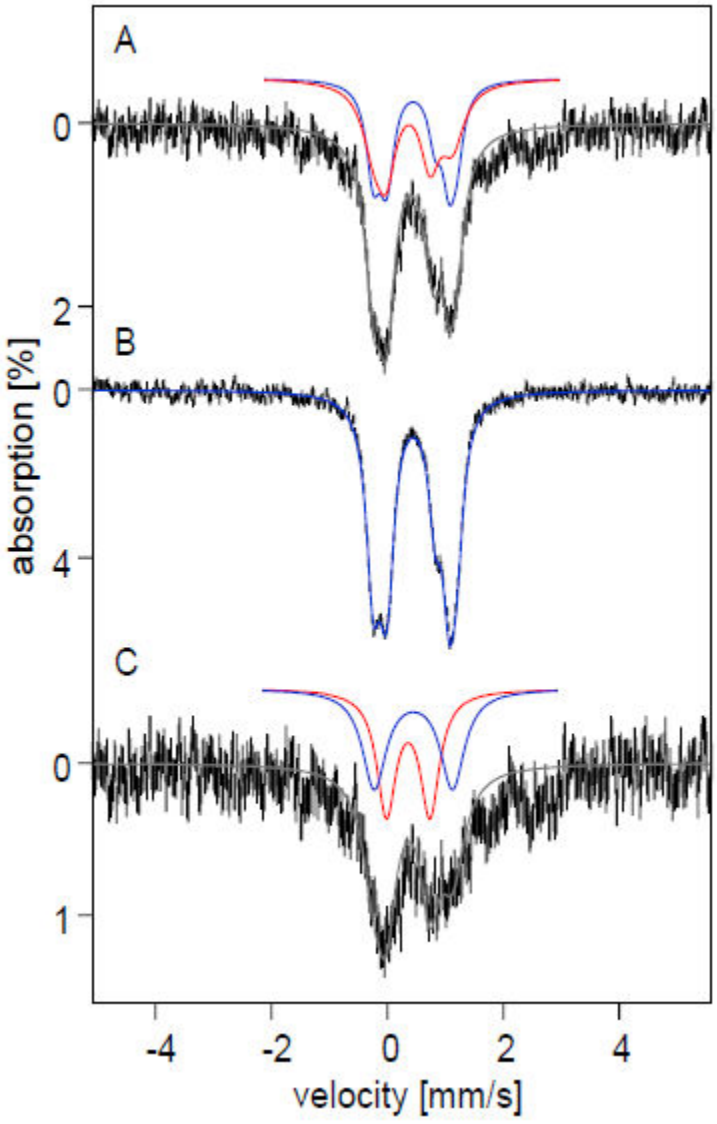

Figure 2.47: Zero-field Mössbauer spectra recorded at 150 K. (A) One-electron reduced IspH in the presence of HMBPP. (B) As-isolated IspH incubated with HMBPP. (C) Spectrum obtained by subtracting B from A.

The hatched black line and solid gray traces are the experimental data and simulation respectively. Spectra in blue and red represent individual components $Fe^{2.5+}$ pair and Fe^{3+} pair respectively (A and C). In spectrum B simulation is labeled in blue. Data collected by Sebastian Stoian.

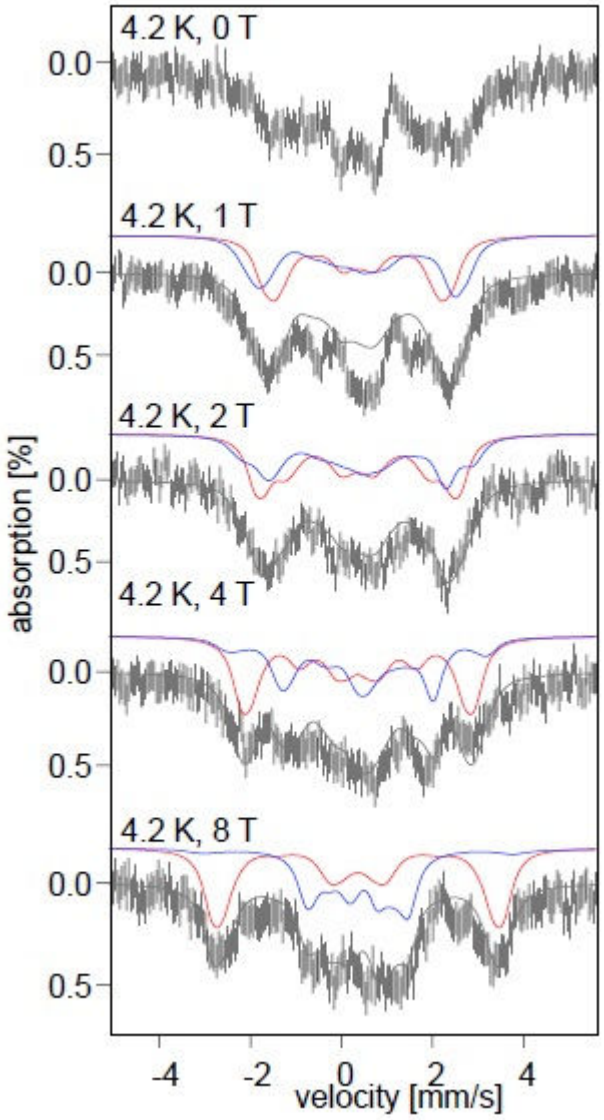

Figure 2.48: Field-dependent Mössbauer spectra of FeS-I.
The intermediate spectrum was obtained by subtracting spectra for the as-isolated enzyme in the presence of HMBPP that of the one-electron reduced enzyme in the presence of HMBPP. The hatched and solid gray lines represent the experimental data and the spectral simulation respectively. The blue and red spectra represent component contributions. Data collected by Sebastian Stoian.

Temperature based analysis of the paramagnetic $[4Fe\text{-}4S]^{3+}$ intermediate showed that the intermediate is slow relaxing and can be observed up to 180 K without broadening **(Fig 2.49)**. The EPR sample that was made in parallel to the Mössbauer sample showed the FeS-I EPR signal (data not shown).

The Mössbauer spectra for reduced WT IspH incubated with IPP and reduced E126Q with HMBPP have not been analyzed yet.

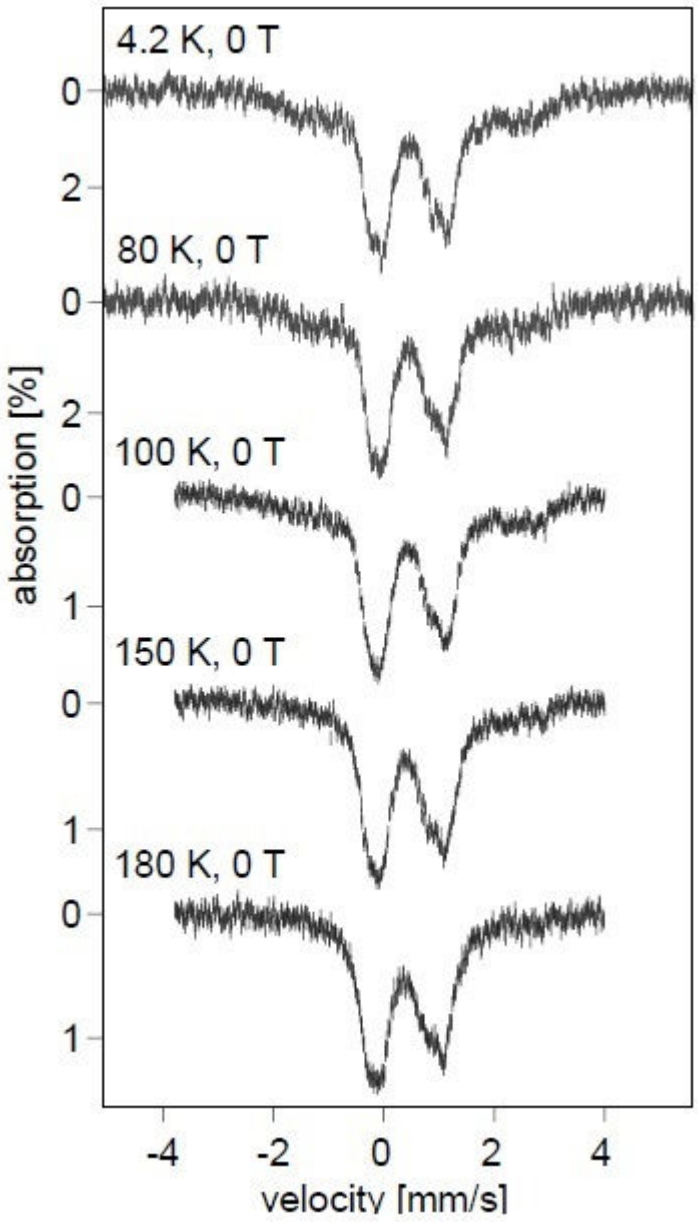

Figure 2.49: Temperature-dependent, zero-field ^{57}Fe Mössbauer spectra of FeS-I.
The intermediate was trapped when one-electron-reduced was incubated with HMBPP. Data collected by Sebastian Stoian.

2.4 Discussion and Conclusion

2.4.1 The [4Fe-4S] cluster in wild type IspH

IspH contains a single [4Fe-4S] cluster in the active site, whose electronic properties change depending on the active site environment such as the presence of a reductant, an oxidant, substrates and/or products. In the EPR analysis of the as-isolated IspH no paramagnetic species was detected, indicative for the presence of a $[4Fe\text{-}4S]^{2+}$ cluster and the absence of a $[3Fe\text{-}4S]^{+}$ cluster **(Fig 2.45)**. The Mössbauer data for the as-isolated enzyme also corroborates this observation. Conventional $[4Fe\text{-}4S]^{2+}$ clusters exhibit two overlapping equal intensity doublets with δ = 0.40-0.45 mm/s and ΔE_Q = 1.0-1.2 mm/s that are indicative of two valence-delocalized $Fe^{2.5+}/Fe^{2.5+}$ pairs and all Fe ions are coordinated by sulfur ions in a tetrahedral orientation (77). In IspH, however, three distinct Fe sites were identified **(Table 2.7)**, a valence-delocalized $Fe^{2.5+}/Fe^{2.5+}$ pair, an Fe^{2+} site, and an Fe^{3+} site. The parameters for both the $Fe^{2.5+}$ and the Fe^{3+} sites are within the ranges observed for tetrahedrally sulfur-coordinated Fe sites. On the other hand the large isomer shift for the Fe^{2+} is indicative of the presence of a unique Fe ion with an atypical coordination environment, most likely due to the presence of a fourth non-sulfur ligand. There have been reports on the presence of such unique Fe^{2+} iron sites in other $[4Fe\text{-}4S]^{2+}$ clusters. In aconitase (**section 1.3.2.1**) a 6-fold coordination of the unique Fe ion with 3S and 3O atoms from a carboxylate and a hydroxyl group of the citrate/cis-aconitate/isocitrate and a water molecule resulted in an isomer shift of 0.84-0.89 mm/s (76). Another unique iron with an unusual coordination environment, a total of 5 S atoms was observed in ferredoxin:thioredoxin reductase (FTR) (**section 1.3.2.2**) (82). In IspH the identity of the fourth ligand still remains to be determined.

Mössbauer spectroscopy analysis of the as-isolated IspH incubated with HMBPP showed the cluster to be a $[4Fe\text{-}4S]^{2+}$ with a valence-delocalized $Fe^{2.5+}/Fe^{2.5+}$ pair and a valence-localized Fe^{3+} site with parameters identical to those observed in the as-such enzyme. On the other hand the isomer shift for the unique valence-localized Fe^{2+} has decreased, but still larger than the typical Fe^{2+} isomer shift **(Table 2.7)**. The alteration in the isomer shift is due to a change in the coordination environment of the Fe^{2+} ion in the presence of HMBPP. Cocrystallization of the as-isolated *E. coli* IspH with HMBPP showed the coordination of the hydroxyl oxygen of the substrate to the unique Fe of the [4Fe-4S] cluster (110).

Rapid-freeze-quench experiments were performed to trap and analyze EPR active reaction intermediates during the conversion of HMBPP into IPP and DMAPP by the catalytic action of IspH. Time-dependent studies on wild type IspH from *E. coli* and *A. aeolicus* under single turnover and multiple turnover conditions revealed the presence of two paramagnetic species. In *E. coli*, the first transient intermediate trapped at 70 K resembles the paramagnetic species that was observed when one-electron-reduced IspH was incubated with HMBPP, which we denoted FeS-I. The species is a near-axial low spin (S = 1/2) signal with g values of 2.176, 2.008 and 2.00. Similar signals were detected in FTR and IspG (another DOXP pathway enzyme). The observed average of the g values is greater than g_e, 2.0023, which is similar to the value observed in oxidized high-potential iron-sulfur proteins (HiPIPs) with a $[4Fe\text{-}4S]^{3+}$ cluster. The third enzyme that has been proposed to incorporate the HiPIP-like paramagnetic species in its catalytic action is heterodisulfide reductase (Hdr). The g values (2.013, 1.993 and 1.938) of the signal are slightly different than the other enzymes and the observed average of the g values is less than g_e (80, 83, 87, 131). On the other hand the EPR active intermediate that was trapped in *A. aeolicus* was a high spin (S = 3/2) species with two visible g values of 4.668 and 3.384

which was only detected at lower temperature, 7 K.

Both ENDOR and Mössbauer spectroscopy have been used to assess the ground state electronic properties of intermediate FeS-I. ENDOR spectroscopy investigations of ^{57}Fe enriched FeS-I intermediate from *P. falciparum* showed large negative hyperfine coupling constants (A_{iso}) representative of an $Fe^{2.5+}/Fe^{2.5+}$ pair and a smaller and positive A_{iso} value consistent with a valence-localized Fe^{3+}/Fe^{3+} pair. The hyperfine coupling constant are comparable to the values observed for a HiPIP-like $[4Fe\text{-}4S]^{3+}$ cluster in FTR and Hdr as well as in typical HiPIPs and model systems with $[4Fe\text{-}4S]^{3+}$ S = 1/2 cluster (132, 133). The anisotropy of the hyperfine tensors ($\Delta A = A_{max} - A_{min}$) could be used to differentiate the unique Fe ion from the typical Fe ion, in which a large anisotropy will be expected for the unique Fe due to distortion of the coordination environment. As reported in **Table 2.6,** the anisotropy of Fe_1 is ΔA = 15.5 MHz and 1.8 MHz for Fe_2, indicating that Fe_1 is proximal to the substrate. Mössbauer spectroscopy analysis of the FeS-I intermediate from *E. coli* **(Table 2.7)** showed valence-delocalized $Fe^{2.5+}/Fe^{2.5+}$ pairs and valence-localized Fe^{3+}/Fe^{3+} pairs, whose hyperfine coupling constant magnitude and sign are comparable to those observed for a $[4Fe\text{-}4S]^{3+}$ cluster in HiPIPs as well as FTR. In IspH the two Fe^{3+} ions are indistinguishable. In FTR, however, the hyperfine coupling constant for the two ferric ions are different, in which the unique Fe^{3+} ion with distorted ligation environment has a pronounced anisotropy (82).

The second intermediate, that was detected during catalysis is a slightly rhombic high spin (S = 1/2) signal with g values of 2.080, 2.006 and 1.991 and was observed in both *E. coli* and *A. aeolicus.* This paramagnetic signal, which we are designating as FeS-II, was also detected when dithionite-reduced IspH from *E. coli* was incubated with IPP or DMAPP. We are proposing that this signal represents the rebinding of the products to the reduced cluster, or

Table 2.7: Mössbauer parameters of wild type IspH from *E. coli.*

Cluster	S		Site	δ (mm/s)	ΔE_Q (mm/s)	A_x (T)	A_y (T)	A_z (T)	Rel. area
Substrate-free $[4Fe\text{-}4S]^{2+}$	0	a	$[Fe^{2.5+}]_2$	0.44	1.23	n.a.			2
		b	Fe^{2+}	0.90	1.93				1
		c	Fe^{3+}	0.37	0.94				1
Substrate-bound $[4Fe\text{-}4S]^{2+}$	0	a	$[Fe^{2.5+}]_2$	0.43	1.35	n.a.			2
		b	Fe^{2+}	0.64	1.22				1
		c	Fe^{3+}	0.38	-0.88				1
FeS-I intermediate $[4Fe\text{-}4S]^{3+}$	1/2	a	$[Fe^{2.5+}]_2$	0.43	1.35	-24	-24	-20	1
		b	$[Fe^{3+}]_2$	0.36	0.75	+22	+22	+20	1
Dithionite-reduced $[4Fe\text{-}4S]^{1+}$	1/2	a	$[Fe^{2.5+}]_2$	t.b.d.					1
		b	$[Fe^{2+}]_2$						1

n.a. = not available
t.b.d. = to be determined

dependent how you look at it, product still bound to the cluster.

In the freeze-quench experiment we can distinguish two steps. First the substrate binds to the $[4Fe\text{-}4S]^{+}$ cluster, converting it into a $[4Fe\text{-}4S]^{3+}$-intermediate species. This step is fast in *A. aeolicus*, and most of it is already done within 4.6 ms. In the second step the product is formed and the cluster is reduced to the 1+ state. It is not clear if the product is first released and then rebinds or whether the cluster-product complex gets reduced after the reaction is completed. In both enzymes this appears to be a direct transformation where FeS-I converts into FeS-II and no obvious delays can be detected.

IspH is involved in a two one-electron step reductive dehydration of HMBPP and the active site [4Fe-4S] cluster is involved in electron transfer. The cluster would in theory only transfer one electron at-a-time. Therefore, during catalysis, transfer of the first electron from the cluster to the substrate will result in the formation of a substrate based radical. In a radical-type mechanism, the phosphate group would be a better leaving group, instead of the hydroxyl group of HMBPP. The formation of a radical can be avoided by the internal transfer of two electrons from the cluster to the substrate, resulting in a $[4Fe\text{-}4S]^{3+}$ cluster. In FTR, Hdr and IspG, this is achieved by binding of cluster to the substrate or a reaction intermediate. Spectroscopy studies (EPR, ENDOR and Mössbauer) strongly indicated the formation of an intermediate in IspH similar to the HiPIP-like $[4Fe\text{-}4S]^{3+}$ species that was detected in FTR. In FTR there is direct binding of the substrate to the cluster. Even though the HYSCORE spectrum of WT IspH incubated with [4-^{17}O]-HMBPP has shown the absence of bonding between the cluster and hydroxyl group of the substrate, the exact binding mode of the cluster to the substrate has not been established. Side-on π-interaction of the unique Fe to HMBPP has been proposed based on the ENDOR spectroscopy studies of E126A IspH incubated with [U-^{13}C]-HMBPP (114). Recent

DFT calculations performed on WT IspH in the presence of HMBPP, have shown that the one electron reduced [4Fe-4S] cluster preferably interacts with the HMBPP double bond forming an η^2 complex (134). Further experimental ENDOR studies of the FeS-I intermediate using ^{13}C-labeled HMBPP are needed to confirm this binding mode.

2.4.2 Active site amino acid residues

In the crystal structure of *E. coli* IspH incubated with HMBPP, conserved amino acids in the active site such as E126, H124 and T167 form a network of hydrogen-bonds with the substrate. Site-directed mutagenesis coupled with kinetic assays and spectroscopic studies have been employed to investigate the effect of the mutations on IspH activity, on the iron-sulfur cluster and on the reaction intermediate, which will be instrumental in deducing the role of the residues in catalysis.

In EPR-monitored rapid-freeze-quench experiments with mutant IspH (H124F, E126Q and T167C) similar and additional paramagnetic intermediates were observed. When reduced H124F *(A. aeolicus)* and T167C (*E. coli)* IspH were incubated with HMBPP, two EPR active intermediates are detected that are similar to the species detected in WT enzymes. This is in line with the fact that both these mutants were active, albeit with lower catalytic activity. In the hypothetical mechanism II **(Fig 2.9)** T167 was the proposed proton donor for the dehydration of HMBPP. The kinetic and spectroscopic analyzes shows otherwise. With the T167 gone, E126 would take over as the direct hydrogen donor. The hydroxyl group of Thr doesn't have the pKa in the range, whereas the carboxyl side chain of Glu has a pKa of 4.25 (can be a bit higher). Most likely the hydrogen comes from water and Glu and Thr are just passing the hydrogen along. We are proposing that T167 is involved in the proper orientation of HMBPP during catalysis.

Likewise the work of Wieya Xu showed that the H124 is important in the correct orientation of the substrate.

The E126Q mutant (from both organisms) on the other hand, has no activity and a paramagnetic species (designated FeS-III) can be detected that is different from the EPR active species in the WT enzyme. The FeS-III species was also detected in the as-isolated as well as the dithionite-reduced E126Q mutant IspH from *E. coli*. The fact that this signal is trapped in the dithionite-reduced enzyme would indicate it is a $[4Fe\text{-}4S]^{+}$ cluster-based signal. When dithionite-reduced E126Q IspH was incubated with IPP or DMAPP, the same signal was observed. The RFQ data that is available indicates a clean conversion of the $[4Fe\text{-}4S]^{+}$ species into the $[4Fe\text{-}4S]^{+}$-substrate species without the intermediate formation of other paramagnetic or diamagnetic species. Another group has reported a paramagnetic species that resembles the product bound cluster in WT IspH (FeS-II), when dithionite-reduced E126Q IspH was incubated with IPP (113). The FeS-III species detected in the E126Q mutant is considered a reaction intermediate by several groups and several hypothetical mechanisms are based on the electronic and magnetic properties of this species. Our freeze-quench data for the IspH from both *E. coli* and *A. aeolicus*, however, shows that this species appears after the FeS-I species **(Fig 2.26** and **2.38**) and not before as proposed in the hypothetical reaction mechanism (**Fig. 2.10**). The competence of an intermediate in a reaction mechanism can be assessed by determining the individual rate constants of the reaction steps. For FeS-III species to be a catalytically relevant intermediate, its rate of formation should be faster than or as fast as the FeS-I and FeS-II species. The oxidation of the $[4Fe\text{-}4S]^{+}$ cluster is very slow in this mutant. This result would suggest that the E126, besides the proposed dehydration of HMBPP, it might also be involved in the binding of the substrate. Mutation of this residue might change the active site structure. When the His42 residue

in *A. aeolicus* was mutated into an Ala residue all activity was lost. Up to 55% of the activity, however, was still detectable in the H42F mutant showing that the position of the His residue was probably important to keep the active site structure intact and the Phe residue could save most of the activity without providing the H-bond to the substrate phosphate group. The superimposition of the crystal structure of WT and E126Q mutant IspH cocrystallized with HMBPP, however, shows no obvious changes in the local structure. Therefore the Glu126 must be involved in more than the protonation step and must also play a role in the successful binding to or close to the [4Fe-4S] cluster.

2.4.3 Proposed reaction mechanism

For the reductive dehydration of HMBPP two electrons are needed. The [4Fe-4S] cluster in IspH can transfer only one electron at a time, hence a radical intermediate would be expected in the reaction mechanism. The data from the rapid-freeze-quench study of IspH from both *E. coli* and *A. aeolicus* under turn over conditions didn't show the formation of a stable radical. Reduced ^{57}Fe-labeled WT IspH from *E. coli* when incubated with HMBPP as well as IPP showed broadening of the paramagnetic species. ^{57}Fe-labeled E126Q incubated with HMBPP also showed significant broadening of the FeS-III species. In addition, it has been reported that ENDOR investigations of E126A IspH incubated with [U-^{13}C] HMBPP didn't show the large hyperfine coupling expected for a radical substrate (113). The spectroscopic data suggest all the signals in WT and mutant IspH are Fe-S cluster-based and not radical-based. It is possible that the electron is very short-lived and cannot be detected by the technique used here. However, the mechanisms that incorporate substrate-base radical (proposed mechanism I and II **Fig 2.8** and **Fig 2.9**) predict that these would be relatively stable. The absence in our freeze-quench runs would indicate that the mechanisms are probably not correct.

The third hypothetical reaction mechanism for IspH **(Fig 2.8)** is based on the electronic and magnetic properties of the FeS-III species detected in the E126Q mutant, which is considered a reaction intermediate. Our freeze-quench data, however, shows that this species appears much later in the reaction than both the FeS-I and FeS-II species which makes the catalytic relevance of this species questionable. Although the kinetic data obtained here does not argue against the current reaction mechanism there is the real concern that some aspects are based on the properties of the FeS-III species detected in the E126Q mutant and not on the properties of the true reaction intermediate FeS-I. This species from the WT enzyme needs to be further studied, particular using ENDOR studies of IspH incubated with ^{13}C-labeled HMBPP.

CHAPTER 3 : HdrA, subunit of Hetrodisulfide reductase

3.1 Introduction

3.1.1 Electron bifurcation

Electron bifurcation is an electron transfer process in which two electrons enter a system at a certain redox potential, one electron is transferred to an acceptor with low redox potential and the second electron is transferred to an acceptor with a high redox potential. These energetically challenging redox conversions don't involve ATP hydrolysis, instead the endergonic electron transfer is coupled with an exergonic transfer. For the electron transfers to proceed both the endergonic and the exergonic processes should occur almost simultaneously. Electron bifurcation is important in biological energy transduction. Enzyme complexes involved in electron bifurcation contain either quinone or flavin, 2-electron carrier cofactors (135).

The classic example of an electron bifurcation process is the Q-cycle, in complex III, of the electron transfer chain in mitochondria. In this system quinone ($E^{o'}$ = +110 mV) is the organic electron carrier and the bifurcating molecule. The endergonic reduction of cytochrome b_L ($E^{o'}$ = -20 mV) is coupled to the exergonic reduction of the Rieske [2Fe-2S] cluster ($E^{o'}$ = +290 mV). Of two electrons entering the Q-cycle, one electron flows through the Rieske cluster to cytochrome c. The second electron flows to cytochrome b_H via cytochrome b_L and eventually reduces another quinone molecule. Crystallographic data have shown conformational changes in the protein during the different stages of this process. It was reported that the Rieske cluster moves back and forward between its electron donor, QH_2, and its electron acceptor, cytochrome c, as it is reduced and oxidized. This movement prevents the transfer of the second electron to the Rieske cluster and instead it will be directed to the low potential cytochrome b_L (135, 136).

3.1.2 Flavin-based electron bifurcation

Flavin-based electron bifurcation was discovered recently in clostridia, an anaerobic bacterium (137). Electron bifurcation is one of the mechanisms through which energy is conserved in anaerobic bacteria and methanogenic archaea. Protein complexes involved in electron bifurcation contain at least one flavin, either FAD or FMN, and other redox active prosthetic groups. The enzyme complexes are composed of different subunits and it is proposed that the prosthetic groups, which are adjustable relative to each other, are strategically spaced between the electron donor and the electron acceptor in the subunits. The bifurcation process is crucial in the production of the reduced low potential ferredoxin that is essential for some processes in anaerobic organisms. Since the discovery of the flavin-based electron bifurcation, in 2008, a number of electron bifurcating protein complexes have been identified. Two of the protein complexes will be discuss in the next sections.

3.1.2.1 Electron transferring flavoprotein-butyryl-CoA dehydrogenase (Etf-Bcd) complex.

Etf-Bcd complex from clostridia was the first flavin-based electron bifurcating complex identified (137). It is involved in the coupled reduction of ferredoxin ($E^{o'}$ = -500 mV) and crotonyl-CoA ($E^{o'}$ = -10 mV) by NADH ($E^{o'}$ = -280 mV) **(Reaction 1)**. In Etf-Bcd complex FAD is the only cofactor present. It has been shown that the Etf is a heterodimer with two subunits, α and β, each housing one FAD: α-FAD and β-FAD respectively. The Bcd sub-complex is a homotetramer and contains one FAD (dehydrogenase FAD, Dh-FAD). β-FAD has been proposed as the site of electron bifurcation and the hydride acceptor from the NADH that is docked in its proximity. The ferredoxin and crotonyl-CoA are in close proximity to the β-FAD and the Dh-FAD respectively (138).

$$\text{Crotonyl-CoA} + 2\ \text{NADH} + \text{Fd}_{ox} \rightarrow \text{Butyryl-CoA} + 2\ \text{NAD}^+ + \text{Fd}_{red} \quad (1)$$

In the proposed mechanism of electron bifurcation, NADH binds to the β-subunit of Etf that is followed by two electron and a hydride transfer to β-FAD forming β-FADH$^-$ **(Fig 3.1)**. Subsequently one electron is transferred to the α-FAD resulting in the formation of α-FAD$^{-\bullet}$ and the unstable β-FADH$^\bullet$. After the first electron transfer there is a conformational change, bringing the α-subunit of Etf closer to Bcd and away from β-FAD. The electron is transferred from α-FAD$^{\bullet-}$ to Dh-FAD forming Dh-FADH$^\bullet$. The conformational change prevents the unstable β-FADH$^\bullet$ from donating the second electron to α-FAD$^{\bullet-}$ and instead the second electron is transferred to ferredoxin. This process is repeated, leading to a second reduced ferredoxin and butyryl-CoA, by hydride transfer from Dh-FADH to crotonyl-CoA. In the cell, the reduced ferredoxin is used to regenerate NADH in a reaction that involves the H^+/Na^+-pumping ferredoxin-NAD$^+$ reductase and ultimately produce ATP. In the proposed electron bifurcation mechanism the binding order has not been established experimentally (138). Recent work done by Carly Engle with just Etf showed that bifurcation indeed takes place when NADH is added. Both the unstable β-FADH$^\bullet$ and the stable α-FAD$^{\bullet-}$ could be detected within 5 msec

3.1.2.2 NADH-dependent reduced ferredoxin: NADP oxidoreductase (NfnAB) complex

NfnAB complex is a transhydrogenase found in various anaerobic bacteria and archaea. It catalyzes the coupled reversible ferredoxin ($E^{o'}$ = -500 mV) and NAD$^+$ ($E^{o'}$ = -280 mV) reductions by NADPH ($E^{o'}$ = -380 mV). In **Reaction 2** the reversible reaction is the electron bifurcating process. The complex has two subunits, NfnA that houses one FAD (a-FAD) and a [2Fe-2S] cluster and NfnB subunit housing a second FAD (b-FAD) and two [4Fe-4S] clusters. The proposed binding site for NAD(H) is NfnA whereas the NADP(H) is bound to NfnB. The b-

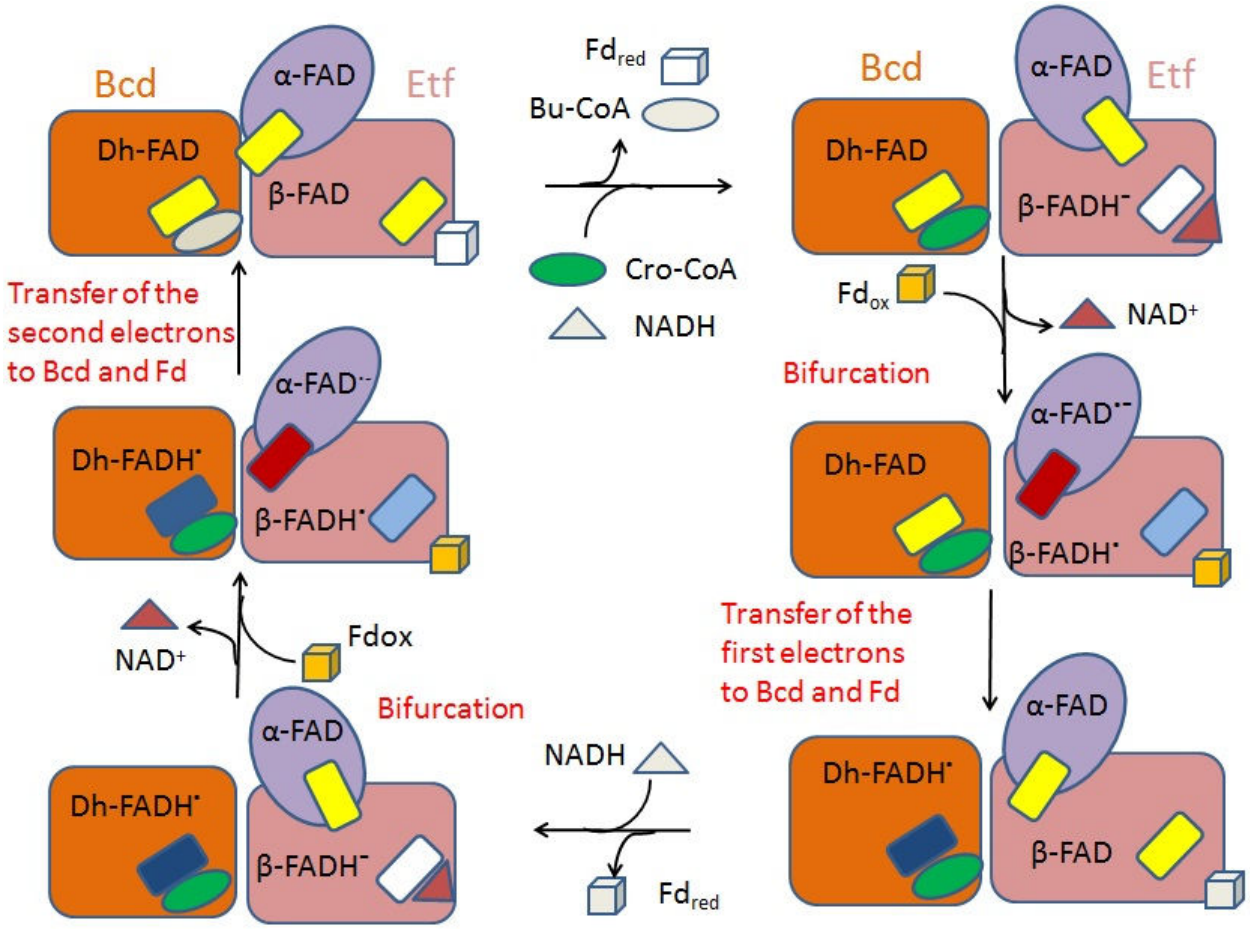

Figure 3.1: Proposed mechanism of electron bifurcation for the EtfBC-BcdA complex. FAD is represented with small rectangles, quinone is yellow, anionic semiquinone is red, neutral semiquinone is light blue (Etf) and dark blue (Bcd) and hydroquinone is white. Adapted from (138).

FAD is found in the center of the NfnAB complex and it has been proposed as the electron bifurcating site, serving as a 2-to-1 electron switch. It has been proposed that the ferredoxin docks on the NfnB subunit near the [4Fe-4S], that is the furthest from the b-FAD (139).

$$2NADPH + 2Fd_{ox} + NAD^{+} \rightleftharpoons 2NADP^{+} + 2Fd_{red} + NADH + H^{+} \quad (2)$$

In the proposed mechanism **(Fig 3.2)** a hydride and 2 electrons are transferred from NADPH to b-FAD, generating b-FADH^{-}. Subsequently one electron is transferred to a-FAD through the [2Fe-2S] cluster generating b-FADH$^{\bullet}$. The second electron from b-FADH$^{\bullet}$ is delivered to ferredoxin via the two [4Fe-4S] clusters in NfnB. This process is repeated in a second round affording a reduced NAD^{+} and a second Fd_{red}. It has been postulated that the transfer of the second electron to the high potential redox center is prevented by the rearrangement of the subunits/domain in the enzyme complex. The NADPH generated is consumed in the acetogenesis of CO_2 by the organism (139).

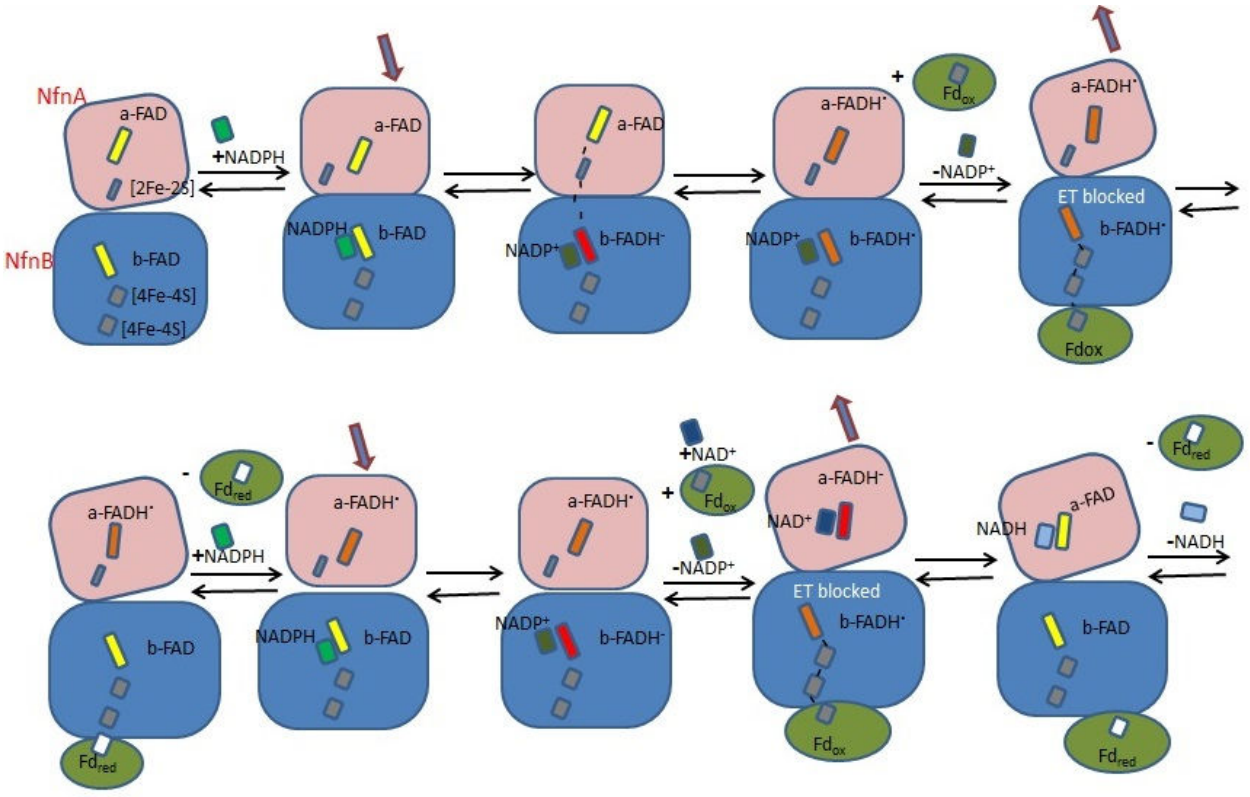

Figure 3.2: Proposed electron bifurcation mechanism for the NfnAB complex.
Adapted from (139).

3.2 Methyl viologen reducing hydrogenase/ heterodisulfide reductase (MvhADG/ HdrABC) complex

The MvhADG/HdrABC complex is a cytoplasmic enzyme complex in methanogenic archaea that catalyzes the coupled endergonic ferredoxin (E_o' = -500 mV) and exergonic CoM-S-S-CoB heterodisulfide ($E^{o'}$ = -140 mV) reductions by H_2 (E_o' = -414 mV) **(Reaction 3)**. The reduced ferredoxin is used in the first step of methanogenesis, the reduction of CO_2 to formyl-methanofuran. The thiol coenzymes enter the last step of methanogenesis and participate in methane synthesis and regeneration of the CoM-S-S-CoB heterodisulfide by the action of Methyl coenzyme M reductase (MCR) (140, 141).

$$2H_2 + Fd_{ox} + \text{CoM-S-S-CoB} \rightarrow 2H^+ + Fd_{red} + \text{CoM-SH} + \text{CoB-SH} \quad (3)$$

The protein complex is a highly oxygen sensitive heterohexamer composed of MvhA, MvhD, MvhG, HdrA, HdrB and HdrC subunits **(Fig 3.3)**. During purification the two components of the complex can be separated. MvhADG sub-complex is a **[**NiFe]-hydrogenase that catalyzes the reduction of methyl viologen by H_2. Sequence analysis has shown that the 51 kDa protein MvhA subunit houses the **[**NiFe] cluster, which is involved in H_2 oxidation. MvhD is the smallest subunit, 17 kDa, carrying a [2Fe-2S] cluster. Sequence analyses of some methanogens have shown the *mvhD* gene to be fused to the *hdrA* gene of the HdrABC sub-complex and it has been proposed that the cluster might link the two components of the complex. The MvhG subunit, with molecular weight of 34 kDa, contains three [4Fe-4S] clusters. HdrA subunit, a 72 kDa protein, contains four [4Fe-4S] clusters and an FAD. HdrA is the proposed site of the electron bifurcation. Besides the cofactors the subunit contains 4 conserved cysteines that are not involved in cluster coordination. It has been proposed that ferredoxin docks onto HdrA. The proposed heterodisulfide reduction site is the 33 kDa protein HdrB, which harbors a Zn and

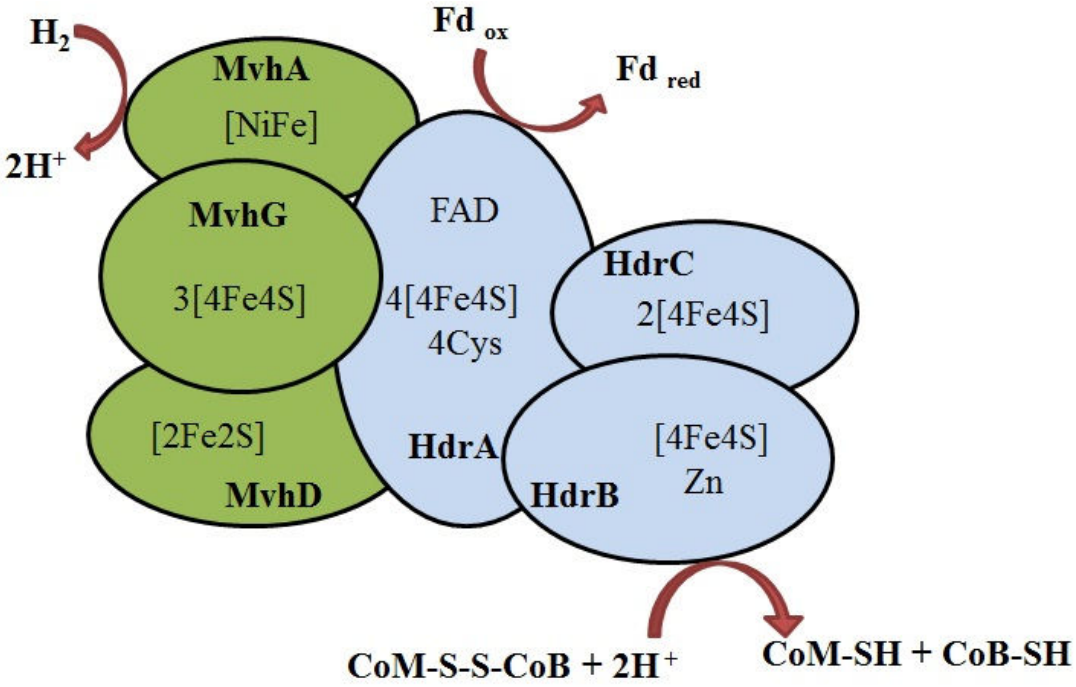

Figure 3.3: MvhADG/HdrABC complex from *M. marburgensis*.

a [4Fe-4S] cluster. The third subunit of the HdrABC sub-complex HdrC (21 kDa) contains two [4Fe-4S] cluster (142).

3.3 Hetrodisulfide reductase (HdrABC) and HdrA

Hetrodisulfide reductase (Hdr) **(**EC 1.8.98.1) is an iron-sulfur flavoprotein disulfide reductase that catalyzes the reversible cleavage of the heterodisulfide CoM-S-S-CoB to CoM-SH and CoB-SH. In the HdrA amino acid sequence analysis, a consensus sequence for FAD-binding, $GXGX_2GX_3AX_{13}E$, and four copies of $CX_2CX_2CX_3C(P)$ sequences that are characteristic for [4Fe-4S] cluster binding site were detected. A motif that indicates the presence of four cysteines, which are not involved in cluster coordination, was also detected. The loosely bound FAD in the subunit is the bifurcating site in the CoM-S-S-CoB coupled reduction of Fd. The [4Fe-4S] clusters have been proposed to be involved in electron transfer but their arrangement and their redox properties haven't been established. The position and the role of the cysteines are unknown. The presence of two [4Fe-4S] clusters in HdrC was confirmed by the presence of two copies of the sequence motif $CX_2CX_2CX_3C(P)$ (143). The HdrB and HdrC from *Methanothermobacter marburgensis* showed sequence similarity with the membrane bound Hdr in *Methanosarcina* that is capable of reducing the CoM-S-S-CoB. In this organism the HdrA subunit is absent. This was used as a basis for the assignment of HdrB and HdrC subunits as possible catalytic sites for the heterodisulfide reduction (144).

Indirect spectroscopic studies have been used to deduce the role of HdrB subunit in catalysis as well as to identify the cofactor in the subunit. When HdrB was incubated with CoM-SH in oxidizing condition an EPR active species with g values 2.013, 1.991 and 1.938 was observed. The same signal was detected when Hdr was incubated with CoM-SH. When ^{57}Fe-enriched Hdr was incubated with CoM-SH there was broadening of the signal, suggesting that

the paramagnetic species is iron-based. Incubation of either enzyme or subunit with ^{33}S-labeled CoM-SH resulted in the broadening of the EPR signal indicating a direct binding of the CoM-SH thiol group to a [4Fe-4S] cluster. Variable-temperature magnetic circular dichroism (VTMCD) spectroscopy of Hdr incubated with CoM-SH showed the presence of a $[4Fe\text{-}4S]^{3+}$ cluster. This was supported by ^{57}Fe-pulsed ENDOR of both Hdr and HdrB which showed an unusually large isotropic hyperfine coupling for two distinct Fe sites, a mixed-valence Fe^{2+}/Fe^{3+} pair and a Fe^{3+}/Fe^{3+} pair, with a unique iron that is coordinated to a fifth ligand. The Fe site that binds the ligand has not been identified. Based on the above results it has been deduced that the prosthetic group in HdrB is a [4Fe-4S] cluster that is involved in direct substrate binding, electron transfer and disulfide bond cleavage. It is important to mention that HdrB alone was unable to catalyze the reduction of CoM-S-S-CoB (132, 144–146).

To measure the different midpoint potentials of all the cofactors in Hdr, a redox titration experiment was performed **(Fig 3.4)**. In the redox titration of *M. marburgensis* Hdr in the presence of CoM-SH, a paramagnetic species with g values 2.052, 1.933 and 1.887 was detected. This signal was due to the $[4Fe\text{-}4S]^{+}$ clusters in Hdr, with midpoint potential below -400mV. Another signal with g values 2.058, 1.933 and 1.863 was detected. This signal has a midpoint potential of -154 mV and was proposed to represent one of the [4Fe-4S] clusters. Another peak with g = 1.937 started forming at -151 and it has been proposed the signal represents a [4Fe-4S] cluster bound to the substrate CoM-SH. A radical signal was also detectable at g value 2.033 whose intensity increased at -120 mV. The fact this paramagnetic species was detected in a very small potential window indicates that the species is unstable and it has been proposed that this radical could be due the flavinsemiquinone or possibly a thiol radical (112). A large radical species is present at lower potential. This species is present on the redox dyes methyl viologen

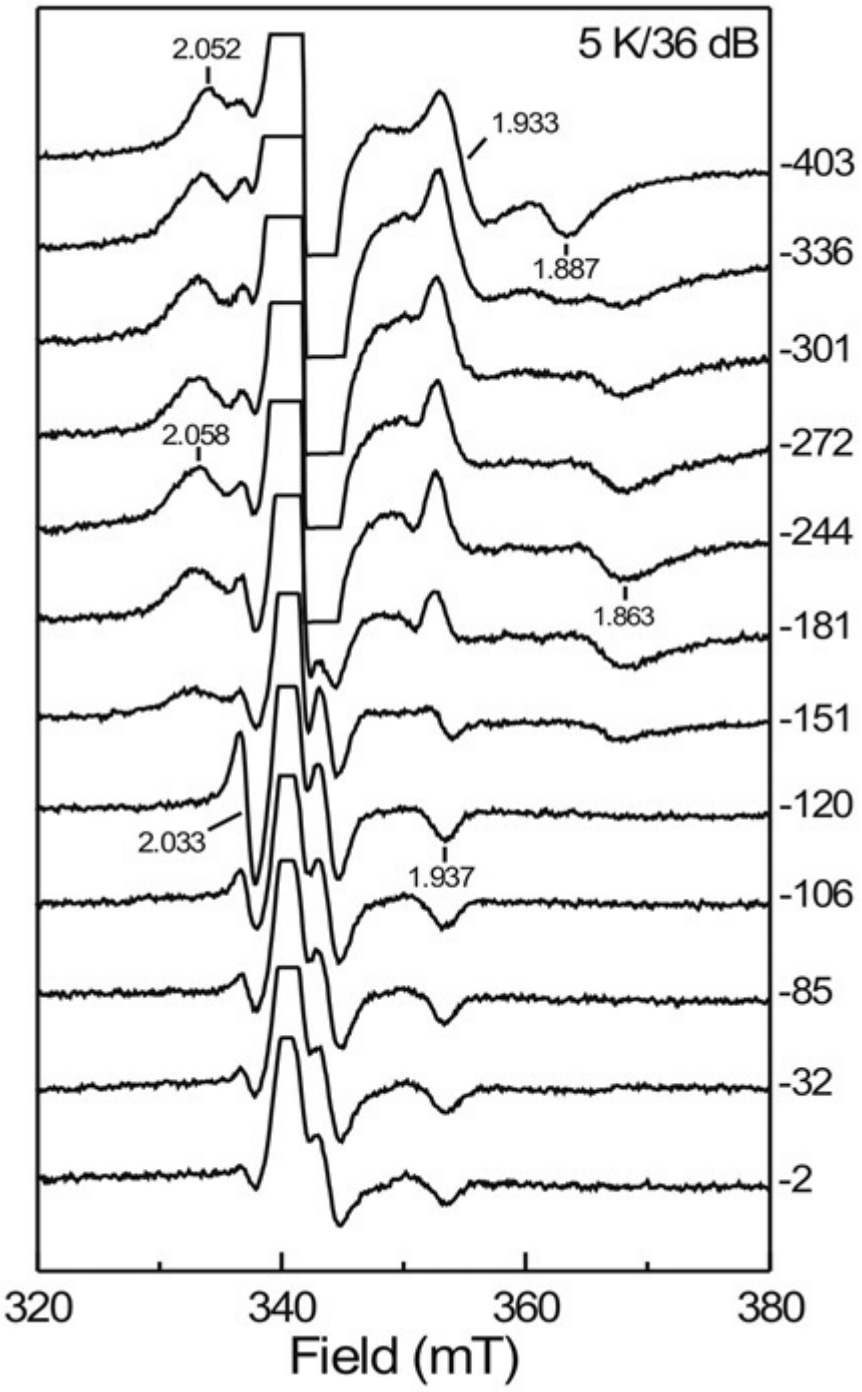

Figure 3.4: Redox titration of Hdr from *M. marburgensis* in the presence CoM-SH. Adapted from (112).

and benzyl viologen.

The mechanism of electron bifurcation in the sub-complex HdrABC is not known. But a crossed-over mechanism has been proposed based on the radical signal, at g value 2.033, detected in the redox titration of Hdr. Due to change in the electrostatic environment of a 2-electron redox compound, such as quinones and flavins, the midpoint potentials of the individual electron transfers are modified. Hence redox process proceeds through two individual reduction steps instead of the simultaneous 2-electron transfer. In the crossed-over model, the potential of the 2-electron transition of the compound is halfway between the two redox potential of the individual 1-electron transfer steps. The first oxidation potential is more positive than the second potential. During catalysis the flavin will be fully reduced ($FADH_2$) by H_2. The low potential Fd is close to the reduced flavin. Electron for CoM-S-S-CoB are probably first transferred to a [4Fe-4S] cluster in the HdrA or HdrB subunits. The first electron transfer from the relatively higher potential first oxidation center to the [4Fe-4S] cluster in HdrA results in the formation of highly reactive "red hot" $FADH^{\bullet}$ flavinsemiquinone. The [4Fe-4S] cluster moves away from the flavin site, passes the electron to HdrC and eventually the CoM-S-S-CoB is reduced. The low potential $FADH^{\bullet}$ semiquinone transfers its electron to Fd, which is in close proximity. This process is repeated a second round and the whole process affords two reduced ferredoxins, CoM-SH and CoB-SH. During redox titration of the FAD a 2-electron Nernst curve would be observed and the semiquinone would be detectable in a very narrow potential range, indicating a crossed-over mechanism (147).

The heterodisulfide reduction involves the transfer of two sequential electrons. In the proposed mode of catalysis the first bifurcated electron is relayed from HdrA through HdrC to HdrB. The $[4Fe\text{-}4S]^{2+}$ in HdrB is reduced to $[4Fe\text{-}4S]^{1+}$. As shown in **Fig 3.5** nucleophilic attack

by the cluster bound cysteine results in the cleavage of the heterodisulfide releasing CoB-SH. It has been proposed that a transient heterodisulfide intermediate is formed by the interaction of coenzyme M to the cysteine of the cluster forming CoM-S-S-Cys heterodisulfide. This is followed by two internal electron transfers from the cluster to the thiol coenzyme, resulting in a $[4Fe\text{-}4S]^{3+}$ cluster with its unique iron bound to the thiol coenzyme. In another proposed mechanism **(Fig 3.6)** the bridging S^{2-} initiates the nucleophilic attack and release of CoM-SH. The subsequent two electron transfer to CoM-SH results in the formation of the paramagnetic $[4Fe\text{-}4S]^{3+}$ intermediate. The EPR active intermediate observed is believed to be the same intermediate as the one trapped when oxidized Hdr was incubated with CoM-SH. From the spectroscopic data it has been proposed that this species is similar to the paramagnetic HiPIP-like intermediate observed in FTR, IspG and IspH, in which the cluster is a $[4Fe\text{-}4S]^{3+}$ based species and directly bound to the substrate. The second electron transfer reduces the cluster back to $[4Fe\text{-}4S]^{2+}$ with concomitant protonation and release of CoM-SH (80, 87, 103, 145).

At present the exact route of electron transfer through the Mvh sub-complex prosthetic groups and their redox properties is unknown. The role of the [2Fe-2S] cluster in MvhD is unknown. The role of the four conserved cysteines in HdrA has not been established, but it has been suggested that two of the cysteines could be involved in electron transfer by forming an active-site disulfide and act as a 1 electron/2 electron switch. The clusters in HdrA that are directly interacting with either the Mvh sub-complex or the flavin have not been identified. In the absence of a crystal structure the characterization and identification of the Fe-S cluster centers in Mvh/Hdr complex becomes complicated due to the presence of multiple clusters.

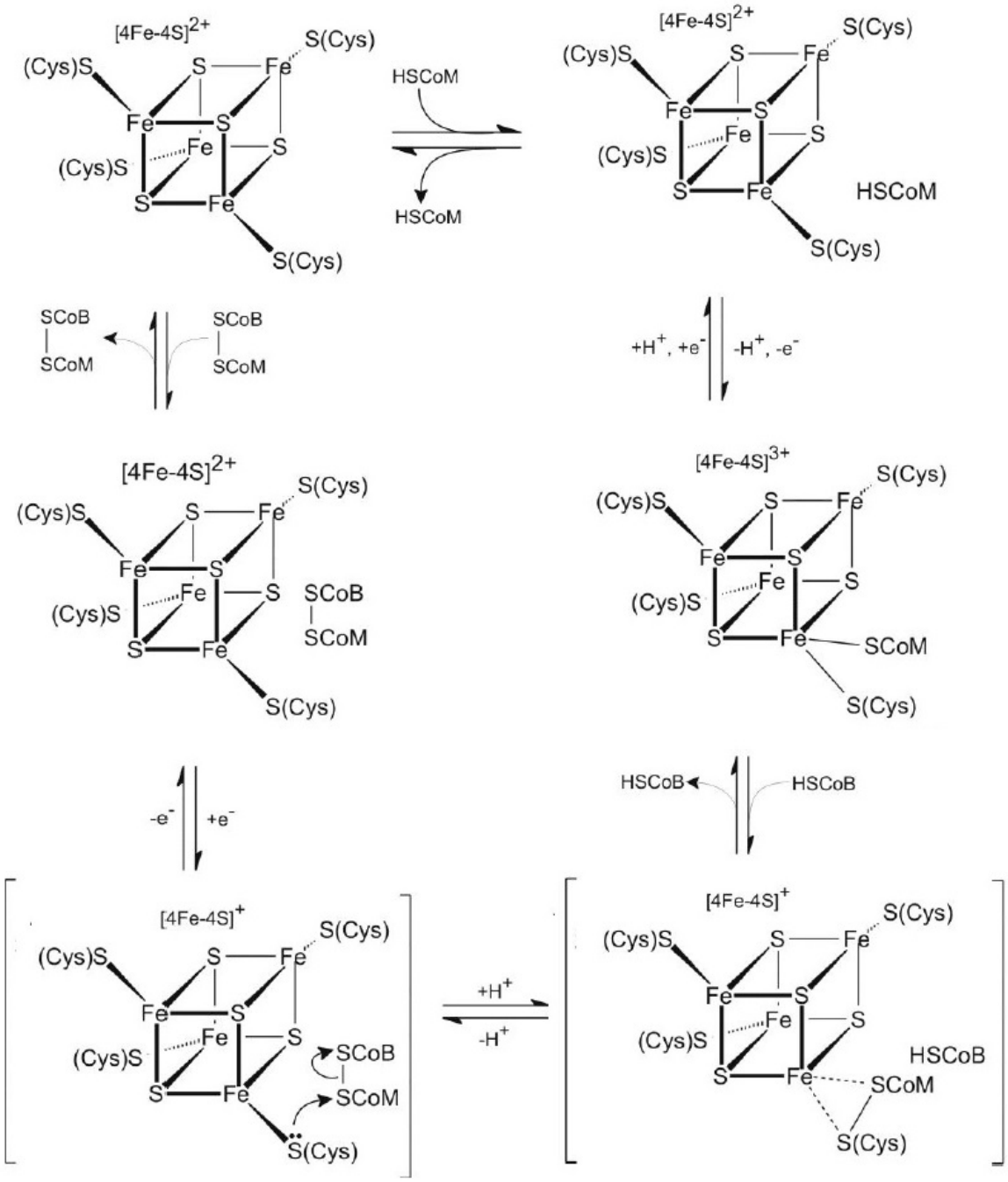

Figure 3.5: Proposed mechanisms for Hdr.
Adapted from (145).

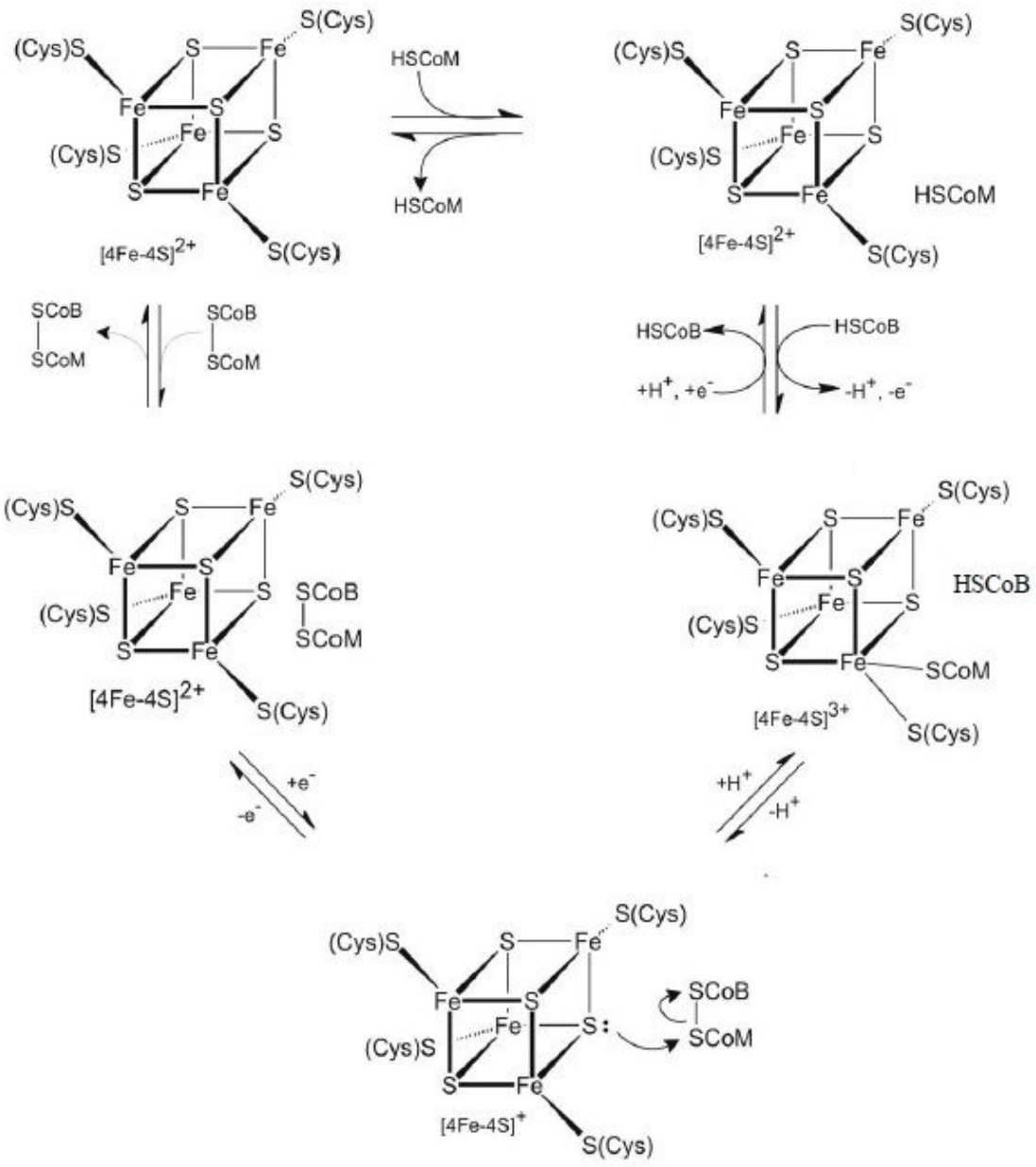

Figure 3.6: Proposed mechanisms for Hdr.
Adapted from (145).

3.4 Statement of research

I. The presence of multiple cofactors renders the Mvh/Hdr enzyme very complex. Hence probing the smallest subunit which contains less cofactors and that still contains all the essential cofactors for electron bifurcation would be an easier system to study. For this purpose the HdrA subunit of the reductase from *M. marburgensis* was overexpress in *M. maripaludis*.

II. It has been reported that the FAD in heterodisulfide reductase was easily lost during purification. Since HdrA houses the FAD, procedures to reconstitution the cofactor in the subunit will be optimized.

III. To understand the flow of electrons in HdrA and identify the cofactors, midpoint potentials of the cofactors in the subunit will be determined by performing redox titrations.

3.5 Materials and Methods

All purification steps, sample handling and experiments were done in a glove box (Coy Laboratory Products, Inc., Grass Lake, USA) filled with 95% N_2 and 5% H_2 or a Vacuum Atmospheres Co. (Hawthorne, CA) dry box filled with argon. Also, all buffers and solutions used in the procedures were filtered with 0.45 μm membrane, degassed by boiling them, and purged with nitrogen. The buffers were subsequently stirred under vacuum for 2 to 3 hrs. The closed off bottles were repressurized with argon and directly used or stored. All buffers and solutions were equilibrated and stirred overnight inside the glove box before use.

3.5.1 Chemicals

Sodium dithionite was from Alfa Aesar (Haverhill, MA). All gases and gas mixtures were from Airgas (Radnor Township, PA). FAD was from TCI (Tokyo, Japan). Dialysis membrane was from Spectrum Labs (Rancho Dominguez, CA). All other chemicals were from AMRESCO (Solon, OH), Acros (New Jersey, USA) or Sigma-Aldrich (St. Louis, MO). His-trap Ni^{2+} affinity, Mono Q and PD-10 columns were purchased from GE Healthcare (Uppsala, Sweden). Serdolit Pad II resins were from Serva electrophoresis (Heidelberg, Germany). Centricon and amicon ultrafiltration units were from Millipore (Billerica, MA).

3.5.2 Synthesis of the hetrodisulfide CoM-S-S-CoB (HDS)

HDS was chemically synthesized by following the steps in the literature (148).

3.5.2.1 7,7'- Dithiodiheptanoic acid

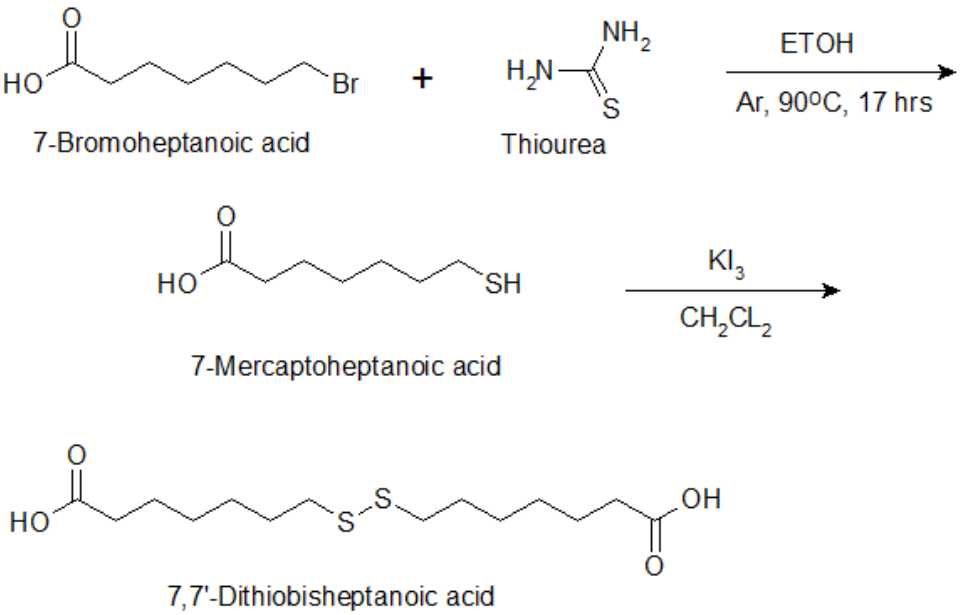

7-Mercaptoheptanoic acid was synthesized by dissolving 7-bromoheptanoic acid (9.60 g, 46.6 mmol) in 110 ml of ethanol and adding 17.4 g (228 mmol) of thiourea in the stirred solution. After the mixture was refluxed, under argon, at 90°C for 17 hrs, it was cooled to room temperature followed by the addition of 25 ml 60% NaOH. The mixture was refluxed under argon for an addition 2 hrs and cooled to room temperature. The yellow/white solution was concentrated to around half of the original volume with a rotavap, at 60-70°C. To the concentrated solution a 100 ml 1 M HCl was added followed by 20 ml concentrated HCl. The thiol was extracted 3 times with 100 ml dichloromethane. The dichloromethane phase was

extracted 3 times with 150 ml of an aqueous solution of 1 M sodium bicarbonate. The aqueous extract was acidified with HCl to a pH of 1-2, and extracted 3 times with 200 ml dichloromethane. The organic phase was filtered and dried over cotton layered with anhydrous magnesium sulfate, and concentrated at room temperature to 70 ml. The thiol was oxidized to a disulfide by mixing the dichloromethane phase with an aqueous solution of 10% (w/v) iodine and 20% (w/v) potassium iodide until the brown color persisted. The aqueous phase was removed and the dichloromethane phase was washed 3 times each with an aqueous solution of 1 M sodium thiosulfate and water. The organic phase was filtered and dried with anhydrous magnesium sulfate over cotton layer, and concentrated under vacuum. The product was crystallized twice from benzene and dried under high-vacuum to yield a white crystal.

3.5.2.2 7, 7'- Dithiobis(succinimido-oxyheptanoate)

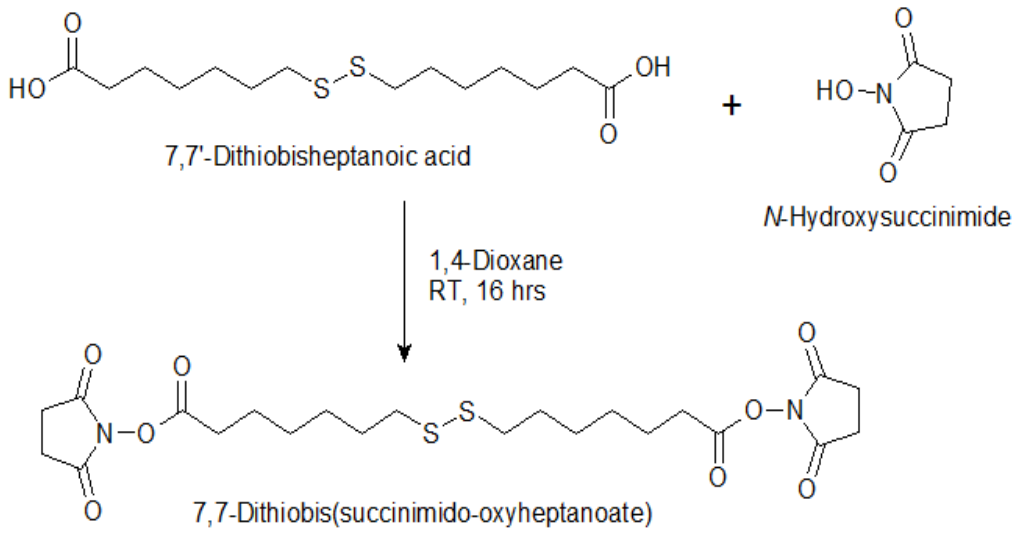

At room temperature 7,7'-dithiodiheptanoic acid (388 mg, 1.20 mmol) was dissolved in 8 ml of 1,4-dioxane followed by the addition of 290 mg (2.50 mmol) *N*-hydroxysuccinimide under stirring. A solution of 505 mg (2.40 mmol) dicyclohexylcarbodiimide in 3 ml 1,4-dioxane was added drop-wise and the resulting solution was stirred for 16 hrs at room temperature. The

precipitated dicyclohexylurea was removed by filtration over a glass filter and the filtrate was washed 2 times with 5 ml 1,4-dioxane, and dried to a clear oil under vacuum. The product was recrystallized twice from boiling 2-propanol, and dried for 1 day under high vacuum to give white crystals.

3.5.2.3 (+)-N, N'-(7,7'-Dithio-diheptanoyl) bis(O-phospho-L-threonine) (CoB-S-S-CoB)

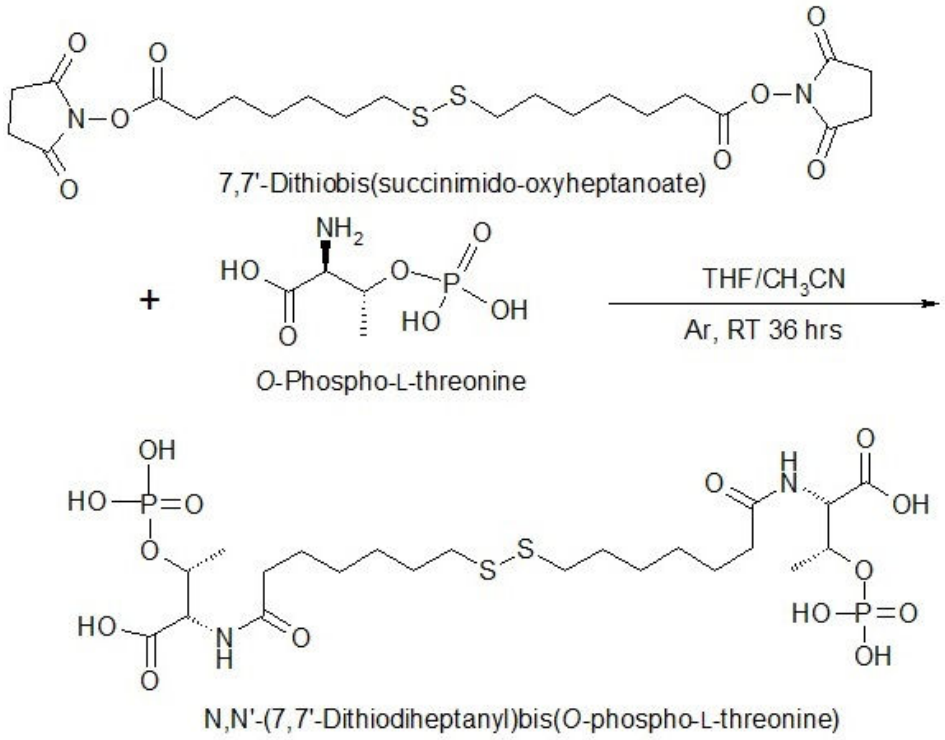

O-phospho-L-threonine (400 mg, 2.00 mmol) and triethylamine (0.560 ml, 4.00 mmol) were dissolved in 4 ml water. This solution was added to 7,7'-dithiobis(succinimido-oxyheptanoate) (362 mg, 0.700 mmol) dissolved in 18 ml tetrahydrofuran and 4 ml acetonitrile. The solution was stirred at room temperature under argon for 36 hrs and followed by the removal of solvents under vacuum at 30°C. The resulting white residue was dissolved in 25 ml 1 M HCl and washed three times with 8 ml dichloromethane. Traces of dichloromethane were removed

from the aqueous phase under vacuum. The aqueous phase was applied to a 2 × 13 cm column of polystyrene Serdolit Pad II preequilibrated overnight with 1 M HCl. The column was washed with 100 ml of 1 M HCI, followed by 150 ml H_2O. The product was eluted with a methanol gradient (80 ml H_2O/MeOH, 4:1; 120 ml H_2O/MeOH, 1:1; 80 ml H_2O/MeOH, 1:4, 100 ml MeOH). The collected fractions were concentrated under vacuum (50°C) to 1/10 of the original volume. Subsequently, 2 ml 2 M ammonia was added to obtain the ammonium salt followed by lyophilization. The white solid obtained from each fraction was analyzed with NMR spectroscopy.

^{1}H-NMR (D_2O, 300 MHz): 4.71 (*s*, D_2O), 4.53-4.62 (*m*, 1H, $CHPO_3^{2-}$), 4.2 (*d*, J = 4, 2H, CHCOO), 2.77 (*t*, J = 7, 4H, SCH_2), 2.31-2.42 (*m*, 4H, $COCH_2$), 1.59-1.74 (*m*, 8H. SCH_2CH_2, $COCH_2CH_2$), 1. 34-1. 48 (*m*, 8H, CH_2CH_2), 1.30 (*d*, J = 6Hz, 6H CH_3).

3.5.2.4 CoM-S-S-CoB

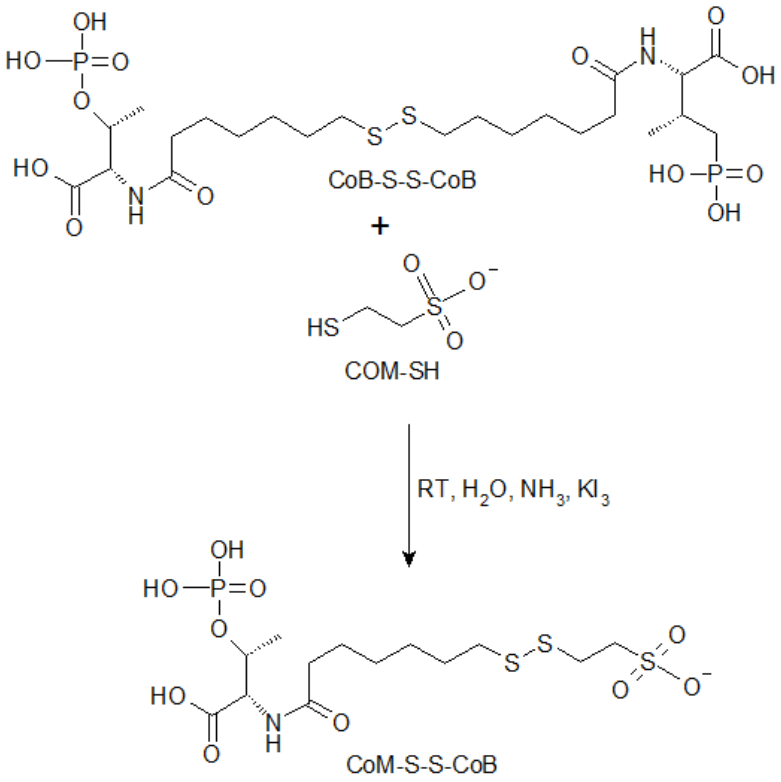

Coenzyme B disulfide tetraammonium salt (73.0 mg, 0.0970 mmol) and coenzyme M sodium salt (330 mg, 2.00 mmol) were dissolved in water (5 ml) and NH_3 (aq., conc., 0.50 ml). The solution was stirred for one hour followed by dropwise addition of KI_3 (0.5 M in water) until the brown color fades away very slowly. The solution was acidified with HCl (20%) to pH 0 and loaded to a Serdolit Pad II column equilibrated overnight with 20% HCl. The column was washed with HCl (aq., 1 M, 0.5 M, 0.2 M, 0.1 M and 0.025 M) until all coenzyme M homodisulfide had eluted (UV: λmax ca. 240 nm). The product was eluted with water, followed by methanol in water (10%, 25% and 50%). Each fraction was collected separately, pH adjusted to 5 with NH_3 (aq., 100 mM), lyophilized and analyzed with NMR.

^{1}H-NMR (600 MHz, D_2O, dioxane = 3.665 ppm): 4.74 (overlapping with the solvent signal at 4.72 ppm, $CHOPO_3^{2-}$), 4.41 (*dd*, *J* = 2.67, 2.01, 1 H, CHNCO); 3.23 (2 H; $CH_2SO_3^-$), 2.98 (2 H; CH_2S), 2.73 (*t*, *J* = 7.29, 2 H, CH_2S); 2.35 (*dt*, *J* = 14.22, 7.53, 1 H, CH_2CO); 2.31 (*dt*, *J* = 14.16, 7.32, 1 H, $CH_2C{=}O$); 1.65 (*quint*, *J* = 7.34, 2 H, CH_2); 1.59 (*quint*, *J* = 7.46, 2 H, CH_2); 1.38 (*quintetoid*, J_{obs} = 7.3, 2 H, CH_2); 1.31 (*quartetoid*, J_{obs} =7.1, 2 H, CH_2); 1.26 (*d*, *J* = 6.42, 3 H, CH_3).

3.5.3 Expression and purification

M. maripaludis cells containing a *M. marburgensis* HdrA gene with a His-tag was graciously supplied by the Leigh group (Department of Microbiology, University of Washington)

The *M. maripaludis* cell pellets were resuspended in buffer A (50 mM Tris/HCl, 100 mM NaCl pH 7.6). The suspended cells were then lysed by sonication on ice 3 times for a total of 7 min at 80% power using a pulse of 0.5 sec on/0.5 sec off, followed by anaerobic ultracentrifugation at 126,603 x g for 20 min at 4°C (Beckman XL-70 Ultracentrifuge, TYPE 45 Ti Rotor, Beckman Coulter, Inc.). The supernatant was filtered with a 0.2 µM filter (Millipore) and loaded on a His-trap Ni^{2+}-affinity column pre-washed and pre-equilibrated with buffer A. The protein was eluted with an imidazole gradient (0% to 100%) of buffer B (50 mM TrisHCl, 100 mM NaCl, 500 mM imidazole pH 7.6). The fractions were pooled and analyzed with 12% SDS-PAGE. Fractions containing HdrA were washed with buffer A, concentrated and loaded on a Mono Q column. A NaCl step gradient was used to elute the protein, buffer C (buffer A + 2 M NaCl). Fractions were analyzed with 12% SDS PAGE.

3.5.4 Protein concentration

The protein concentration was determined with Bradford assay using bovine serum albumin as a standard (127). Alternatively the absorbance at 280 nm ($\varepsilon = 42750\ M^{-1}cm^{-1}$) was also measured.

3.5.5 Iron determination

Rapid ferrozine-based colorimetry was used to determination the iron content of the protein (128). All containers and pipette tips used were boiled in 1 M HCl and washed with ultra-pure water. Iron standards (0, 10, 20, 30, 40, 50 μM) were prepared by dissolving ferrous ethylenediammonium sulfate in 10 mM HCl. The iron releasing reagent was prepared by mixing equal volumes of 0.6 M HCl and 4.5% potassium permanganate. The iron chelating and reducing reagent contained 6.5 M ferrozine, 13.1 mM neocuprine, 2 M ascorbic acid, and 5 M ammonium acetate in a 25 ml solution. To 1 ml iron standard samples and the protein samples, 0.5 ml of the iron releasing reagent was added, followed by incubation at 60°C for 2 hrs. To each sample 100 μl of the iron chelating and reducing reagent was added followed by incubation for at least another 30 mins. The absorbance at 562 nm was used to obtain the value for the samples and to generate a standard curve, from which the iron concentration in the protein samples was determined.

3.5.6 [4Fe-4S] cluster reconstitution

Most of the HdrA samples showed substoichiometric amounts of the expected [4Fe-4S] clusters. An in vitro chemical reconstitution of the cluster was achieved by an overnight incubation (room temperature) of the enzyme with dithiothreitol (at least 5 mM), $FeCl_3$ (10x

protein concentration), and Na_2S (10x protein concentration) in buffer A. To remove black iron-containing precipitate, the samples were centrifuged at 6000 rpm for 5 min or filtered with a 0.2 µM filter (Millipore). The supernatant was concentrated using a 30 kD cut-off filter and desalted by passing through a PD-10 column. The eluted protein was used directly.

3.5.7 FAD reconstitution

Since the as purified HdrA doesn't contain FAD, the following procedure was followed to insert the FAD. The enzyme was incubated in buffer A containing 0.7 mM FAD, 8 mM urea for 10 min. The enzyme mixture was transferred to a 15 kD cut-off dialysis membrane and dialyzed overnight against buffer A containing 0.7 mM FAD. Excess FAD was washed with buffer A using an amicon device with 30 kDa cut-off. In each step UV-Vis spectroscopy was used to check the insertion of FAD.

3.5.8 Redox titration

To trap EPR active species of HdrA at different potentials, a redox titration was performed using sodium dithionite as the reductant and potassium ferricyanide as the oxidant in the presence of dye-mediators. Indigo-disulphonate ($E^{\circ\prime}$= -125 mV), 2-hydroxy-l, 4-naphthoquinone ($E^{\circ\prime}$= -145 mV), phenosafranin ($E^{\circ\prime}$= -252 mV), anthraquinone-2-sulfonate ($E^{\circ\prime}$= -255 mV), safranin O ($E^{\circ\prime}$= -289 mV), neutral red ($E^{\circ\prime}$= -325 mV), benzyl viologen ($E^{\circ\prime}$= -350 mV) and methyl viologen ($E^{\circ\prime}$= -453 mV) were used as mediators at a final concentration of 50 µM. The potential was measured, at 25°C while stirring, with a Ag/AgCl reference electrode that was connected to the redox titration cell. The enzyme was placed in the titration cell and the dye mediators were added. The protein-dye mediator mixture was fully reduced by adding dithionite, to a potential of -621 mV vs Ag/AgCl (-421 mV vs SHE). The sample was

titrated in the oxidizing direction with potassium ferricyanide. When the mixture has equilibrated at the desired potential, 300 µl aliquots were transferred into an EPR tube and frozen in liquid nitrogen.

3.5.9 EPR data collection

CW EPR spectra were collected at X-band frequency with a Bruker EMX spectrometer (Bruker Biospin Corporation, Billerica, MA) fitted with the ER-4119-HS high sensitivity perpendicular-mode cavity. An Oxford Instruments ESR 900 helium flow cryostat in combination with an ITC 503S temperature controller was used for measurements in the 4.5-300 K range. A liquid nitrogen finger Dewar was fitted to the cavity for 77 K measurements. Instrument conditions were: microwave frequency of 9.386 GHz; field modulation frequency of 100 kHz and modulation amplitude of 0.6 mT. Sample specific settings are given in the legends to the figures.

Quantitation of the spin concentration of EPR-active species within a sample was determined by comparison of the double integral of the EPR intensity with that of a 10 mM copper perchlorate standard (10 mM $CuSO_4$, 2 M $NaClO_4$, 10 mM HCl). The spin concentration was corrected for the amount of [4Fe-4S] cluster present in the sample. When multiple paramagnetic species were present in the samples, a spectrum that has only one of the species was subtracted from the overlapping spectrum to get the second spectrum and vice versa. If this was not possible the individual signals were simulated. The double integration value of individual species was obtained and spin concentration determined the same as for the single species spectra. The software packages developed by either S. P. J. Albracht or Fred Hagen were used for spectral simulation and double integration of the signals (129, 130).

3.6 Results

3.6.1 Synthesis CoM-S-S-CoB

The last step of the HDS synthesis is the Serdolit Pad II column. The collected fractions were lyophilized and analyzed by ^{1}H NMR **(Fig 3.7)**. The fractions eluted with 25% and 50% methanol in water contained CoM-S-S-CoB. The final product also contained coenzyme B and CoB-S-S-CoB.

3.6.2 Purification

HdrA from *M. marburgensis* that was overexpressed in *M. maripaludis* was successfully purified from the cell extract using two column steps, a Ni-affinity column and a Mono Q column. The purity of the protein was determined by SDS-PAGE which showed a prominent band around 75 kDa **(Fig 3.8)**.

3.6.3 [4Fe-4S] cluster reconstitution

To increase the cluster content of HdrA, which was substoichiometric, in vitro reconstitution was performed. After reconstitution the cluster content of HdrA increased from 2 to 3.5.

3.6.4 FAD reconstitution

The FAD in HdrA was lost during the purification process (or was never present) and hence attempts were made to reconstitute the cofactor. The reconstitution process was followed using UV-Vis spectroscopy (**Fig 3.9).** After the overnight dialysis of HdrA in the presence of excess FAD, two peaks were observed at 375 and 450 nm (**Fig 3.9 - dashed line)**. To remove the

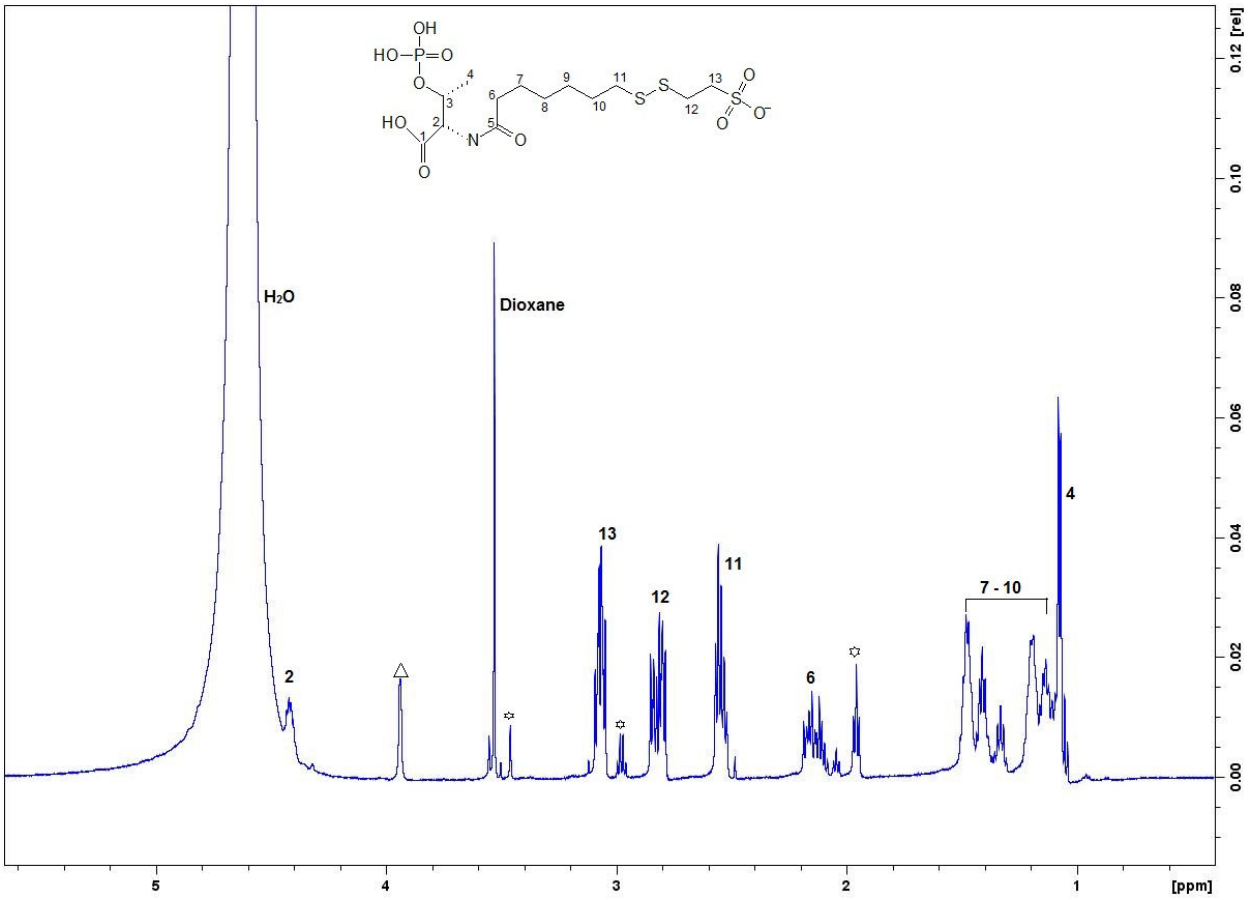

Figure 3.7: ^{1}H NMR spectrum of CoM-S-S-CoB (D_2O, 600 MHz).

* Unassigned impurity. $^{\Delta}$ Impurity from Coenzyme B or CoB-S-S-CoB.

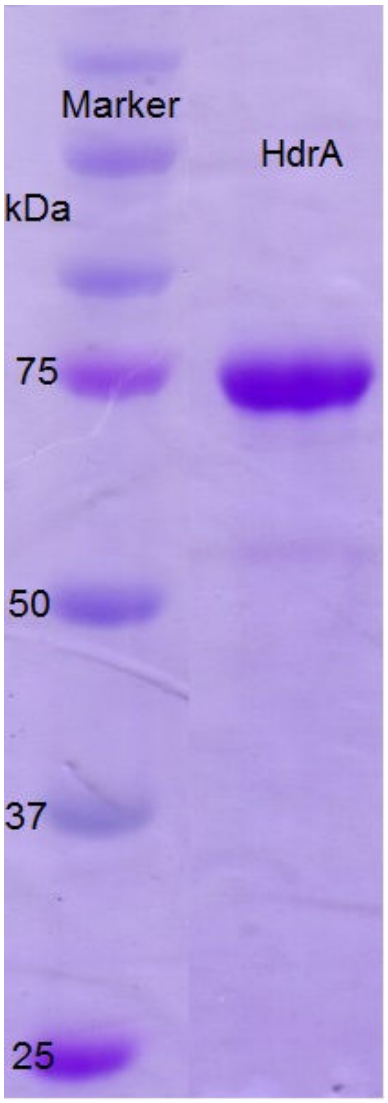

Figure 3.8: SDS-PAGE analysis of HdrA after the Mono Q column purification step.

excess FAD, the enzyme was washed with buffer A (50 mM Tris/HCl, 100 mM NaCl pH 7.6). This resulted in the bleaching of the peaks at 375 and 450 nm (**Fig 3.9 - dotted line).**

3.6.5 Redox titration

In the redox titration of HdrA from *M. marburgensis* a broader EPR signal that represents a $[4Fe\text{-}4S]^{+}$ cluster with g values 2.078, 1.935 and 1.886 was detected at potentials -421 to -295 mV **(Fig 3.10)**. At higher potential a signal due to the presence of $[3Fe\text{-}4S]^{+}$ clusters was detected at g = 2.029. Besides the Fe-based EPR signal the entire sample series showed a radical signal around g = 2. This signal is due to benzyl viologen and methyl viologen, dye mediators, which show a radical signal. This signal was truncated to better present the EPR data.

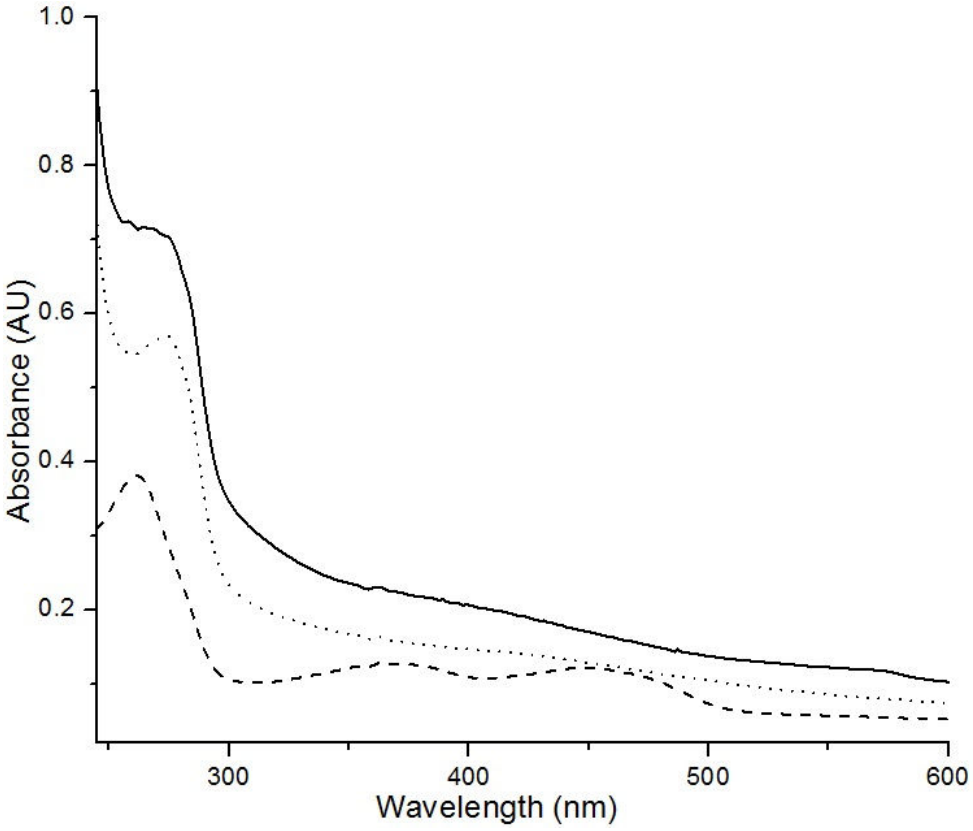

Figure 3.9: UV-visible absorption spectra of as-isolated HdrA (Solid line), HdrA after an overnight dialysis in the presence of excess FAD (Dashed line) and HdrA after washing away excess FAD (Dotted line).

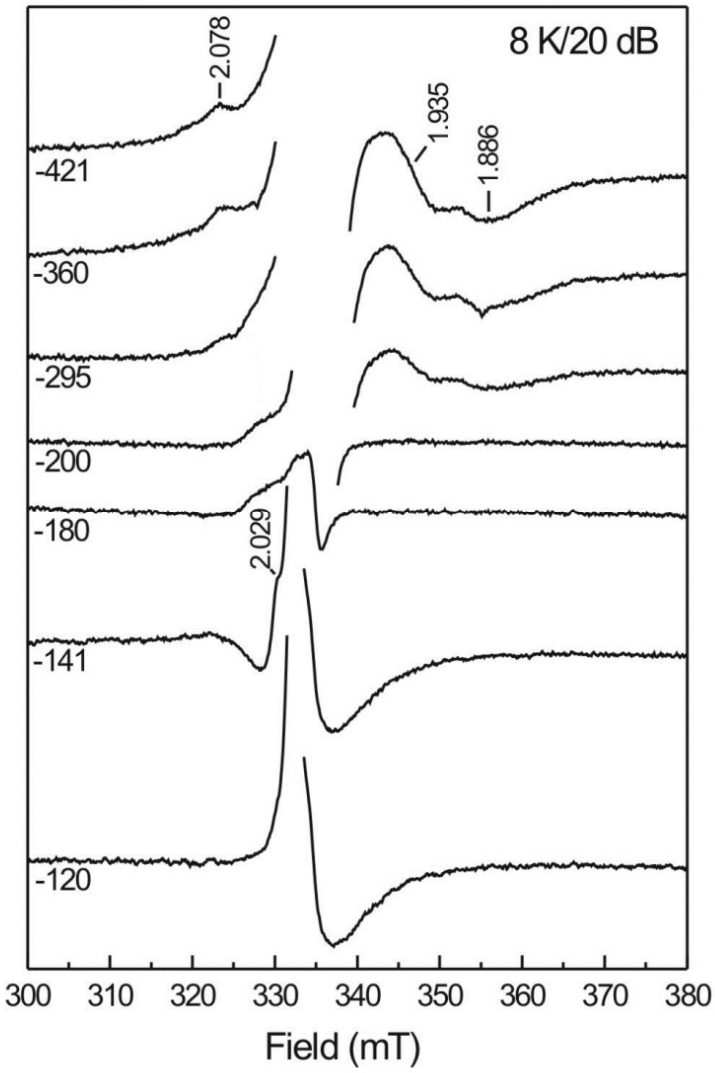

Figure 3.10: Redox titration of HdrA from *M. marburgensis*.

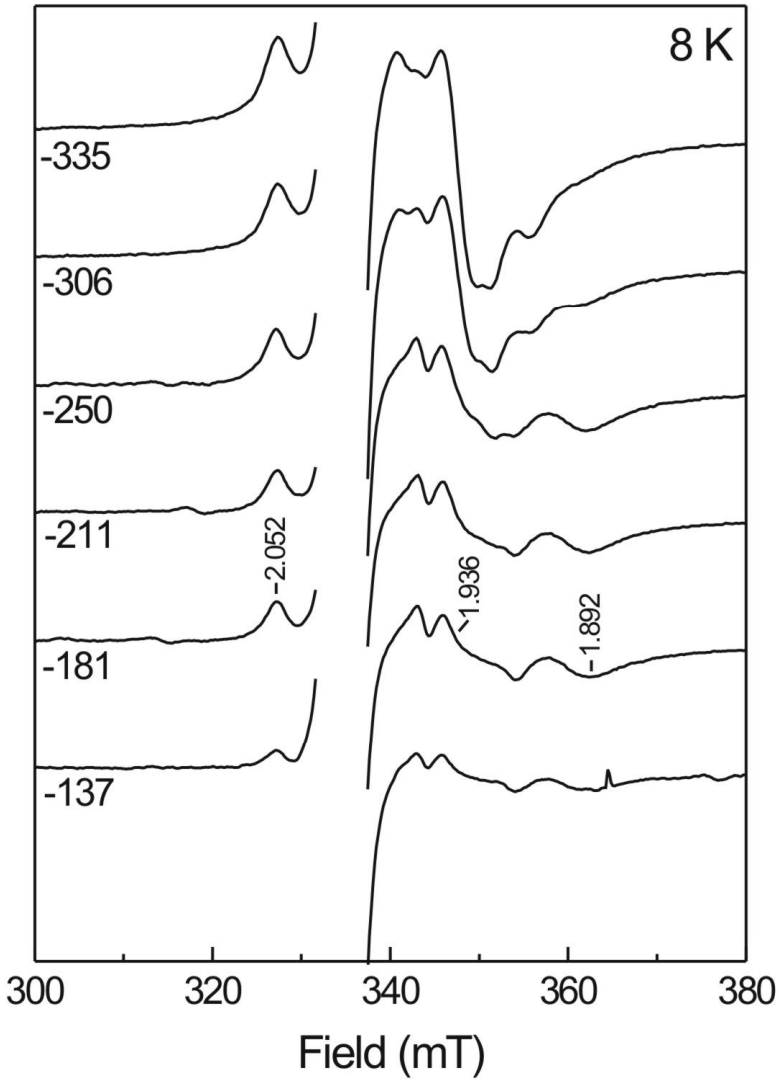

Figure 3.11: Redox titration of the Mvh/Hdr complex from *M. marburgensis*. Sample preparation and data collection were done by Carly Engel.

3.7 Discussion and conclusions

When HdrA from *M. marburgensis* was expressed in *M. maripaludis*, the enzyme contained enough Fe ions to form 2[4Fe-4S] clusters and no FAD was detected. A cluster reconstitution procedure was performed with the goal to restore the cluster content up to the expected amount of 4. After this procedure enough Fe ions were present to accommodate for 3.5 [4Fe-4S] clusters. Attempts to reconstitute the FAD were not successful when performed on enzyme with partial amount (~2) of cluster present. This is indicated by the broad weak band at 410 nm in the absorption spectrum **(Fig. 3.9 - Dotted line)** of the HdrA after this procedure and the absence of the flavin peaks.

In the redox titration performed with the Hdr enzyme **(Fig 3.4)** and the whole Mvh/Hdr complex **(Fig 3.11)** there is a 4Fe cluster that has a midpoint potential, around -154 mV, which is a value clearly different than the bulk of the 4Fe clusters. The relatively high midpoint potential of this cluster makes it the best candidate as the direct electron acceptor of the first electron from $FADH_2$. The redox titrations were performed on the HdrA subunit to see if the characteristic signature of this 'high-potential' cluster was detectable. This does not appear to be the case. At low potential the 'regular'-type 4Fe EPR signals can be detected. The tell-tale g = 1.863 peak was not detectable in the -200 to -100 mV range or at any other range.

If we assume, based on the cluster content, that almost all 4 clusters are at least partially present, we have to conclude that in the isolated HdrA subunit this cluster does not show its characteristic properties. This might be due to need for the presence of the other subunits, but it can also be due to the fact that no FAD is present. The FAD molecule is not that tightly bound to the Mvh/Hdr complex. To purify the complex with a full content the enzyme needs to be purified

in a buffer containing FAD. The assumption, however, that only HdrA is needed to binds and contain FAD might be wrong and the HdrB and/or HdrC subunits might also be required.

In *M. maripaludis*, the Hdr is part of a much larger enzyme complex that in addition to Hdr contains hydrogenase (Vhu), formylmethanofuran dehydrogenase (Fwd), formate dehydrogenase (Fdh), and the electron acceptor polyferredoxin (FwdF subunit). It was found that when the cells are grown with H_2 as the electron source the Fdh is no longer part of the complex (Hdr/Vhu/Fwd). When formate is used as an electron source the hydrogenase is absent (Hdr /Fwd/Fdh). The VhuD subunit, which contains the [2Fe-2S] cluster however is still part of the latter complex (149). It appears that the VhuD plays a very important role in these complexes. Most likely this is related to the presence of the [2Fe-2S] cluster. There is not a good reason why there would be a [2Fe-2S] cluster in the middle of a row of [4Fe-4S] clusters unless this cluster is important for the bifurcation process. VhuD is homologous to the [2Fe-2S] cluster containing MvhD in *M. marburgensis.* As mentioned earlier in some organisms the MvhD and HdrA subunits form one subunit. We propose that the [2Fe-2S] cluster in MvhD could play the same role the Rieske [2Fe-2S] cluster plays in the complex III of the electron transfer chain in mitochondria. This would also imply that the electron flow through the system is from the hydrogenase units to HdrA, to MvhD and to HdrBC. This is still under the assumption that HdrA contains the FAD site. Such an electron flow pattern might actually be correct based on preliminary crystallization data (Rudolph Thauer, personal communication).

We propose that the combination of the HdrA and the MvhD subunits might be the core of the bifurcation process. Coexpression of these two subunits could result in a properly folded 2 subunit protein that might even contain the FAD. Currently the group of John Leigh at the

University of Washington, Seattle, is working at the coexpression of *M. marburgensis* HdrA and MvhD subunits in a *M. maripaludis* host.

CHAPTER 4 : Summary and Future work

Protein-bound iron–sulfur clusters are one of the most ubiquitous and functionally versatile prosthetic groups in nature. The most common clusters in Fe-S proteins are the mono nuclear [Fe], rhombic [2Fe-2S], cuboidal [3Fe-4S] and cubane [4Fe-4S] types. Both enzymes that have been studies, IspH and HdrA, are [4Fe-4S] cluster-containing proteins. IspH is involved in the DOXP pathway for isoprenoid biosynthesis and converts HMBPP into IPP and DMAPP. HdrA is a subunit of the heterodisulfide reductase, an enzyme that is involved in the reductive catalysis of heterodisulfide CoM-S-S-CoB to CoM-SH and CoB-SH.

4.1 IspH

The [4Fe-4S] cluster in IspH is involved in electron transfer and substrate binding. Mössbauer studies of the as-isolated IspH as well as in the presence of HMBPP supported the presence of an active site $[4Fe\text{-}4S]^{2+}$ cluster with a unique iron ion which has a fourth non-sulfur ligand.

EPR-monitored rapid-freeze-quench experiments were used to analyze the overall reaction of wild type and mutant IspH under single and multiple turnover conditions. In the wild type IspH from both *E. coli* and *A. aeolicus* in the presence of a reductant and substrate two cluster-associated paramagnetic reaction intermediates, FeS-I and FeS-II, were observed. During the two one-electron step reductive dehydration of HMBPP there was a time-based appearance and disappearance of the FeS-I species and the appearance of the FeS-II species. The first transient intermediate trapped, FeS-I species, has a g_{av} value that is characteristic for high-potential iron-sulfur proteins (HiPIP) with a $[4Fe\text{-}4S]^{3+}$ cluster. The interesting aspect is that in this case the signal is produced under reductive conditions. Further investigation of the

intermediate using ENDOR and Mössbauer spectroscopy indicated that the paramagnetic signal is indeed due to a HiPIP-like [4Fe-4S]$^{3+}$ cluster. There are only a couple of enzymes: FTR, IspG and Hdr, which show a HiPIP-like signal in the presence of a reductant. The main theme is that the reaction that is catalyzed requires two electrons but the iron-sulfur protein can only donate one electron at-a-time. Instead of creating a radical species by transferring one electron, the substrate is bound to the unique iron of the cluster and in that process two electrons are transferred from the reduced cluster to the substrate and the cluster becomes [4Fe-4S]$^{3+}$. The second cluster-based species, FeS-II, is the result of the products IPP or DMAPP binding to the reduced [4Fe-4S]$^{1+}$ cluster. A similar signal was observed when dithionite-reduced enzyme was incubated with IPP or DMAPP. Mössbauer studies are underway to determine the redox state of the FeS-II species. An alternative experiment would be to look at the redox behavior of this signal. If the signal is due to a [4Fe-4S]$^{+}$ species it should be detectable when reduced. If it is a HiPIP like form, it should be detectable when oxidized.

For both EPR active intermediates, the exact binding model of the cluster to the substrate or the product is unclear. Based on the signal obtained for the E126Q IspH mutant (FeS-III) a side-on binding to the π-bond has been proposed but we are not sure how comparable the two signals are (see below). Several experiments can be performed to further investigate this. The binding of compounds would change the midpoint potential of the iron-sulfur cluster. EPR-based redox titrations in the presence IPP and DMAPP could be used to determine this change in midpoint potential of the cluster. Labeling of the substrate and/or products with ^{13}C and subsequent investigation of the observed signals with ^{13}C and ^{57}Fe-ENDOR spectroscopy can provide very detailed insight to the binding mode.

Based on sequence analysis and crystal structure of IspH, three conserved residues (H124, E126 and T167) that are believed to be involved in the reaction mechanism or substrate binding were mutated. H124F and T167C IspH mutants showed decreased activity. Two EPR active intermediates, similar to the species observed in the WT enzyme, are detected in the RFQ studies of both mutants. The data presented shows that mutation of the two residues have an effect on the cluster environment and therefore the reaction. The role of the H124 in the docking and proper orientation of the substrate has been confirmed. T167 is involved in stabilization of HMBPP through hydrogen bonding.

The E126 mutant has no activity and a new stable Fe-S cluster-based paramagnetic species was detected. It was also found that the same signal can be induced by simply adding the product to reduced E126Q mutant enzyme. The signal should most likely be due to a $[4Fe\text{-}4S]^{1+}$ and not a $[4Fe\text{-}4S]^{3+}$. To clarify the oxidation state, the intermediate is currently under investigation using ^{57}Fe-ENDOR and Mössbauer. The FeS-III species is already present in the as-isolated as well as dithionite-reduced E126Q mutant IspH from *E. coli*. It is not clear why this does not happen for the *A. aeolicus* enzyme. Since both enzymes have similar Km and k_{cat} values we should expect the same to happen for the *A. aeolicus* enzyme. One possible explanation is that IspH and IspG and maybe some of the other DOXP enzymes, may form a complex where the substrates/products are directly transferred between the different enzymes. Pull down experiments with WT IspH and IspG from both organisms should be performed to test this hypothesis.

The loss of activity and formation of a paramagnetic intermediate different than the WT could support the role of Glu126 as a proton donor, however, the role might be more complex. Attempts to determine dependence of kinetic parameters of IspH on pH and hence identify the

ionizable amino acids were not successful. This was mainly due to the fact that the redox potential of the reductant dithionite is also highly pH dependent making it impossible to figure out a trend.

The fact that the signal develops much slower than the FeS-I species put doubt on the proposal that this species comes before the FeS-I species in the reaction mechanism. Most likely it is not catalytically competent. If we compare the behavior of the reduced Fe-S signal we see an almost immediate disappearance in the WT enzyme but a much slower change in the E126Q mutant. Assuming that the disappearance indicates the binding of the substrate it can be concluded that this is now much slower. We have to consider that the mutation of E126 into a Gln must have more than one effect. Something similar was found in previous work for the H42 residue, where mutation into an Ala completely removed all activity while mutation into a Phe salvaged a large part of the activity. We concluded that the local structure integrity must be affected by changing this residue. Something similar might be the case with the E126 residue, but on the other hand crystallization studies of WT and E126Q/D mutant IspH show no obvious changes in the local structure**.** Therefore mutating this residue also has a huge effect on the binding of substrate.

4.2 HdrA

The subunit A of heterodisulfide reductase (HdrA) from *M. marburgensis* was overexpressed in *M. maripaludis* and was successfully purified. HdrA is an iron-sulfur flavoprotein with four [4Fe-4S] clusters and one FAD. The Fe-S clusters are involved in electron transfer. The purified enzyme contained enough Fe ions to accommodate two [4Fe-4S] clusters. In vitro cluster reconstitution successfully increased the cluster content close to the expected four [4Fe-4S] clusters. In the redox titration of HdrA the signature EPR signal proposed to be due to a

[4Fe-4S] cluster that accepts the electrons from FAD was not detected. The titration was performed in the absence of FAD, this experiment has to be repeated in a buffer containing FAD. We did not observed an obvious binding of FAD but we cannot exclude that the presence of FAD might have an effect on the clusters.

The FAD in HdrA is the proposed site of the electron bifurcation, but in the purified enzyme the cofactor was absent. In vitro reconstitution of the FAD was not successful. Other subunits might be important for the proper binding of FAD to HdrA, and hence in the future HdrA will be coexpressed with HdrB and/or the HdrC subunits. In some methanogens the MvhD of the hydrogenase is fused to HdrA. Combination of the two subunits might be needed for the FAD binding and the bifurcation process. The HdrA and MvhD subunits from *M. marburgensis* have already been coexpression in *M. maripaludis* and will soon be available for study.

Reference

1. **Holstein SA**, **Hohl RJ**. 2004. Isoprenoids: Remarkable diversity of form and function. Lipids **39**:293–309.

2. **Wolfgang E**, **Felix R**, **Adelbert B**. 2001. Deoxyxylulose phosphate pathway to terpenoids. Trends Plant Sci **6**:78–84.

3. **Sacchettini JC**, **Poulter CD**. 1997. Creating Isoprenoid Diversity. Science **277**:1788–1789.

4. **Lange BM**, **Rujan T**, **Martin W**, **Croteau R**. 2000. Isoprenoid biosynthesis: The evolution of two ancient and distinct pathways across genomes. Proc Natl Acad Sci U S A **97**:13172–13177.

5. **Katsuki H**, **Bloch K**. 1967. Studies on the Biosynthesis of Ergosterol in Yeast. Formation of methylated intermediates. J Biol Chem **242**:222–227.

6. **Rohmer M**, **Knani M**, **Simonin P**, **Sutter B**, **Sahm H**. 1993. Isoprenoid biosynthesis in bacteria: a novel pathway for the early steps leading to isopentenyl diphosphate. Biochem J **295**:517–524.

7. **Lombard J**, **Moreira D**. 2011. Origins and Early Evolution of the Mevalonate Pathway of Isoprenoid Biosynthesis in the Three Domains of Life. Mol Biol Evol **28**:87–99.

8. **Miziorko HM**. 2011. Enzymes of the mevalonate pathway of isoprenoid biosynthesis. Arch Biochem Biophys **505**:131–143.

9. **Vinokur JM**, **Korman TP**, **Cao Z**, **Bowie JU**. 2014. Evidence of a Novel Mevalonate Pathway in Archaea. Biochemistry (Mosc) **53**:4161–4168.

10. **Dellas N**, **Thomas ST**, **Manning G**, **Noel JP**. 2013. Discovery of a metabolic alternative to the classical mevalonate pathway. eLife **2**.

11. **Vannice JC**, **Skaff DA**, **Keightley A**, **Addo JK**, **Wyckoff GJ**, **Miziorko HM**. 2014. Identification in *Haloferax volcanii* of phosphomevalonate decarboxylase and isopentenyl phosphate kinase as catalysts of the terminal enzyme reactions in an archaeal alternate mevalonate pathway. J Bacteriol **196**:1055–1063.

12. **Eisenreich W**, **Schwarz M**, **Cartayrade A**, **Arigoni D**, **Zenk MH**, **Bacher A**. 1998. The deoxyxylulose phosphate pathway of terpenoid biosynthesis in plants and microorganisms. Chem Biol **5**:221–233.

13. **Rohmer M**. 1999. The discovery of a mevalonate-independent pathway for isoprenoid biosynthesis in bacteria, algae and higher plants. Nat Prod Rep **16**:565–574.

14. **Arigoni D**, **Sagner S**, **Latzel C**, **Eisenreich W**, **Bacher A**, **Zenk MH**. 1997. Terpenoid biosynthesis from 1-deoxy-D-xylulose in higher plants by intramolecular skeletal rearrangement. Proc Natl Acad Sci **94**:10600–10605.

15. **Thomas J. Bach**, **Hartmut K. Lichtenthaler**. 1987. Plant Growth Regulation by Mevinolin and Other Sterol Biosynthesis Inhibitors. In Ecology and Metabolism of Plant Lipids. American Chemical Society. 109–139.

16. **Zhang M**, **Li K**, **Zhang C**, **Gai J**, **Yu D**. 2009. Identification and characterization of class 1 DXS gene encoding 1-deoxy-D-xylulose-5-phosphate synthase, the first committed enzyme of the MEP pathway from soybean. Mol Biol Rep **36**:879–887.

17. **Eisenreich W**, **Bacher A**, **Arigoni D**, **Rohdich F**. 2004. Biosynthesis of isoprenoids via the non-mevalonate pathway. Cell Mol Life Sci **61**.

18. **Eubanks LM**, **Poulter CD**. 2003. *Rhodobacter capsulatus* 1-deoxy-D-xylulose-5-Phosphate Synthase: Steady-State Kinetics and Substrate Binding. Biochemistry (Mosc) **42**:1140–1149.

19. **Wiesner J**, **Jomaa H**. 2007. Isoprenoid Biosynthesis of the Apicoplast as Drug Target. Curr Drug Targets **8**:3–13.

20. **Hoeffler J-F**, **Tritsch D**, **Grosdemange-Billiard C**, **Rohmer M**. 2002. Isoprenoid biosynthesis via the methylerythritol phosphate pathway. Mechanistic investigations of the 1-deoxy-D-xylulose-5-phosphate reductoisomerase. Eur J Biochem FEBS **269**:4446–4457.

21. **Kuzuyama T**, **Takagi M**, **Kaneda K**, **Dairi T**, **Seto H**. 2000. Formation of 4-(cytidine 5′-diphospho)-2-*C*-methyl-D-erythritol from 2-*C*-methyl-D-erythritol-4-phosphate by 2-*C*-methyl-D-erythritol-4-phosphate cytidylyltransferase, a new enzyme in the nonmevalonate pathway. Tetrahedron Lett **41**:703–706.

22. **Rohdich F**, **Wungsintaweekul J**, **Fellermeier M**, **Sagner S**, **Herz S**, **Kis K**, **Eisenreich W**, **Bacher A**, **Zenk MH**. 1999. Cytidine 5′-triphosphate-dependent biosynthesis of isoprenoids: YgbP protein of *Escherichia coli* catalyzes the formation of 4-diphosphocytidyl-2-*C*-methylerythritol. Proc Natl Acad Sci U S A **96**:11758–11763.

23. **Herz S**, **Wungsintaweekul J**, **Schuhr CA**, **Hecht S**, **Luttgen H**, **Sagner S**, **Fellermeier M**, **Eisenreich W**, **Zenk MH**, **Bacher A**, **Rohdich F**. 2000. Biosynthesis of terpenoids: YgbB protein converts 4-diphosphocytidyl-2C-methyl-D-erythritol 2-phosphate to 2-*C*-methyl-D-erythritol 2,4-cyclodiphosphate. Proc Natl Acad Sci U S A **97**:2486–2490.

24. **Kuzuyama T**, **Takagi † M**, **Kaneda K**, **Watanabe H**, **Dairi T**, **Seto H**. 2000. Studies on the nonmevalonate pathway: conversion of 4-(cytidine 5′-diphospho)- 2-*C*-methyl-D-erythritol to its 2-phospho derivative by 4-(cytidine 5′-diphospho)-2-*C*-methyl-D-erythritol kinase. Tetrahedron Lett **41**:2925–2928.

25. **Miallau L**, **Alphey MS**, **Kemp LE**, **Leonard GA**, **McSweeney SM**, **Hecht S**, **Bacher A**, **Eisenreich W**, **Rohdich F**, **Hunter WN**. 2003. Biosynthesis of isoprenoids: Crystal

structure of 4-diphosphocytidyl-2-*C*-methyl-D-erythritol kinase. Proc Natl Acad Sci **100**:9173–9178.

26. **Lüttgen H**, **Rohdich F**, **Herz S**, **Wungsintaweekul J**, **Hecht S**, **Schuhr CA**, **Fellermeier M**, **Sagner S**, **Zenk MH**, **Bacher A**, **Eisenreich W**. 2000. Biosynthesis of terpenoids: YchB protein of *Escherichia coli* phosphorylates the 2-hydroxy group of 4-diphosphocytidyl-2-*C*-methyl-D-erythritol. Proc Natl Acad Sci U S A **97**:1062–1067.

27. **Richard SB**, **Ferrer J-L**, **Bowman ME**, **Lillo AM**, **Tetzlaff CN**, **Cane DE**, **Noel JP**. 2002. Structure and Mechanism of 2-*C*-methyl-D-erythritol-2,4-cyclodiphosphate Synthase an enzyme in the mevalonate-independent isoprenoid biosynthetic pathway. J Biol Chem **277**:8667–8672.

28. **Altincicek B**, **Kollas A-K**, **Sanderbrand S**, **Wiesner J**, **Hintz M**, **Beck E**, **Jomaa H**. 2001. GcpE Is Involved in the 2-*C*-methyl-D-erythritol-4-phosphate Pathway of Isoprenoid Biosynthesis in *Escherichia coli*. J Bacteriol **183**:2411–2416.

29. **Kollas A-K**, **Duin EC**, **Eberl M**, **Altincicek B**, **Hintz M**, **Reichenberg A**, **Henschker D**, **Henne A**, **Steinbrecher I**, **Ostrovsky DN**, **others**. 2002. Functional characterization of GcpE, an essential enzyme of the non-mevalonate pathway of isoprenoid biosynthesis. FEBS Lett **532**:432–436.

30. **Altincicek B**, **Kollas A-K**, **Eberl M**, **Wiesner J**, **Sanderbrand S**, **Hintz M**, **Beck E**, **Jomaa H**. 2001. LytB, a novel gene of the 2-*C*-methyl-D-erythritol-4-phosphate pathway of isoprenoid biosynthesis in *Escherichia coli*. FEBS Lett **499**:37–40.

31. **Wolff M**, **Seemann M**, **Tse Sum Bui B**, **Frapart Y**, **Tritsch D**, **Estrabot AG**, **Rodríguez-Concepción M**, **Boronat A**, **Marquet A**, **Rohmer M**. 2003. Isoprenoid biosynthesis via the methylerythritol phosphate pathway: the (*E*)-4-hydroxy-3-methylbut-2-enyl diphosphate reductase (LytB/IspH) from *Escherichia coli* is a [4Fe–4S] protein. FEBS Lett **541**:115–120.

32. **Carretero-Paulet L**, **Cairó A**, **Botella-Pavía P**, **Besumbes O**, **Campos N**, **Boronat A**, **Rodríguez-Concepción M**. 2006. Enhanced flux through the methylerythritol 4-phosphate pathway in *Arabidopsis* plants overexpressing deoxyxylulose 5-phosphate reductoisomerase. Plant Mol Biol **62**:683–695.

33. **Mao J**, **Eoh H**, **He R**, **Wang Y**, **Wan B**, **Franzblau SG**, **Crick DC**, **Kozikowski AP**. 2008. Structure–activity relationships of compounds targeting mycobacterium tuberculosis 1-deoxy-D-xylulose-5-phosphate synthase. Bioorg Med Chem Lett **18**:5320–5323.

34. **Humnabadkar V**, **Jha RK**, **Ghatnekar N**, **Sousa SMD**. 2011. A High-Throughput Screening Assay for Simultaneous Selection of Inhibitors of *Mycobacterium tuberculosis* 1-deoxy-D-xylulose-5-phosphate Synthase (Dxs) or 1-Deoxy-D-Xylulose-5-Phosphate Reductoisomerase (Dxr). J Biomol Screen **16**:303–312.

35. **Banerjee A**, **Wu Y**, **Banerjee R**, **Li Y**, **Yan H**, **Sharkey TD**. 2013. Feedback Inhibition of 1-deoxy-D-xylulose-5-phosphate Synthase Regulates the Methylerythritol 4-Phosphate Pathway. J Biol Chem **288**:16926–16936.

36. **Kuzuyama T**, **Shimizu T**, **Takahashi S**, **Seto H**. 1998. Fosmidomycin, a specific inhibitor of 1-deoxy-D-xylulose-5-phosphate reductoisomerase in the nonmevalonate pathway for terpenoid biosynthesis. Tetrahedron Lett **39**:7913–7916.

37. **Murkin AS**, **Manning KA**, **Kholodar SA**. 2014. Mechanism and inhibition of 1-deoxy-D-xylulose-5-phosphate reductoisomerase. Bioorganic Chem **57**:171–185.

38. **Zeidler J**, **Schwender J**, **Müller C**, **Wiesner J**, **Weidemeyer C**, **Beck E**, **Jomaa H**, **Lichtenthaler HK**. 2014. Inhibition of the Non-Mevalonate 1-deoxy-D-xylulose-5-phosphate Pathway of Plant Isoprenoid Biosynthesis by Fosmidomycin. Z Für Naturforschung C **53**:980–986.

39. **Jomaa H**, **Wiesner J**, **Sanderbrand S**, **Altincicek B**, **Weidemeyer C**, **Hintz M**, **Türbachova I**, **Eberl M**, **Zeidler J**, **Lichtenthaler HK**, **Soldati D**, **Beck E**. 1999. Inhibitors of the Nonmevalonate Pathway of Isoprenoid Biosynthesis as Antimalarial Drugs. Science **285**:1573–1576.

40. **Witschel MC**, **Höffken HW**, **Seet M**, **Parra L**, **Mietzner T**, **Thater F**, **Niggeweg R**, **Röhl F**, **Illarionov B**, **Rohdich F**, **Kaiser J**, **Fischer M**, **Bacher A**, **Diederich F**. 2011. Inhibitors of the Herbicidal Target IspD: Allosteric Site Binding. Angew Chem Int Ed **50**:7931–7935.

41. **Kunfermann A**, **Witschel M**, **Illarionov B**, **Martin R**, **Rottmann M**, **Höffken HW**, **Seet M**, **Eisenreich W**, **Knölker H-J**, **Fischer M**, **Bacher A**, **Groll M**, **Diederich F**. 2014. Pseudilins: Halogenated, Allosteric Inhibitors of the Non-Mevalonate Pathway Enzyme IspD. Angew Chem Int Ed **53**:2235–2239.

42. **Lillo AM**, **Tetzlaff CN**, **Sangari FJ**, **Cane DE**. 2003. Functional expression and characterization of eryA, the erythritol kinase of *Brucella abortus*, and enzymatic synthesis of l-Erythritol-4-phosphate. Bioorg Med Chem Lett **13**:737–739.

43. **Crane CM**, **Hirsch AKH**, **Alphey MS**, **Sgraja T**, **Lauw S**, **Illarionova V**, **Rohdich F**, **Eisenreich W**, **Hunter WN**, **Bacher A**, **Diederich F**. 2008. Synthesis and Characterization of Cytidine Derivatives that Inhibit the Kinase IspE of the Non-Mevalonate Pathway for Isoprenoid Biosynthesis. ChemMedChem **3**:91–101.

44. **Crane CM**, **Kaiser J**, **Ramsden NL**, **Lauw S**, **Rohdich F**, **Eisenreich W**, **Hunter WN**, **Bacher A**, **Diederich F**. 2006. Fluorescent Inhibitors for IspF, an Enzyme in the Non-Mevalonate Pathway for Isoprenoid Biosynthesis and a Potential Target for Antimalarial Therapy. Angew Chem Int Ed **45**:1069–1074.

45. **Mombelli P**, **Le Chapelain C**, **Munzinger N**, **Joliat E**, **Illarionov B**, **Schweizer WB**, **Hirsch AKH**, **Fischer M**, **Bacher A**, **Diederich F**. 2013. Imidazole- and Benzimidazole-

Based Inhibitors of the Kinase IspE: Targeting the Substrate-Binding Site and the Triphosphate-Binding Loop of the ATP Site. Eur J Org Chem **2013**:1068–1079.

46. **Nakagawa K**, **Takada K**, **Imamura N**. 2013. Probable novel MEP pathway inhibitor and its binding protein, IspG. Biosci Biotechnol Biochem **77**:1449–1454.

47. **Wang W**, **Oldfield E**. 2014. Bioorganometallic Chemistry with IspG and IspH: Structure, Function, and Inhibition of the [4Fe-4S] Proteins Involved in Isoprenoid Biosynthesis. Angew Chem Int Ed **53**:4294–4310.

48. **Lell B**, **Ruangweerayut R**, **Wiesner J**, **Missinou MA**, **Schindler A**, **Baranek T**, **Hintz M**, **Hutchinson D**, **Jomaa H**, **Kremsner PG**. 2003. Fosmidomycin, a novel chemotherapeutic agent for malaria. Antimicrob Agents Chemother **47**:735–738.

49. **Borrmann S**, **Adegnika AA**, **Matsiegui P-B**, **Issifou S**, **Schindler A**, **Mawili-Mboumba DP**, **Baranek T**, **Wiesner J**, **Jomaa H**, **Kremsner PG**. 2004. Fosmidomycin-clindamycin for Plasmodium falciparum Infections in African children. J Infect Dis **189**:901–908.

50. **Zerbe P**, **Bohlmann J**. 2015. Plant diterpene synthases: exploring modularity and metabolic diversity for bioengineering. Trends Biotechnol **33**:419–428.

51. **Matsuda K**, **Kikuta Y**, **Haba A**, **Nakayama K**, **Katsuda Y**, **Hatanaka A**, **Komai K**. 2005. Biosynthesis of pyrethrin I in seedlings of *Chrysanthemum cinerariaefolium*. Phytochemistry **66**:1529–1535.

52. **Jordan MA**, **Wilson L**. 2004. Microtubules as a target for anticancer drugs. Nat Rev Cancer **4**:253–265.

53. **Raja R**, **Hemaiswarya S**, **Rengasamy R**. 2007. Exploitation of *Dunaliella* for beta-carotene production. Appl Microbiol Biotechnol **74**:517–523.

54. **Ajikumar PK**, **Xiao W-H**, **Tyo KEJ**, **Wang Y**, **Simeon F**, **Leonard E**, **Mucha O**, **Phon TH**, **Pfeifer B**, **Stephanopoulos G**. 2010. Isoprenoid Pathway Optimization for Taxol Precursor Overproduction in *Escherichia coli.* Science **330**:70–74.

55. **Yuan LZ**, **Rouvière PE**, **LaRossa RA**, **Suh W**. 2006. Chromosomal promoter replacement of the isoprenoid pathway for enhancing carotenoid production in *E. coli*. Metab Eng **8**:79–90.

56. **Harker M**, **Bramley PM**. 1999. Expression of prokaryotic 1-deoxy-D-xylulose-5-phosphatases in *Escherichia coli* increases carotenoid and ubiquinone biosynthesis. FEBS Lett **448**:115–119.

57. **Kim SW**, **Keasling JD**. 2001. Metabolic engineering of the nonmevalonate isopentenyl diphosphate synthesis pathway in *Escherichia coli* enhances lycopene production. Biotechnol Bioeng **72**:408–415.

58. **Rohdich F**, **Bacher A**, **Eisenreich W**, **others**. 2005. Isoprenoid biosynthetic pathways as anti-infective drug targets. Biochem Soc Trans **33**:785–791.

59. **Johnson DC**, **Dean DR**, **Smith AD**, **Johnson MK**. 2005. Structure, Function, and Formation of Biological Iron-sulfur Clusters. Annu Rev Biochem **74**:247–281.

60. 1979. Nomenclature of Iron-sulfur Proteins. Eur J Biochem **93**:427–430.

61. **Meyer J**, **Gagnon J**, **Gaillard J**, **Lutz M**, **Achim C**, **Münck E**, **Pétillot Y**, **Colangelo CM**, **Scott RA**. 1997. Assembly of a $[2Fe\text{-}2S]^{2+}$ cluster in a molecular variant of *Clostridium pasteurianum* rubredoxin. Biochemistry (Mosc) **36**:13374–13380.

62. **Crack JC**, **Green J**, **Cheesman MR**, **Brun NEL**, **Thomson AJ**. 2007. Superoxide-mediated amplification of the oxygen-induced switch from [4Fe-4S] to [2Fe-2S] clusters in the transcriptional regulator FNR. Proc Natl Acad Sci **104**:2092–2097.

63. **Kent TA**, **Dreyer JL**, **Kennedy MC**, **Huynh BH**, **Emptage MH**, **Beinert H**, **Münck E**. 1982. Mössbauer studies of beef heart aconitase: evidence for facile interconversions of iron-sulfur clusters. Proc Natl Acad Sci U S A **79**:1096–1100.

64. **Kennedy MC**, **Emptage MH**, **Beinert H**. 1984. Incorporation of ^{35}S-sulfide into the Fe-S cluster of aconitase. J Biol Chem **259**:3145–3151.

65. **Plank DW**, **Kennedy MC**, **Beinert H**, **Howard JB**. 1989. Cysteine labeling studies of beef heart aconitase containing a 4Fe, a cubane 3Fe, or a linear 3Fe cluster. J Biol Chem **264**:20385–20393.

66. **Michael K. Johnson**. 1994. Iron-sulfur Proteins, Encyclopedia of Inorganic Chemistry. Wiley, New York, USA.

67. **Beinert H**. 1997. Iron-sulfur Clusters: Nature's Modular, Multipurpose Structures. Science **277**:653–659.

68. **Rees DC**. 2002. Great Metalloclusters in Enzymology. Annu Rev Biochem **71**:221–246.

69. **Capozzi F**, **Ciurli S**, **Luchinat C**. 1998. Coordination sphere versus protein environment as determinants of electronic and functional properties of iron-sulfur proteins, p. 127–160. In Metal Sites in Proteins and Models Redox Centres. Springer.

70. **J R Mason**, **Cammack R**. 1992. The Electron-Transport Proteins of Hydroxylating Bacterial Dioxygenases. Annu Rev Microbiol **46**:277–305.

71. **Beinert H**. 2000. Iron-sulfur proteins: ancient structures, still full of surprises. J Biol Inorg Chem **5**:2–15.

72. **Angove HC**, **Yoo SJ**, **Münck E**, **Burgess BK**. 1998. An All-ferrous State of the Fe Protein of Nitrogenase. Interaction with nucleotides and electron transfer to the MoFe protein. J Biol Chem **273**:26330–26337.

73. **Noodleman L**, **Lovell T**, **Liu T**, **Himo F**, **Torres RA**. 2002. Insights into properties and energetics of iron–sulfur proteins from simple clusters to nitrogenase. Curr Opin Chem Biol **6**:259–273.

74. **Robbins AH**, **Stout CD**. 1985. Iron-sulfur cluster in aconitase. Crystallographic evidence for a three-iron center. J Biol Chem **260**:2328–2333.

75. **Emptage MH**, **Dreyers JL**, **Kennedy MC**, **Beinert H**. 1983. Optical and EPR characterization of different species of active and inactive aconitase. J Biol Chem **258**:11106–11111.

76. **Emptage MH**, **Kent TA**, **Kennedy MC**, **Beinert H**, **Münck E**. 1983. Mössbauer and EPR studies of activated aconitase: development of a localized valence state at a subsite of the [4Fe-4S] cluster on binding of citrate. Proc Natl Acad Sci **80**:4674–4678.

77. **Beinert H**, **Kennedy MC**, **Stout CD**. 1996. Aconitase as iron-sulfur protein, enzyme, and iron-regulatory protein. Chem Rev **96**:2335–2374.

78. **Lauble H**, **Kennedy MC**, **Beinert H**, **Stout CD**. 1994. Crystal Structures of Aconitase with Trans-aconitate and Nitrocitrate Bound. J Mol Biol **237**:437–451.

79. **Walters EM**, **Johnson MK**. 2004. Ferredoxin:thioredoxin Reductase: Disulfide Reduction Catalyzed via Novel Site-specific [4Fe-4S] Cluster Chemistry. Photosynth Res **79**:249–264.

80. **Walters EM**, **Garcia-Serres R**, **Jameson GNL**, **Glauser DA**, **Bourquin F**, **Manieri W**, **Schürmann P**, **Johnson MK**, **Huynh BH**. 2005. Spectroscopic Characterization of Site-Specific [4Fe-4S] Cluster Chemistry in Ferredoxin:Thioredoxin Reductase: Implications for the Catalytic Mechanism. J Am Chem Soc **127**:9612–9624.

81. **Dai S**, **Friemann R**, **Glauser DA**, **Bourquin F**, **Manieri W**, **Schürmann P**, **Eklund H**. 2007. Structural snapshots along the reaction pathway of ferredoxin:thioredoxin reductase. Nature **448**:92–96.

82. **Jameson GNL**, **Walters EM**, **Manieri W**, **Schürmann P**, **Johnson MK**, **Huynh BH**. 2003. Spectroscopic Evidence for Site Specific Chemistry at a Unique Iron Site of the [4Fe-4S] Cluster in Ferredoxin:Thioredoxin Reductase. J Am Chem Soc **125**:1146–1147.

83. **Staples CR**, **Gaymard E**, **Stritt-Etter A-L**, **Telser J**, **Hoffman BM**, **Schürmann P**, **Knaff DB**, **Johnson MK**. 1998. Role of the [Fe4-S4] Cluster in Mediating Disulfide Reduction in Spinach Ferredoxin:Thioredoxin Reductase. Biochemistry (Mosc) **37**:4612–4620.

84. **Adedeji D**, **Hernandez H**, **Wiesner J**, **Köhler U**, **Jomaa H**, **Duin EC**. 2007. Possible direct involvement of the active-site [4Fe–4S] cluster of the GcpE enzyme from *Thermus thermophilus* in the conversion of MEcPP. FEBS Lett **581**:279–283.

85. **Rekittke I**, **Jomaa H**, **Ermler U**. 2012. Structure of the GcpE (IspG)-MEcPP complex from *Thermus thermophilus*. FEBS Lett **586**:3452–3457.

86. **Seemann M**, **Wegner P**, **Schunemann V**, **Bui BTS**, **Wolff M**, **Marquet A**, **Trautwein AX**, **Rohmer M**. 2005. Isoprenoid biosynthesis in chloroplasts via the methylerythritol phosphate pathway: the (*E*)-4-hydroxy-3-methylbut-2-enyl diphosphate synthase (GcpE) from Arabidopsis thaliana is a [4Fe-4S] protein. J Biol Inorg Chem **10**:131–137.

87. **Xu W**, **Lees NS**, **Adedeji D**, **Wiesner J**, **Jomaa H**, **Hoffman BM**, **Duin EC**. 2010. Paramagnetic Intermediates of (*E)*-4-hydroxy-3-methylbut-2-enyl Diphosphate Synthase (GcpE/IspG) under Steady-State and Pre-Steady-State Conditions. J Am Chem Soc **132**:14509–14520.

88. **Quitterer F**, **Frank A**, **Wang K**, **Rao G**, **O'Dowd B**, **Li J**, **Guerra F**, **Abdel-Azeim S**, **Bacher A**, **Eppinger J**, **Oldfield E**, **Groll M**. 2015. Atomic-Resolution Structures of Discrete Stages on the Reaction Coordinate of the [4Fe-4S] Enzyme IspG (GcpE). J Mol Biol **427**:2220–2228.

89. **Palmer G**. 1985. The electron paramagnetic resonance of metalloproteins. Biochem Soc Trans **13**:548–560.

90. **Hagen WR**. 2006. EPR spectroscopy as a probe of metal centres in biological systems. Dalton Trans 4415–4434.

91. **Cammack R**, **Patil DS**, **Fernandez VM**. 1985. Electron-spin-resonance/electron-paramagnetic-resonance spectroscopy of iron-sulphur enzymes. Biochem Soc Trans **13**:572–578.

92. **Graham Palmer**, **Lawrence Que Jr**. 2000. Electron Paramagnetic Resonance in Metaloproteins. University Science Books, Sausalito, California.

93. **Cutsail GE**, **Telser J**, **Hoffman BM**. 2015. Advanced paramagnetic resonance spectroscopies of iron–sulfur proteins: Electron nuclear double resonance (ENDOR) and electron spin echo envelope modulation (ESEEM). Biochim Biophys Acta BBA - Mol Cell Res **1853**:1370–1394.

94. **Chasteen ND**, **Snetsinger PA**, **Que Jr L**. 2000. ESEEM and ENDOR Spectroscopy. University Science Books, Sausalito, California.

95. **Munck E**, **Que Jr L**. 2000. Aspects of ^{57}Fe Mössbauer Spectroscopy. University Science Books, Sausalito, California.

96. **Gütlich P**. 2012. Fifty Years of Mössbauer Spectroscopy in Solid State Research - Remarkable Achievements, Future Perspectives. Z Für Anorg Allg Chem **638**:15–43.

97. **Bill E**. 2012. Iron-sulfur clusters—new features in enzymes and synthetic models. Hyperfine Interact **205**:139–147.

98. **Middleton P**, **Dickson DPE**, **Johnson CE**, **Rush JD**. 1980. Interpretation of the Mössbauer Spectra of the High-Potential Iron Protein from *Chromatium.* Eur J Biochem **104**:289–296.

99. **Cosper MM**, **Jameson GN.**, **Eidsness MK**, **Huynh BH**, **Johnson MK**. 2002. Recombinant *Escherichia coli* biotin synthase is a $[2Fe–2S]^{2+}$ protein in whole cells. FEBS Lett **529**:332–336.

100. **Altincicek B**, **Duin EC**, **Reichenberg A**, **Hedderich R**, **Kollas A-K**, **Hintz M**, **Wagner S**, **Wiesner J**, **Beck E**, **Jomaa H**. 2002. LytB protein catalyzes the terminal step of the 2-*C*-methyl-D-erythritol-4-phosphate pathway of isoprenoid biosynthesis. FEBS Lett **532**:437–440.

101. **Rohdich F**, **Hecht S**, **Gärtner K**, **Adam P**, **Krieger C**, **Amslinger S**, **Arigoni D**, **Bacher A**, **Eisenreich W**. 2002. Studies on the nonmevalonate terpene biosynthetic pathway: metabolic role of IspH (LytB) protein. Proc Natl Acad Sci **99**:1158–1163.

102. **Xiao Y**, **Chu L**, **Sanakis Y**, **Liu P**. 2009. Revisiting the IspH Catalytic System in the Deoxyxylulose Phosphate Pathway: Achieving High Activity. J Am Chem Soc **131**:9931–9933.

103. **Xu W**, **Lees NS**, **Hall D**, **Welideniya D**, **Hoffman BM**, **Duin EC**. 2012. A Closer Look at the Spectroscopic Properties of Possible Reaction Intermediates in Wild-Type and Mutant (*E*)-4-Hydroxy-3-methylbut-2-enyl Diphosphate Reductase. Biochemistry (Mosc) **51**:4835–4849.

104. **Gräwert T**, **Kaiser J**, **Zepeck F**, **Laupitz R**, **Hecht S**, **Amslinger S**, **Schramek N**, **Schleicher E**, **Weber S**, **Haslbeck M**, **Buchner J**, **Rieder C**, **Arigoni D**, **Bacher A**, **Eisenreich W**, **Rohdich F**. 2004. IspH Protein of *Escherichia coli*: Studies on Iron−Sulfur Cluster Implementation and Catalysis. J Am Chem Soc **126**:12847–12855.

105. **Span I**, **Wang K**, **Wang W**, **Zhang Y**, **Bacher A**, **Eisenreich W**, **Li K**, **Schulz C**, **Oldfield E**, **Groll M**. 2012. Discovery of acetylene hydratase activity of the iron–sulphur protein IspH. Nat Commun **3**:1042.

106. **Gräwert T**, **Rohdich F**, **Span I**, **Bacher A**, **Eisenreich W**, **Eppinger J**, **Groll M**. 2009. Structure of Active IspH Enzyme from *Escherichia coli* Provides Mechanistic Insights into Substrate Reduction. Angew Chem Int Ed **48**:5756–5759.

107. **Rekittke I**, **Wiesner J**, **Röhrich R**, **Demmer U**, **Warkentin E**, **Xu W**, **Troschke K**, **Hintz M**, **No JH**, **Duin EC**, **Oldfield E**, **Jomaa H**, **Ermler U**. 2008. Structure of (*E*)-4-hydroxy-3-methyl-but-2-enyl diphosphate reductase, the terminal enzyme of the non-mevalonate pathway. J Am Chem Soc **130**:17206–17207.

108. **Seemann M**, **Janthawornpong K**, **Schweizer J**, **Böttger LH**, **Janoschka A**, **Ahrens-Botzong A**, **Tambou EN**, **Rotthaus O**, **Trautwein AX**, **Rohmer M**, **Volker Schünemann**. 2009. Isoprenoid Biosynthesis via the MEP Pathway: In Vivo Mössbauer

Spectroscopy Identifies a [4Fe-4S]$^{2+}$ Center with Unusual Coordination Sphere in the LytB Protein. J Am Chem Soc **131**:13184–13185.

109. **Ahrens-Botzong A**, **Janthawornpong K**, **Wolny JA**, **Tambou EN**, **Rohmer M**, **Krasutsky S**, **Poulter CD**, **Schünemann V**, **Seemann M**. 2011. Biosynthesis of Isoprene Units: Mössbauer Spectroscopy of Substrate and Inhibitor Binding to the [4Fe-4S] Cluster of the LytB/IspH Enzyme. Angew Chem Int Ed **50**:11976–11979.

110. **Grawert T**, **Span I**, **Eisenreich W**, **Rohdich F**, **Eppinger J**, **Bacher A**, **Groll M**. 2010. Probing the reaction mechanism of IspH protein by x-ray structure analysis. Proc Natl Acad Sci **107**:1077–1081.

111. **Span I**, **Gräwert T**, **Bacher A**, **Eisenreich W**, **Groll M**. 2012. Crystal Structures of Mutant IspH Proteins Reveal a Rotation of the Substrate's Hydroxymethyl Group during Catalysis. J Mol Biol **416**:1–9.

112. **Madadi-Kahkesh S**, **Duin EC**, **Heim S**, **Albracht SP**, **Johnson MK**, **Hedderich R**. 2001. A paramagnetic species with unique EPR characteristics in the active site of heterodisulfide reductase from methanogenic archaea. Eur J Biochem **268**:2566–2577.

113. **Wang W**, **Wang K**, **Span I**, **Jauch J**, **Bacher A**, **Groll M**, **Oldfield E**. 2012. Are Free Radicals Involved in IspH Catalysis? An EPR and Crystallographic Investigation. J Am Chem Soc **134**:11225–11234.

114. **Li J**, **Wang K**, **Smirnova TI**, **Khade RL**, **Zhang Y**, **Oldfield E**. 2013. Isoprenoid Biosynthesis: Ferraoxetane or Allyl Anion Mechanism for IspH Catalysis? Angew Chem Int Ed **52**:6522–6525.

115. **Chang W**, **Xiao Y**, **Liu H**, **Liu P**. 2011. Mechanistic Studies of an IspH-Catalyzed Reaction: Implications for Substrate Binding and Protonation in the Biosynthesis of Isoprenoids. Angew Chem Int Ed **50**:12304–12307.

116. **Wang W**, **Wang K**, **Liu Y-L**, **No J-H**, **Li J**, **Nilges MJ**, **Oldfield E**. 2010. Bioorganometallic mechanism of action, and inhibition, of IspH. Proc Natl Acad Sci **107**:4522–4527.

117. **Xiao Y**, **Chang W**, **Liu H**, **Liu P**. 2011. Study of IspH, a Key Enzyme in the Methylerythritol Phosphate Pathway Using Fluoro-Substituted Substrate Analogs. Org Lett **13**:5912–5915.

118. **Rohdich F**, **Zepeck F**, **Adam P**, **Hecht S**, **Kaiser J**, **Laupitz R**, **Gräwert T**, **Amslinger S**, **Eisenreich W**, **Bacher A**, **others**. 2003. The deoxyxylulose phosphate pathway of isoprenoid biosynthesis: studies on the mechanisms of the reactions catalyzed by IspG and IspH protein. Proc Natl Acad Sci **100**:1586–1591.

119. **World Health Organization**. 2015 World malaria report.

120. **World Health Organization**. 2015 Global tuberculosis report.

121. **Tanwar J**, **Das S**, **Fatima Z**, **Hameed S**, **Tanwar J**, **Das S**, **Fatima Z**, **Hameed S**. 2014. Multidrug Resistance: An Emerging Crisis, Multidrug Resistance: An Emerging Crisis. Interdiscip Perspect Infect Dis Interdiscip Perspect Infect Dis: e541340.

122. **Span I**, **Wang K**, **Wang W**, **Jauch J**, **Eisenreich W**, **Bacher A**, **Oldfield E**, **Groll M**. 2013. Structures of Fluoro, Amino, and Thiol Inhibitors Bound to the [4Fe-4S] Protein IspH. Angew Chem Int Ed **52**:2118–2121.

123. **Wang K**, **Wang W**, **No J-H**, **Zhang Y**, **Zhang Y**, **Oldfield E**. 2010. Inhibition of the Fe4S4-Cluster-Containing Protein IspH (LytB): Electron Paramagnetic Resonance, Metallacycles, and Mechanisms. J Am Chem Soc **132**:6719–6727.

124. **Span I**, **Wang K**, **Eisenreich W**, **Bacher A**, **Zhang Y**, **Oldfield E**, **Groll M**. 2014. Insights into the Binding of Pyridines to the Iron–Sulfur Enzyme IspH. J Am Chem Soc **136**:7926–7932.

125. **Hecht S**, **Amslinger S**, **Jauch J**, **Kis K**, **Trentinaglia V**, **Adam P**, **Eisenreich W**, **Bacher A**, **Rohdich F**. 2002. Studies on the non-mevalonate isoprenoid biosynthetic pathway. Simple methods for preparation of isotope-labeled (*E*)-1-hydroxy-2-methylbut-2-enyl 4-diphosphate. Tetrahedron Lett **43**:8929–8933.

126. 1988. Trisammonium geranyl diphosphate. Org Synth **66**:211.

127. **Bradford MM**. 1976. A rapid and sensitive method for the quantitation of microgram quantities of protein utilizing the principle of protein-dye binding. Anal Biochem **72**:248–254.

128. **Fish WW**. 1988. Rapid colorimetric micromethod for the quantitation of complexed iron in biological samples. Methods Enzymol **158**:357–364.

129. **Beinert H**, **Albracht SP**. 1982. New insights, ideas and unanswered questions concerning iron-sulfur clusters in mitochondria. Biochim Biophys Acta **683**:245–277.

130. **Hagen W**. 2008. Biomolecular EPR Spectroscopy. CRC Press.

131. **Mouesca J-M**, **Lamotte B**. 1998. Iron–sulfur clusters and their electronic and magnetic properties. Coord Chem Rev **178–180, Part 2**:1573–1614.

132. **Bennati M**, **Weiden N**, **Dinse K-P**, **Hedderich R**. 2004. ^{57}Fe ENDOR Spectroscopy on the Iron−Sulfur Cluster Involved in Substrate Reduction of Heterodisulfide Reductase. J Am Chem Soc **126**:8378–8379.

133. **Mouesca J-M**, **Noodleman L**, **Case DA**, **Lamotte B**. 1995. Spin Densities and Spin Coupling in Iron-sulfur Clusters: A New Analysis of Hyperfine Coupling Constants. Inorg Chem **34**:4347–4359.

134. **Blachly PG**, **Sandala GM**, **Giammona DA**, **Bashford D**, **McCammon JA**, **Noodleman L**. 2015. Broken-Symmetry DFT Computations for the Reaction Pathway of IspH, an Iron–Sulfur Enzyme in Pathogenic Bacteria. Inorg Chem **54**:6439–6461.

135. **Buckel W**, **Thauer RK**. 2013. Energy conservation via electron bifurcating ferredoxin reduction and proton/Na^+ translocating ferredoxin oxidation. Biochim Biophys Acta BBA - Bioenerg **1827**:94–113.

136. **Brandt U**. 1996. Bifurcated ubihydroquinone oxidation in the cytochrome bc1 complex by proton-gated charge transfer. FEBS Lett **387**:1–6.

137. **Li F**, **Hinderberger J**, **Seedorf H**, **Zhang J**, **Buckel W**, **Thauer RK**. 2008. Coupled Ferredoxin and Crotonyl Coenzyme A (CoA) Reduction with NADH Catalyzed by the Butyryl-CoA Dehydrogenase/Etf Complex from *Clostridium kluyveri*. J Bacteriol **190**:843–850.

138. **Chowdhury NP**, **Mowafy AM**, **Demmer JK**, **Upadhyay V**, **Koelzer S**, **Jayamani E**, **Kahnt J**, **Hornung M**, **Demmer U**, **Ermler U**, **Buckel W**. 2014. Studies on the Mechanism of Electron Bifurcation Catalyzed by Electron Transferring Flavoprotein (Etf) and Butyryl-CoA Dehydrogenase (Bcd) of *Acidaminococcus fermentans*. J Biol Chem **289**:5145–5157.

139. **Demmer JK**, **Huang H**, **Wang S**, **Demmer U**, **Thauer RK**, **Ermler U**. 2015. Insights into Flavin-based Electron Bifurcation via the NADH-dependent Reduced Ferredoxin: NADP oxidoreductase Structure. J Biol Chem. **290**:21985–95.

140. **Kaster A-K**, **Moll J**, **Parey K**, **Thauer RK**. 2011. Coupling of ferredoxin and heterodisulfide reduction via electron bifurcation in hydrogenotrophic methanogenic archaea. Proc Natl Acad Sci **108**:2981–2986.

141. **Costa KC**, **Wong PM**, **Wang T**, **Lie TJ**, **Dodsworth JA**, **Swanson I**, **Burn JA**, **Hackett M**, **Leigh JA**. 2010. Protein complexing in a methanogen suggests electron bifurcation and electron delivery from formate to heterodisulfide reductase. Proc Natl Acad Sci **107**:11050–11055.

142. **Stojanowic A**, **Mander GJ**, **Duin EC**, **Hedderich R**. 2003. Physiological role of the F_{420}-non-reducing hydrogenase (Mvh) from *Methanothermobacter marburgensis*. Arch Microbiol **180**:194–203.

143. **Hedderich R**, **Koch J**, **Linder D**, **Thauer RK**. 1994. The Heterodisulfide Reductase from *Methanobacterium Thermoautotrophicum* Contains Sequence Motifs Characteristic of pyridine-Nucleotide-Dependent Thioredoxin Reductases. Eur J Biochem **225**:253–261.

144. **Hamann N**, **Mander GJ**, **Shokes JE**, **Scott RA**, **Bennati M**, **Hedderich R**. 2007. A Cysteine-Rich CCG Domain Contains a Novel [4Fe-4S] Cluster Binding Motif As Deduced from Studies with Subunit B of Heterodisulfide Reductase from *Methanothermobacter marburgensis*. Biochemistry (Mosc) **46**:12875–12885.

145. **Duin EC**, **Madadi-Kahkesh S**, **Hedderich R**, **Clay MD**, **Johnson MK**. 2002. Heterodisulfide reductase from *Methanothermobacter marburgensi*s contains an active-site [4Fe-4S] cluster that is directly involved in mediating heterodisulfide reduction. FEBS Lett **512**:263–268.

146. **Duin EC**, **Bauer C**, **Jaun B**, **Hedderich R**. 2003. Coenzyme M binds to a [4Fe–4S] cluster in the active site of heterodisulfide reductase as deduced from EPR studies with the [^{33}S] coenzyme M-treated enzyme. FEBS Lett **538**:81–84.

147. **Nitschke W**, **Russell MJ**. 2012. Redox bifurcations: Mechanisms and importance to life now, and at its origin. BioEssays **34**:106–109.

148. **Noll KM**, **Donnelly MI**, **Wolfe RS**. 1987. Synthesis of 7-mercaptoheptanoylthreonine phosphate and its activity in the methyl coenzyme M methyl reductase system. J Biol Chem **262**:513–515.

149. **Costa KC**, **Lie TJ**, **Xia Q**, **Leigh JA**. 2013. VhuD Facilitates Electron Flow from H2 or Formate to Heterodisulfide Reductase in *Methanococcus maripaludis*. J Bacteriol **195**:5160–5165.